

**MODELLING AND EXPERIMENTATION
ON AIR HYBRID ENGINE CONCEPTS
FOR AUTOMOTIVE APPLICATIONS**

A thesis submitted for the degree of Doctor of Philosophy

by

Christodoulos Psanis

School of Engineering and Design

Brunel University

West London, United Kingdom

July 2007

Brunel University

School of Engineering and Design

West London, United Kingdom

Christodoulos Psanis

Modelling and Experiments on Air Hybrid Engine Concepts for Automotive Applications

July 2007, PhD

Abstract

Hybrid powertrains that use compressed air to help power a vehicle could dramatically improve the fuel economy, particularly in cities and urban areas where the traffic conditions involve a lot of starts and stops. In such conditions, a large amount of fuel is needed to accelerate the vehicle, and much of this is converted to heat in brake friction during decelerations. Capturing, storing and reusing this braking energy to produce additional power can therefore improve fuel efficiency.

In this study, three approaches towards air hybrid powertrains are proposed and analyzed. In the first approach, an energy recovery valve or two shut-off valves connected to a convenient access hole on the engine cylinder is proposed to enable the cylinder to operate as a regenerative compressor and/or expander when required. In the second approach, one of the exhaust valves in an engine equipped with a Fully Variable Valve Actuation (FVVA) system is pneumatically or hydraulically operated as a dedicated gas transfer valve connected to an air reservoir. The third approach combines the advantages of the conventional valvetrain's simplicity with emerging production technologies. In order to achieve this, two well established technologies are used in addition to valve deactivation; Variable Valve Timing (VVT) and/or Cam Profile Switching (CPS). Provided that a conventional, camshaft-operated variable valvetrain is used, the need of adopting fully variable valve actuation is eliminated and thus only minor modifications to the engine architecture are required.

The aforementioned concepts are described in details. Some basic principles of their operation are also discussed in order to provide a better understanding on how fuel economy is achieved by means of engine hybridization and regenerative braking. Both

experimental and computational results are presented and compared. Finally, a vehicle and driveline model, which simulates the operation of a typical passenger vehicle in urban driving conditions and predicts the efficiency of the energy regeneration, has been set up and used to study the effects of the application of each air hybrid concept on the vehicle's energy usage throughout the New European Driving Cycle (NEDC) and the 10-15 driving cycle.

The results have shown that each concept involves the optimization of valve timing for the best regenerative energy recovery and its subsequent usage. For the modelled vehicle, it has been shown that any of the three concept engines is capable of providing more braking power than needed during every deceleration and braking process, especially throughout the urban driving part of each cycle. The recovered braking energy in the form of compressed air has proved to be always sufficient to start the engine, if stop-and-start engine operation strategy is to be adopted.

Acknowledgments

Many people have been helpful in the completion of this dissertation and it is with appreciation that these individuals are acknowledged here.

First of all, I would like to express my thankfulness to my supervisor, Professor Hua Zhao, for his keen interest, excellent supervision, continuous support and encouragement throughout this work. I am also grateful to Dr. Xi Jiang and Dr. Tom Ma for their valuable assistance, generous support, excellent advice and overall project directions during the preparation of this Thesis.

Furthermore, thanks are due to Mr. Navin Kalian, Mr. Panagiotis Braimakis and Mr. Athanasios Liakos for their valuable help in using Labview, Matlab and Photoshop software respectively. I would also like to thank Mr. Johnathon Soddy from Lotus Cars for his valuable help in setting up and using Lotus's Active Valve Train (AVT) for the experimental facility.

Most of my deepest gratitude is expressed to my parents, Kyriakos and Eirini, my grandmother Theodoti and my brother Manos for all their help, financial and moral support and encouragement during my postgraduate studies in the United Kingdom.

Last, but not least, I would like to express my gratitude and appreciation to my friends and colleagues: Konstantinos, Dimitris, Nikos, Gregory, Arash, Shervin, George, Kostas, Thimios, Sotiris, Mario, Nikos and Andriana for their constant encouragement, support and understanding.

Thank you all. Without your help it would have been never possible for me to pursue a Philosophy Doctorate Degree. I will be forever grateful.

Nomenclature

Acronyms

ABDC	After Bottom Dead Centre
AC	Alternating Current
AEVC	After Exhaust Valve Close
AEVO	After Exhaust Valve Open
AFM	Air Flow Meter
AGVC	After Gas transfer Valve Close
AGVO	After Gas transfer Valve Open
AIVC	After Exhaust Valve Close
AIVC	After Exhaust Valve Open
ATDC	After Top Dead Centre
AVCS	Active Valve Control System
AVT	Active Valve Train
BBDC	Before Bottom Dead Centre
BDC	Bottom Dead Centre
BEVC	Before Exhaust Valve Close
BEVO	Before Exhaust Valve Open
BGVC	Before Gas transfer Valve Close
BGVO	Before Gas transfer Valve Open
BIVC	Before Exhaust Valve Close
BIVC	Before Exhaust Valve Open
bmep	brake mean effective pressure
BTDC	Before Top Dead Centre
CA	Crank Angle
CAI	Controlled Auto-Ignition
CATC	Compressed Air Transfer Coefficient
CAFE	Corporate Average Fuel Economy
CFD	Computational Fluid Dynamics
CI	Compression Ignition
CM	Compressor Mode
CNG	Compressed Natural Gas
CPS	Cam Profile Switching

CVT	Continuously Variable Transmission
DAC	Digital to Analogue Converter
DAQ	Data Acquisition
DC	Direct Current
DCL	Differential Cylinder Loading
DNR	Drive Neutral Reverse
ECE	Economic Commission for Europe
ECV	Energy Control Valve
EGR	Exhaust Gas Recirculation
EHSV	Electro-Hydraulic Servo Valve
EM	Expander Mode
emf	electromotive force
ERV	Energy Recovery Valve
EU	European Union
EUDC	European Urban Driving Cycle
EVC	Exhaust Valve Open
EVO	Exhaust Valve Close
EVPG	Engine Valve Profile Generator
f _{mep}	frictional mean effective pressure
FTP	Federal Test Procedure
FVVA	Fully Variable Valve Actuation
FVVT	Fully Variable Valve Train
GDI	Gasoline Direct Injection
GVC	Gas transfer Valve Close
GVO	Gas transfer Valve Open
HCCI	Homogeneous Charge Compression Ignition
HEV	Hybrid Electric Vehicle
HPP	Hydraulic Power Pack
i _{mep}	indicated mean effective pressure
IC	Internal Combustion
IVC	Intake Valve Close
IVO	Intake Valve Open
kmph	kilometres per hour (km/h)
LA	Los Angeles
LCD	Liquid Crystal Display

map	manifold absolute pressure
mpg	miles per gallon (m/g)
mph	miles per hour (m/h)
NA	Naturally Aspirated
NEDC	New European Driving Cycle
NYC	New York City
PC	Personal Computer
PID	Proportional-Integral-Differential
ppr	pulses per revolution
rpm	revolutions per minute
rps	revolutions per second
SI	Spark Ignition
SUV	Sport Utility Vehicle
TDC	Top Dead Centre
TTL	Transistor-Transistor Logic
UPS	Uninterruptible Power Supply
USA	United States of America
VANOS	VARiable NOckenwellen Steuerung
VTEC	Variable valve Timing and lift Electronic Control
VVTi	Variable Valve Timing with intelligence

Notation

η_{air}	compressed air discharge efficiency
η_f	fuel conversion efficiency
η_{fd}	mechanical efficiency of the final drive
η_g	mechanical efficiency of the transmission gear
η_m	mechanical efficiency
η_v	volumetric efficiency
π	pi (3.14159)
ρ_a	air density
a	acceleration
A_v	vehicle frontal area

C_1, C_2, C_3, C_4, C_5	rolling resistance coefficients
C_D	aerodynamic drag coefficient
C_r	rolling drag coefficient
D	piston diameter (bore)
F_a	aerodynamic drag force
F_b	brake force
F_r	rolling drag force
F_w	wheel force
g	gravitational acceleration
H_f	calorific or heating value of the fuel
k_{fd}	final drive ratio
k_g	transmission gear ratio
$m_{a,ex}$	mass of air past the exhaust valve
$m_{a,gtv}$	mass of air past the gas transfer valve
$m_{a,in}$	mass of air past the intake valve
\dot{m}_f	fuel mass flow
m_v	vehicular mass
N	rotational speed
p	pressure
P_b	brake power
p_c	in-cylinder pressure
P_f	frictional power
P_i	indicated power
p_{max}	maximum cylinder pressure
p_t	airtank pressure
R	universal gas constant
R_c	compression ratio
r_w	wheel radius
S	piston stroke
sfc	specific fuel consumption
t	time
T	temperature
T_b	brake torque
T_f	frictional torque
T_i	indicated torque

u	vehicle speed
V	volume
V _c	clearance volume
V _d	displacement volume
W _b	brake work
W _f	frictional work
W _i	indicated work

Subscripts

b	braking
d	driving

Chemical symbols

CO	carbon monoxide
CO ₂	carbon dioxide
HC	hydrocarbons
NO _x	nitrogen oxides

Table of Contents

Abstract	i
Acknowledgments	iii
Nomenclature	iv
Chapter 1: Introduction	1
1.1. Introduction	1
1.2. Project objectives	4
1.3. Thesis outline	4
Chapter 2: Literature Review	7
2.1. Introduction	7
2.2. IC engine efficiency	8
2.3. Benefits of vehicle hybridization	9
2.4. Classification of hybrid engines.....	10
2.4.1. Series hybrids	10
2.4.2. Parallel hybrids	11
2.4.3. Series-parallel hybrids.....	12
2.5. Hydraulic, electric and mechanical hybrid vehicles	13
2.5.1 Hydraulic hybrids.....	13
2.5.2 Electric hybrids	15
2.5.3 Mechanical hybrids	18
2.6. Air hybrids	22
2.7. Motivation for novel air hybrid concepts.....	27
2.8. Summary	28
Chapter 3: Air Hybrid Concepts	31
3.1. Introduction	31
3.2. Air hybrid engine with an Energy Recovery Valve (ERV)	31
3.2.1. Description	31
3.2.2. Operation.....	34
3.3. Air hybrid engine with Fully Variable Valve Actuation (FVVA)	37
3.3.1. Description	37
3.3.2. Operation.....	38
3.4. Air hybrid engine with a reed valve inside the intake port	42
3.4.1. Description	42

3.4.2. Operation.....	44
3.5. Summary	47
Chapter 4: Modeling of the Concepts	49
4.1. Introduction.....	49
4.2. Engine modeling tool.....	49
4.3. Normal firing and air hybrid engine operating parameters.....	50
4.3.1. Performance coefficients.....	50
4.3.2. Compressed Air Transfer Coefficients (CATC)	52
4.3.2.1. Air compressor	53
4.3.2.2. Air expander.....	54
4.4. Concept 1: Engine with Energy Recovery Valve (ERV).....	55
4.4.1. Model description	55
4.4.2. Valve timing optimization	58
4.3.2.1. ERV timing for air compressor mode.....	58
4.3.2.2. ERV timing for air expander mode.....	62
4.3.3. Modeling results and discussion	68
4.3.3.1. Airtank charging (air compressor mode)	68
4.3.3.2. Braking bmep (air compressor mode).....	70
4.3.3.3. Braking CATC (air compressor mode).....	72
4.3.3.4. Airtank discharging (air expander mode)	73
4.3.3.5. Driving bmep (air expander mode).....	76
4.3.3.6. Driving CATC (air expander mode).....	77
4.4. Concept 2: Engine with Fully Variable Valve Actuation (FVVA).....	79
4.4.1. Model description	79
4.4.2. Valve timing optimization	80
4.4.2.1. Valve timing for air compressor mode	81
4.4.2.2. Valve timing for air expander mode	86
4.4.3. Modeling results and discussion	88
4.3.3.1. Airtank charging (air compressor mode)	89
4.3.3.2. Braking bmep (air compressor mode).....	90
4.3.3.4. Airtank discharging (air expander mode)	90
4.3.3.5. Driving bmep (air expander mode).....	91
4.5. Concept 3: Engine with reed valve inside the intake port.....	93
4.5.1. Model description	93
4.5.2. Valve timing optimization	96

4.5.2.1. Valve timing for air compressor mode	96
4.5.2.2. Valve timing for air expander mode	102
4.5.3. Modeling results and discussion	108
4.5.3.1. Airtank charging (air compressor mode)	108
4.5.3.2. Braking bmep (air compressor mode).....	109
4.5.3.3. Air mass transfer (air compressor mode).....	111
4.5.3.4. Airtank discharging (air expander mode)	112
4.5.3.5. Driving bmep (air expander mode).....	114
4.5.3.6. Air mass transfer (air expander mode).....	116
4.5.4. Alternative actuation of intake valve 6	117
4.6. Summary	119
Chapter 5: Experimental Test Facility.....	122
5.1. Introduction	122
5.2. Single cylinder base engine and valve actuation system	122
5.2.1. Intake and exhaust systems	124
5.2.2. Combustion chamber geometry	125
5.2.3. Airtank	126
5.3. Dynamometer control panel and test bed.....	126
5.3.1. Test bed	126
5.3.2. Dynamometer.....	127
5.3.3. Control panel.....	128
5.4. Lotus AVT system	129
5.4.1. Cylinder head	129
5.4.2. Hydraulic Power Pack (HPP).....	131
5.4.3. User interface software	132
5.4.4. Uninterruptible Power Supply (UPS)	132
5.4.5. AVT controller	132
5.4.6. Crankshaft encoder	134
5.4.7. Hydraulic fluid	134
5.5. Pressure and temperature measurement instrumentation.....	134
5.5.1. Compressed air temperature measurement	134
5.5.2. In-cylinder pressure measurement	135
5.5.3. Airtank pressure measurement.....	137
5.5.4. Data acquisition (DAQ) system	138
5.6. Experimental work.....	140

5.6.1. Conventional 4-stroke cycle - air compressor mode.....	142
5.6.1.1. Airtank pressure	142
5.6.1.2. Braking imep, fmep and bmep.....	145
5.6.2. 2-stroke engine cycle - air compressor mode.....	148
5.6.2.1. Airtank pressure	149
5.6.2.2. Braking imep, bmep and fmep.....	152
5.6.3. Conventional 4-stroke cycle - air expander mode	155
5.6.3.1. Airtank pressure	158
5.6.3.2. Driving imep, bmep and fmep	159
5.7. Comparison between predicted and experimental results.....	161
5.8. Summary	163
Chapter 6: Vehicle Simulation.....	166
6.1. Introduction.....	166
6.2. Driving cycles	167
6.2.1 European driving cycles.....	167
6.2.1.1. ECE 15	167
6.2.1.2. EUDC.....	167
6.2.1.3. EUDCL	168
6.2.1.4. NEDC.....	168
6.2.1.5. HYZEM	168
6.2.2. US driving cycles	168
6.2.2.1. NYCC.....	168
6.2.2.2. FTP-72	168
6.2.2.3. LA-92	169
6.2.2.4. US-06	169
6.2.2.5. FTP-75	169
6.2.3. Japanese driving cycles	169
6.2.3.1. 10 Mode	169
6.2.3.2. 15 Mode	169
6.2.3.3. 10-15 Mode	169
6.3. Vehicle and driveline model	170
6.3.1. Acceleration	170
6.3.2. Rolling drag force	170
6.3.3. Aerodynamic drag force.....	171
6.3.4. Wheel force	171

6.3.5. Brake force	172
6.4. Airtank pressure and temperature model	173
6.5. Response maps	175
6.6. Vehicle simulation	176
6.6.1. Gear shift pattern and simulation decision diagram.....	177
6.6.2. Acquisition of user-defined inputs	180
6.6.3. Data processing	181
6.6.4. Extraction of the simulation results	182
6.7. Simulation results and discussion	183
6.7.1. Engine speed	183
6.7.2. Torque, power and energy demand.....	184
6.7.3. Braking energy recovered and driving energy generated	187
6.7.4. Airtank pressure	192
6.8. Summary	195
Chapter 7: Conclusions and Recommendations for Further Work.....	196
7.1. Conclusions.....	196
7.1.1. Modelling work.....	196
7.1.1.1. Concept 1	196
7.1.1.2. Concept 2	197
7.1.1.3. Concept 3	198
7.1.2. Experimental work.....	199
7.1.2.1. 4-stroke compressor	199
7.1.2.2. 2-stroke air compressor.....	200
7.1.2.3. 4-stroke expander.....	201
7.1.3. Vehicle simulation	201
7.2. Recommendations for further work	202
7.2.1. Modelling work.....	202
7.2.2. Experimental work.....	203
7.2.3. Vehicle simulation	203
References	204
Appendix.....	214

Chapter 1: Introduction

1.1. Introduction

Although J. J. E. Lenoir was the inventor of the internal combustion (IC) engine in 1860, it was in 1876 when Nicolaus A. Otto developed the spark-ignition (SI) engine, which is also called “*Otto*” or “*gasoline*” or “*petrol*” engine. More than one decade later, in 1892, Rudolf Diesel introduced the compression-ignition (CI) engine. Since then, huge steps have been made in the direction of the development of IC engines. Due to the absence of viable alternatives, both SI and CI engines have played a dominant role in the fields of transportation and energy production for over a century and are currently growing exponentially. The cost and availability of suitable fuels have become an issue, provided that the majority of engine fuels derive from crude oil and it is difficult to estimate how long oil supplies will last, while in the same time current world consumption of oil is rising proportionally to engine utilization. As the future of IC engines is also influenced by environmental constraints, especially after the global warming became an important concern, the search has moved on to find new, cleaner, more efficient and economic alternatives.

With the continuous development of research methods throughout these years, our knowledge of engine processes has increased. The application of new technologies, such as the three-way catalytic converter, variable valve timing (VVT), electronic engine management and direct fuel injection in both diesel and gasoline engines (GDI), led to the development of modern IC engines which display high overall global efficiencies. In addition, the introduction of selective cylinder deactivation, as well as alternative combustion technologies, such as Exhaust Gas Recirculation (EGR) and Controlled AutoIgnition (CAI), have reduced the emission of harmful Nitrogen Oxides (NO_x), Hydrocarbons (HC), Carbon Monoxide (CO) and particulates, making the engines less polluting for the environment than ever.

However, the fuel economy potentials cannot be fully exploited in automotive applications as in real driving conditions the average engine load (and thus efficiency) levels are relatively low. When it comes to a typical pattern of urban driving, the situation is even worse as a significant portion of fuel is spent during frequent accelerations and long time periods of engine idling. In addition, kinetic energy during decelerations is lost, mainly

transformed in unused thermal energy on the brakes, as it cannot be converted back to chemical energy due to the irreversibility of the process. The key to improve fuel consumption is to develop a system which would efficiently capture part of this energy and reuse it upon demand, without sacrificing the engine's driveability and credibility. Furthermore, it should not necessitate drastic modifications to the engine or the drivetrain and it must be cost-effective enough to be widely applied to all types of vehicles, from commercial passenger cars to large trucks and other means of transportation. Leading car manufacturers over the globe are currently developing and promoting hybrid powertrains to propel their vehicles. Most of them combine a conventional IC engine, a reversible energy converter and an energy storage subsystem. During regenerative braking, the kinetic energy of the vehicle is stored in an energy storing device instead of being dissipated as heat by the conventional braking system. The stored energy is then recycled to cover the power demand of the vehicle during a subsequent acceleration or cruise. The energy converter is most commonly an electric generator and the energy storing subsystem is a battery or super-capacitor, which is used to power the vehicle via an electric motor.

Although this is an effective approach to improve fuel economy and reduce emissions, especially for vehicles in heavy stop-and-go traffic conditions, research in the field of alternative hybrid powertrains is currently conducted to overcome the downsides of electric hybrids, such as cost and weight. Even though it does not need as many batteries as a pure electric vehicle, an electric hybrid car has to carry the additional weight of the electric motor, the generator and the power cells, which in some applications can weigh several hundred kilograms, implying a large vehicular mass penalty to energy efficiency. The manufacturing and fitting cost of all the necessary electrical components is considerably high, compared to a conventional car. Furthermore, regenerative torque is not large enough to cover the required braking torque and regenerative braking cannot be used when the batteries are of a high state of charge (SOC), in order to increase the anticipated battery life.

In order to overcome the aforementioned drawbacks, research in the field of hybrid engines has pursued alternative concepts, where the energy converter and storage subsystems are different than the commonly used electric generator/motor and batteries respectively. In the case of a mechanical hybrid, for example, a massive flywheel is driven by the wheels during deceleration, via a convenient gearbox and clutch. The same arrangement is used to propel the vehicle when required. The kinetic energy that is stored and conserved in the flywheel is a function of the square of the flywheel's rotational speed.

Hydraulic hybrids utilize an accumulator as an energy storage subsystem and one or more hydraulic pumps/motors to convert kinetic energy to dynamic. During braking, the vehicle's kinetic energy is captured as hydraulic fluid is pumped from a low-pressure reservoir to the accumulator. During acceleration, fluid in the pressurized accumulator drives the hydraulic motor, thus providing torque to the drive shaft to supplement or substitute the engine's power during acceleration. An air hybrid is a far more sophisticated concept. During deceleration, a convenient engine management takes ignition and fuel injection off. That allows the engine itself to be used as an air compressor, absorbing power through the pistons and the crankshaft and thus braking the vehicle while using the existing drivetrain. Compressed air is stored in an airtank and it can be used either to propel the vehicle by operating the engine as an air expander or improving the drivability of turbo diesel and downsized high-performance engines by supplementing the supercharger and thus eliminating turbo lag.

Both electric and hydraulic hybrid engines are *dual-stage* hybrids because energy absorption and storage takes place in two steps: (1) Kinetic energy is transformed to electric or potential energy by means of a generator or hydraulic pump respectively and then (2) the energy is stored in a battery or an accumulator. The reverse pattern is followed during discharge: (1) Energy from the storage medium is transferred to the secondary propulsion system (electric or hydraulic motor) and (2) it is transformed to kinetic energy to propel the vehicle. Regenerative braking is a single-step procedure in mechanical and air hybrids and thus they are *single-stage* hybrids. Both storage devices (flywheel and airtank) are directly linked to the vehicle's drivetrain through a convenient gearbox and the engine cylinder respectively.

Along with experimentation, extensive simulation studies have been widely undertaken. Engine modeling can be both cheaper and less time consuming than conducting the corresponding experiments. It is also a tool for identifying important influential factors in parametric studies and helps the researchers to evaluate various hybrid engine concepts at low cost. Most researchers prefer commercial packages such as Ricardo's Wave or its main competitor, GT-POWER by Gamma Technologies. Apart from the simulation of gas flow and heat transfer, they contain many specialized features needed for IC engine modelling, such as fuel injection, valve actuation and turbocharging. However, some others prefer to use software like Simulink's Matlab to create their own simulation programs, geared to their particular needs and requirements.

1.2. Project objectives

The present project aims for the following goals:

- i) Provide a better understanding of the hybrid engines and air hybrids in particular, by giving detailed information on the design and operation of a number of viable air hybrid designs that demonstrate satisfactory energy storage and regeneration efficiencies as well as improved fuel consumption.
- ii) Employ a commercial simulation software (Ricardo's WAVE) to carry out systematic studies on the effects of various parameters, such as airtank volume, air pressure and temperature, engine speed, valve timing, etc on engine torque output, compressed air transfer coefficient (CATC) and airtank charge and discharge rate.
- iii) Develop an appropriate algorithm to investigate the application of regenerative braking on a passenger car driven throughout the New European Driving Cycle (NEDC) and the Japanese 10-15 Mode driving cycle and examine the global fuel efficiency improvement in particular.
- iv) Develop and commission an experimental air hybrid engine, featuring a Fully Variable Valve Actuation (FVVA) camless valvetrain provided by Lotus Cars and compare the experimental results against the simulation data.

1.3. Thesis outline

Following the present introduction, Chapter two contains a review of literature related to this project and it is arranged under seven sections. An introductory outline of modern IC engines, with an emphasis on their performance coefficients and fuel economy in regard to vehicles, is given in the first two sections. The next section refers to the benefits which derive from the utilization of hybrid engines in order to provide a context for the necessity of research and development of that area, followed by a section which discusses the classification of hybrid engines. The following section details current hybrid concepts and the various technologies upon which they are based. Apart from the well-known electric hybrid, mechanical and hydraulic hybrids are also discussed briefly. The penultimate section covers a range of papers on the research which has already been done on air hybrid engines. Finally, both the benefits and drawbacks of the current concepts are highlighted, thus providing a basis for the investigation of novel air hybrid engines.

Three novel air hybrid concepts are presented in Chapter three: The first one incorporates a two-step Energy Recovery Valve (ERV) and a buffer volume between the engine cylinder and the air storage tank. A fully variable valve operation, realized by hydraulic camless valvetrain, is utilized for the second concept and it allows for the direct connection of the engine cylinder to the airtank. The last air hybrid model incorporates a reed valve in one of the intake ports as well as an intake camshaft phasing mechanism, in order to divert the flow of compressed air to the airtank through an auxiliary chamber. A detailed description of the gas exchange cycles which are experienced by the working fluid is given in order to enhance the understanding on the operation of each one of the air hybrid models.

Chapter four contains the systematic studies carried out to investigate the parameters which have an impact on the performance of an air hybrid engine, in order to optimise them for maximum regenerative braking efficiency over a wide range of engine speeds. Ricardo's Wave simulation software is employed for creating *response maps*, which describe how the engine responds to engine speed and airtank pressure variations. Response maps are two-dimensional tables containing data for engine torque, pressure, temperature and mass of the air charge transferred between the airtank and the engine at the end of each compressor or expander cycle, for a wide range of engine speeds (at 500 rpm intervals) and airtank pressures (at 5 bar intervals). The results are analyzed and discussed in a separate section.

The experimental test facility is described in Chapter five. The research engine with its specially designed cylinder head is discussed in detail together with the valve control hardware and software, the diagnostic instrumentation and the data acquisition system. The methodology followed for the performed tests is also detailed and the experimental results are discussed in a separate section.

The performance of a hybrid engine fitted on a typical passenger car driven throughout the NEDC and 10-15 Mode driving cycle is the subject of Chapter six. Torque output, compressed air charge mass, pressure and temperature response maps for each air hybrid concept are used for feeding data points to a cycle-by-cycle vehicle simulation algorithm, based on the Simulink's MatLab software. Useful conclusions for the engine operation and valve timing strategies that must be followed in order to fully exploit the benefits of regenerative braking are established by the simulation results.

Chapter seven contains the general outcomes which are drawn together from separate sections and they give a broad overview of the knowledge gained during the progress of this project. Recommendations for further work are also made in the direction of exploiting the air hybrid engine potentials for further fuel economy.

Finally, in order to provide a better understanding of the air hybrid arrangement and operation, supplementary schematics are provided in the Appendix.

Chapter 2: Literature Review

2.1. Introduction

Any device which converts heat energy into mechanical work and only heat and work may pass across its boundaries is a *heat engine*. It typically uses energy provided in the form of heat to do work and then rejects a portion of heat that cannot be used. The IC engine is a type of heat engine where the working fluid consists of the air-fuel mixture and the products of combustion. Like all heat engines, IC engines are subjected to the second law of thermodynamics. The law is a general principle that places constraints upon the direction of heat transfer and the attainable efficiency of the heat engine. It states that it is impossible to extract an amount of heat from a high energy temperature reservoir and use it all to do work; some amount of heat must be exhausted to a low temperature energy reservoir [1]. In the case of the IC engine, the hot reservoir (also called the “*hot source*”) is the engine cylinder, the cold reservoir (also called the “*cold sink*”) is the atmosphere and the resulting work done is the imposed motion of the piston.

Unlike ideal thermodynamic cycles, not all of the heat content of a fuel can be transferred into useable work during the combustion process in an IC engine. The many different losses that occur during the transformation of heat energy into work can be divided into two main categories; thermodynamic and mechanical. Thermodynamic losses mainly include heat loss to the cooling system and losses by radiation and convection to the surrounding air, heat rejected and lost to the atmosphere in the exhaust gases, inefficient combustion or lack of perfect combustion and cylinder pressure loss due to leaking piston rings.

There are several kinds of mechanical losses and not all of them are present in every engine. These losses (also called “*frictional losses*”) include power consumed to overcome bearing friction, piston and piston ring to cylinder wall friction, power required to operate valves, scavenging air blowers, mechanically driven superchargers, as well as other auxiliary components, such as fuel pumps, oil pumps, electricity generators and so forth. Although frictional losses cannot be eliminated, they can be kept at a minimum by maintaining all engine components in their best mechanical condition. The brake horsepower, finally delivered as useful work by the engine, is given by deducting the total sum of the mechanical losses from the indicated horsepower developed in the cylinders.

2.2. IC engine efficiency

The purpose of an IC engine is to convert the chemical energy contained in the fuel to mechanical power. The fuel consumption is expressed as a flow rate; fuel mass flow per unit time. The *specific* fuel consumption is the fuel flow rate per unit power output and it is an indicator of how efficiently an engine is using the supplied fuel to produce work. It is obvious that lower specific fuel consumption values enhance fuel economy.

$$sfc = \frac{\dot{m}_f}{P} \quad \text{Equation 2.1}$$

where \dot{m} is the fuel flow rate (mass per unit time) and P is the engine's power output in watts. When that is brake power (P_b), the above equation defines the brake thermal efficiency. When that is indicated power (P_i), the above equation defines the indicated thermal efficiency.

Fuel conversion efficiency (η_f), also called "*thermal efficiency*", expresses a comparison between the amount of power developed by an engine to the energy it consumes. That energy is measured by means of the heating value of the consumed fuel:

$$\eta_f = \frac{P}{\dot{m} \cdot H_f} \quad \text{Equation 2.2}$$

where H_f is the fuel calorific value or heating value which expresses the amount of heat released from the combustion process per unit mass of fuel and it can be measured experimentally with a bomb calorimeter (see Figure A1 in the Appendix) [2]. At this point it should be noted that only a portion of the potential thermal energy of the fuel supplied to the engine is released during combustion, as the actual process is incomplete due to the insufficient time available for combustion. When enough air is present in the cylinder to fully oxidize the fuel, η_f can be as high as 96% [3].

Mechanical efficiency (η_m) expresses the portion of indicated power that is finally delivered to the engine output and it is the ratio of P_b to P_i . Typical values are high as 90% for low engine speeds and descend down to 75% for higher speeds, as fmep increases. It is close to zero when the engine is idling [3]:

$$\eta_m = \frac{P_b}{P_i} = \frac{W_b}{W_i} = \frac{bmep}{imep} \quad \text{Equation 2.3}$$

Volumetric efficiency (η_v) is a measure of the effectiveness of the induction and exhaust processes and it is expressed by the ratio of the mass of air inhaled per cylinder per cycle to the mass of air needed to occupy the swept volume of the cylinder at ambient pressure and temperature conditions:

$$\eta_v = \frac{m_a}{\rho_a \cdot V_d} \quad \text{Equation 2.4}$$

where m_a is the mass of air inducted per cycle, ρ_a is the air density at ambient conditions and V_d is the displacement volume. Typical values of η_v are within the range of 80% - 90% for naturally aspirated gasoline engines. Diesel engines display somewhat higher volumetric efficiencies because of the absence of the throttle valve in their intake system, while forced induction engines realize volumetric efficiencies higher than 100% [3].

2.3. Benefits of vehicle hybridization

Vehicles need substantial power for initial acceleration, as described by the second Newtonian law, and much less when cruising at constant speed. Since automobile engines are sized to meet peak power needs, they are typically over-designed by roughly ten times in order to meet performance targets, such as acceleration and starting gradeability [4]. They are therefore being operated under part-load and thus low efficiency for most of the time, as the optimal operation point moves away from the cruising operation point by oversizing the engine [5].

A hybrid system draws on its alternative power source side when peak power is needed. Thus, a downsized IC engine can be used because the engine can be sized for average rather than peak load requirements, which results in enhanced fuel efficiency. More importantly, hybrids have the potential to save fuel by recapturing energy from decelerations (regenerative braking). While friction brakes reject that energy in the form of heat, hybrids can use their energy conversion subsystem to recapture braking energy and store it for later use in acceleration.

Reducing specific fuel consumption lowers exhaust emissions in two ways: Since less fuel is burned, there is a direct reduction in emissions. Additionally, since there is power contribution from the secondary propulsion system when a diesel or gasoline engine is least efficient (i.e. accelerating a vehicle from a stop at low engine speed), emissions are reduced beyond what would be realized simply from lower fuel consumption. Finally, regenerative braking extends the conventional brake system's life and reduces maintenance and servicing needs.

2.4. Classification of hybrid engines

2.4.1. Series hybrids

In 1898 Ferdinand Porsche designed the first series-hybrid vehicle, the *Lohner-Porsche carriage*, which was equipped with a one-cylinder gasoline IC engine that drove an electric generator which powered four electric motors mounted on the wheels. The car was presented at the 1900 World Exhibition in Paris and over 300 of the Lohner-Porsche carriages were sold to the public.

In a series hybrid configuration, the source which provides all of the required power to the transmission and thus to the wheels is other than the IC engine. That can be an electric or hydraulic motor, a flywheel, etc. However, a small, effective IC engine and an energy generator are used to provide power to the main propulsion system. Thus, the engine is not mechanically connected to the drivetrain and can be controlled at the optimum efficiency and low emission points, regardless the driving conditions, as it is not required to respond to the rapid changes occurring in traction power demand.

Usually, the propulsion system cannot be operated as a power generator in order to capture energy during decelerations; this is why purely series hybrid configurations are not adopted for energy regeneration. On the other hand, they are more efficient for large energy demands compared to other hybrid arrangements and therefore they are better suited for large vehicles rather than passenger cars, such as trucks and buses, where large weight is of more concern than high acceleration [6]. The name "*series hybrid*" is derived from the fact that the power produced by the IC engine is connected in series to the vehicle propulsion system. A typical series hybrid is shown in Figure 2.1a below.

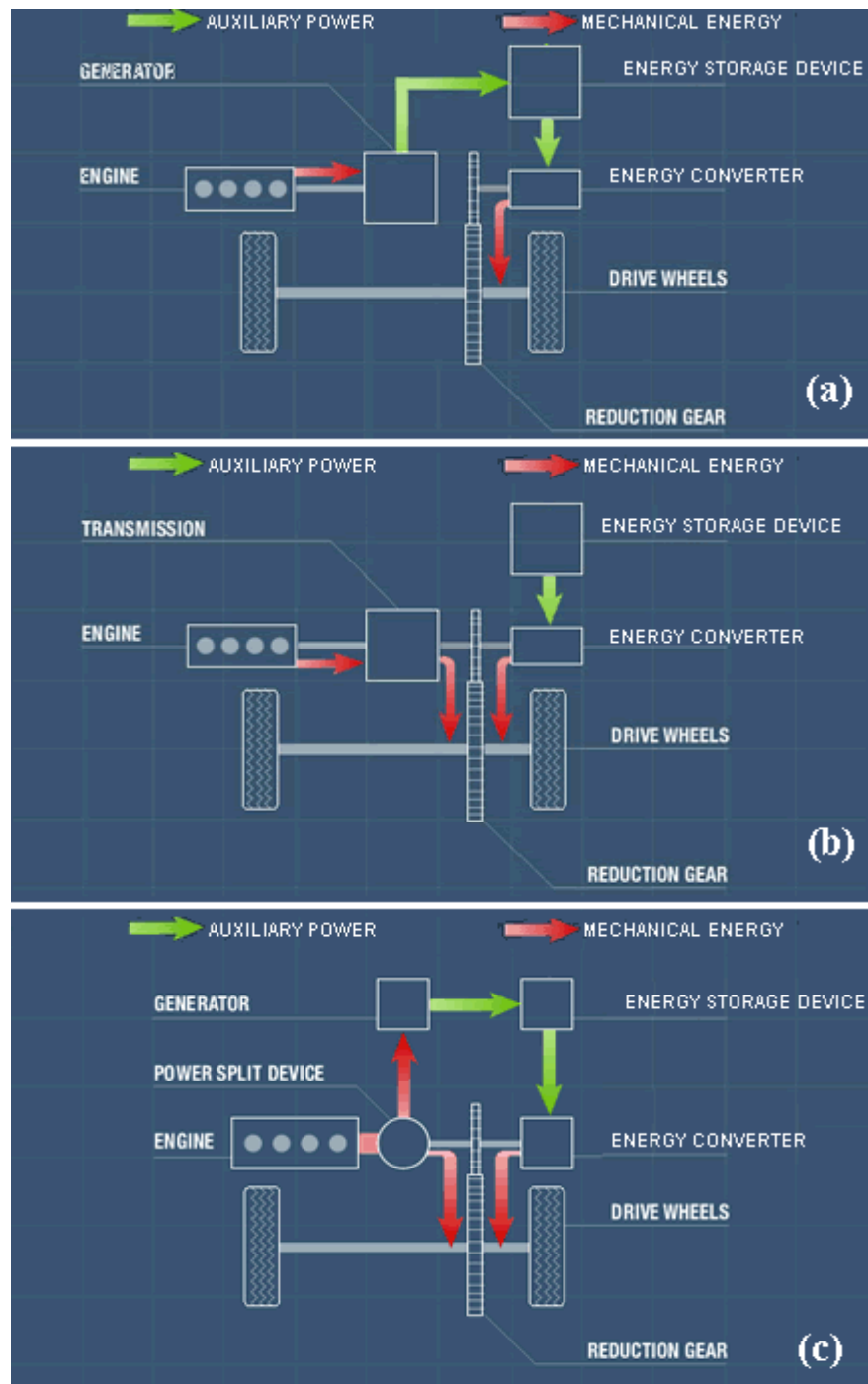


Figure 2.1: Typical series (a), parallel (b) and series-parallel (c) hybrids [7].

2.4.2. Parallel hybrids

Parallel hybrid configurations tend to be more flexible and powerful than series hybrids, but they are also more complex and in some cases they can be more costly. In parallel hybrids, the IC engine is connected to the wheels through a conventional drivetrain (gearbox and clutch) and can therefore directly supply mechanical power to the wheels. Here, an electric or hydraulic motor or flywheel plays the role of the secondary propulsion system and it is added to the drivetrain in parallel to the IC engine, so that it can

supplement the engine's torque. During decelerations, the wheels can drive the electric or hydraulic motor as a generator or pump respectively and charge the energy storage device (accumulator, battery, capacitor, etc) or drive the flywheel and store kinetic energy on it. Honda Insight is a typical electric parallel hybrid car currently in production, where the electric motor also functions as generator for the charging system during decelerations and as a starter, quickly spinning the engine up from stop to idle speed, during start-ups [8]. The schematic of a typical parallel hybrid design is shown in Figure 2.1b above.

2.4.3. Series-parallel hybrids

The first series-parallel hybrid was made back in 1915 by the Woods Motor Vehicle electric car maker and was equipped with a four-cylinder IC engine and an electric motor. Below 15 mph (25 km/h) the electric motor alone drove the vehicle, while above this speed the IC engine cut in to take the car up to its top speed of 35 mph (55 km/h). About 600 “*Dual Power*” cars were made up to 1918.

Series-parallel combined systems feature the characteristics of both series and parallel hybrids. A part of the IC engine's output is used to cover the power demand of the vehicle, while the other part propels the energy generator of the secondary propulsion system. The portion of power is adjusted through a suitable power split device, depending on the driving conditions. This arrangement takes advantage of the energy-efficient secondary propulsion system when the vehicle runs in the low speed range, and shifts to the IC engine when it runs in the high speed range. In other words, the system can control the dual sources of power for optimum energy-efficient operation under any driving conditions. With the series-parallel hybrid system, it is possible to drive the wheels using the dual sources of power (IC engine and/or other propulsion system) simultaneously to cover extreme power demands. It is also possible to charge the energy storage device while the vehicle is running, since the electric generator or hydraulic pump or flywheel is integrated into the system.

Series-parallel hybrids are currently employed in passenger cars. Toyota Prius is an example of this so-called “*dual system*”. The mechanical power from the engine is split by a specially designed planetary gear set into the series path (from the engine to the generator) and into the parallel path (from the engine to the driving wheels). It uses a 52kW IC engine which is mechanically coupled to a 23kW electric motor. The motor is used to assist the engine during accelerations and to propel the vehicle at low speeds, when

the engine is not efficient. The electric motor also captures braking energy during decelerations and therefore further lowering the vehicle's fuel consumption [8,9]. A common series-parallel arrangement is shown in Figure 2.1c above.

There are also many other designs currently under research and development that suggest variations to the aforementioned major hybrid categories, such as input-split hybrids, combined-split hybrids, assist hybrids, mild hybrids and plug-in hybrids (also termed "*griddable hybrids*").

2.5. Hydraulic, electric and mechanical hybrid vehicles

2.5.1 Hydraulic hybrids

The inherent power density of hydraulic regenerative braking systems promises a robust, cost-effective means of achieving significant fuel economy in city driving. Typical hydraulic hybrids consist of a single pump/motor, usually of variable displacement, a reservoir and an accumulator. A bleed valve is needed to let the air out of the fluid circuit. There is also a cooling subsystem, which consists of a small circulator, usually electric, which is in charge of circulating the hydraulic fluid through the radiator. Convenient hydraulic poppet-type, spool or solenoid valves serve to:

- i. Connect the pump inlet to the reservoir and the pump outlet to the accumulator during braking.
- ii. Connect the motor inlet to the accumulator and the motor outlet to the reservoir during driving.
- iii. Reverse the aforementioned connections to switch between energy storage and energy regeneration.
- iv. Seal-off the accumulator while idling.

Provided that liquids are incompressible, the fundamental means of storing energy is by compressing hydraulic fluid against an inert gas, most commonly nitrogen, contained in a gas bladder inside the accumulator. There is also an elastomer foam contained in the gas volume, which reduces the loss of stored energy through heat transfer by means of thermally isolating the heated gas and absorbing the liberated heat from the gas during compression (see Figure A2 in the Appendix). Accumulator performance highly affects the

behaviour of the system and it is discussed in detail by Pourmovahed [10]. When extra power is needed, pressure from the gas pushes the fluid through the hydraulic motor, which ties into the vehicle's powertrain. This process reverses during braking; the vehicle's kinetic energy drives the hydraulic motor, which pushes hydraulic fluid back into the accumulator, compressing the nitrogen gas (see Figure 2.2). Common working hydraulic fluid pressure values vary between 300 and 350 bar.

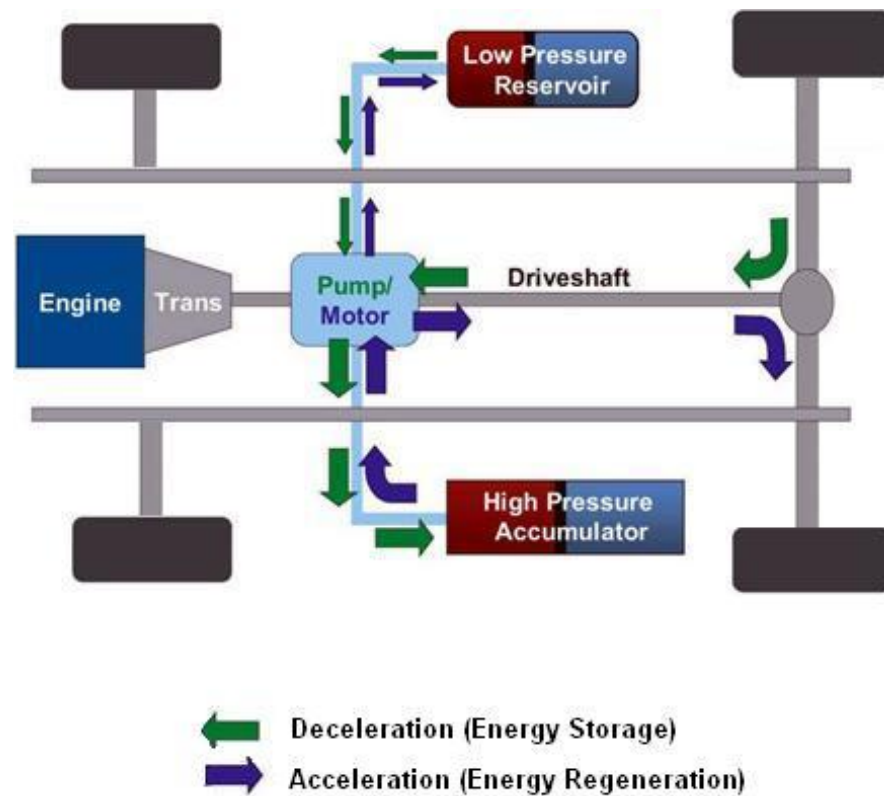


Figure 2.2: Hydraulic hybrid vehicle schematic [11].

While electric hybrids usually apply to light vehicles, hydraulic and mechanical hybrids are mainly employed in trucks, buses and SUVs. The Ford Tonka truck, unveiled at the 2002 North American International Auto Show, adopts a hydraulic parallel hybrid power plant capable of regenerating 80% of the braking energy, resulting in a 35% fuel saving over a conventional truck [12]. Motavalli also claims that the energy recovered from a 32-0 mph deceleration is enough to propel the truck for a 0-25 mph acceleration, which is equivalent to a 61% charge-discharge efficiency.

However, Kepner's parametric analysis showed that it was possible for the system to absorb 72% of the braking energy and predicted a fuel economy improvement of 24%, close to what was realized during experiments on a 1999 Lincoln Navigator SUV, in spite of neglecting flow and thermal losses [13]. With an estimated return of 56% of the braking

energy to the drive wheels, Kepner's hydraulic hybrid demonstrates 40% charge-discharge efficiency, much lower than Ford claims for its Tonka SUV. In order to further elevate the system's efficiency, he uses a low-pressure accumulator instead of a reservoir. This is a common practice for avoiding cavitations at the hydraulic pump/motor inlet.

Researchers have also examined the prospect of exploiting the thermal energy included in the engine exhaust to recover more than 100% of the truck's kinetic energy by heating the gas in the accumulator after compression and then cool it after discharge. That enhanced energy regeneration option can only be realized if the temperature of the compressed gas after the end of the compression is lower than that of the engine exhaust. Wicks et al tried to further enhance the efficiency of the above system by carrying out a parametric analysis of operating parameters such as the optimal accumulator volume and nominal pressure for several cases [14]. Their research showed that the thermally enhanced system option could virtually double the amount of stored energy but its implementation is constrained by practical difficulties. They also concluded that the hydraulic hybrid used in heavy vehicles for energy regeneration has advantages over other designs.

The fact that the accumulator can be charged only while the vehicle is moving, since the hydraulic pump/motor is connected to the vehicle's driveshaft, sets several constraints on the power which can be delivered to the wheels during accelerations. It is possible for a vehicle with an unusual driving sequence (light decelerations and heavy accelerations) to end up at zero speed with little or no stored energy and thus limited acceleration performance. It is therefore necessary to adopt a control strategy which would maintain the stored energy at a nominal level in order to reduce variation and improve drivability. The added weight of the aforementioned components is also an important drawback when it comes to highway driving, where no regenerative braking takes place as the vehicle is mainly cruising at constant speed and thus hydraulic hybrids tend to get worse fuel economy there.

2.5.2 Electric hybrids

A hybrid electric vehicle (HEV) combines two sources of propulsion or energy conversion; an electric motor and a conventional IC engine. Thus, they offer the advantage of the extended driving range and rapid refuelling of conventional vehicles, together with many of the energy and environmental benefits of electric vehicles. A few HEVs are widely available on the market today, such as the Ford Prodigy and Escape hybrid SUV, Nissan

Altima, Toyota Camry and Prius, Honda Insight, Accord hybrid and Civic hybrid, with many other major car manufacturers planning to introduce HEVs in the near future.

Although there are numerous different approaches for electric hybridization, they are all based on the same basic principles. Most popular designs include an electric motor which can also be operated as a generator and/or a starter for the engine and it is connected to the drivetrain through a speed-reduction gearbox [15], an electronic power control system to regulate the torque and/or the speed of the motor [16] and an energy storage system, which most likely is a rechargeable battery cell or a pack of cells connected together. Most commonly used battery types are lead-acid (Pb-acid), sodium-sulphur (Na-S), nickel-cadmium (Ni-Cd) and nickel-metal hydride (Ni-MH). Other energy storage devices, such as ultracapacitors, are also sometimes considered as means of energy storage. A separate cooling system may also be required for the motor and the power electronics. There are three types of motors/generators which are most widely used: Alternating current (AC), direct current (DC) commutated and DC brushless. The advantages and downsides of each type of energy converter are discussed in detail by Cuenca et al [17].

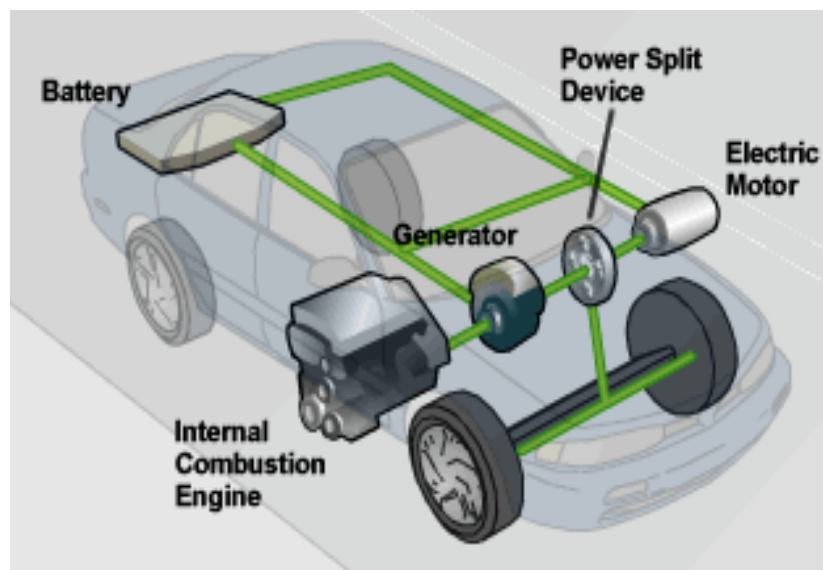


Figure 2.3: Typical electric hybrid vehicle components.

Throughout the deceleration process of a HEV, the torque required to slow down the vehicle is provided by the electric generator which is coupled to the drivetrain, in both series and parallel structures. Therefore, the kinetic energy of the vehicle is recovered and stored in the battery pack, while the IC engine can be stopped. The maximum braking power that the generator can absorb depends on its base rotational speed. At speeds less than the base speed, the power is proportional to the motor speed. Beyond the base speed,

it remains constant. If the braking power is completely enveloped by the maximum power-speed profile, the braking power can be fully recovered. If not, then the synergy of the frictional brake system is required. In most cases, the generator itself can function as the electric starter of the engine or as the electric motor to propel the vehicle during accelerations or to supplement the IC engine when extra power is needed. A typical electric hybrid arrangement is shown in Figure 2.3.

Studies in the past showed that a HEV's range for in-city driving can be extended between 14% and 40% by using regenerative braking [18]. However, all the currently available cars have zero or minimal pure electric range and low on-board electrification, which mean that only a fraction of the demanded propulsion derives from the electric motor. It ranges from only 17% for Honda Insight up to 44% for the next generation hybrid prototype vehicle manufactured by General Motors, according to An et al, who compare and analyze the fuel economy benefits of several light-duty hybrid vehicles [19]. Their study is not only based on commercially available vehicles, but it also includes prototyped gasoline and diesel hybrids.

As for regenerative braking, researchers suggested a parallel brake system with such a structure that both regenerative and mechanical braking can share the braking force of the driven axle at a fixed rate. They claim that it is possible for an energy storage and regeneration system to fully recuperate the braking energy of the vehicle, provided that the regenerative braking control strategy followed allows for the ideal energy recovery, according to the results derived from their vehicle simulation throughout various driving conditions, such as the American (EPA 75) urban driving cycle, the European (NEDC), the Japanese 10-15 Mode and the New York City driving cycles [20,21].

The design process of a HEV starts with the evaluation of the trade-offs which are associated with components' size and weight for a targeted fuel economy and performance. The majority of design optimization studies available in the open literature focus mostly on conventional powertrains. Work on hybrid powertrains has been directed mainly to parametric studies to assess energy management strategies by means of using a variety of models and simulations [22-32]. However, there are only a few references on the potential of optimizing the regenerative braking for HEVs. In particular, Zoelch and Schroeder present a method which calculates the optimal torque output for the electric motor and the IC engine, as well as the optimal gear ratios of the Continuously Variable Transmission (CVT) throughout a simple driving cycle by means of dynamic optimization [33]. Finally,

Bumby and Forster employ a direct search technique to obtain a minimum energy path throughout the driving cycle, with the control variables being the gear ratio and the torque split between the IC engine and the electric motor [34].

On the downsides of the electric hybrids design are high production cost and weight. The energy that is stored in the battery cell can only be of electrochemical form, which implies a variety of limitations. In particular, batteries tend to be bulky and heavy because of the limited amount of energy per unit mass and volume they are capable of storing. A battery pack with the energy equivalent of 1 US gallon (approximately 3.8 l) of gasoline would weight about 340 kg and occupy a volume of 180 l, according to Kalhammer et al [35]. The vehicle must therefore possess the structural strength to carry the additional weight, which implies a negative effect on energy consumption.

Furthermore, average anticipated lifetime for the batteries is much shorter for vehicle applications and thus the batteries have to be replaced at least once, which implies a significantly high maintenance cost. In addition, battery efficiency drops rapidly in extreme temperature conditions, which means that a dedicated cooling and/or heating system needs to be installed in the battery compartment at locations with extreme weather conditions. Finally, in order to increase the life of the batteries, they must not be completely discharged, they should stop charging when they reach a high state of charge (SOC) and they cannot be fully charged-up rapidly. All the above imply limitations to the regenerative braking of HEVs [36].

2.5.3 Mechanical hybrids

The relatively recent availability of suitable and affordable high-strength, lightweight composite materials used for the construction of flywheels is the main reason for recent technical developments in the area of flywheel technology and their use on mechanical or electric (when combined with an electric motor/generator) hybrid cars. However, the use of flywheel technology for mechanical energy storage purposes began several hundred years ago and was developed during the Industrial Revolution, when flywheels were used to keep machinery running smoothly from cycle to cycle [37].

Most commonly reviewed mechanical hybrids consist of a flywheel connected to the drivetrain through a CVT and a clutch. As the energy storage device is charged, its rotating components speed up (commonly to speeds measured in tens of thousands of rpm). In the contrary, when energy is drawn from the system, they slow down. Flywheel energy storage

is proportional to its moment of inertia and the square of its rotational velocity. A flywheel rotor consists of a metallic hub and a composite wheel, made of high-strength carbon fibres, especially at high-power applications. However, solid flywheels are used in some lower-energy applications. Herbst et al. describe the design, fabrication and spin testing of two composite flywheel energy storage rotors which utilize flexible composite arbors to connect a composite rim to a metallic shaft, resulting in lightweight, compact and high energy density structures [38]. Carbon fibre structures allow high flywheel rotational speeds, thus providing large amounts of energy density. They also disintegrate on failure, instead of parts sent flying outward with considerable force in the unlikely event that the system breaks down. This is a significant safety benefit, especially when used in passenger cars. Anticipated failure modes are examined by Grudkowski et al. by means of tests performed on flywheels of various masses, running at a variety of speeds [39]. Flywheels usually rotate inside a sealed compartment, in a vacuum, in order to reduce frictional losses.

The major advantage of mechanical hybrids lies on the fact that they store a vehicle's energy in the same form as when the vehicle starts braking and they regenerate it in the form which must inevitably be when the vehicle is back up to speed. In other words, there are no low-efficiency, energy-consuming transformations from one form of energy to another, as it happens, for instance, in electric hybrids where kinetic energy is transformed into electrical energy in a motor/generator and then electrical energy is transformed into chemical energy as the battery charges up during regenerative braking and vice versa during acceleration. Therefore, energy conversion efficiency in mechanical hybrids depend solely on the frictional losses and windage of the rotating components of the hybrid powertrain (bearings, CVT, etc). Having the significant advantage of better energy recovery efficiency and power density, composite flywheels are combined with advanced electric motors/generators to replace electrochemical battery banks in satellites and other aerospace applications [40-42]. Research on this field concluded that such systems can provide significant reduction in volume and weight as well as extended operating life, which is essential in spacecrafts.

The kinetic energy stored in a flywheel is given by Equation 2.5:

$$U = \frac{I \cdot N^2}{2} \quad \text{Equation 2.5}$$

where N is the rotational speed of the flywheel and I is its moment of inertia, which is defined with respect to the longitudinal axis of the flywheel according to Equation 2.6:

$$I = \frac{m \cdot R^2}{2} \quad \text{Equation 2.6}$$

where m is the mass of the flywheel and R is the flywheel radius.

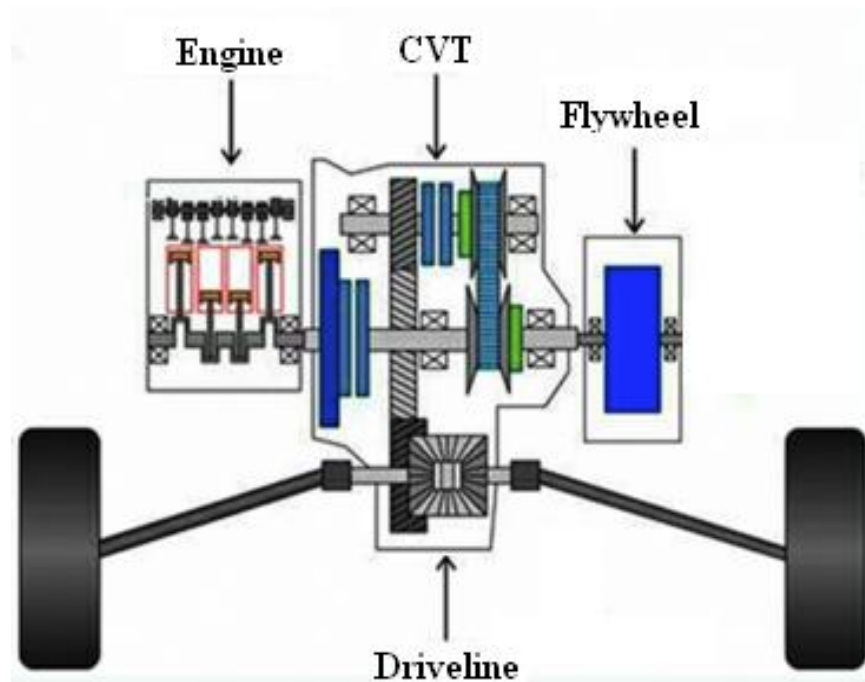


Figure 2.4: Mechanical hybrid vehicle drivetrain.

Delivering power to the wheels from the flywheel and vice versa requires a steel-belt-driven CVT with sufficiently large gear ratio coverage and with a planetary gear set for neutral and reverse. The so-called “drive-neutral-reverse” (DNR) torque converter is required to cover all possible driveline and/or flywheel speeds. Figure 2.4 briefly illustrates the main components of a mechanical hybrid system. The flywheel is directly connected to the input shaft of the gearbox in a way that its speed is not controlled solely by the primary engine clutch, but there is also a secondary clutch to engage and disengage the CVT in selected times.

When the vehicle decelerates, the CVT is shifted-up and the flywheel speed increases (and thus kinetic energy is stored in it) at a decreasing driveline speed. When extra power demand is needed, during acceleration or when traversing a steep slope, the secondary clutch (most commonly electromagnetically actuated) ties the CVT to the driveline and supplementary kinetic energy is provided to the vehicle. In such an arrangement, energy

can also be stored in the flywheel during cruising or even during idling, provided that the engine is not stopped. The IC engine of a mechanical hybrid vehicle is much lighter compared to a conventional one, as it does not require an electric starter to start or a flywheel to keep torque constant, as the clutch that ties the flywheel to the engine would start it and provide plenty of flywheel.

Other CVT designs and control solutions are suggested by Shen and Velpaus [43] and Serrarens et al [44]. They propose a vehicular driveline consisting of an IC engine, a CVT and a flywheel which only plays part in transient situations, where instant, high-power demands occur (such as a sudden accelerator pedal kick-down) and it partly compensates for the engine inertia, enabling both optimal fuel economy in stationary situations and driveability during transients. Their proposed power assist unit, very similar to the design described above, is embodied as a flywheel and a planetary gear set in parallel to a standard CVT driveline. The main difference in this arrangement is that the sun gear is connected to the flywheel, the annulus gear is connected to the engine shaft and the planet carrier is connected to the wheels. This design is also known as *Zero Inertia (ZI) driveline* because the engine inertia is cancelled by the flywheel inertia from the model point of view. Despite the many advantages that arrangement has, it introduces additional non-linearity in the driveline, demanding a more sophisticated control system, which they describe in detail.

In spite of being a promising technology, mechanical hybrids are not as highly developed as hybrids of other types. Rosen Motors, founded in 1993, had been developing a mechanical hybrid vehicle which incorporated a flywheel and a petrol turbine engine since 1997 [45]. They have adopted dedicated controllers which divert power from or to the turbine engine and/or the flywheel. The later supplies most of the power when the driver steps on the accelerator pedal, while it absorbs energy otherwise lost during braking. The turbine engine is mostly used during cruising and for maintaining the flywheel at its optimum speed. However, Rosen Motors failed to redefine the automobile with their hybrid car when major manufacturers rejected their new engine technology and the business closed in 1997.

On the other hand, a system that combines a steel flywheel of medium storage capacity and a mechanical variator coupled to the axle of a mini-tram has been successfully demonstrated by Jefferson and Ackerman [46]. The experimentally realized vehicular acceleration is controlled by means of the variation of the CVT ratio, while brake energy

recovery is realized by reversing the power flow. The application of such systems in heavy vehicles, such as railcars, trucks and buses, has been tried with a degree of success as the excessive weight of the mechanical hybrid configuration is not so critical and does not significantly affect the vehicle's power to mass ratio.

2.6. Air hybrids

The main difference between a conventional IC engine and a pneumatic engine lies on the fact that the later runs on the internal energy inhered in compressed air, rather than a combustion engine that runs on the explosive destruction of the fuel. Compressed air was known to be a power medium for vehicles before fossil fuels were widely adopted as the status quo. The notion of using compressed air as a medium of storing and reusing energy lies back to the late 1880s. The first pneumatic engine appeared in 1886 and it was the Mekariski air engine, which was a single-stage engine (air expanded in the cylinder and then exhausted to the atmosphere) and had been used in public transportation on the Mekariski compressed air locomotive. Because of its obvious advantages, such as simplicity, safety, economy, and cleanliness, the air-powered locomotive was a serious contender for the top spot in transportation for half a century. Pneumatic engines were commercially available and used routinely, as metropolitan street transit at first and later for haulage in mines [47]. However, after the Second World War, when gas engines had been perfected, the oil industry was established, and gas was cheap, the term "*pneumatic engine*" disappeared from the engineering textbooks. Serious interest in compressed air-powered vehicles was rekindled by the energy glitches of the 1970s.

Since then, many designs have been presented for hybrid, closed cycle, and self-fuelling pneumatic engines, as well as conversions for existing engines and designs. In 2000, Guy Negre designed and evaluated an air-powered vehicle, codenamed "Evolution", which in fact is a series-hybrid pneumatic car. It incorporates a compressed-air motor to power the drivetrain and a small IC engine to drive the air compressor and charge a 300-litre air bottle which is sufficient to run the vehicle at 96 km/h for more than 200 kilometres [48].

According to Thermodynamic laws, compressing a gas produces pressure and heat. Excellent reversibility can be achieved when both are stored together. However, heat can be removed from the gas by using a heat exchanger to cool it, which is a necessity if multi-

stage higher pressure is desired, and can be given back later, sometimes from a free heat sink (ambient) during relaxation, to still produce a fairly good reversibility. For short term uses, it may be beneficial to store both the pressure and the associated heat. Following the aforementioned fundamentals, Huang et al. introduced a series air-hybrid powertrain where a small IC engine is coupled to an air-compressor, while the waste heat from the engine can be recycled and converted to mechanical energy in the air motor, thus elevating the overall efficiency of the system by about 20% [49-51].

Although the aforementioned innovations are very promising, they do not exploit the prospect of regenerative braking. Capturing, storing and reusing braking energy to provide additional power in air hybrid vehicles can be achieved by using the momentum of the vehicle during coasting and deceleration to drive the engine itself as an air compressor. The compressed air can be stored and later used by the engine operated as an air expander to propel the vehicle during coasting and acceleration. Therefore, energy conversion becomes a single-step procedure, implying a significant improvement to the overall efficiency. This design can be applied to a wide variety of engines, including reciprocating, rotary, 4-stroke or 2-stroke cycle, petrol or diesel, etc. Fuel must be denied into cylinders when the engine is operated in regenerative compressor or expander modes, which can be achieved by means of individual cylinder fuel shut-off. This is very easy to be implemented, provided that all modern engines use electronically controlled fuel injection systems.

Another prerequisite for pneumatic regenerative braking integrated in the IC engine is a fully variable and deactivatable mechanism to control the intake and exhaust valves. Governing the three basic valve event dimensions (valve opening and closing points and valve lift) would also have several other benefits, like reduced throttling loss in Otto engines, as the throttle valve can be eliminated if the airflow is controlled by the inlet valve timing. Consequently, fuel consumption can be improved. In addition, an optimized torque curve can be realized as the engine is allowed to breathe in the best possible way, regardless the engine speed, while the conventional valve timing is a compromise between the ambitions towards the best possible performance at high and low speed bands.

Lotus and Eaton have been collaborating to bring to market a production, closed-loop control, fully variable valve timing (FVVT) system, named Active Valve Train (AVT) in the 2008-9 timeframe [52]. The system, which is currently being engineered in prototype form, uses electro-hydraulic operation. Movement of the engine popped valves is initiated

by oil flow into and out of a hydraulic chamber which is controlled by state-of-the-art, fast acting servo valves developed by Moog Inc, a worldwide manufacturer of precision control components and systems. Following the same design fundamentals, Ford Motor Company developed its own electro-hydraulic camless valvetrain which uses solenoids to control the valve lift by varying the duration of the solenoid voltage pulse, while valve acceleration, velocity and travel time are controlled by hydraulic pressure. The basic concept of the system as well as the camless engine and its components are described in details by Schechter and Levin [53].

At present, there are only partly variable valvetrains in production which allow the valve event timing and duration to be varied continuously between limits, such as BMW's Valvetronic, Porsche's VarioCam Plus and Honda's V-TEC [54-57]. However, the aforementioned systems are not suitable for air hybrids.

An air hybrid that adopts a fully variable valve actuation like the ones described above is reviewed by Andersson et al. They proposed an IC engine which is modified to also work as an air compressor or expander and/or it is claimed to be more efficient when employed by automobiles with low engine capacity to vehicular mass ratio (such as urban buses), where high levels of imep are of high importance. Although they have not carried out any experimental work, they used the commercial engine simulation software GT-POWER for systematic studies on a model of a pneumatic hybrid turbocharged Diesel engine. The engine is connected to two air tanks through separate intake manifolds. The low-pressure, large-volume tank is connected to one of the intake valves of each cylinder. It discharges during compressor mode (CM) and charges during expander mode (EM). The high-pressure, small-volume tank is connected to the other intake valve. It discharges during EM and charges during CM. Actuation of both intake valves is hydraulic and fully variable, while valve timing is controlled by look-up maps, according to the desired level of imep. The low-pressure airtank substitutes the role of the atmosphere as supplier of ambient air to the engine's intake system during all modes. Andersson et al. concluded that an estimated total reduction of 23% in fuel consumption could be achieved for a typical 15-tonne city bus driven according to the Braunschweig cycle, also taking into consideration adverse factors such as increased vehicle weight [58,59]. Also according to their simulations, 55% of the energy absorbed during compression braking mode can be regenerated and returned to the drivetrain.

A similar air hybrid approach, however more effective, has been developed by Professor Tsu-Chin Tsao from the University of California and his industrial collaborators from Ford Motor Company. Although no actual air hybrid was built, the concept was modeled in GT-POWER. The predicted fuel economy improvement was as high as 64% for city driving and 12% for highway driving [60-63]. For their simulation they used a 1.5-tonne passenger car with a 2.5-litre V6 petrol engine. An electro-hydraulic camless valvetrain system that allows for variable valve operation was adopted. Methods to precisely control the valve operation over a wide engine speed range were developed. There are two separate inlet manifolds on the engine. The low-pressure manifold connects one of the intake valves of each cylinder to the atmosphere and thus it always contains air in atmospheric pressure, like in conventional IC engine designs. The other manifold is connected to the other intake valve and it employs a poppet valve switching system to switch between atmospheric air during normal engine firing mode and pressurized air from the airtank during compressor or expander modes. An important feature of the air-switching method chosen is a complete non-interference with the exhaust system of the engine. Tsao proposed a valve system that allows the engine to operate in four different modes: When a vehicle decelerates, the engine is used as an air compressor to absorb the braking energy and store it into the airtank. Whenever the vehicle stops, the engine is stopped. Once the driver touches the accelerator pedal, the engine is started by compressed air. As the car speeds up, the engine is used as an air motor to drive the vehicle until the compressed air is depleted, at which point the engine is switched to conventional combustion mode and begins burning fuel. The options of 2-stroke compressor and expander modes are also discussed.

In order to avoid complicating the intake system with switching valves and to eliminate the necessity of dual intake manifolds, Turner et al. [64,65] proposed an air hybrid approach where no alteration is made to the conventional dual intake valve system, while one of the exhaust valves is used as air transfer valve and it is directly connected to the airtank. The simplicity of having a dedicated air transfer valve yields benefits in intake system conventionality. The fully variable AVT system was used to meet the requirements of high degree of control over the valve timing. The engine was modeled using GT-POWER and the implementation of the concept is described in detail in Chapter 5. Systematic studies were carried out for air reservoir volume and valve timing optimization [64,65]. Apart from the above distinctions, engine operation is the same as in Tsao's concept, as fully variable valve actuation allows every possible engine cycle to be realized. In addition, the potential of Differential Cylinder Loading (DCL) break-through is reviewed here. The

practical illustration of DCL is that a FVVT system is in fact a collection of single-cylinder engines which share the same cyclic speed due to their connection by the crankshaft. Thus, each cylinder can be individually deactivated or operated in normal firing, compressor or expander modes.

Engines that embody DCL technology, also known as *split-cycle* engines, have been around since the early 1900s but until now they have had much lower thermal and volumetric efficiencies than a conventional IC engine. Sal Scuderi, president of the Scuderi group, introduced an engine with separate cylinders for compression and power. He also used a unique valve design and technology taken from the compressor industry to raise volumetric efficiency. He also found that the thermal efficiency can be improved by retarding the ignition timing. The design of the valves and their actuation system are the issue which the Scuderi group is currently dealing with. Their first prototype engines, a two-cylinder petrol and a six-cylinder diesel, will use conventional camshafts for the firing cylinders and pneumatically operated valves for the compressor/expander cylinders and they are expected to be ready for testing in mid-2007 [66].

Finally, Higelin et al. proposed a pneumatic hybrid design much different than the above, which is based on a conventional IC engine with camshaft-operated valvetrain. There is an additional air transfer valve which connects the combustion chamber of each cylinder to an air tank and it is operated by a dedicated camshaft. In addition to the pneumatic pump, normal firing and pneumatic motor modes, two new processes are reviewed: supercharged and undercharged engine operation. The positive effect of the supercharging capability is that the engine can be optimized for maximum power, meeting 80% – 90% of the driving conditions, while the remaining 10% – 20% high-power-demand conditions are met with transient supercharging with the compressed air from the airtank. With the undercharged operation, the airtank can charge while the engine is in normal combustion mode and thus obtaining a high SOC. Their driving cycle simulation included an 800-kg vehicle driven throughout the NEDC, following an optimal gear shift and clutch operation strategy. They considered a 50-litre airtank and a 1-litre engine. The results indicated that fuel economy is improved by more than 15%. It has been also estimated that, by optimizing critical parameters, such as airtank volume and maximum allowed pressure as well as engine displacement, a further improvement of the overall fuel economy as high as 31% could be realized [67-69].

2.7. Motivation for novel air hybrid concepts

Air hybrid engines have a big advantage compared to electric hybrids: they are cheap and do not require impractically expensive battery maintenance. A 40-kg compressed air cylinder, which is the same size as the steel types already used in natural gas vehicles, can store 4 kWh of energy. Assuming that 50% can be recovered, the real-world density is as high as 50 Wh/kg [70]. This is a much better energy to mass ratio than the best batteries, which can achieve 50 Wh/kg only by 100% discharge, something that would be catastrophic for battery life. The only drawback is that an air engine can provide torque (and thus power) only transiently because not only does the air run out but the engine temperature drops (unless provided with elaborate heat exchangers) due to the adiabatic expansion of the air and loses efficiency.

Unlike other hybrid engines, powertrains that use compressed air for energy regeneration do not require an energy converter or secondary propulsion system to be connected to their drivetrain. This approach allows for significant improvements in fuel economy without the added complexity, weight and cost of the auxiliary subsystems required by electric, mechanical and hydraulic hybrids. Air hybrids typically employ one or more air transfer valves between the engine cylinder and the air storage tank, operated at selected times in a synchronized fashion to let compressed air in the cylinder or to force it out to the airtank.

The actuation of the valves is an important issue. Air hybrid potentials would be fully exploited if FVVA systems could be adopted for all intake and exhaust valves which would also allow further volumetric efficiency increase. Such a valvetrain would require the use of hydraulically, pneumatically or electromagnetically actuated valves together with dedicated electronic control systems instead of the conventional camshaft valvetrain. One common trait shared by all FVVA systems is that for each extra level of flexibility, another degree of complication is unavoidable. On the other hand, the use of a conventional valvetrain (camshaft) has the restriction of the fixed or partially variable valve timing. In order to operate with sufficient effectiveness, air hybrids need flexible valve actuation to shift between air compressor, air expander and normal firing modes as well as part compressor or part expander using selective cylinder deactivation during cruising. This cannot be achieved without the utilization of a hydraulic valvetrain, which is more preferred than a pneumatic one due to the control accuracy, which lies upon the fact

that air used as a compression medium is compressible whereas liquids are regarded as incompressible.

Some simplified designs adopt only one valve separating the air storage tank from the engine cylinder and thus making airtank charging and discharging a single-step process. This has a great impact on the smoothness of the vehicle braking behaviour as the braking power that can be absorbed by regenerative braking is a function of the airtank SOC. That makes braking power unpredictable for the driver and thus reduces the vehicle drivability. In order to overcome this downside, alternative arrangements which utilize two-stage processes for airtank charging and discharging could be adopted. Dedicated spring-preloaded poppet valves or reed valves are possible alternative solutions for isolating the cylinder from the airtank without the use of one or more engine valves. However, those designs require robust valves, capable of sustaining high pressures and temperatures.

2.8. Summary

When driving a vehicle at a uniform speed on a flat highway, only a small portion of the engine power is used to overcome rolling and aerodynamic resistances and drag. Therefore, the engine is operated in part load and low efficiency. On the other hand, the urban traffic driving pattern includes many subsequent starts and stops, as well as low vehicle speeds and therefore drag plays a minor role. Instead, considerable power is used for frequent accelerations (i.e. to increase the kinetic energy of the vehicle) while a large part of this power is then dissipated into useless heat when braking the vehicle (e.g. when stopping in front of a red traffic light). It would therefore be desirable to find a practical way of capturing and reusing the kinetic energy otherwise lost during braking. If the kinetic energy could be absorbed during braking, stored and finally returned to the vehicle during the subsequent acceleration, fuel consumption and exhaust gas emissions would be significantly reduced. Figure 2.5 shows the reduction in fuel consumption due to hybridization on vehicles using spark-ignition, IC engines, relative to their non-hybrid equivalent, through different standard driving cycles, as estimated by Heywood et al [71].

There are numerous ways to store the potential and kinetic energy. A common term for all these methods is regenerative braking. Batteries, flywheels, capacitors and hydraulics are some examples of the methods that have been suggested and reviewed. However, it is still

questioned whether the fuel saving benefits of such systems are great enough to compensate for the increased technical complexity and costs or not. Additional downsides when fitting these systems are weight, bulkiness and/or short service life (batteries normally have a shorter service life than the vehicle). A major consideration for most of these methods is that they not only require an energy storage device (batteries, capacitors, flywheel etc.) but also a secondary energy converter, usually in the form of an electrical or hydraulic machine.

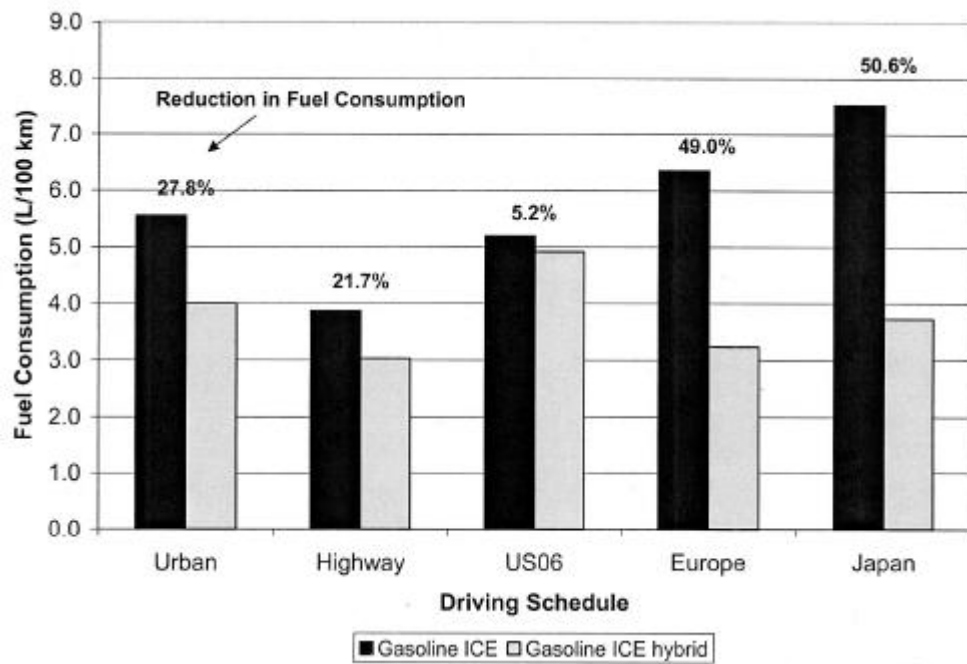


Figure 2.5: Fuel consumption improvement in spark-ignition, IC engines due to hybridization [71].

Table 2.1: Summary of hybrid system advantages and disadvantages [64].

	Control	Simplicity	Energy Density	Mass	Cost
Electric	+	--	-	--	--
Mechanical	+	+	+	-	-
Hydraulic	-	-	++	--	-
Pneumatic	--	++	-	++	+

If hybrid vehicles reach a commercial break-through in urban traffic, it will be a result of the attractive mix of the benefits that they provide. Then the regenerative braking feature would not have to carry all its own costs as the required components will be used for more than one purpose. While waiting for that break-through (although there is no guarantee that it will happen) there is one seemingly robust and simple method of regenerative braking which can be achieved without the addition of a secondary energy converter. This method is called pneumatic regenerative braking or air hybrid and it is based on the principle that a modified ICE can also work as an air compressor during decelerations and as an air motor when accelerating. Table 2.1 summarizes the advantages and disadvantages of the currently viable hybrid solutions.

Chapter 3: Air Hybrid Concepts

3.1. Introduction

Three different air hybrid engines are described in detail in this Chapter. Apart from efficiently storing and regenerating energy, the effort is put on combining the advantages of electric, hydraulic and mechanical hybrid engines, with the additional advantage of the simplicity and conventionality. In order for a pneumatic hybrid engine to achieve this, the emphasis is put on producing high levels of braking or driving torque, similar to hydraulic and mechanical hybrids, as well as producing smooth and predictable braking and driving torque, similar to electric hybrids. Of course, a compromise must be inevitably made between hybrid efficiency (and therefore fuel economy) and conventionality. The more flexible the system, the more hybridization options available, as shown below.

3.2. Air hybrid engine with an Energy Recovery Valve (ERV)

The system introduced below combines a conventional IC engine with a pneumatic energy converter and storage subsystem in such a way that there is no need of major changes to the base engine, in order to lower the production cost and weight of the system and stay with the well-known technologies which are already in production. As the standard camshaft-operated valvetrain remains in use, the need of adopting fully flexible valve actuation which adds to the system's complexity is eliminated. Therefore, only minor modifications in some engine components are required, although their normal function is not altered in any way when operating the engine in air hybrid mode.

3.2.1. Description

Figure 3.1 shows the schematic of an air hybrid, four-stroke IC engine with a piston (1) reciprocating in a cylinder (2). Exhaust and intake valves (3 and 4 respectively), which connect the cylinder with exhaust and intake ports (5 and 6 respectively), are shown in their fully closed position at the end of the compression stroke. In petrol engines, where a throttle valve (7) controlled by the accelerator pedal is present in the intake to control the engine's power output (shown at its fully opened position), a bypass throttle valve (8) is needed to allow air to be induced into the cylinder during decelerations (shown at its fully

closed position) when the main throttle valve is closed. However, in Diesel engines, throttles 7 and 8 are omitted. High-pressure air is stored into an air reservoir (9) which is connected to the cylinder through a buffer chamber (10). Air flow to and from the engine in hybrid mode is controlled by first and second shut-off valves (11 and 12 respectively) which are operated in a synchronized fashion to let air in and out of the airtank and the buffer chamber in respect with the gas exchange and work strokes of the engine cycle. First and second shut-off valve opening and closing events are described in section 3.2.2 and investigated in Chapter 4. Intake and exhaust manifolds as well as ignition, cooling and fuelling systems are not shown in Figure 3.1 for simplicity reasons, as they are not the subject of the present study.

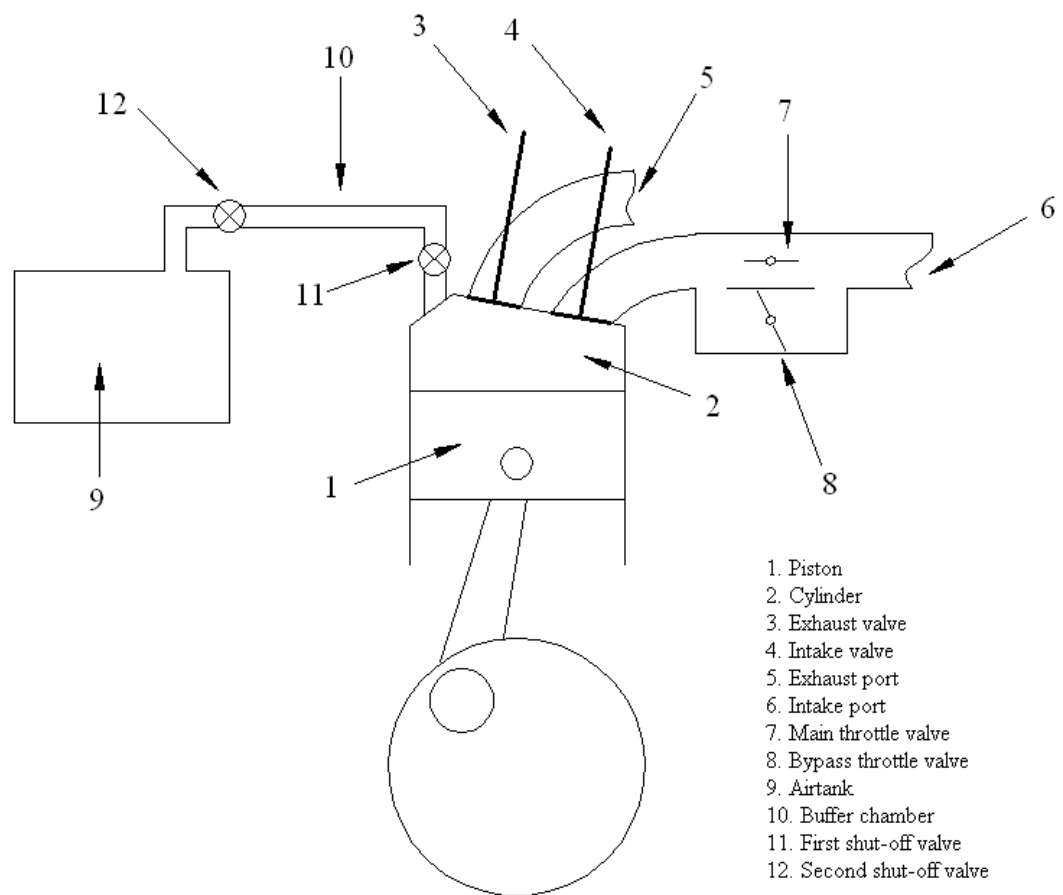


Figure 3.1: Air hybrid engine with an Energy Recovery Valve.

In order to enable energy storage and regeneration, a key system needs to be incorporated. The system consists of two valves which seal the buffer chamber and practically confine its volume between two boundaries; the cylinder and the airtank. That arrangement is called Energy Recovery Valve (ERV) and is connected to the engine through a convenient access hole located on the cylinder head. This is the only modification required to be done to the base engine. ERV is controlled by a two-position actuator and enables the cylinder

to operate as a regenerative expander or compressor during accelerations or decelerations respectively.

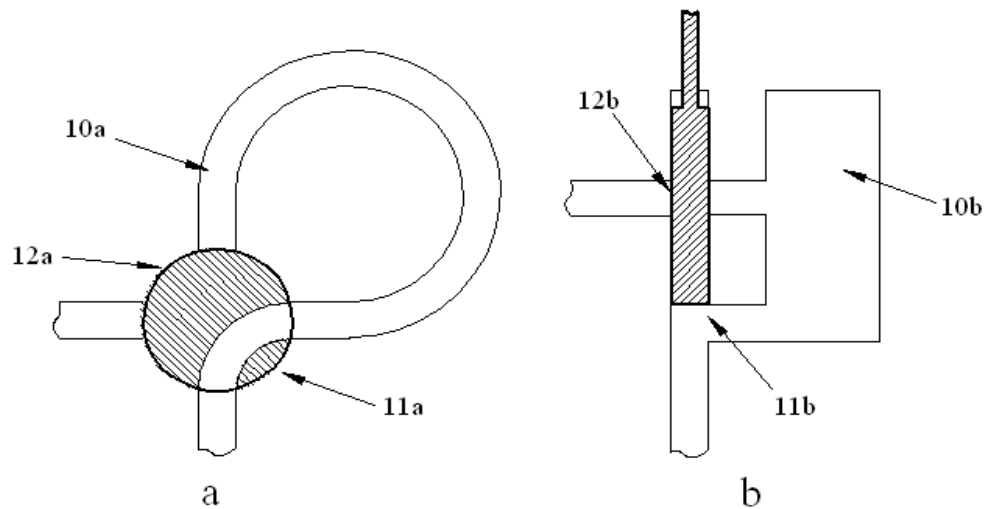


Figure 3.2: Proposed ERV designs; rotary valve (a) and poppet valve (b) type.

The existing conventional valvetrain remains unaffected and the intake and exhaust valves continue to operate normally during the gas exchange and work phases of the engine according to the operating IC engine cycle. Figure 3.2 shows two different possible ERV designs where the buffer chamber and the first and second shut-off valves comprise a compact unit. Design (a) adopts a multi-channel rotary valve, while design (b) uses a shuttle valve. In both cases the valves can be operated by a variety of two-position actuators (not shown in Figure 3.2), such as electric, hydraulic or pneumatic, which makes it relatively easy and cheap to manufacture, compared to other methods. ERV operation is detailed in Chapter 4.

The volume of the buffer chamber plays a significant role in the performance of the hybrid engine. Preferably, the volume isolated between valves 11 and 12 should be small enough to be included in the clearance volume of the engine cylinder. A substantially constant compression ratio can then be achieved by compressed air into the buffer chamber, irrespective of the state of charge (SOC) of the airtank when operating in compressor mode (CM) and thus providing a predictable braking behaviour to the driver. Similarly, a constant expansion ratio should be realized in expander mode (EM), relative to the volume of the buffer chamber and ideally sufficient to bring the expanded air to ambient pressure at the end of the expansion stroke. Also ideally, valve 11 must be located as close to the cylinder head as possible in order to minimize the dead volume of the duct connecting the airtank to the cylinder. This might introduce some difficulties in implementation because

there is usually little room available in the combustion chamber, as the areas of the conventional inlet and exhaust valves of modern engines are already maximized for optimal gas exchange.

Similar to many air hybrid designs, the compressed air reservoir could either be integrated inside the vehicle's frame or be a separate tank located inside the boot. Its volume and nominal pressure, which have significant effects on the performance of the air compressor or expander, are investigated in Chapter 4. The walls of the airtank and the pipes which connect it to the cylinder must be thermally isolated in order to minimize heat losses and elevate the efficiency of the system. This can be practically achieved by applying a thin layer of a very low heat transfer coefficient material. From the thermodynamic point of view, airtank filling or discharging can be considered as reversible, adiabatic compression or expansion processes, given that the tank is of constant volume. Finally, a safety valve on the airtank (not shown in Figure 3.1) relieves the pressure when it reaches a maximum limit. It should be noted here that the energy storage tank is not directly connected to the cylinder and the gas exchange process takes place in two stages through the ERV and the intermediate buffer chamber. This allows for further independency and adds to system's flexibility.

3.2.2. Operation

When the engine is operated as an air compressor during regenerative braking, a mass of air is sucked into the cylinder during the intake stroke and it is trapped there after intake valve close (IVC). That mass is transferred to the buffer chamber during the compression stroke, whilst valve 11 is open and valve 12 is closed. At the end of the compression stroke, valve 11 closes and valve 12 opens to allow the high-pressure, high-temperature air charge trapped between the two shut-off valves (thus inside the buffer chamber) to expand into the low-pressure, low-temperature airtank until the system pressure stabilizes. In order to ensure that no fuel will enter the airtank, engine cylinders must be purged of any residual fuel by cutting off the fuel a few cycles before connecting to the buffer chamber. During expansion stroke, the mass of air remaining between the piston face and valve 11 (i.e. inside the clearance volume) expands back into the cylinder. The piston moves upstroke during exhaust stroke, pushing the air remaining into the cylinder towards the atmosphere through the opened exhaust valve. Valve 12 may be still open but valve 11 must remain closed, preventing air stored in the airtank to flow back to the cylinder. During early intake stroke, valve 12 closes, while valve 11 opens towards the end of the

stroke, and allows the remaining air in the buffer chamber to expand into the cylinder, resulting in an improved engine volumetric efficiency. Therefore, buffer chamber pressure resets to ambient at the beginning of each cycle. The excessive air mass escapes to the atmosphere through the open intake valve. In order to obtain the highest possible level of brake energy absorption from the engine, an ideal cycle should include a high-pressure compression stroke followed by a low-pressure expansion stroke and therefore the engine indicator diagram should follow an anti-clockwise direction.

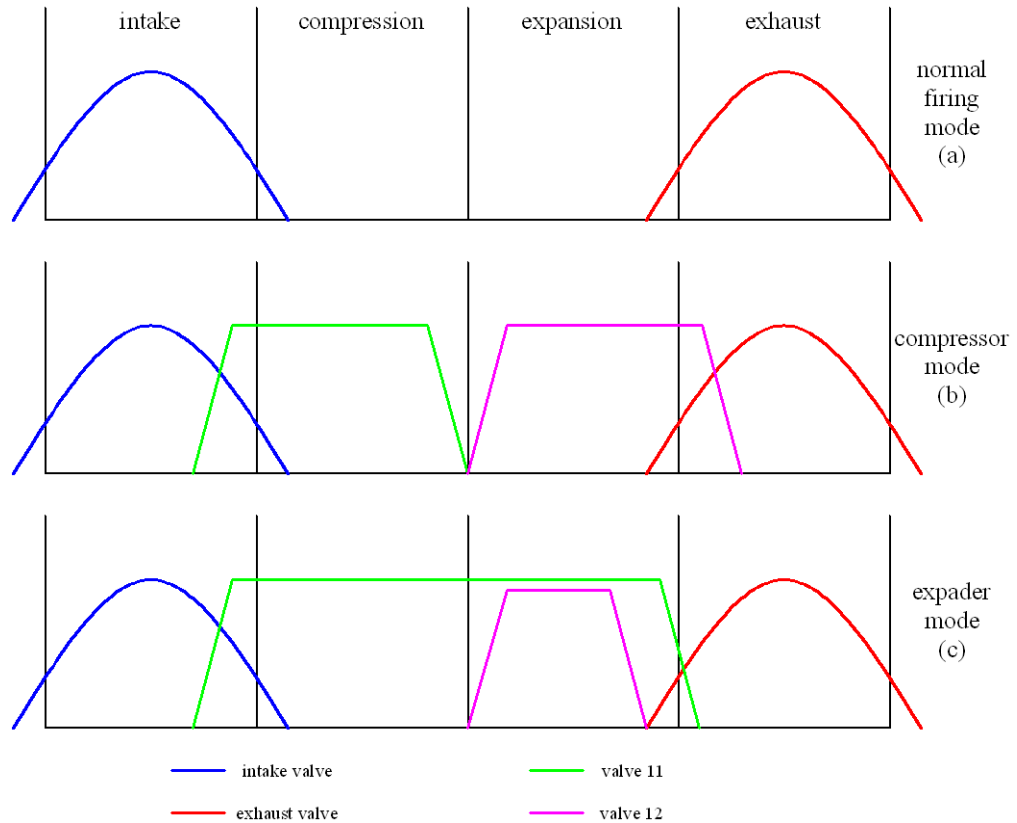


Figure 3.3: Engine valve and ERV timing for normal firing mode (a), CM (b) and EM (c).

When the engine is operated as an air expander during start-ups and accelerations, intake valve opens and a charge of air is sucked into the cylinder during the intake stroke. Valve 11 opens towards the end of the downstroke and remains open throughout the whole compression stroke, while valve 12 is closed. Buffer chamber volume is added to cylinder's clearance volume and thus the compression ratio drops, minimizing the negative torque on the engine shaft which is developed because of cylinder compression. The air induced into the cylinder is pushed into the buffer chamber during the compression stroke. Valve 12 opens at TDC and high-pressure air from the airtank enters the low-pressure cylinder through the open valve 11 and pushes the piston during the power stroke. Valve 12 closes when exhaust valve opens (EVO) to prevent compressed air from escaping to the

atmosphere through the exhaust valve, which would result to potential energy loss and would lower the efficiency of the process. Valve 11 closes at BDC to prevent air remaining in the cylinder from entering into the buffer chamber when it is pushed to the atmosphere through the exhaust valve during the exhaust stroke. In order to obtain the highest possible torque output from the engine, an ideal pneumatic motor cycle should include a low-pressure compression stroke and a high-pressure expansion stroke and therefore the engine indicator diagram should follow a clockwise direction. Figure 3.3 shows the valve timings for normal firing mode, CM and EM by means of a graph, while the corresponding piston events are shown in Figure 3.4.

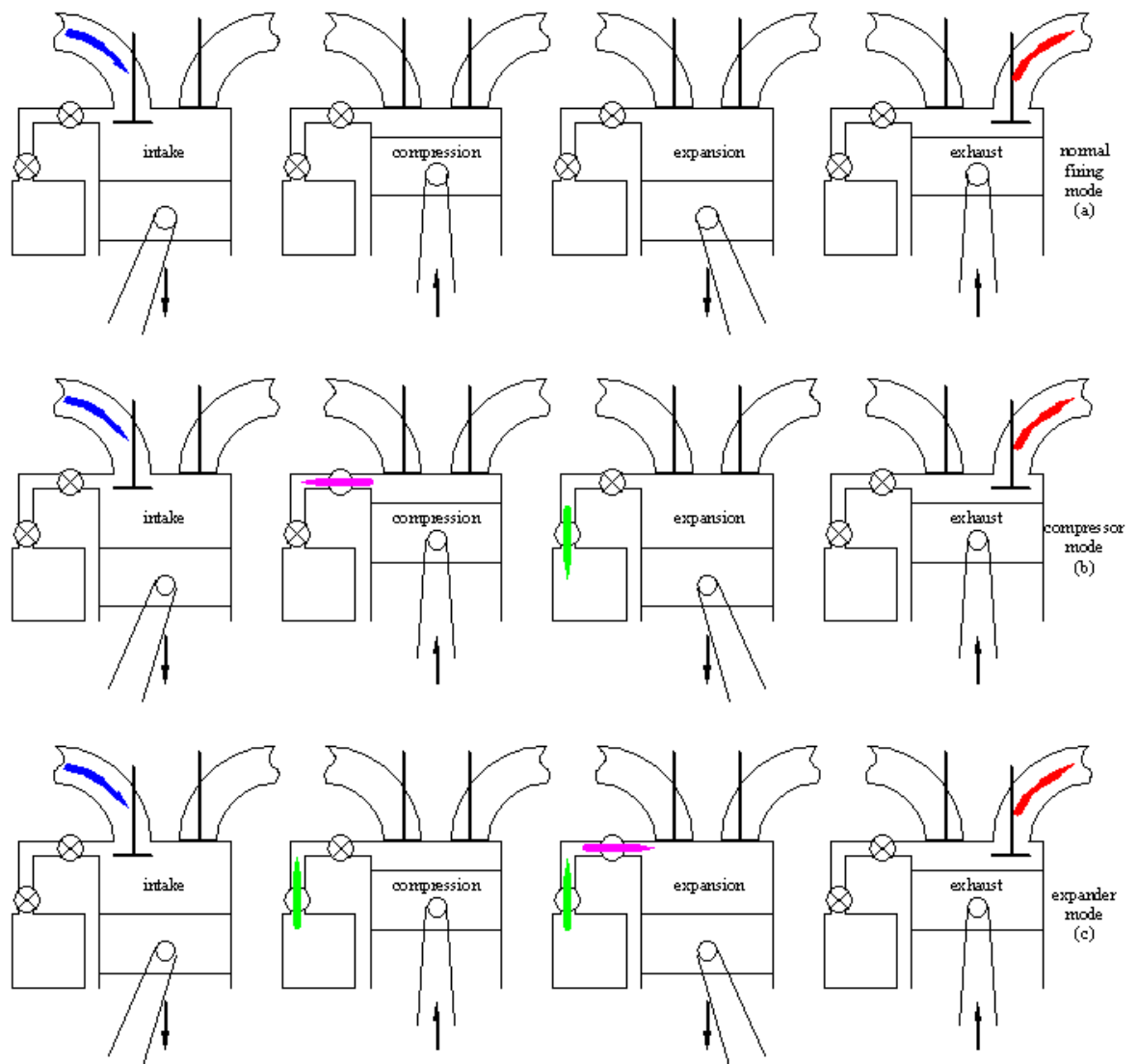


Figure 3.4: Four-stroke engine cycle for normal firing mode (a), CM (b) and EM (c).

3.3. Air hybrid engine with Fully Variable Valve Actuation (FVVA)

The system described here introduces an IC engine with camless valve actuation which can operate in three different modes: normal firing, air compressor and air expander. The purpose of this versatile system is to fully exploit the potentials of the engine by incorporating a pneumatic energy converter and storage subsystem in such a way that the accumulated energy can be reimbursed to the vehicle, without the need of a separate propulsion system, unlike electric hybrids. One of the engine valves connects the cylinder to the airtank and it is operated as a dedicated gas transfer valve. This design eliminates the need of control over additional shut-off valves and does not alter the cylinder head characteristics in any way (clearance volume, etc). The greatest advantage of the present concept lies on the fact that two-stroke air compressor and expander cycles can be realized, which improves hybrid performance. This is achieved by employing electro-hydraulic, Fully Variable Valve Actuation (FVVA), which is an emerging and very promising technology.

3.3.1. Description

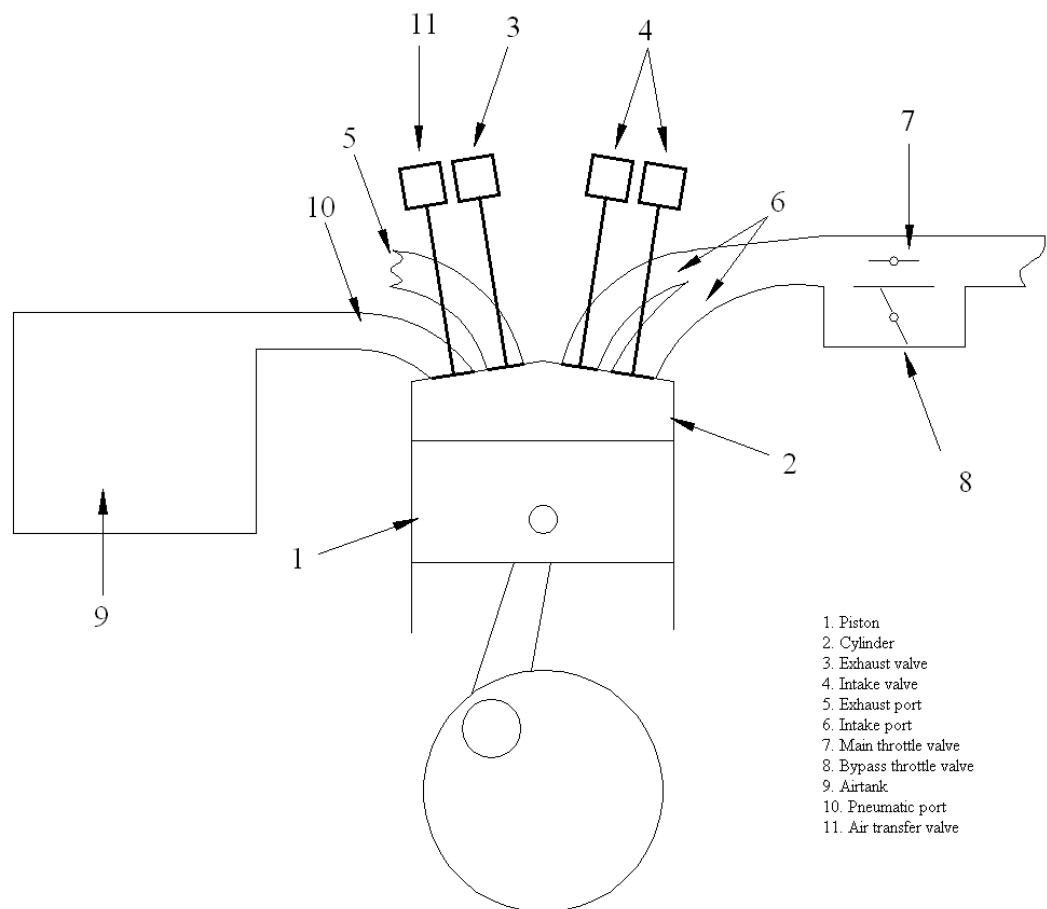


Figure 3.5: Air hybrid engine with Fully Variable Valve Actuation.

Figure 3.5 shows the schematic of an air hybrid, four-stroke IC engine with a piston (1) reciprocating in a cylinder (2). Electro-hydraulically actuated exhaust and intake valves (3 and 4 respectively), which connect the cylinder with exhaust and intake ports (5 and 6 respectively), are shown in their fully closed position towards the end of the compression stroke. In petrol engines, where a throttle valve (7) controlled by the accelerator pedal is present in the intake to control the engine's power output (shown at its fully opened position), a bypass throttle valve (8) is needed to allow air to be induced into the cylinder during decelerations (shown at its fully closed position) when the main throttle valve is closed. However, in Diesel engines, throttles 7 and 8 are omitted. High-pressure air is stored into an air reservoir (9) which is connected to the cylinder through a pneumatic port (10) that is controlled by an air transfer valve (11) which is operated in a synchronized fashion to let air in and out of the airtank in respect with the gas exchange and work strokes of the engine cycle. Air transfer valve opening and closing events are described in section 3.3.2 and investigated in Chapter 4. Intake and exhaust manifolds as well as ignition, cooling and fuelling systems are not shown in Figure 3.5 for simplicity reasons, as they are not the subject of the present study.

3.3.2. Operation

When the engine is operated as an air compressor during regenerative braking, a mass of air is sucked into the cylinder during the intake stroke and it is trapped there after IVC, similarly to the concept described in section 3.2. During compression stroke the gas transfer valve opens and air is transferred to the airtank. There is a backflow from the airtank to the cylinder during compression stroke initiation, before in-cylinder pressure reaches airtank pressure but after that pressure is exceeded, air is pushed in the airtank through the pneumatic port. At the end of the upstroke, gas transfer valve closes. In order to ensure that no fuel will enter the airtank, engine cylinders must be purged of any residual fuel by cutting-off the fuel a few cycles before connecting to the buffer chamber. The compressed air mass trapped between the piston and the cylinder head (i.e. the clearance volume) expands during expansion stroke and it escapes to the atmosphere during exhaust stroke. In order to obtain the highest possible level of brake energy absorption from the engine, an ideal cycle should include a high-pressure compression stroke followed by a low-pressure expansion stroke and therefore the engine indicator diagram should follow an anti-clockwise direction.

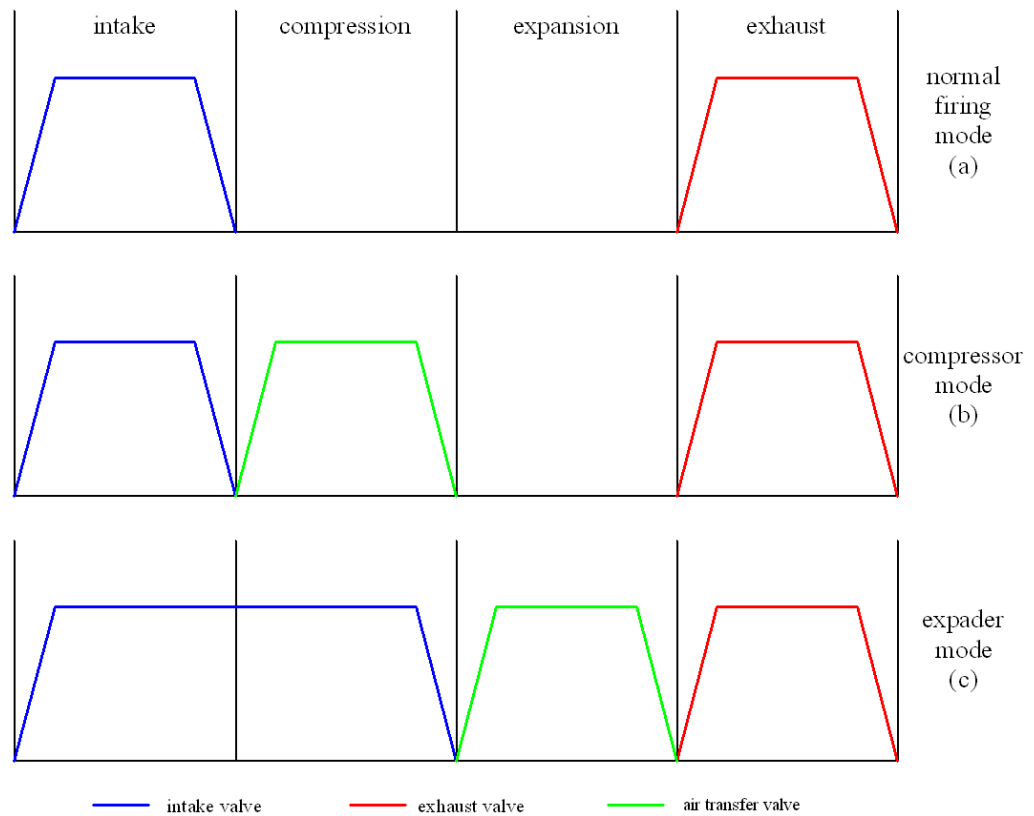


Figure 3.6: Valve events for normal firing mode (a), CM (b) and EM (c).

When the engine is operated as an air expander during start-ups and accelerations, powered by the high-pressure airtank, intake valve opens and a charge of air is sucked into the cylinder during the intake stroke, similarly to the concept described in section 3.2. FVVA flexibility allows for elimination of the negative torque developed on the engine shaft during compression stroke because of cylinder increasing pressure, by keeping the intake valve open and allowing the air to be pushed out of the cylinder through the intake ports. This significantly raises air expander's performance. The air transfer valve opens during the power stroke and high-pressure air from the airtank enters the low-pressure cylinder, pushing the piston down and thus forcing the crank to rotate. Transfer valve closes at BDC, so no greater mass of air than that can be expanded efficiently is permitted in the cylinder. Exhaust valve opens during exhaust stroke, allowing residual air mass escape to the atmosphere. Similarly to the concept described in section 3.2, the engine indicator diagram should follow a clockwise direction. Figure 3.6 shows the valve timings for normal firing mode, CM and EM by means of a graph, while the corresponding piston events are shown in Figure 3.7. It should be noted here that air transfer during compressor and expander modes is a single-step procedure as the cylinder and the airtank communicate directly through the pneumatic port, making the present concept simpler but in the meantime less flexible compared the concept of section 3.2.

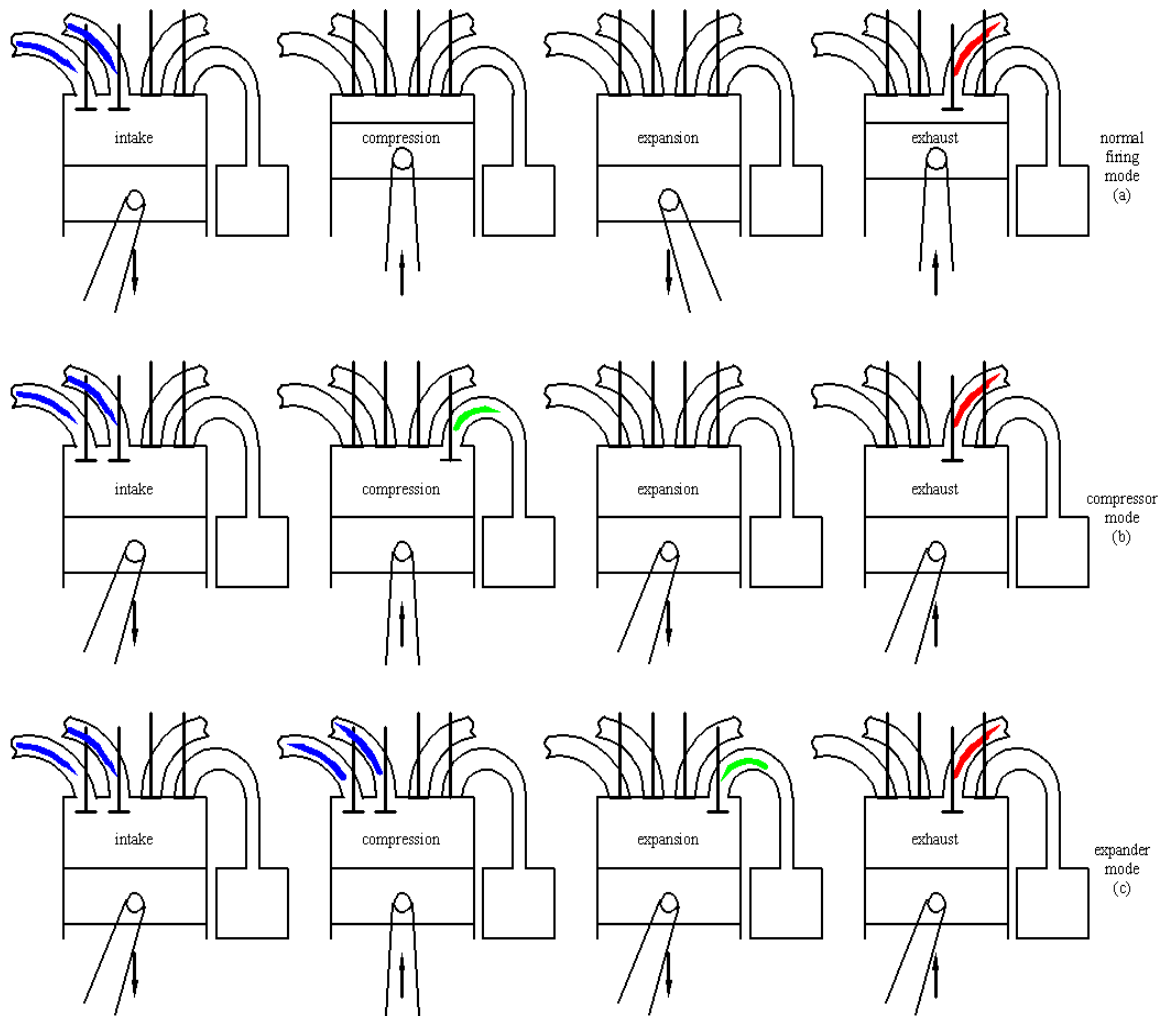


Figure 3.7: Four-stroke engine cycle for normal firing mode (a), CM (b) and EM (c).

As mentioned before, the high degree of control over valve timing and lift provided by FVVA allows for trapezoidal valve lift profiles to be implemented. This elevates the efficiency of engine cycles, as valves can open and close exactly at TDC or BDC without sacrificing the effective lift duration, by having a sharper opening and closing ramp (see Figures 3.6 and 3.8). It also makes two-stroke air compressor and expander operation possible. It can be concluded, from the observation of Figures 3.6 and 3.7, that expansion and exhaust strokes can be omitted from the air compressor cycle, as the gas exchange between the cylinder and the airtank is accomplished during intake and compression strokes. Therefore, after the end of compression stroke a new cycle can be initiated, including only one intake and one compression stroke.

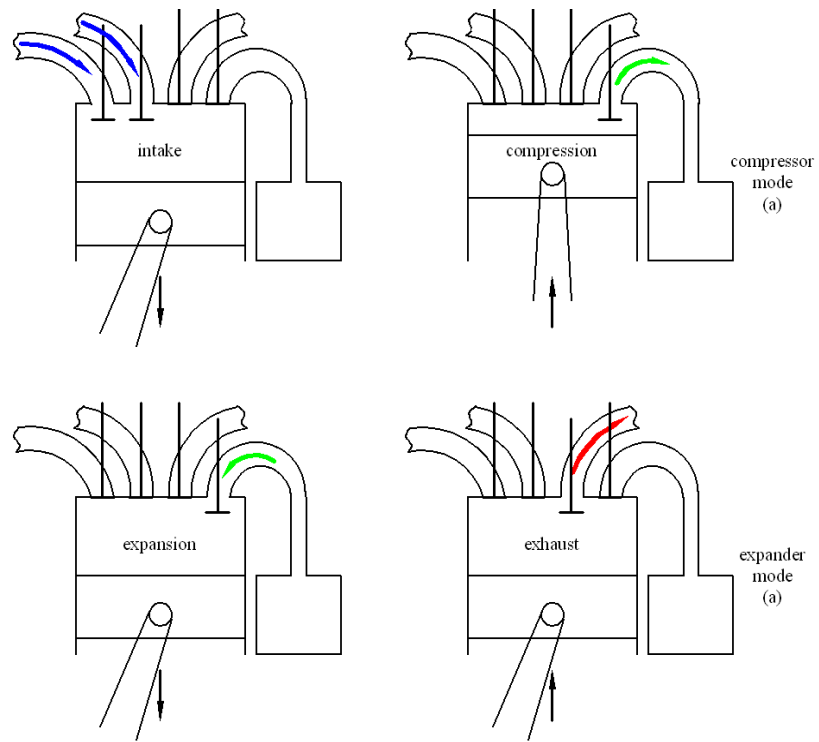


Figure 3.8: Two-stroke compressor cycle (a) and two-stroke expander (b).

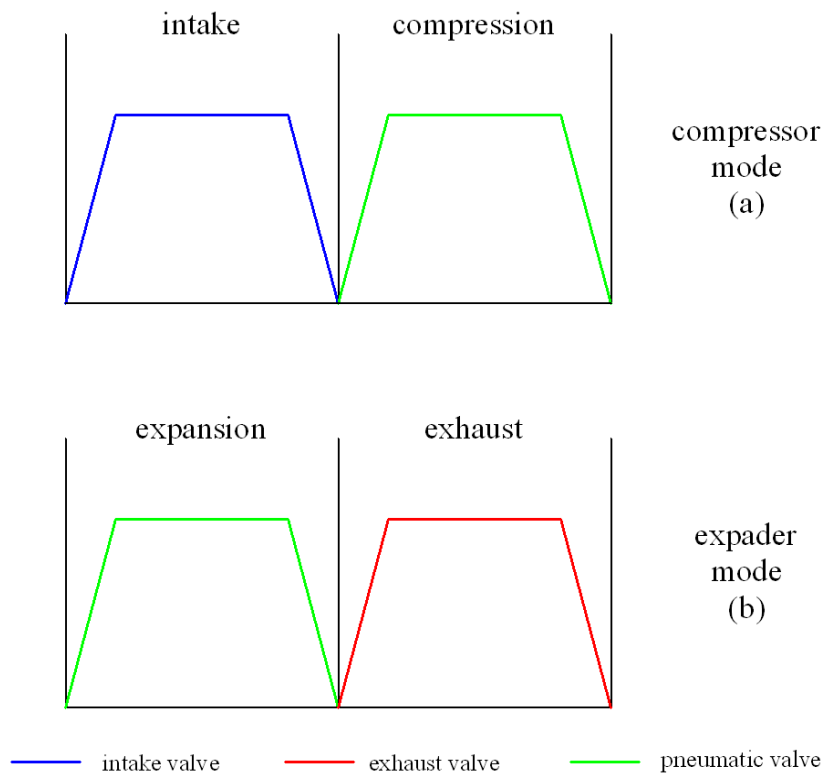


Figure 3.9: Valve events for two-stroke compressor (a) and two-stroke expander (b).

Similar to the air expander cycle, intake and compression strokes can be omitted as the gas exchange between the cylinder and the airtank is accomplished during expansion and exhaust strokes. Therefore, after the end of exhaust stroke, a new cycle can be initiated, including only one expansion and one exhaust stroke. Figure 3.8 shows the valve events of the processes described above and the corresponding piston events are shown in Figure 3.9. It should be mentioned here that only two-stroke air compressor and expander operations are adopted when FVVA is provided [55,60,62,63,64].

3.4. Air hybrid engine with a reed valve inside the intake port

This concept aims to combine the advantages of the conventional valvetrain's simplicity and conventionality of the hybrid engine described in section 3.2 with the flexibility of FVVA described in section 3.3. In order to achieve this, two well established technologies are used here; valve deactivation, Variable Valve Timing (VVT) and/or Cam Profile Switching (CPS). The later is widely used by major car manufacturers and it is known with many other commercial names. In some cases it is hydraulically actuated, two-stage cam phasing system, like Honda's V-TEC or Toyota's VVTi, while in some other cases it is continuously variable, like BMW's VANOS and Subaru's AVCS. CPS has been also successfully used for experimental studies in hybrid engines at past [72,73]. As a conventional, camshaft-operated variable valvetrain is used, the need of adopting fully variable valve actuation is eliminated and thus only minor modifications to the engine architecture are required. However, the function of the engine is not altered in any way when operating in normal firing mode.

3.4.1. Description

Figure 3.10 shows the schematic of an air hybrid, four-stroke IC engine with a piston (1) reciprocating in a cylinder (2). Exhaust valves (3) connect the cylinder with exhaust ports (4), while intake valves (5 and 6) connect the cylinder with intake ports (7 and 8 respectively). All engine valves are shown in their fully closed position towards the end of the compression stroke. Actuation of valve 5 can be deactivated and valve 6 is controlled by a CPS system. In petrol engines, where a throttle valve (9) controlled by the accelerator pedal is present in the intake to control the engine's power output (shown at its fully opened position), a bypass throttle valve (10) is needed to allow air to be induced into the

cylinder during decelerations (shown at its fully closed position) when the main throttle valve is closed. However, in Diesel engines, throttles 9 and 10 are omitted. High-pressure air is stored into an air reservoir (11) which is connected to intake port 8 through an Energy Control Valve (ECV) and an auxiliary chamber (12 and 13 respectively). ECV is operated in a synchronized fashion to let air in and out of the airtank in respect with the gas exchange and work strokes of the engine cycle and in regard to intake valve 6. In order to prevent backflow from the cylinder to the atmosphere through intake port 8 when air pressure inside the port is higher than atmospheric, a non-return reed valve (14) is located inside intake port 8. When air pressure is lower than atmospheric (i.e. during normal intake stroke), the reed valve pedals open and air is induced into the port. Valve 6 opening and closing events as well as valve 5 deactivation are described in section 3.4.2 and investigated in Chapter 4. Intake and exhaust manifolds as well as ignition, cooling and fuelling systems are not shown in Figure 3.10 for simplicity reasons, as they are not the subject of the present study.

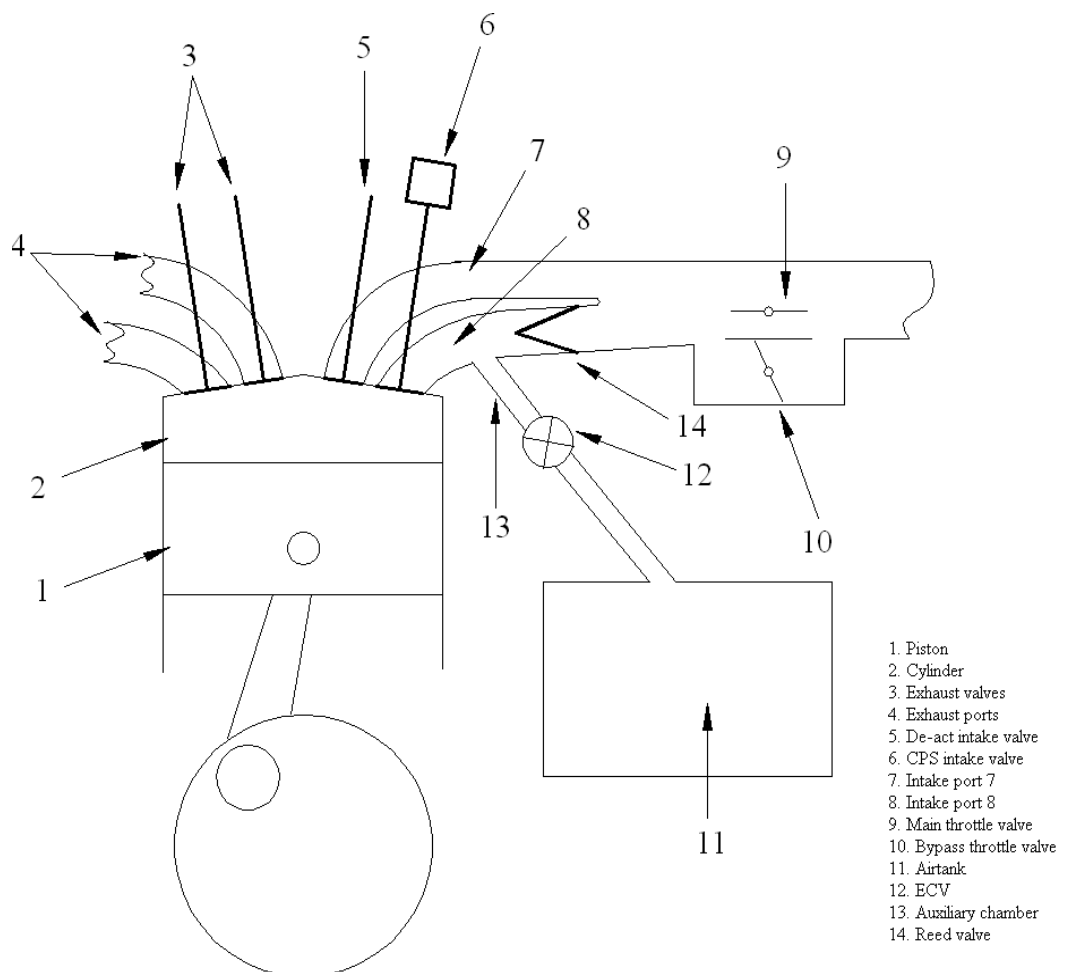


Figure 3.10: Air hybrid engine with a reed valve inside the intake port.

The volume isolated between intake valve 6, ECV and reed valve plays a significant role in the performance of the hybrid engine. Preferably, this volume should be small enough to be included in the clearance volume of the engine cylinder. A substantially constant compression ratio can then be achieved by compressed air into the buffer chamber, irrespective of the state of charge of the airtank when operating in CM and thus providing a predictable braking behaviour to the driver. Similarly, a constant expansion ratio should be realized in EM, sufficient to bring the expanded air to ambient pressure at the end of the expansion stroke. Also ideally, the reed valve must be located as close to intake valve 6 as possible in order to minimize the isolated volume. This might introduce some difficulties in implementation because there is usually little room available inside the intake port for a reed valve to be mounted and in addition the reed valve must be robust, capable of withstanding pressures in the area of peak cylinder pressure when no combustion takes place (i.e. around 20 bar).

3.4.2. Operation

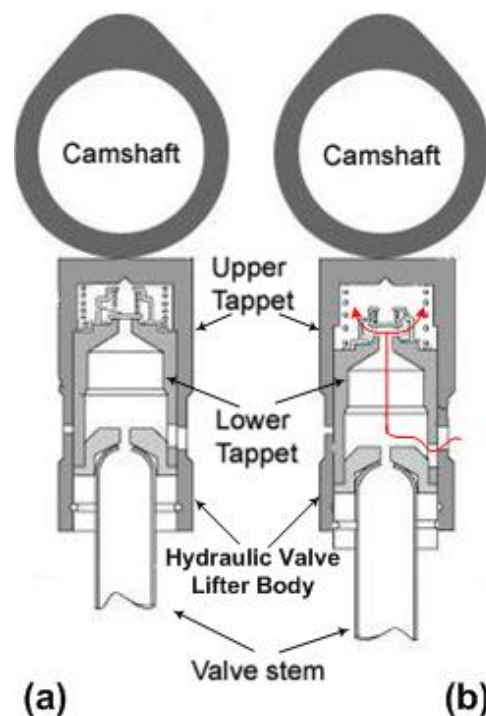


Figure 3.11: Hydraulic valve lifter for intake valve 6 selective actuation, shown in normal operating position (a) and actuated by hydraulic pressure (b).

When the engine is operated as an air compressor during regenerative braking, intake valve 5 opens during intake stroke and a mass of air is sucked into the cylinder. Intake valve 6 is timed to open towards the end of the intake period, as VVT is activated. Alternatively, a hydraulic tappet may be used to jam open intake valve 6 throughout the intake and

compression strokes. Pressurized engine oil may be provided to the hydraulic tappet and act as a hydraulic spring in order to expand valve lifter and push the valve stem and open the intake valve, while the upper part of the tappet is in contact to the camshaft ramp, which keeps it in closed position (see Figure 3.11).

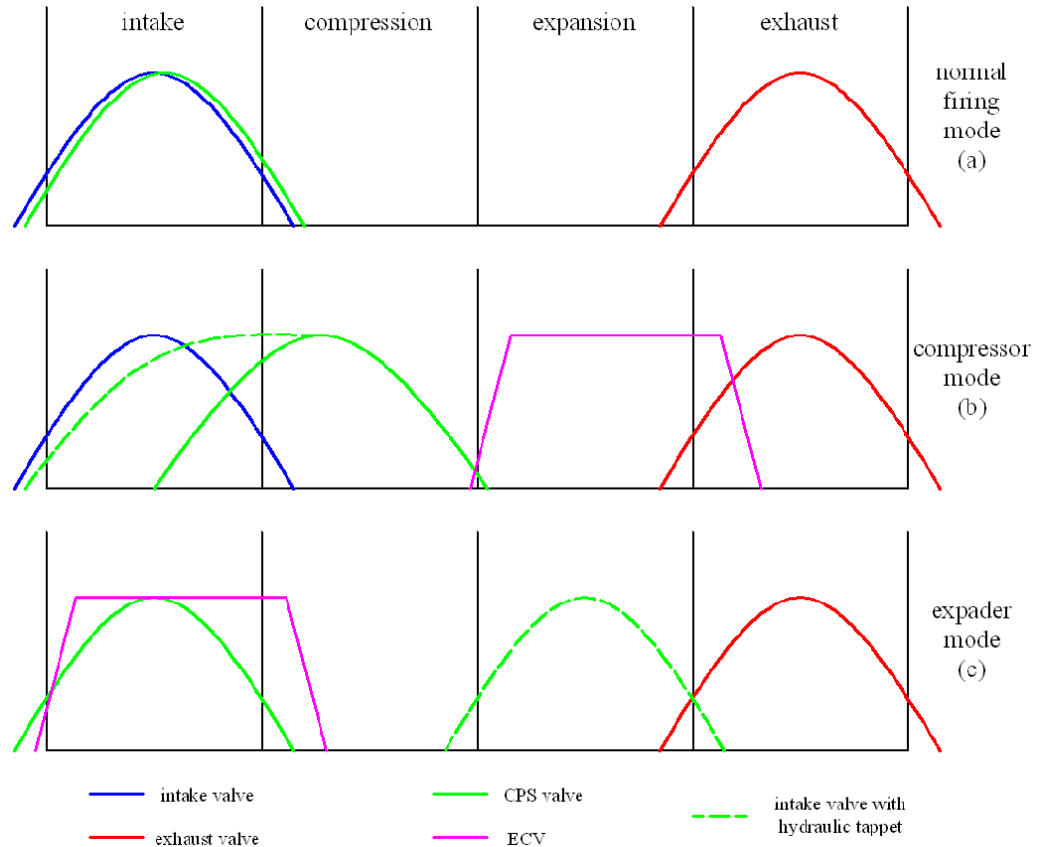


Figure 3.12: Engine valve, CPS valve and ECV events for normal firing mode (a), CM (b) and EM (c).

The reed valve may open during the intake period, provided that air flow direction is towards the engine cylinder. Air is then transferred to the auxiliary chamber during compression stroke, whilst intake valve 6 is kept open, ECV is closed and reed valve is automatically shut as it is subjected to a pressure higher than the intake air supply (ambient) pressure. During expansion period, valve 6 closes and ECV opens, allowing high-pressure, high-temperature air mass previously trapped between valve 6, ECV and reed valve to expand into the low-pressure, low-temperature airtank until the system pressure stabilizes. The mass of air remaining inside the cylinder's clearance volume expands into the cylinder as the piston travels downstroke. In order to ensure that no fuel will enter the airtank, engine cylinders must be purged of any residual fuel by cutting-off the fuel a few cycles before connecting to the buffer chamber. The piston moves upstroke during exhaust stroke, pushing the air remaining into the cylinder towards the atmosphere

through the opened exhaust valve. In order to obtain the highest possible level of brake energy absorption from the engine, an ideal cycle should include a high-pressure compression stroke followed by a low-pressure expansion stroke and the engine indicator diagram therefore follows an anti-clockwise direction.

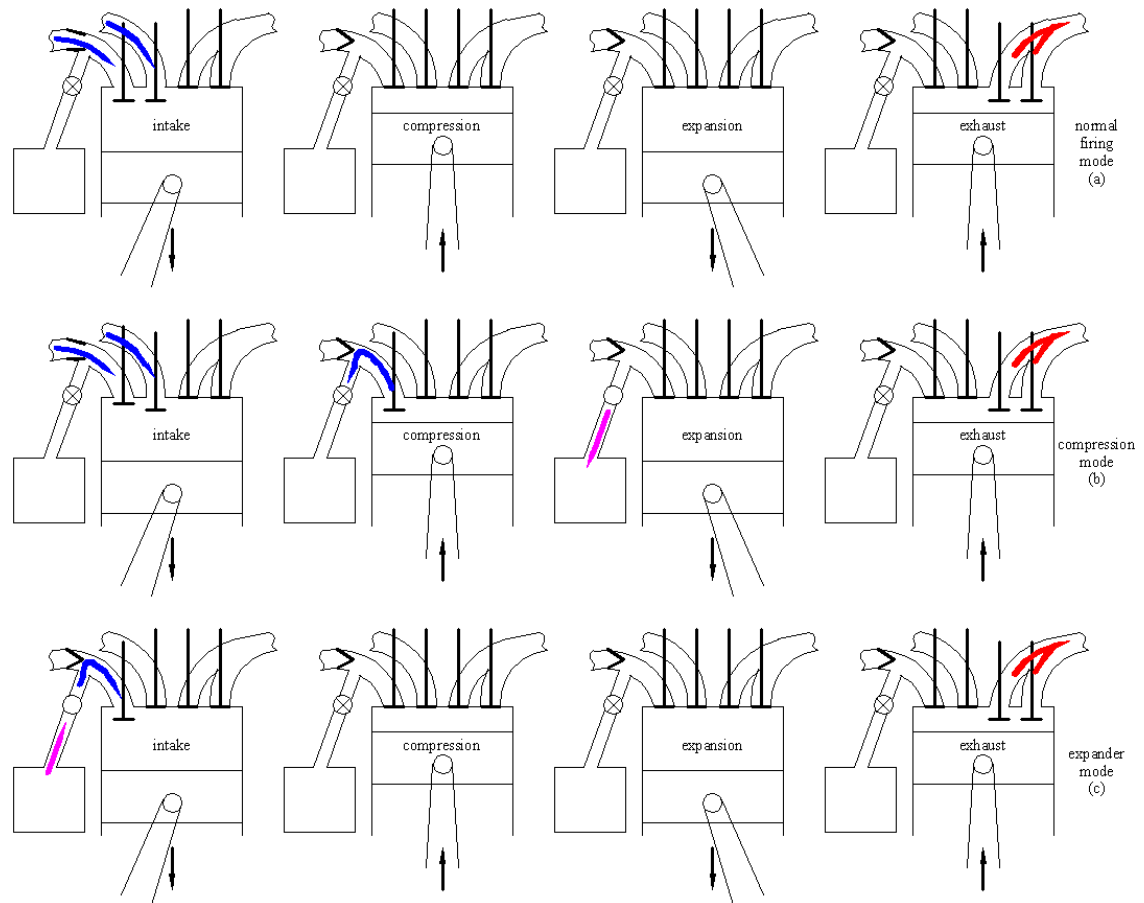


Figure 3.13: Four-stroke engine cycle for normal firing mode (a), CM (b) and EM (c).

When the engine is operated as an air expander during start-ups and accelerations, ECV and intake valve 6 open during normal intake period (while intake valve 5 is disabled) and a charge of high-pressure air from the airtank enters the low-pressure cylinder and pushes the piston down. During this time, the reed valve is automatically shut as it is subjected to the pressure released from the airtank, which is higher than ambient pressure. Therefore, intake stroke is the actual power stroke of the cycle here. Intake valve 6 closes and the piston moves upstroke during compression stroke and the mass of air released in the cylinder during intake stroke is compressed, to expand again during the subsequent expansion stroke. Alternatively, both intake valves may open normally during intake stroke and close during the compression stroke. At the beginning of the subsequent expansion stroke, intake valve 6 and ECV open so greater expansion work can be obtained. In this case, the same hydraulic tappet can be used to reopen intake valve 6 during the expansion

stroke, without the additional need of deactivation of intake valve 5. The benefit is that the actuation mechanism of valve 5 remains entirely conventional.

Finally, exhaust valve opens and the air mass remaining in the cylinder escapes to the atmosphere. In order to obtain the highest possible torque output from the engine, an ideal pneumatic motor cycle should include a high-pressure intake stroke and a low-pressure exhaust stroke, while compression and exhaust strokes should ideally be identical. Figure 3.12 shows the valve timings for normal firing mode, CM and EM by means of a graph, while the corresponding piston events are shown in Figure 3.13.

3.5. Summary

Three different gas transfer methods for operating an air hybrid engine for automotive applications are described in the present Chapter. The common characteristic of all three concepts is that no alterations to the conventional vehicle drive train are required and therefore any modification needed is limited to the engine. The energy storage and regeneration method of the air hybrids described here has similarities to that of the mechanical hybrids in that they store energy in what is effectively an air spring; during braking, the engine is operated as an air compressor and is driven by the wheels to charge an air accumulator (airtank), while it is switched to become an air motor during launch.

A conventional IC engine is combined with a pneumatic energy converter and storage subsystem in the first concept, in such a way that there is no need of major changes to the base engine. This not only can lower the production cost and weight of the system, but also provides simplicity over valve control as it is based on well-known technologies which are already in production. The energy storage tank is not directly connected to the engine cylinder but it communicates in two stages by means of an ERV, which allows for flexibility in air transfer procedures during pneumatic pump and pneumatic motor cycles as the buffer chamber embodied into the ERV dictates the compression and expansion ratio respectively. However, one of the main drawbacks of the concept is that it requires extra access to the cylinder head to connect to the buffer chamber and therefore the additional clearance volume may be problematic. It also requires a fairly complicated ERV actuation.

The second concept introduces an IC engine with a versatile, camless FVVA system. One of the engine's exhaust valves is operated as a gas transfer valve and connects the cylinder

directly to the airtank in such a way that air compressor and expander modes can be realized. The trapezoidal valve lift profiles, which provide increased valve effective duration, compensate for the complexity of the system. The highlight of the concept is that FVVA makes two-stroke air compressor and expander cycles possible, which increases hybrid engine performance. However, fast and accurate control is required, as well as complicated coordination of all valves to switch to air hybrid mode.

The last concept adopts well established technologies which use conventional camshaft valvetrains: variable valve timing and hydraulic tappet valvetrain. Both technologies are currently widely used in automotive engines. An ECV connects the airtank to one of the intake ports and a one-way reed valve controls the direction of the air flow, while no further modification to the engine or to the exhaust valvetrain is necessary. The concept is therefore similar to the first concept, with a two stage air transfer process controlled by an intake valve of variable timing and an ECV for compressor and expander modes. Switching back to normal firing mode is easier than in the second concept, as no electro-hydraulic actuation for the engine valves is involved. However, a robust reed valve is required.

Chapter 4: Modeling of the Concepts

4.1. Introduction

The three concepts described in Chapter 3 are modelled here. Therefore, the present Chapter comprises the modelling part of this Thesis. Prior to the simulation results, a systematic study on the optimal valve timing for each one of the air compressor and air expander cycles of every concept is undertaken. Parameterization of a model air hybrid engine is obviously much simpler and less time-consuming than that of a real engine in a test facility. Therefore, the effects of operating parameters, such as airtank volume, buffer chamber volume, auxiliary chamber volume, compression ratio, etc, on compressed air transfer, braking and driving efficiencies are examined in this Chapter.

4.2. Engine modeling tool

Ricardo's WAVE software is utilized so that the modeling work on a baseline hybrid engine described in this Chapter can be undertaken. This computer-aided engineering code is an engine simulation tool specifically designed for both steady state and transient simulations and can be used to model the complete IC engine. It is based on one-dimensional gas dynamics (general fluid dynamics simulation tools like Fluent or STAR-CD are three-dimensional) and it can simulate the gas flow and heat transfer in the pipes, cylinders and other components of any engine. WAVE analyzes the dynamics of pressure waves, mass flows, and energy losses in ducts, plenums, and the manifolds of various systems. It also provides a fully integrated treatment of time-dependent fluid dynamics and thermodynamics by means of a one-dimensional finite-difference formulation incorporating a general thermodynamic treatment of working fluids including air, air-hydrocarbon mixtures and products of combustion.

The piping and manifolds of the intake and exhaust systems are modeled using the duct and junction components of the basic WAVE code (described in the WAVE basic user manual [74]). Every element has a number of user-defined attributes, such as length, diameter, initial pressure and temperature, friction and heat transfer coefficients, etc. These networks are then linked together through models, which have been calibrated to provide accurate driving inputs for the intake and exhaust pressure-wave dynamics. In addition to

the fluid flow and heat transfer capabilities, the code contains many specialized features needed for IC engine modeling, such as fuel injection, valve actuation and turbocharging. The details of the flow in ducting systems are obtained as a solution of quasi-one dimensional compressible flow equations governing the conservation of mass, momentum and energy. The duct system is discretized into a series of small volumes and the governing equations are then written in a finite difference form for each of these elementary volumes. A staggered mesh system is used, with equations of mass and energy solved for each volume and the momentum equation solved for each boundary between volumes. Three engine modeling options are available: the basic engine model, an advanced engine model (IRIS) and a crankcase scavenging model for 2-stroke engines. The basic engine model is adopted for the present simulation.

WAVE provides detailed printed output of a large number of key parameters of engineering importance. This includes integrated quantities such as time-mean pressures, temperatures and flow rates at many locations within the duct/manifold network. In addition, the time variation of important variables is available in the form of detailed plots through simple input specifications. Variables such as mass flow, velocity, composition and thermodynamic variables throughout the duct system are available for plotting.

4.3. Normal firing and air hybrid engine operating parameters

4.3.1. Performance coefficients

Cylinder pressure can be plotted against the corresponding cylinder volume on a p - V diagram, also known as “indicator diagram”. This term derives from a device which had been used in the past to generate this diagram, called “the engine indicator” (see Figure A3 in the Appendix). The area enclosed by the indicator diagram is the indicated work (W_i) done by the gas on the piston:

$$W_i = \sum_{cylinders} \oint p \, dV \quad \text{Equation 4.1}$$

It should be noted here that V is the total cylinder volume: $V = V_c + V_d$ (V_c : clearance volume, V_d : displacement or swept volume – $V_d = \frac{\pi \cdot D^2}{4} \cdot S$ where D is the cylinder bore and S is the piston stroke).

Indicated mean effective pressure (*imep*) is a measure of the indicated work output per unit swept volume, in a form independent of engine size and engine speed. The term *imep* arises because its unit is force per unit area (i.e. pressure):

$$imep = \frac{W_i}{V_d} \quad \text{Equation 4.2}$$

Indicated power (P_i) is defined as in Equation 4.3:

$$P_i = \frac{W_i \cdot N}{n_R} \quad \text{Equation 4.3}$$

Where N is the engine rotational speed and n_R the number of crank revolutions for each power stroke per cylinder. That is 1 for two-stroke and 2 for four-stroke engines.

Thus, indicated torque (T_i) is:

$$T_i = \frac{P_i}{2 \cdot \pi \cdot N} \quad \text{Equation 4.4}$$

The torque output of the engine can be measured on a dynamometer. While the engine is running, the dynamometer brakes it mechanically (friction brakes), electromagnetically (electricity generator) or hydraulically (hydraulic pump). Therefore, the torque exerted on the dynamometer's stator is called *brake torque* (T_b) and the power which is produced, *brake power* (P_b):

$$P_b = 2 \cdot \pi \cdot N \cdot T_b \quad \text{Equation 4.5}$$

Therefore, brake work (W_b) and brake mean effective pressure (*bmep*) is respectively:

$$W_b = 2 \cdot \pi \cdot T_b \cdot n_R \quad \text{Equation 4.6}$$

$$bmep = \frac{W_b}{V_d} \quad \text{Equation 4.7}$$

Frictional power (P_f) equals the difference between P_i and P_b :

$$P_f = P_i - P_b \quad \text{Equation 4.8}$$

Thus, frictional work (W_f) and frictional mean effective pressure ($f MEP$) are respectively:

$$W_f = W_i - W_b \quad \text{Equation 4.9}$$

$$f MEP = i MEP - b MEP \quad \text{Equation 4.10}$$

Furthermore, $f MEP$ is a strong function of engine speed and peak cylinder pressure and can be calculated numerically by Equation 4.11 [75]:

$$f MEP = A + B \cdot P_{max} + C \cdot \frac{N \cdot S}{2} + D \cdot \left(\frac{N \cdot S}{2} \right)^2 \quad \text{Equation 4.11}$$

where P_{max} is the maximum cylinder pressure, S is the piston stroke and A , B , C , D are constants. The typical values of these constants are: $A = 0.5$, $B = 0.006$, $C = 600$, $D = 0.2$ [76]. Apart from the numerical method, a way to practically measure frictional power is to drive the engine with a dynamometer (i.e. use the dynamometer to motor the engine) and measure the torque (and thus the power) which must be consumed to overcome all these frictional losses. However, this method is not very accurate as the forces applied to engine's components are much higher when the engine is firing.

4.3.2. Compressed Air Transfer Coefficients (CATC)

During pneumatic pump and motor operations, there is gas exchange taking place between the cylinder, the atmosphere and the airtank. Therefore, air mass is transferred through three boundaries of interest: the intake valve, the exhaust valve and the gas transfer valve. The amount of air past these boundaries during the engine cycle is enclosed by the trace of air mass flow against crank angle (CA) and it can be calculated by integrating the $\dot{m}_{air} - t$ diagram predicted by WAVE, after having converted CA to time units:

$$m_{air,in} = \left| \int \dot{m}_{air,in} dt \right| \quad \text{Equation 4.12}$$

$$m_{air,ex} = \left| \int \dot{m}_{air,ex} dt \right| \quad \text{Equation 4.13}$$

$$m_{air,gtv} = \left| \int \dot{m}_{air,gtv} dt \right| \quad \text{Equation 4.14}$$

4.3.2.1. Air compressor

CATC for braking mode ($CATC_b$) is indicative of the air hybrid braking efficiency and it is a measure of the fraction of the vehicle's kinetic energy which can be stored in the air reservoir in the form of potential energy. It is defined as the ratio of air mass transferred to the airtank from the cylinder to air mass transferred to the cylinder from the atmosphere, as described by Equation 4.15:

$$CATC_b = \frac{m_{air,gtv}}{m_{air,in}} \quad \text{Equation 4.15}$$

The following Equations express the application of the law of mass conservation:

$$m_{air,in} = m_{air,ex} + m_{air,gtv} \quad \text{Equation 4.16}$$

$$\frac{m_{air,gtv}}{m_{air,in}} + \frac{m_{air,ex}}{m_{air,in}} = 1 \quad \text{Equation 4.17}$$

From Equations 4.15 and 4.17, another expression of $CATC_b$ derives:

$$CATC_b = 1 - \frac{m_{air,ex}}{m_{air,in}} \quad \text{Equation 4.18}$$

The work is done from the wheels to the engine and thus imep and bmep during braking ($imep_b$ and $bmep_b$ respectively) are:

$$imep_b = |imep| \quad \text{Equation 4.19}$$

$$bmep_b = |bmep| \quad \text{Equation 4.20}$$

$$fmep_b = bmep_b - imep_b \quad \text{Equation 4.21}$$

The range of $CATC_b$ values is between 0 and 1. Values close to zero indicate that most of the air induced during intake period is exhausted to the atmosphere during exhaust stroke and thus only little air mass is stored to the airtank at the end of the cycle. Values close to

the unit indicate that most of the air induced during intake period is stored to the airtank and thus only little air mass is exhausted to the atmosphere at the end of the cycle.

4.3.2.2. Air expander

CATC for driving mode ($CATC_d$) is indicative of the air hybrid driving efficiency and it is a measure of the fraction of the potential energy stored in the airtank which can be reimbursed to the vehicle in the form of kinetic energy. It is defined as the ratio of air mass transferred to the cylinder from the atmosphere during intake to air mass transferred to the atmosphere from the cylinder during exhaust, as described in Equation 4.22:

$$CATC_d = \frac{m_{air,in}}{m_{air,ex}} \quad \text{Equation 4.22}$$

The range of $CATC_d$ values is between 0 and 1. Values close to zero indicate that only little air mass is induced during intake period and thus most of the compressed air released from the airtank during power stroke is exhausted to the atmosphere during exhaust period. Values close to the unit indicate that most of the air induced during intake period is exhausted during exhaust period and thus only little compressed air from the airtank is dissipated to the atmosphere.

Equations 4.23 and 4.24 express the application of the law of mass conservation:

$$m_{air,ex} = m_{air,in} + m_{air,gtv} \quad \text{Equation 4.23}$$

$$\frac{m_{air,gtv}}{m_{air,ex}} + \frac{m_{air,in}}{m_{air,ex}} = 1 \quad \text{Equation 4.24}$$

From Equations 4.22 and 4.24, another expression of $CATC_d$ derives:

$$CATC_d = 1 - \frac{m_{air,gtv}}{m_{air,ex}} \quad \text{Equation 4.25}$$

In contrast to air compressor mode, the work is done from the engine to the wheels during air expander mode and thus $imep$ and bmp during driving ($imep_d$ and bmp_d respectively) are:

$$imep_d = |imep| \quad \text{Equation 4.26}$$

$$bmep_d = |bmep| \quad \text{Equation 4.27}$$

$$fmep_d = imep_d - bmep_d \quad \text{Equation 4.28}$$

It should be noted at this point that the term “*braking*” is used here to express the flow of energy from the vehicle to the engine and therefore means that the engine is being motored when the vehicle is braking (compression brake). The term “*driving*” is used to express the flow of energy from the engine to the vehicle and therefore means that the engine drives the vehicle when the later is coasting or accelerating.

4.4. Concept 1: Engine with Energy Recovery Valve (ERV)

4.4.1. Model description

Figure 4.1 shows the model of the present concept. The modelled engine has a stroke of 86mm and a bore of also 86mm, giving a displacement volume of 500cm³. The connecting rod length is 160mm. Intake and exhaust valve diameter is 23.5mm and 23.4mm respectively. The air transfer aperture has a diameter of 15mm. The engine speed range is between 1000 and 4000 rpm. The engine cylinder, labelled “*cylinder*” appears in the middle of the canvas and has twin intake and single exhaust valves, as well as an air transfer aperture connected to the first shut-off valve, labelled “*ERV1*” via the connecting duct (“*duct*”). An exhaust pipe connects the exhaust port (“*exhaustport*”) to the atmosphere labelled “*amb3*”.

The twin intake ports (“*intakeport1*” and “*intakeport2*”) are connected to the atmosphere (“*amb1*”) through a simple 2-in-1 intake manifold which consists of two headers (“*manifold1*” and “*manifold2*”), the plenum (“*plenum*”) and one runner (“*manifold3*”). The buffer chamber, labelled “*BUFFERCHAMBER*”, is modelled as a duct connected to one shut off valve at either end. Finally, the airtank, labelled “*AIRTANK*”, is modelled as duct of defined volume and initial pressure and it is connected to the second shut-off valve, labelled “*ERV2*”, and the end ambient (“*amb2*”) which is used here to terminate the airtank network. Table 4.1 summarizes the parameters defined for each of the model elements used.

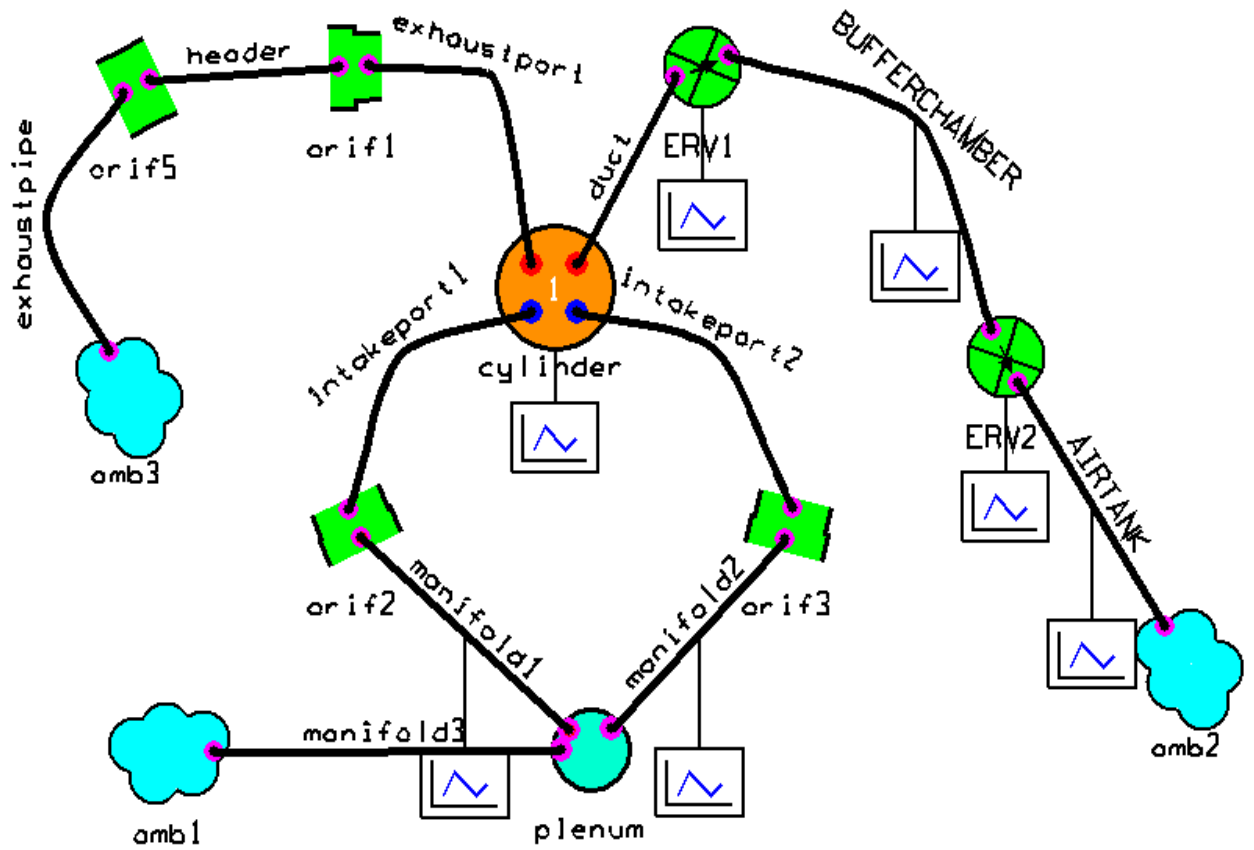


Figure 4.1: Model of air hybrid engine with ERV.

The geometric compression ratio of the engine is 18.4:1; typical for a CI engine. However, the actual compression ratio is lower because of the volume of the duct connecting the cylinder to the first shut-off valve, which must be included to the cylinder's clearance volume. According to Equation 4.29, the actual compression ratio is:

$$R_c = \frac{V_d + V_c}{V_c} = \frac{500 + 28.7 + 17.7}{28.7 + 17.7} = 11.8:1 \quad \text{Equation 4.29}$$

where V_d is the cylinder displacement volume and V_c the clearance volume. When the engine is switched to air hybrid mode, the actual compression (or expansion) ratio drops, as buffer chamber volume is included to the clearance volume. For the buffer chamber volumes of 14.4cm^3 and 28.7cm^3 examined below, the actual compression ratio is respectively:

$$R_c = \frac{500 + 28.7 + 17.7 + 14.4}{28.7 + 17.7 + 14.4} = 9.2:1 \quad \text{Equation 4.30}$$

$$R_c = \frac{500 + 28.7 + 17.7 + 28.7}{28.7 + 17.7 + 28.7} = 7.7:1 \quad \text{Equation 4.31}$$

Table 4.1: Description of the model elements used and parameters which were defined.






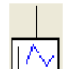

Element symbol	Description	Variables
	An orifice junction is a simple “joint” style junction used to link two ducts. It is, in effect, “massless” with no physical length. It is required to have ducts connected on both sides (i.e. it cannot have one connection and be left floating in space). It is practically a 2-D plane through which flow passes. The ducts on either side can be of different diameters or the same diameter. An orifice junction is frequently used to model a restriction in a system such as a partially shut valve or the change of section in a carburetor.	Diameter
	A basic engine cylinder junction is used to represent the power cylinder of an internal combustion engine (2-stroke or 4-stroke). Every cylinder placed on the canvas has its own properties and each connection point is considered an engine valve. Engine cylinder junctions can have multiple duct connections to represent multi-valve engines.	Engine valves, initial fluid composition, strokes per cycle, bore, stroke, compression ratio, reference pressure, reference temperature, heat transfer, wall thickness, coolant temperature, scavenge, combustion, conduction.
	An ambient junction is used to represent either the “atmosphere” ends of a model or flow terminations. If the diameter of the orifice represented by the ambient is set to 0, then the ambient is considered a flow termination (end of a pipe). An ambient junction can only have one duct connected to it so, if a model has a multiple tailpipe exhaust muffler, each tailpipe must have its own ambient junction.	Initial fluid composition, diameter, pressure, temperature.
	Y-junction: Y-junctions are used to model complex geometrical parts of a system that cannot be represented as ducts. They are typically used to model junctions where more than two ducts come together. System elements that are commonly modelled using y-junctions are air cleaners, inlet manifolds, catalysts, and exhaust mufflers. A y-junction can have any number of ducts attached (within specified limits).	Initial fluid composition, structure, diameter, wall-friction multiplier, heat transfer multiplier, initial pressure, initial fluid temperature, wall temperature.
	A checkvalve junction is placed between two ducts. The valve may have a motion imposed as function of time (as in a poppet valve driven by a cam or actuator) or driven by flow dynamics (as in a reed valve or check ball valve). Checkvalve junctions are used to model a reed valve or cam-actuated valve. Each checkvalve junction may have several valves assigned to it, allowing simulations of a pack of reed valves or a plate with two different types of valves placed in it.	Valve type, valve count, synchronization, flow direction, actuator.
	A large variety of plots are available within WAVE. Plots can be specified in a number of ways, depending on the type of plot required and the element in the model for which the output to be plotted is based. Plots are available for all ducts, junctions, sensors, actuators and external connections to other models. They can be time-based, a variable versus time or crankangle, or FFT style as for noise analysis.	Plot type, location, sampling rate.
	A model of a manifold or pipe system is constructed in WAVE as a network of ducts connected by junctions. Every duct must be terminated by a junction on either end. Some types of junctions simply connect ducts to each other. Some model special types of volumes, such as the connections between more than two ducts. Others are models of more complex systems such as turbines, compressors or engine cylinders. Ducts are used to represent all those sections of a pipe network that can be thought of as a duct (i.e. a region where the flow can be treated as one-dimensional).	Left diameter, right diameter, discretization length, overall length, bend angle, friction coefficient, heat transfer coefficient, pressure loss coefficient, initial pressure, initial fluid temperature, initial wall temperature, initial fluid composition, structure.

Table 4.2: Model dimensions and characteristics.

Engine		Valves		Manifolds	
Number of cylinders	1	Intake valve count	2	Intake header count	2
Cylinder bore	86mm	Diameter	23.5mm	Diameter	30mm
Piston stroke	86mm	Opening point	20° BTDC	Length	300mm
Connecting rod length	160mm	Closing point	60° ABDC	Volume	212cm ³
Displacement volume	500cm ³	Maximum lift	8.75mm	Runner count	1
Clearance volume	28.7cm ³	Exhaust valve count	1	Diameter	50mm
Total volume	528.7cm ³	Diameter	23.4mm	Length	400mm
Compression ratio		Opening point	60° BBDC	Volume	785cm ³
geometric	18.4:1	Closing point	35° ATDC	Plenum volume	65cm ³
at normal mode	11.8:1	Maximum lift	8.75mm	Exhaust header count	1
at air hybrid mode	(a) 9.2:1	Aperture diameter	15mm	Diameter	37mm
	(b) 7.9:1	Other		Length	500mm
Ports		Duct1 length	200mm	Volume	537cm ³
Intake port count	2	Diameter	15mm	Runner count	1
Volume	46cm ³	Volume	18cm ³	Diameter	37mm
Exhaust port count	1	Airtank volume	10 litre	Length	500mm
Volume	53cm ³	Buffer chamber volume	(a) 14.4cm ³	Volume	537cm ³
			(b) 28.7 cm ³		

Air mass flow, pressure and temperature plots are requested for the cylinder, shut-off valves, buffer chamber, airtank and intake manifold. Valve lift profile plots are also requested for engine intake and exhaust valves as well as shut-off valves. Imep, fmep, bmep and indicator diagram plots are requested for the engine cylinder in particular. The dimensions of the model and the piping network, together with other characteristics, are summarized in Table 4.2.

4.4.2. Valve timing optimization

As shown in Table 4.2, intake valves open at 20° BTDC and close at 60° ABDC while exhaust valve open at 60° BBDC and close at 35° ATDC. That valve timing remains unaffected, regardless the engine mode (normal firing or air hybrid). ERV timing highly depends on the mode on which the engine is running, so investigation for air compressor (braking) and air expander (driving) modes must be separately undertaken. It is obvious that in normal firing mode ERV is deactivated and no gas exchange between the cylinder and the airtank takes place. The aims of the valve timing optimization for air compressor and air expander modes are:

- a) Reversible compression during braking at constant compression ratio.
- b) High compressed air mass transfer ratio.
- c) Constant braking torque, regardless the state of charge of the air tank.
- d) Reversible expansion during driving at constant expansion ratio.
- e) High torque output at very low engine speeds during driving (for engine start-up).
- f) Lowest possible energy losses.

4.3.2.1. ERV timing for air compressor mode

As described in Chapter 3, the first shut-off valve opens during the intake stroke to allow the air trapped inside the buffer chamber to expand to the cylinder, and thus increasing volumetric efficiency. A fraction of that air mass escapes to the atmosphere through the open intake valves. Therefore, first shut-off valve opening point is not of importance and does not affect the performance of the air compressor, as far as the valve opens during intake stroke, while intake valves are open. Similarly, second shut-off valve closing point is not of importance as it happens after first shut-off valve closing and thus it does not affect the gas exchange process between the buffer chamber and the cylinder. However, first shut-off valve closing event has a significant effect on the air hybrid compressor cycle and therefore it needs to be optimized below in a systematic way.

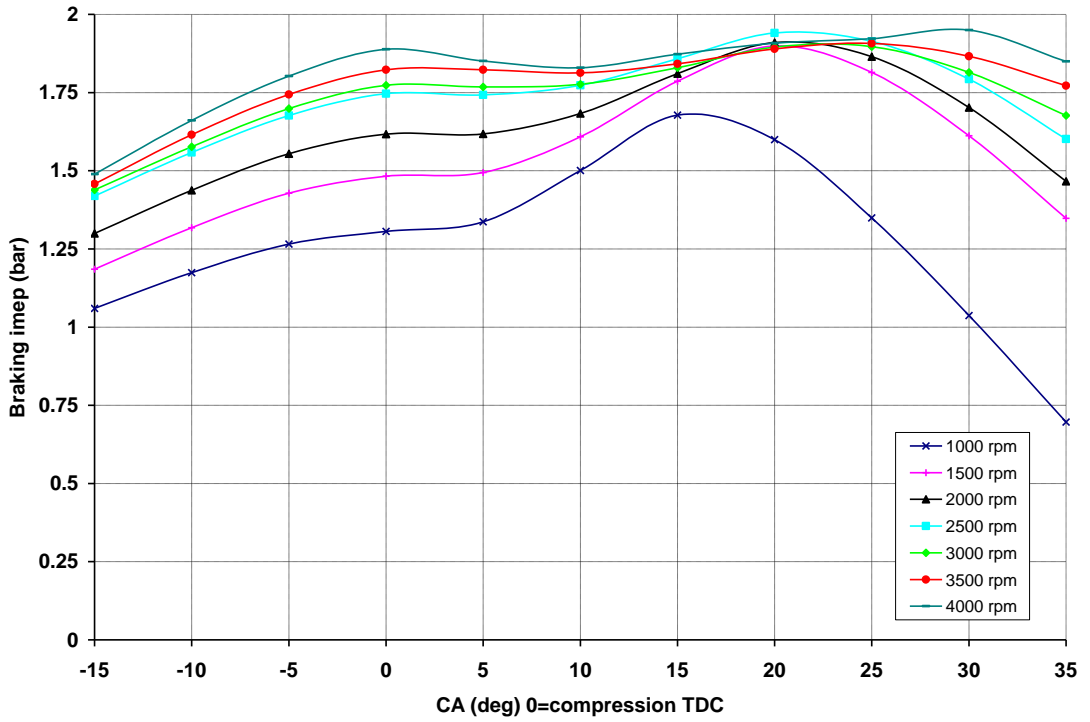


Figure 4.2: Predicted $imep_b$ against first shut-off valve closing point for engine speed range between 1000 and 4000 rpm.

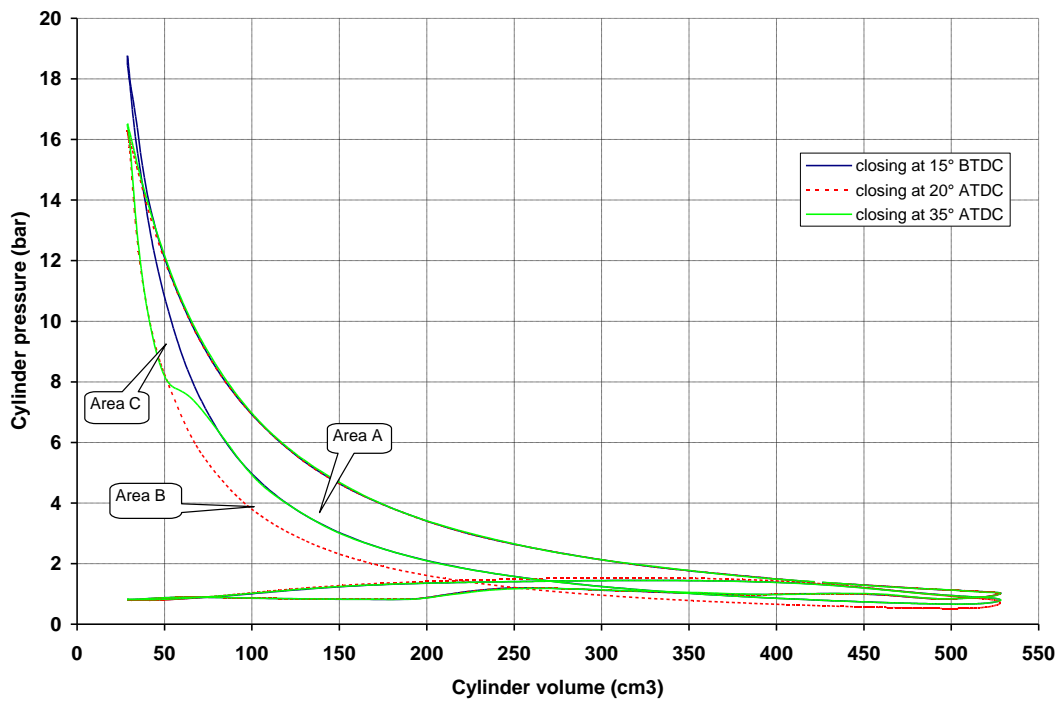


Figure 4.3: Indicator diagram at 2000 rpm engine speed for various first shut-off valve closing points.

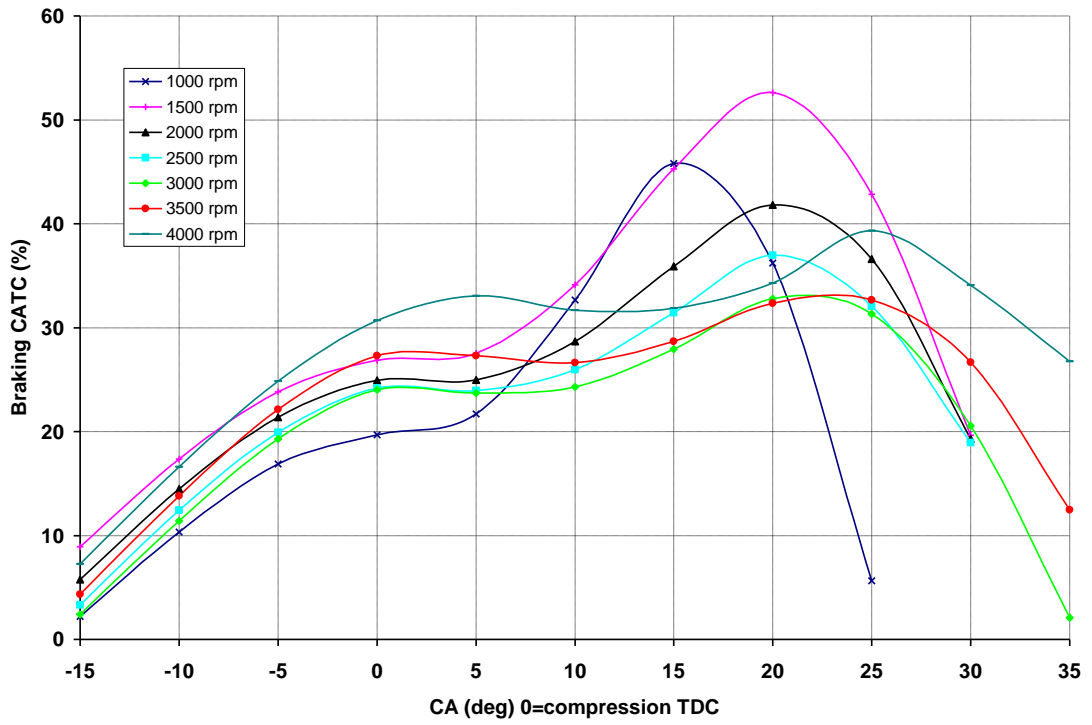


Figure 4.4: Predicted $CATC_b$ against first shut-off valve closing point for engine speed range between 1000 and 4000 rpm.

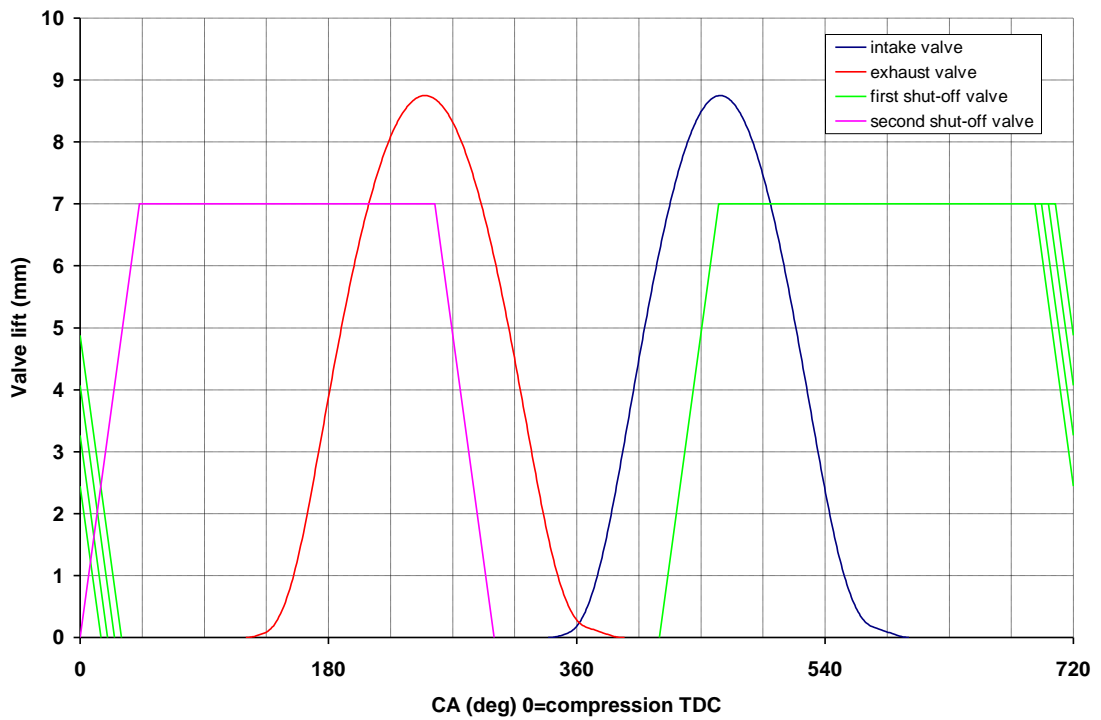


Figure 4.5: Optimal ERV timing and engine valve timing (first shut-off valve closing point is engine-speed dependant).

Finally, second shut-off valve must open at compression TDC in order to achieve a constant compression ratio during the upstroke. Advanced opening (before TDC) effects $imep_b$ depending on state of charge of the airtank. If airtank pressure is higher than cylinder pressure at the point of second shut-off valve opening, then $imep_b$ increases due to air backflow from the airtank to the cylinder. If airtank pressure is lower than cylinder pressure at the point of second shut-off valve opening, then air is pushed to the airtank and cylinder pressure drops, resulting to a decreased $imep_b$. In both cases braking torque is airtank pressure dependant and therefore the braking behaviour of the vehicle becomes unstable and unpredictable for the driver. Retarded opening (after TDC) has no effect on the air compressor performance and behaviour.

Figure 4.2 shows the predicted variation of $imep_b$ in regard to first shut-off valve closing point for the engine speed range between 1000 and 4000 rpm, at intervals of 500 rpm. The advantage of monitoring $imep$ instead of $bmeP$ lies on the fact that $imep$ is not affected by $fmeP$, which is a function of engine speed. It can be seen from the results that retarded closing at $15^\circ - 20^\circ$ ATDC increases $imep_b$ (and hence braking torque) at low engine speeds. Maximum $imep_b$ is achieved at further retarded timings (up to 30° ATDC) at higher engine speeds. For first shut-off valve closing timings after 30° ATDC or before 15° ATDC, it can be noticed that $imep_b$ descends. A variable valve actuation system is therefore needed for the first shut-off valve, capable of retarding its closing timing with increasing engine speed.

The predicted cylinder indicator diagrams for various valve closing timings at 2000 rpm which are shown in Figure 4.3 not only validate the above conclusion, but they also provide a better understanding of the gas exchange process which takes place during the air compressor cycle. For advanced valve closing (blue line), the actual compression ratio increases as the buffer chamber volume is excluded from the cylinder clearance volume and thus higher cylinder pressure is developed. However, the area included by the indicator diagram is significantly narrower than in the other two diagrams (area A). For retarded valve closing at 20° ATDC, expansion is performed at lower cylinder pressure (red line), resulting to a higher $imep_b$, as the cyclic rotation of the diagram is anti-clockwise for air compressor cycles (area A+B+C). Finally, for further retarded valve closing (green line), $imep_b$ drops as air backflow from the airtank to the cylinder increases cylinder pressure during expansion stroke (area A+C), which also has a negative effect in $CATC_b$, as shown in Figure 4.4.

According to the above investigation, optimal ERV timing is shown in the same diagram together with engine valve timing in Figure 4.5. The vast advantage of trapezoidal valve lift profile over conventional should be noted here. ERV valve lift ramp is only limited by maximum valve linear velocity. Most hydraulically actuated valves have a maximum velocity of 4.5 m/s [52,53,57,60], which gives a lift ramp of 43° crank angle at 4000 rpm engine speed, as described by Equation 4.32. This ramp is adopted for all engine speeds at the present simulation for simplicity reasons, assuming lower valve velocities for lower engine speeds.

$$ramp = 6000 \cdot \frac{L}{v} \cdot N \quad \text{Equation 4.32}$$

Where the *ramp* is the valve lift ramp in crank angle degrees, *L* is the valve lift in mm, *v* is the valve velocity in m/s and *N* is the engine speed in rpm.

4.3.2.2. ERV timing for air expander mode

The objective of optimal ERV timing for the air expander operation is to primarily provide enough torque to start the engine and ideally propel the vehicle from stop until the engine is switched to normal firing mode. It is obvious that the engine speed range of interest for expander mode is very low (between 0 rpm and idle speed). Therefore, opening and closing ramp duration for ERV can be reduced to 10° crank angle here, assuming the same valve velocity as in air compressor mode (4.5 m/s). It is also assumed that engine speed (and hence gas velocity which is proportional to piston speed) is too low to govern important aspects of the air flow through nozzles, orifices, valves and restrictions and thus it does not importantly affect $imep_d$. However, $imep_d$ is a strong function of airtank pressure, as the later governs cylinder pressure during the power stroke.

In order to lower cylinder pressure during compression stroke and therefore improve $imep_d$, as the air expander indicator diagram follows a clockwise direction, second shut-off valve must open during compression stroke, when cylinder pressure equals airtank pressure. This might result in air backflow from the cylinder to the airtank towards the end of compression period but that air mass expands reversibly back to the cylinder during expansion stroke because it is assumed that airtank volume is very large compared to cylinder volume and thus airtank pressure is constant during the cycle. Therefore, $CATC_d$ is not affected by advanced opening (before compression TDC) of second shut-off valve, as shown in Figure 4.6.

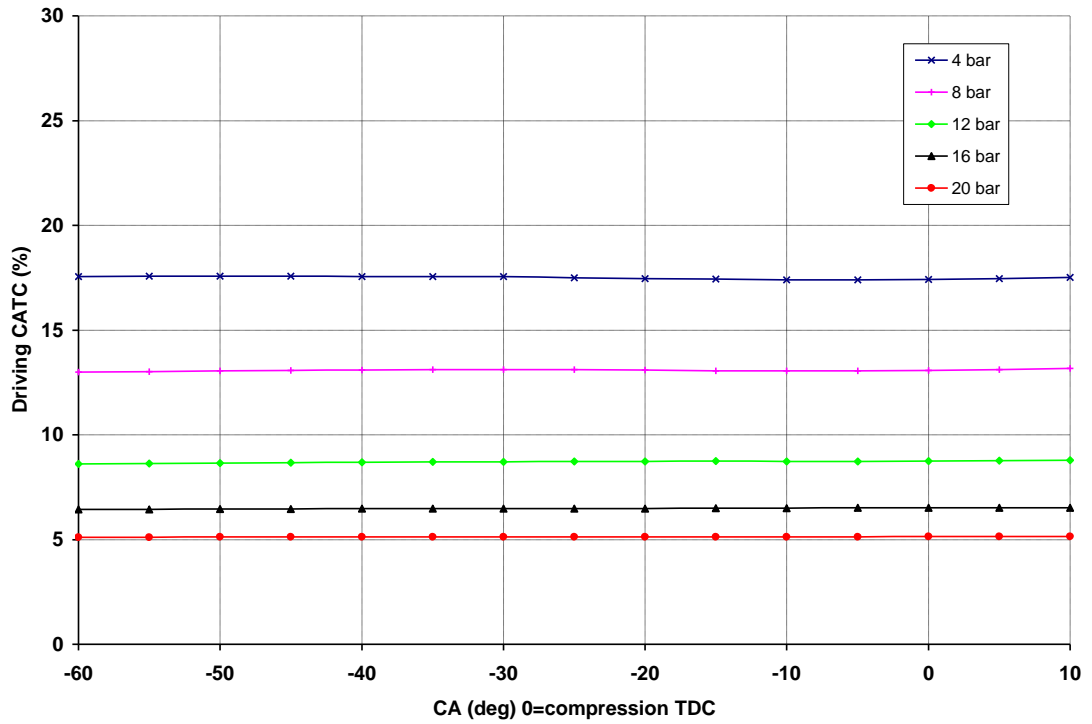


Figure 4.6: Predicted $CATC_d$ against second shut-off valve opening point for airtank pressure range between 4 and 20 bar.

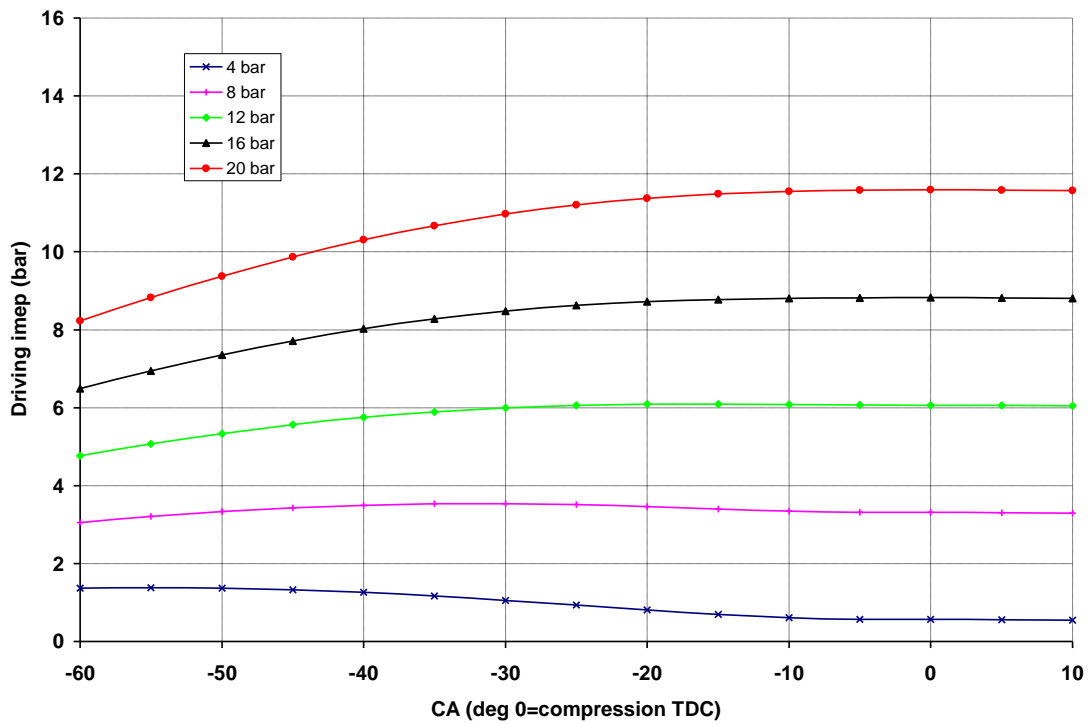


Figure 4.7: Predicted $imep_d$ against second shut-off valve opening for airtank pressure range between 4 and 20 bar.

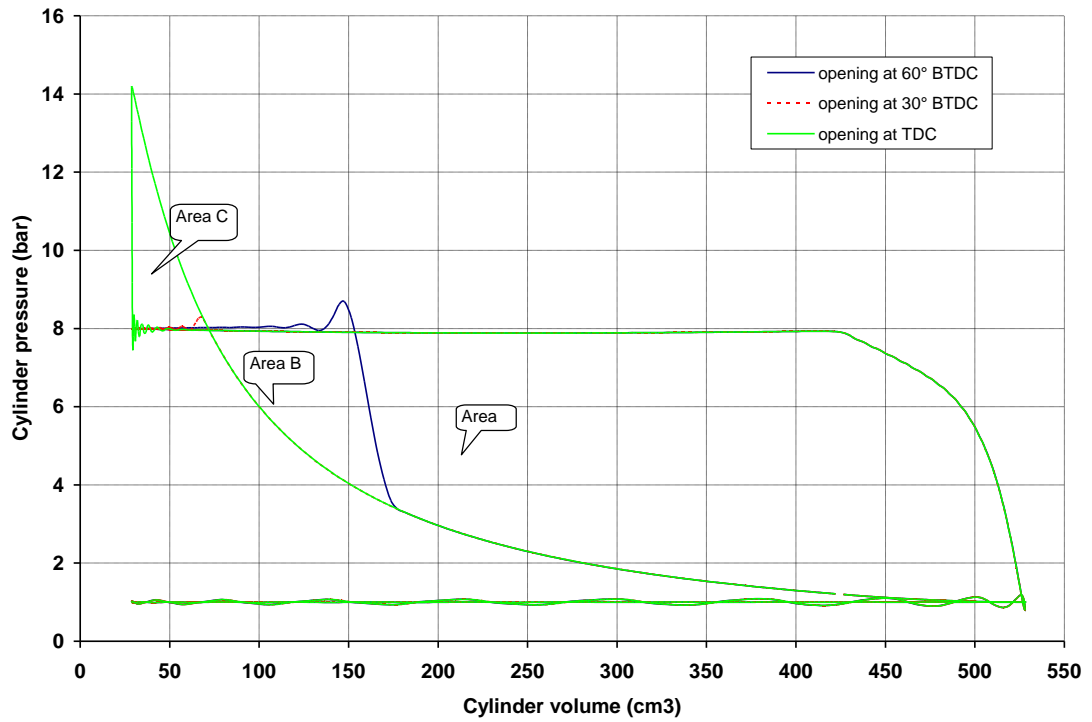


Figure 4.8: Indicator diagram at 8 bar airtank pressure for various second shut-off valve opening points.

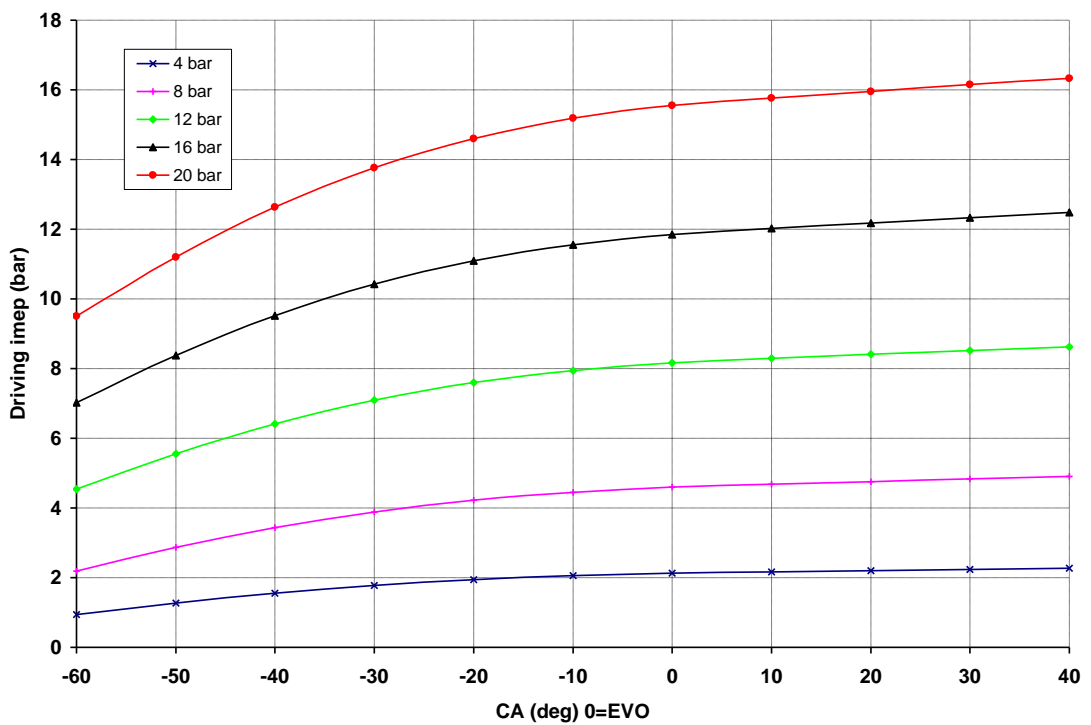


Figure 4.9: Predicted $imep_d$ against second shut-off valve closing point for airtank pressure range between 4 and 20 bar.

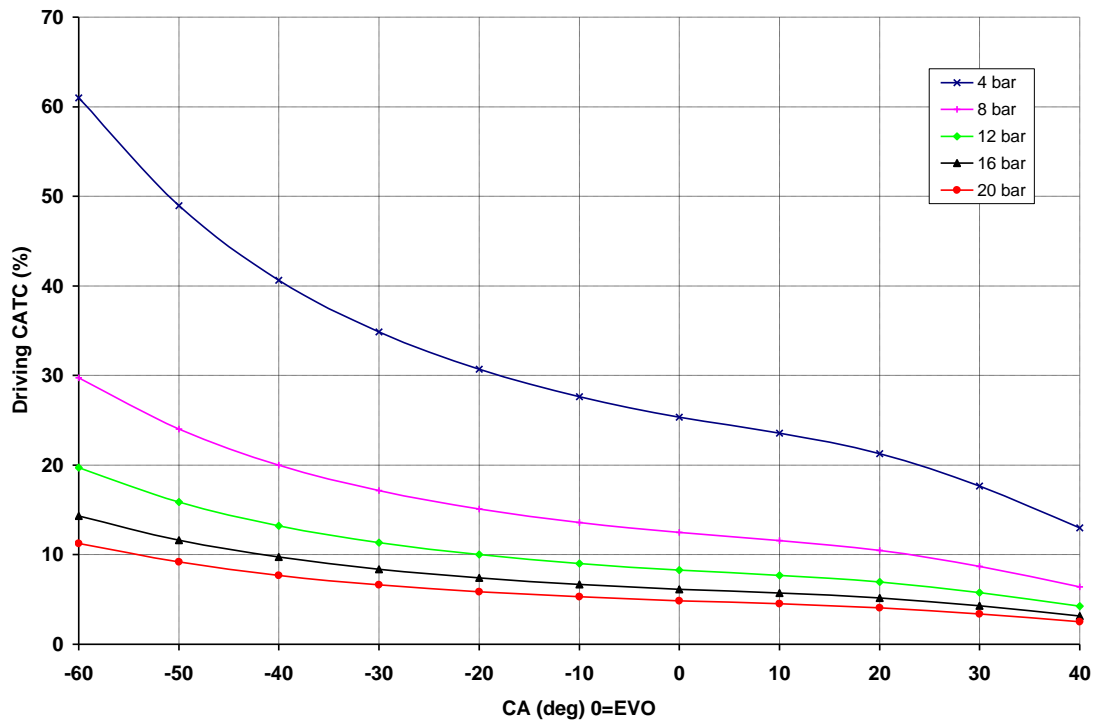


Figure 4.10: Predicted $CATC_d$ against second shut-off valve closing point for airtank pressure range between 4 and 20 bar.

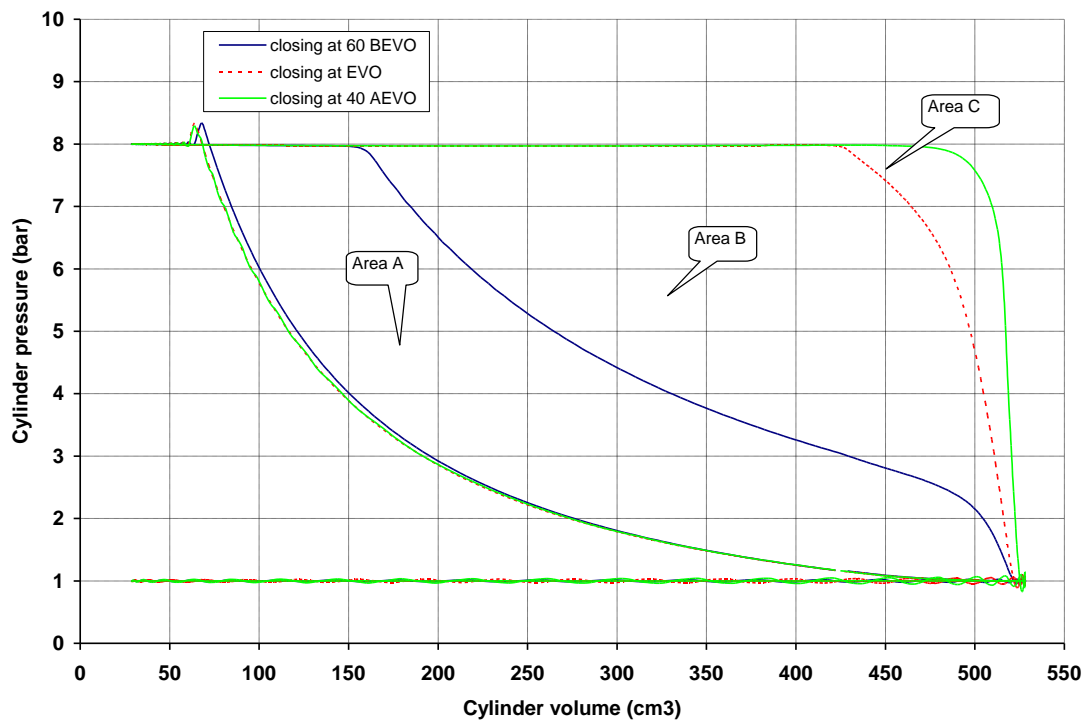


Figure 4.11: Indicator diagram at 8 bar airtank pressure for various second shut-off valve closing points.

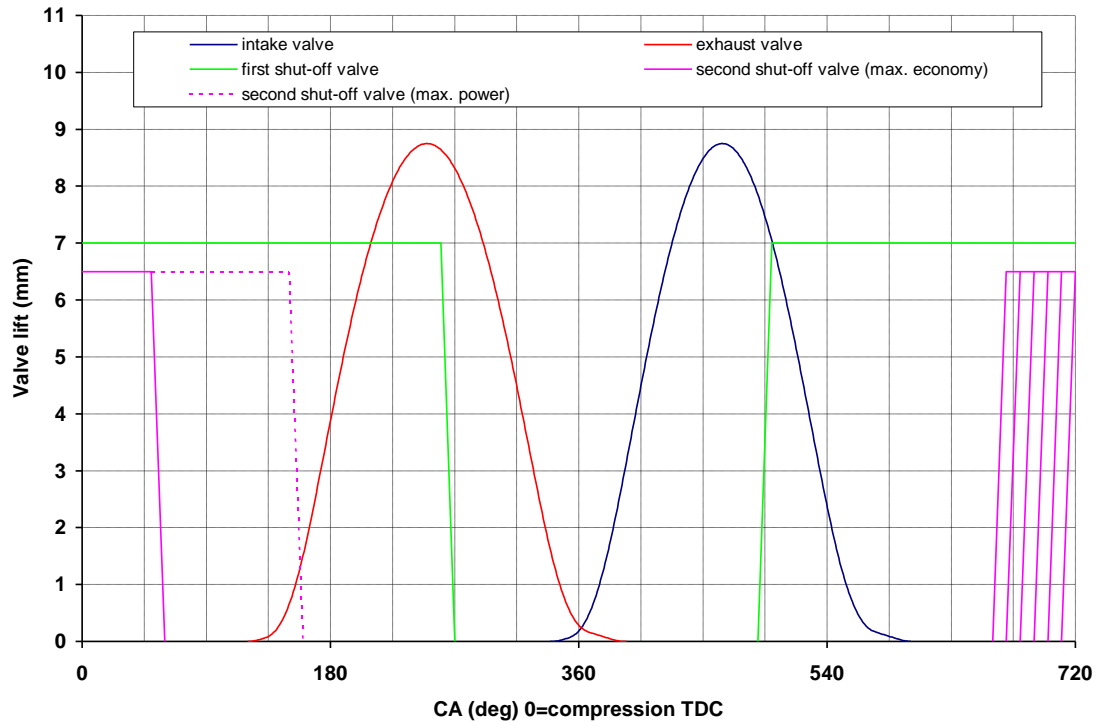


Figure 4.12: Optimal ERV timing and engine valve timing (second shut-off valve opening point is airtank-pressure dependant and closing point is power-demand dependant).

Figure 4.7 shows the predicted variation of $imep_d$ in regard to second shut-off valve opening point for airtank pressure range between 4 and 20 bar, at intervals of 4 bar. It can be seen from the results that advanced opening of second shut-off valve at 50° BTDC increases $imep_d$ (and hence braking torque) when airtank pressure is low. With increasing airtank pressure, optimal opening point is moved towards TDC. It is shown that maximum $imep_d$ is achieved at 10° BTDC - TDC for higher airtank pressures. For opening timings before 50° BTDC or after TDC, it can be noticed that $imep_d$ descends. A variable valve actuation system is therefore needed for the second shut-off valve, dependant upon the instantaneous cylinder pressure during compression and the constant airtank pressure during the cycle. The implementation of such a system should not raise difficulties, as the specific valve is electrically, hydraulically or pneumatically actuated.

The predicted cylinder indicator diagrams for various valve opening timings at 8 bar airtank pressure which are shown in Figure 4.8 provide a better understanding of the gas exchange process which takes place during the air expander cycle. For second shut-off valve opening at 60° BTDC (blue line), when the developed pressure in the cylinder is only 4 bar, compressed air from the airtank is released into the cylinder during compression stroke. This instantly increases cylinder pressure up to the nominal airtank pressure and limits $imep_d$ to area A. For second shut-off valve opening at 30° BTDC (red

line), when the developed cylinder pressure equals airtank pressure, maximum $imep_d$ is realized (area A+B). Finally, for second shut-off valve opening at TDC (green line), when peak cylinder pressure is developed, compressed air from the cylinder backflows to the airtank and then expands back to the cylinder, lowering $imep_d$ (area A+B-C).

Second shut-off valve closing must ensure that the mass of air permitted to the cylinder can be expanded effectively for maximum energy economy and $CATC_d$ (i.e. bring expanded air to ambient pressure at the end of expansion period), for example when only engine start-up is required. Under maximum launch conditions, a different valve timing philosophy is required; here maximum power is achieved by keeping the second shut-off valve open until EVO. This practically realises an $imep$ as high as the mean airtank pressure during the cycle but it increases energy wastage and lowers $CATC_d$, as cylinder pressure at the end of expansion is almost equal to airtank pressure and thus potential energy is dissipated during exhaust.

Figure 4.9 shows the variation of $imep_d$ in regard to second shut-off valve closing point for the airtank pressure range between 4 and 20 bar. As discussed above, $imep_d$ increases with retarded closing of second shut-off valve (after EVO), as more air is allowed to expand into the cylinder. It should be noted that the sensitivity of the system to valve closing is much higher for timings within the range between 60° BEVO and EVO than between EVO and 40° AEVO. The inclination of the curves shows that $imep_d$ increases rapidly as second shut-off valve closing timing moves from 60° BEVO to EVO, especially for higher airtank pressures, while it is approaching a limiting value for closing timings after EVO.

As already mentioned above, second shut-off valve closing is a compromise between engine torque output and energy economy. This can be attested by the observation of $CATC_d$ variation in Figure 4.10, where it can be seen that the inclination of the curves is negative but the rate of reduction of $CATC_d$ is higher for closing timings after EVO. This means that potential energy included in the compressed air is converted to mechanical power less efficiently when second shut-off valve closes after EVO because expanded air escapes to the atmosphere through the open exhaust valve.

The predicted cylinder indicator diagrams for various valve closing timings at 8 bar airtank pressure which are shown in Figure 4.11 provide a better understanding of the gas exchange process which takes place during the air expander cycle. After second shut-off valve closing at 60° BEVO (blue line), cylinder pressure drops from airtank pressure (8

bar) down to 2 bar during expansion period, before exhaust valve opens and drops and cylinder pressure equalizes ambient pressure. Minimum $imep_d$ is realized (area A) but maximum energy economy is achieved. For second shut-off valve closing at EVO, cylinder pressure is kept at airtank pressure level and it drops rapidly when exhaust valve opens. Much higher $imep_d$ is realized (area A+B) but $CATC_d$ drops rapidly (see Figures 4.9 and 4.10). Finally, for second shut-off valve closing at 40° AEVO, cylinder pressure is kept for a longer expansion period at airtank pressure level, resulting in slightly higher $imep_d$ (area A+B+C) but the wastage of potential energy is too high compared to $imep_d$ gain (see Figures 4.9 and 4.10).

According to the above investigation, optimal ERV timing is shown in the same diagram together with engine valve timing in Figure 4.12. It can be seen that second shut-off valve opening depends on the pressure difference between the airtank and the cylinder; the valve opens when the pressures equalize. Second shut-off valve closing appears in the diagram between two extreme closing timings; for maximum potential energy economy (solid line) and for maximum power demand (dotted line). First shut off valve is shown to fully overlap the second shut-off valve and it is timed to open during intake and close during exhaust period.

4.3.3. Modeling results and discussion

After having determined the optimal ERV timing and discussed the effects of first and second shut-off valve timing on various operating parameters, the current section focuses on the unsteady state simulations undertaken to gain a better understanding of how a number of parameters, such as buffer chamber volume, engine speed and number of cycles influence airtank pressure, bme_p , $CATC$, etc. Unsteady state simulations means that all cycle-averaged quantities are changed from one engine cycle to the other, unlikely steady state simulations where engine operating parameters are kept at fixed levels throughout engine cycles and the quantities of interest are measured in a time-averaged basis.

4.3.3.1. Airtank charging (air compressor mode)

Initially the model was used to determine the number of engine cycles required to charge the 10-litre airtank (roughly 1:20 cylinder to airtank volume) which was set at an initial pressure of 5 bar.

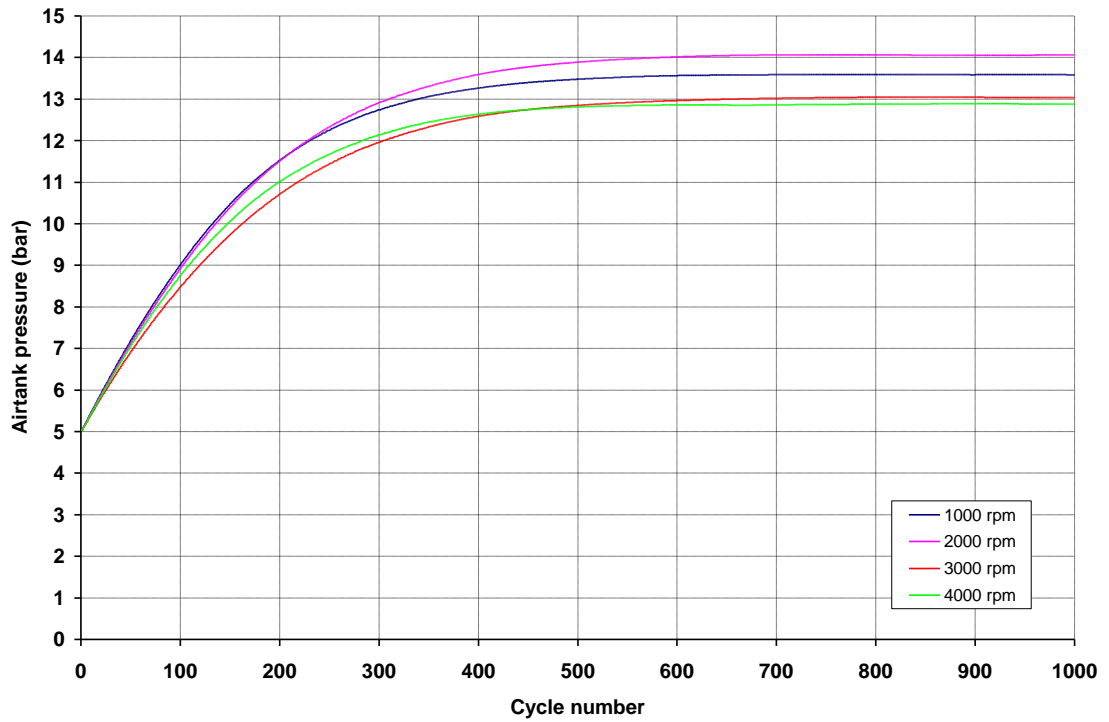


Figure 4.13: Airtank pressure throughout 1000 engine cycles (2000 crankshaft revolutions) for buffer chamber volume equal to 100% of engine clearance volume (28.7 cm^3).

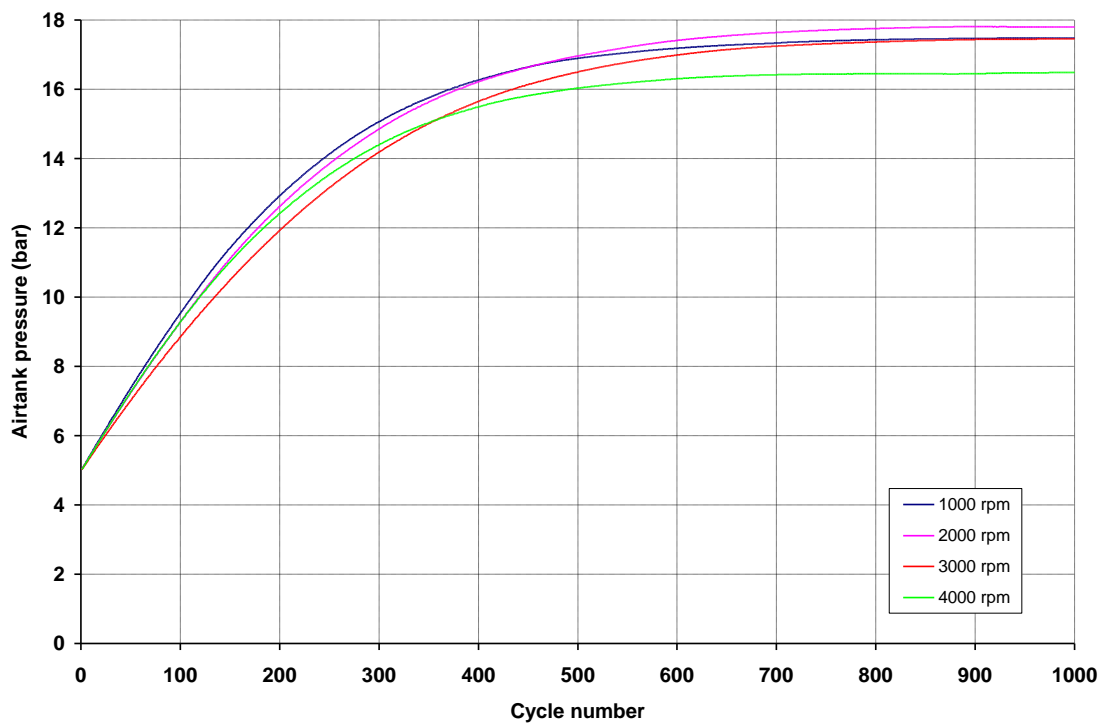


Figure 4.14: Airtank pressure throughout 1000 engine cycles (2000 crankshaft revolutions) for buffer chamber volume equal to 50% of engine clearance volume (14.4 cm^3).

The results are shown in Figures 4.13 and 4.14, where it can be seen that after 1000 engine cycles (2000 crankshaft revolutions) airtank pressure curve is approaching a limiting pressure of 14 – 14.5 bar at low engine speeds and 13.5 bar at higher engine speeds, when the buffer chamber volume is 28.7 cm³ (i.e. equal to engine clearance volume). Although airtank pressure is not a function of engine speed, the variation throughout the engine speed range can be explained by the different volumetric efficiencies that the engine realizes at different speeds because of the gas dynamics of the intake system. This affects the mass of air induced during the intake period and finally transferred to the airtank during compression. When the buffer chamber volume is half the engine clearance volume (i.e. 14.4 cm³), maximum airtank pressure is elevated 17 – 18 bar, depending on the engine speed. It is shown in both diagrams that it takes 120 seconds to fully charge the airtank with the engine operating at 1000 rpm, 60 seconds at 2000 rpm, 40 seconds at 3000 rpm and 30 seconds at 4000 rpm. However, over 95% of this pressure can be achieved within 50% of the aforementioned times (within 500 engine cycles). The results for the intermediate engine speeds of 1500 rpm, 2500 rpm and 3500 rpm are omitted from the diagrams.

4.3.3.2. Braking bmep (air compressor mode)

Following from airtank pressure results, the model was used to study the sensitivity of $bmep_b$ to airtank pressure, engine speed and buffer chamber volume. The advantage of monitoring $bmep$ instead of $imep$ lies on the fact that $bmep$ includes friction losses ($fmep$) and it is therefore indicative of the power realized at the engine shaft, which is of practical interest. As shown in Figures 4.15 and 4.16, $bmep_b$ remains unaffected by buffer chamber volume. Although compression ratio is increased by 20% by reducing buffer chamber volume by 50%, the comparison of the two diagrams shows that there is negligible variation to $bmep_b$ values throughout the 1000 engine cycles. $Bmep_b$ is not a function of airtank pressure, despite the small variation observed because of the gas dynamics of the buffer chamber which is influenced by the state of charge of the airtank. Figures 4.14 and 4.15 show that airtank pressure increases by approximately 9 bar and 12 bar respectively throughout 1000 cycles, while Figures 4.15 and 4.16 show that $bmep_b$ is only reduced by 1 bar. However, $bmep_b$ stabilizes after 500 cycles, having reduced by approximately 1 bar. Finally, engine speed is a factor that influences $bmep_b$. It can be seen that the $bmep_b$ curve is displaced 0.5 bar higher on the diagram for engine speed increasing by 1000 rpm. This is because $fmep_b$ (which is engine-speed dependant) is added to $bmep_b$ (see Equation 4.21).

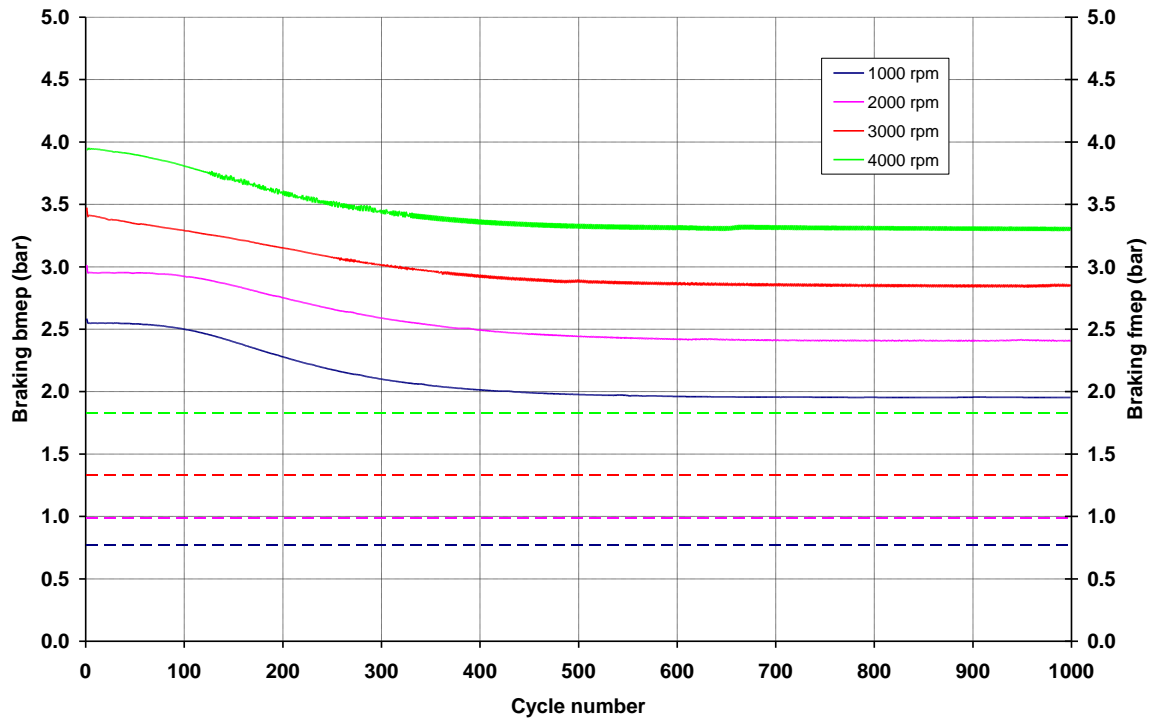


Figure 4.15: $Bmep_b$ (solid lines) and $fmep_b$ (dashed lines) throughout 1000 engine cycles (2000 crankshaft revolutions) for buffer chamber volume equal to 100% of engine clearance volume (28.7 cm^3).

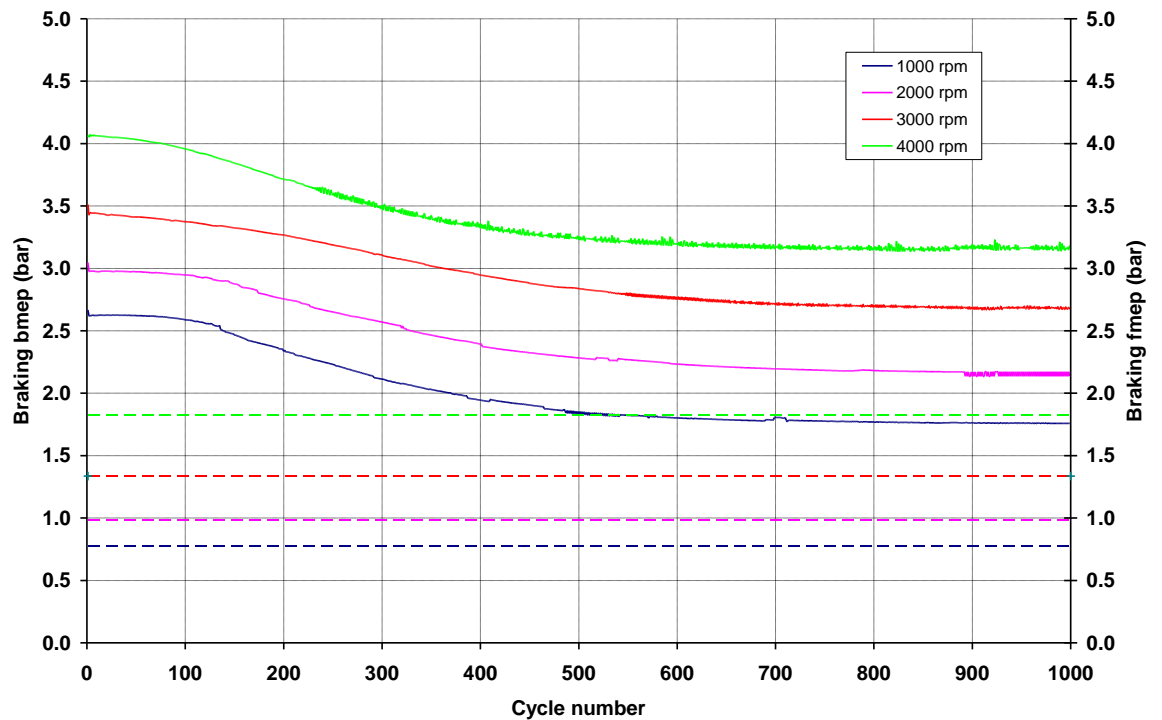


Figure 4.16: $Bmep_b$ (solid lines) and $fmep_b$ (dashed lines) throughout 1000 engine cycles (2000 crankshaft revolutions) for buffer chamber volume equal to 50% of engine clearance volume (14.4 cm^3).

4.3.3.3. Braking CATC (air compressor mode)

The rate of reduction of $CATC_b$, shown in Figures 4.17 and 4.18, is proportional to the rate of increase of airtank pressure. As airtank pressure builds up, the mass of compressed air transferred in it decreases because of the decreasing pressure difference between the airtank and the cylinder. It can be seen that for a buffer chamber volume of 28.7cm^3 there is no air transfer between the airtank and the cylinder after approximately 500 engine cycles. For a buffer chamber volume of 14.4cm^3 , the realized $CATC_b$ values are approximately 5% lower and it takes about 800 cycles until there is no air transfer between the airtank and the cylinder. This can be explained by the lower compression ratio realized with the larger buffer chamber which results in smaller pressure difference between the airtank and the cylinder. Maximum $CATC_b$ at low engine speeds is as high as 43% and 38% for 28.7cm^3 and 14.4cm^3 buffer chamber volume respectively while it drops down to approximately 36% and 30% respectively at higher speeds. This drop is caused by the gas dynamics of the buffer chamber and the intake system. It should be noted here that $bmeP_b$ is not influenced by $CATC_b$ variation and therefore the engine can still produce braking power even when the airtank is fully charged and no more air can be stored in it.

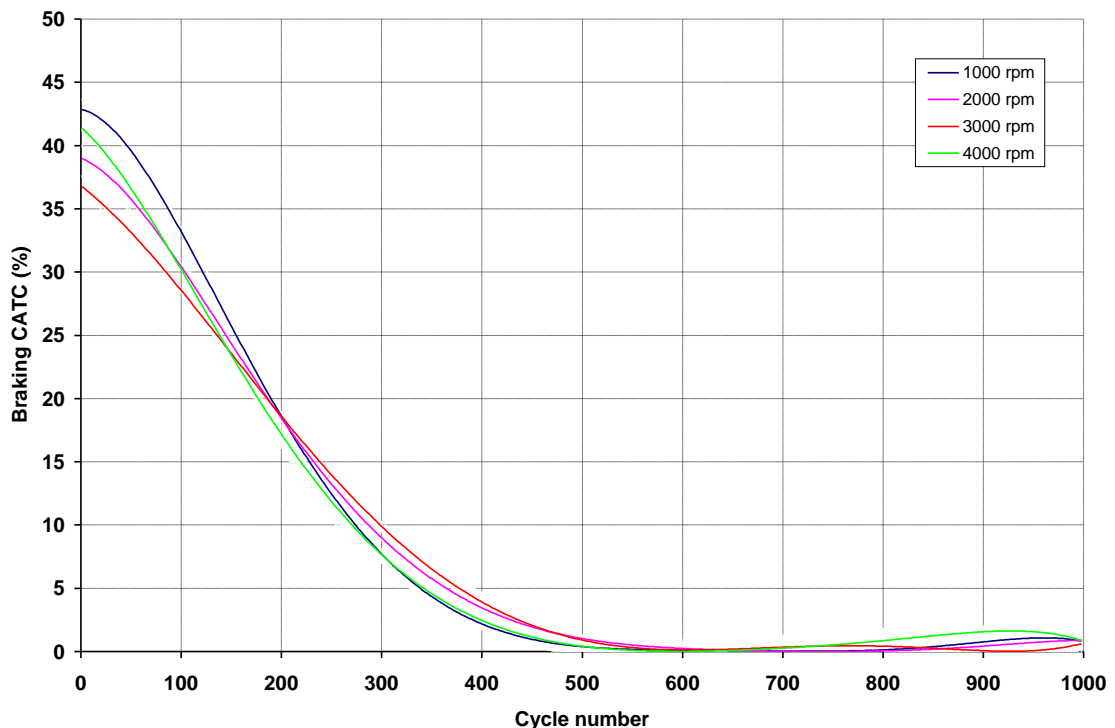


Figure 4.17: $CATC_b$ throughout 1000 engine cycles (2000 crankshaft revolutions) for buffer chamber volume equal to 100% of engine clearance volume (28.7cm^3).

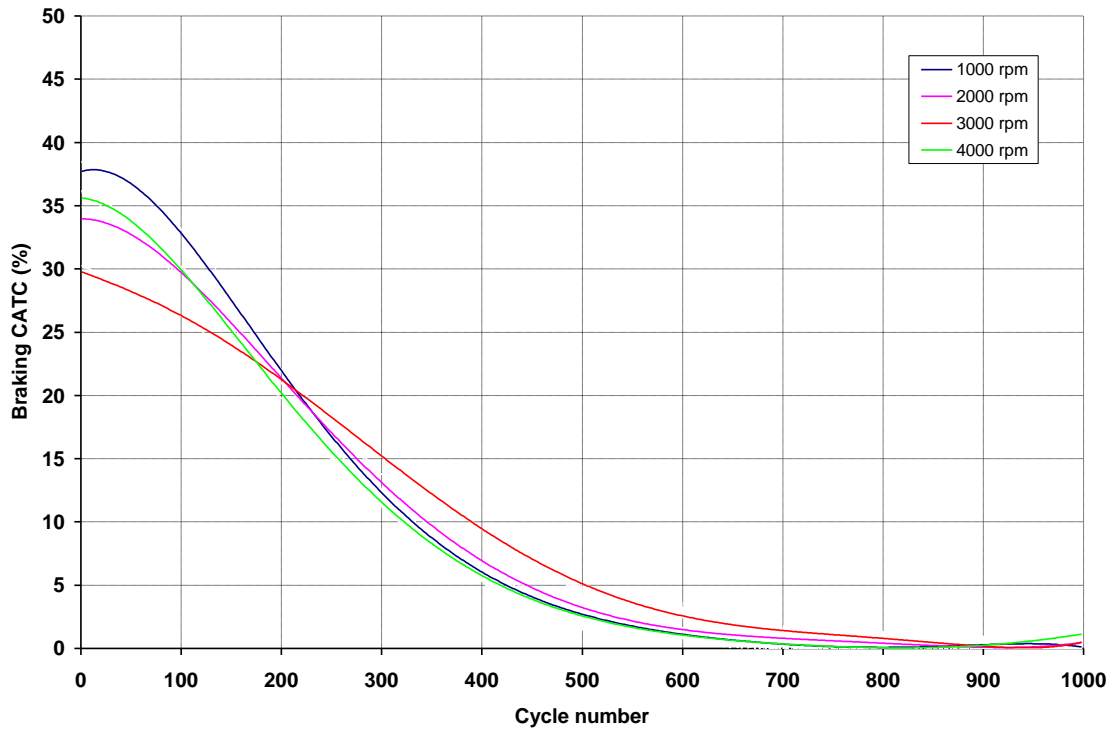


Figure 4.18: $CATC_b$ throughout 1000 engine cycles (2000 crankshaft revolutions) for buffer chamber volume equal to 50% of engine clearance volume (14.4 cm^3).

4.3.3.4. Airtank discharging (air expander mode)

The model was used to examine the rate of reduction of the airtank pressure during discharge, when compressed air is used to power the air motor. The air reservoir is the same 10-litre airtank (roughly 1:20 cylinder to airtank volume) which has also been used for the air compressor modeling and was set at an initial pressure of 20 bar. The results are shown in Figures 4.19 and 4.20, where it can be seen that the minimum useable airtank pressure is 4 bar and below that limit no torque can be generated by the engine (see also Figures 4.21 and 4.22, which show the variation of b_{mep_d} in regard to airtank pressure). The minimal airtank pressure is reached after 55 engine cycles (110 crankshaft revolutions) when second shut-off valve timing is set for maximum energy economy. For higher engine torque demands, this period is limited to 30 engine cycles (60 crankshaft revolutions). Clearly, the larger the airtank the more sustainable the air expander torque but the longer the charging time. Finally, by the observation of Figures 4.19 and 4.20 it can be seen that factors as engine speed and buffer chamber volume do not affect the airtank discharging process, as the curves in both Figures are almost identical for all engine speeds which have been tested.

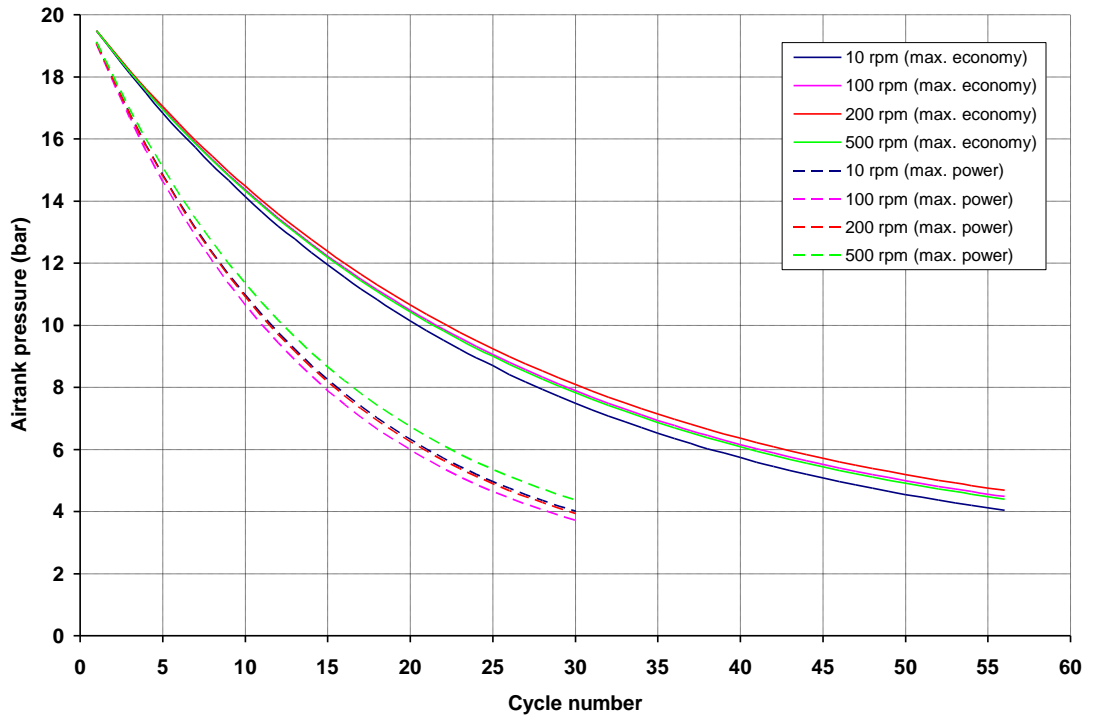


Figure 4.19: Airtank pressure throughout 60 engine cycles (120 crankshaft revolutions) for buffer chamber volume equal to 100% of engine clearance volume (28.7 cm^3).

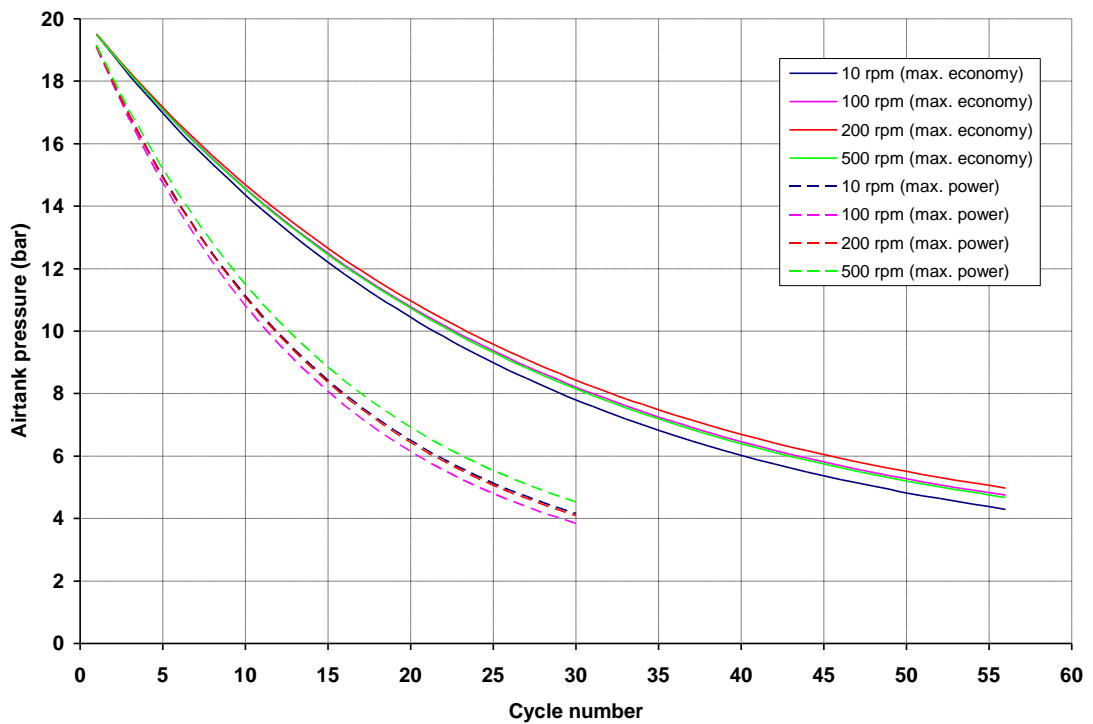


Figure 4.20: Airtank pressure throughout 60 engine cycles (120 crankshaft revolutions) for buffer chamber volume equal to 50% of engine clearance volume (14.4 cm^3).

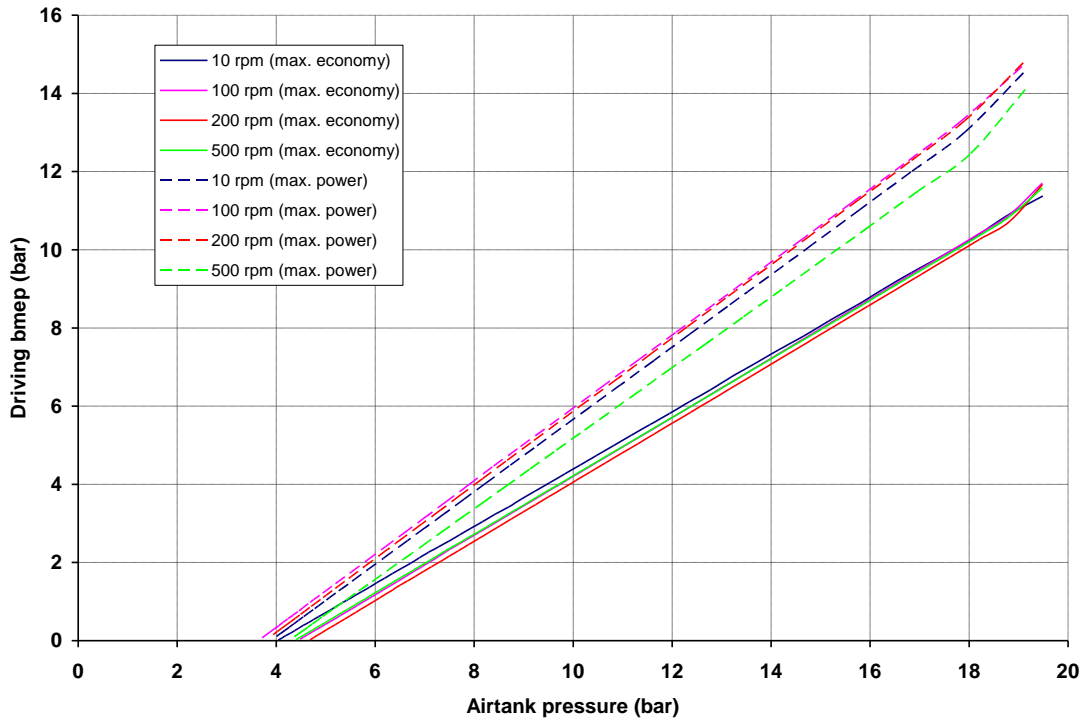


Figure 4.21: $Bmep_d$ against airtank pressure for buffer chamber volume equal to 100% of engine clearance volume (28.7 cm^3) and for maximum economy (solid lines) and maximum power (dashed lines).

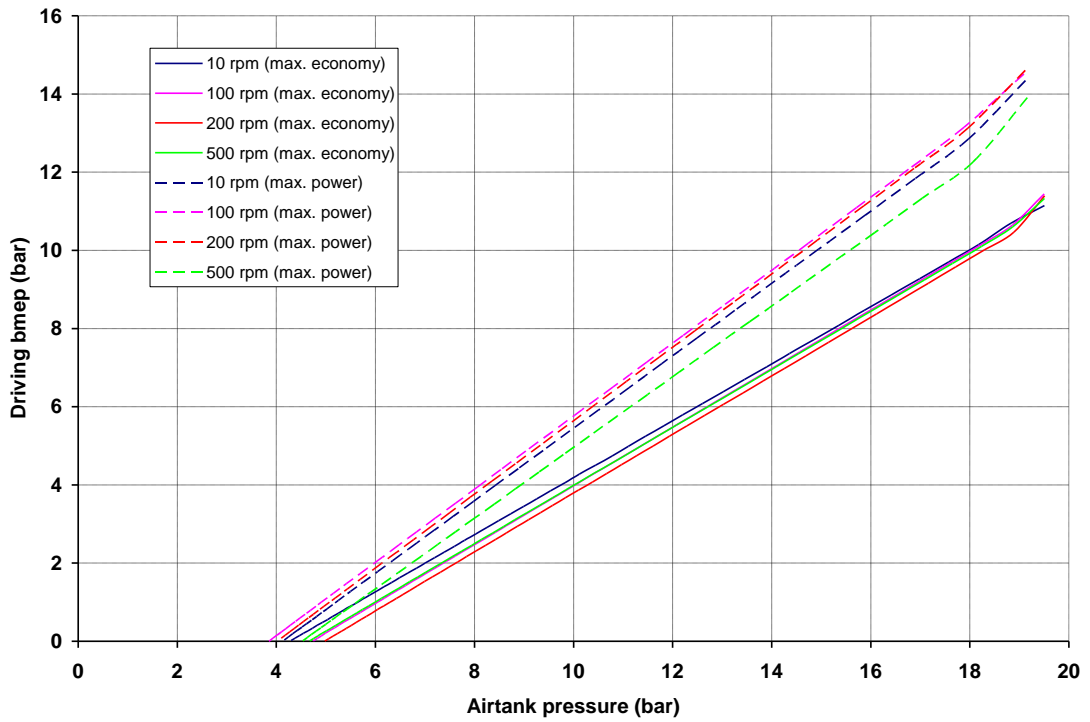


Figure 4.22: $Bmep_d$ against airtank pressure for buffer chamber volume equal to 50% of engine clearance volume (14.4 cm^3) and for maximum economy (solid lines) and maximum power (dashed lines).

4.3.3.5. Driving bmep (air expander mode)

Following from airtank pressure results, the model was used to study the sensitivity of $bmep_d$ to airtank pressure, engine speed and buffer chamber volume, similarly to the air compressor mode. As shown in Figures 4.21, 4.22, 4.23 and 4.24, $bmep_d$ remains unaffected by buffer chamber volume and engine speed. However, it is proportional to airtank pressure and therefore the engine can provide driving torque for a limited number of cycles. It can be seen that for an initial airtank pressure of 20 bar, the engine can produce about 11.5 bar of $bmep_d$ (and hence a starting torque of 45.76 Nm, according to Equations 4.6 and 4.7). $Bmep_d$ drops down to zero after 55 engine cycles (110 crankshaft revolutions). A further factor which influences the rate of reduction of the driving torque is the torque demand. Figures 4.23 and 4.24 show that driving torque, similarly to airtank pressure, is more sustainable at a lower torque demand (i.e. at second shut-off valve timed for maximum economy), as the mass transfer per cycle from the airtank to the cylinder is restricted by second shut-off valve closing. At higher torque demands, $bmep_d$ is slightly higher (12 bar), providing a starting torque of 47.75 Nm but it descends rapidly. As a result, $bmep_d$ at maximum power is lower than at maximum economy after 10 engine cycles.

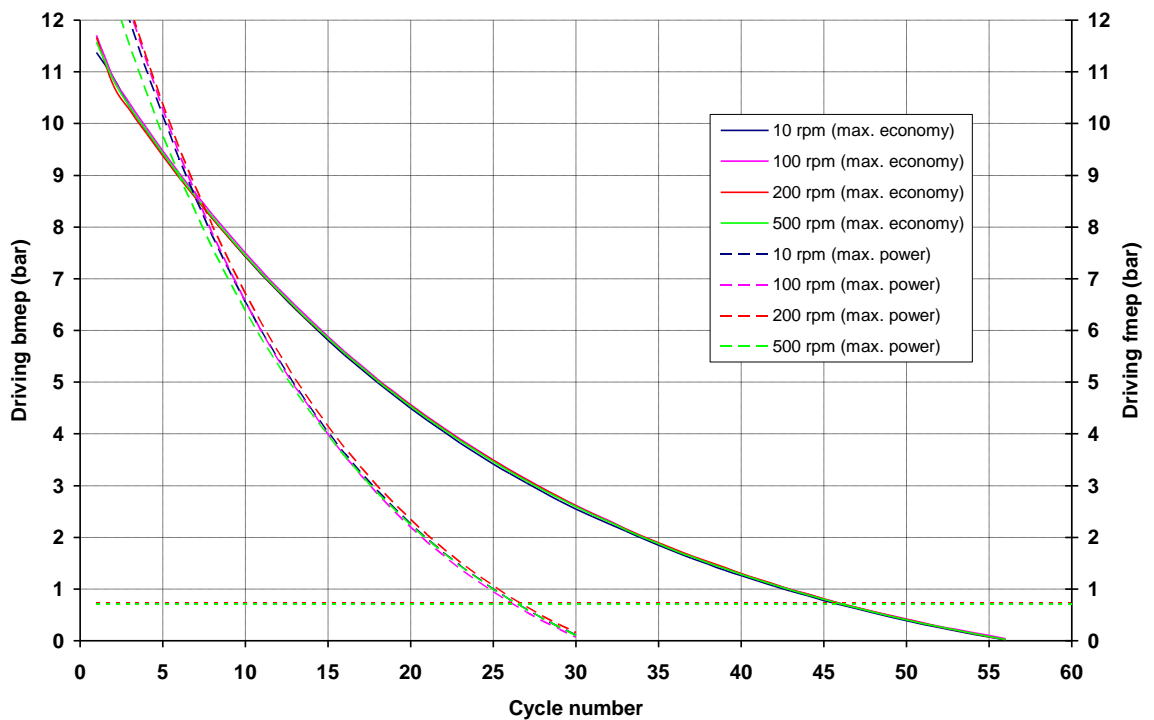


Figure 4.23: $Bmep_d$ and $fmep_d$ throughout 60 engine cycles (120 crankshaft revolutions) for buffer chamber volume equal to 100% of engine clearance volume (28.7 cm^3).

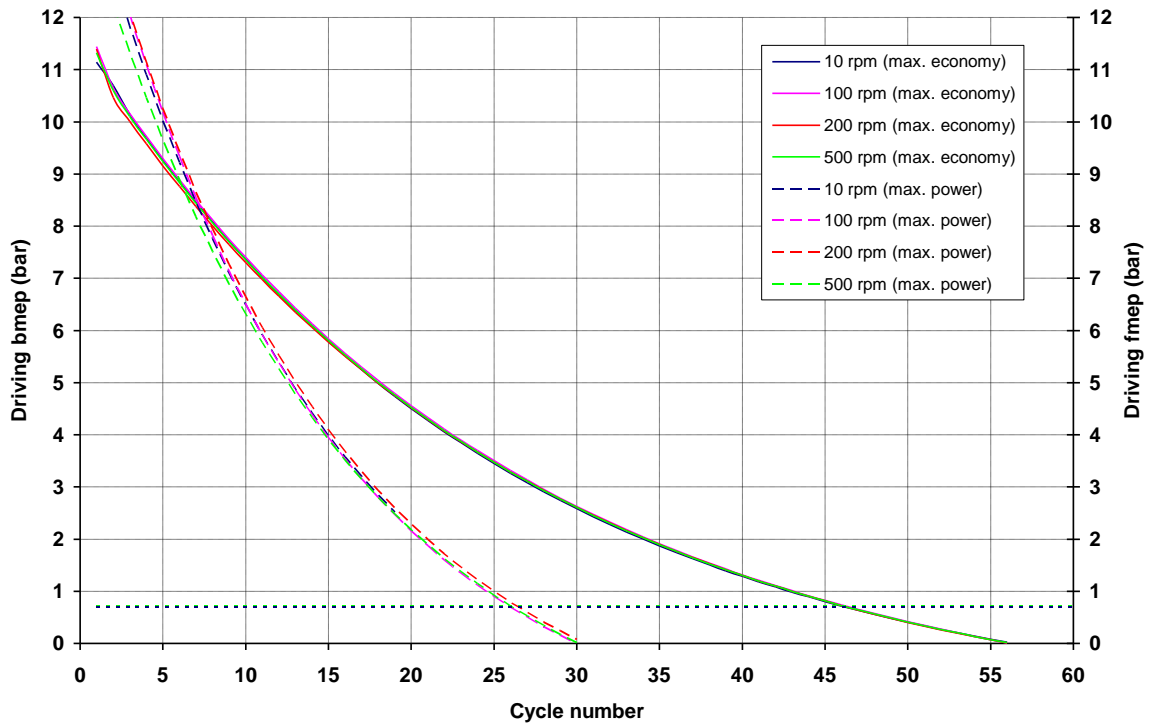


Figure 4.24: $Bmep_d$ and $fmep_d$ throughout 60 engine cycles (120 crankshaft revolutions) for buffer chamber volume equal to 50% of engine clearance volume (14.4 cm^3).

The above results suggest that the air expander should be used to start the engine and only for a limited time for the launch of the vehicle with lighter torque requirements, leading to longer periods of useable pressure availability from the airtank. The use of air expander to start the engine and launch the vehicle at the same time should be highlighted here as there is the additional benefit that the engine can be turned off when the vehicle is stationary. This fact alone provides significant fuel economy benefits (64% reduction in fuel consumption in city driving and 12% in highway driving), as described by Tai et al [60,61].

4.3.3.6. Driving CATC (air expander mode)

In Figures 4.25 and 4.26 the sensitivity of $CATC_d$ to airtank pressure, buffer chamber volume, engine speed and torque demand is illustrated. Closing of the second shut-off valve before EVO, in order to achieve potential energy economy, gives a slight increase in $CATC_d$, as expanded air is brought closer to ambient pressure at the end of the expansion period. $CATC_d$ increases with decreasing airtank pressure, as less air is released in the cylinder per cycle. Finally, the comparison of Figures 4.25 and 4.26 shows that $CATC_d$ is not influenced by buffer chamber volume as the curves in the two diagrams are almost identical.

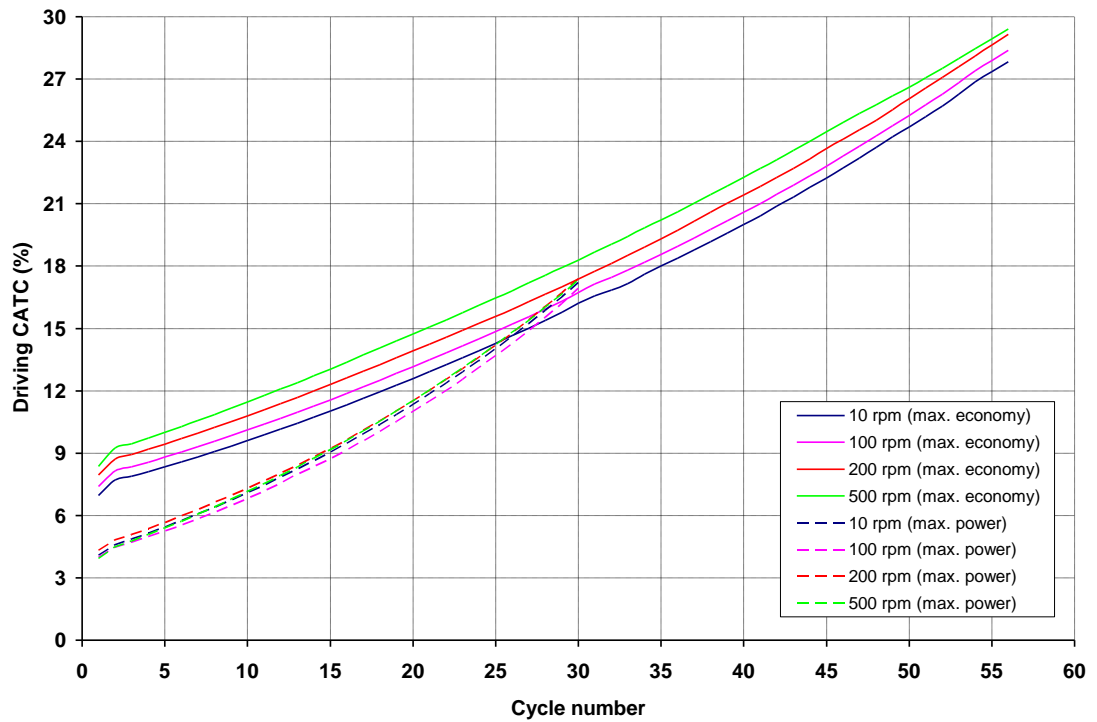


Figure 4.25: $CATC_d$ throughout 60 engine cycles (120 crankshaft revolutions) for buffer chamber volume equal to 100% of engine clearance volume (28.7 cm^3).

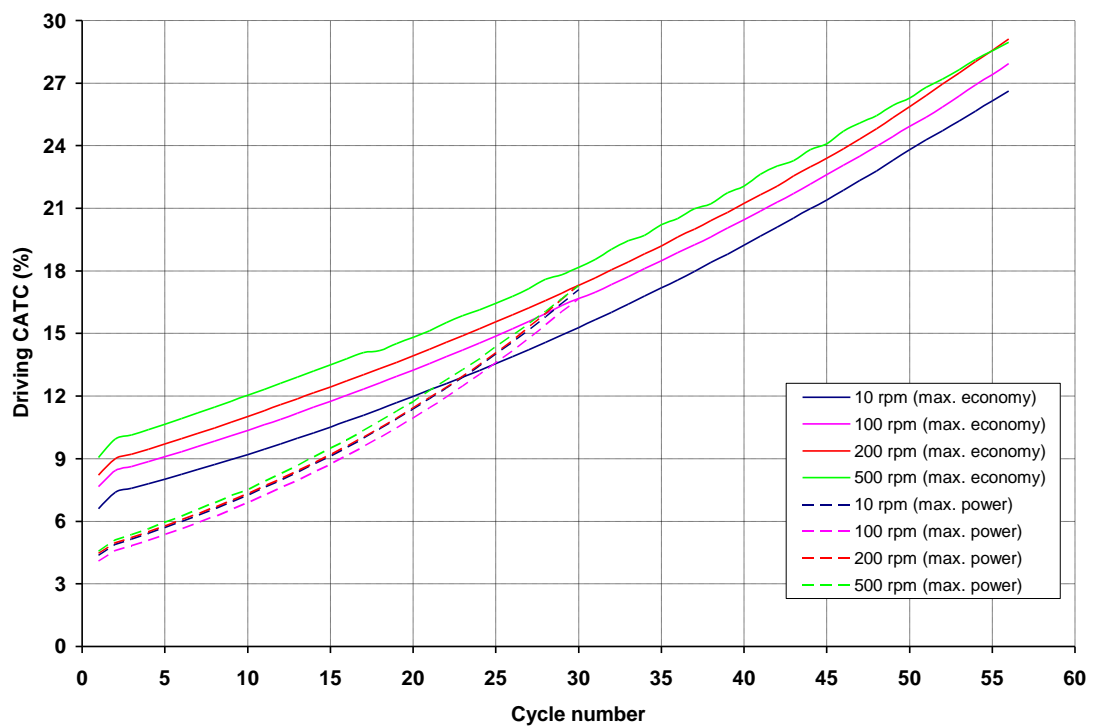


Figure 4.26: $CATC_d$ throughout 60 engine cycles (120 crankshaft revolutions) for buffer chamber volume equal to 50% of engine clearance volume (14.4 cm^3).

4.4. Concept 2: Engine with Fully Variable Valve Actuation (FVVA)

4.4.1. Model description

Figure 4.27 shows the model of the present concept. The modelled base engine has the same characteristics as in the above concept (i.e. a stroke of 86mm and a bore of also 86mm, giving a displacement volume of 500cm³). The connecting rod length is 160mm. Intake and exhaust valve diameter is 23.5mm and 23.4mm respectively. The engine speed range is between 1000 and 4000 rpm. The engine cylinder, labelled “*cylinder*” appears in the middle of the canvas and has twin intake and single exhaust valves, as well as a gas transfer valve. An exhaust pipe connects the exhaust port (“*exhaustport*”) to the atmosphere labelled “*amb3*”. The twin intake ports (“*intakeport1*” and “*intakeport2*”) are connected to the atmosphere (“*amb1*”) through a simple 2-in-1 intake manifold which consists of two headers (“*manifold1*” and “*manifold2*”), the plenum (“*plenum*”) and one runner (“*manifold3*”). Finally, the airtank, labelled “*AIRTANK*”, is modelled as duct of defined volume and initial pressure and it is connected to the gas transfer port, labelled “*pneumaticport*”, and the end ambient (“*amb2*”) which is used here to terminate the airtank network.

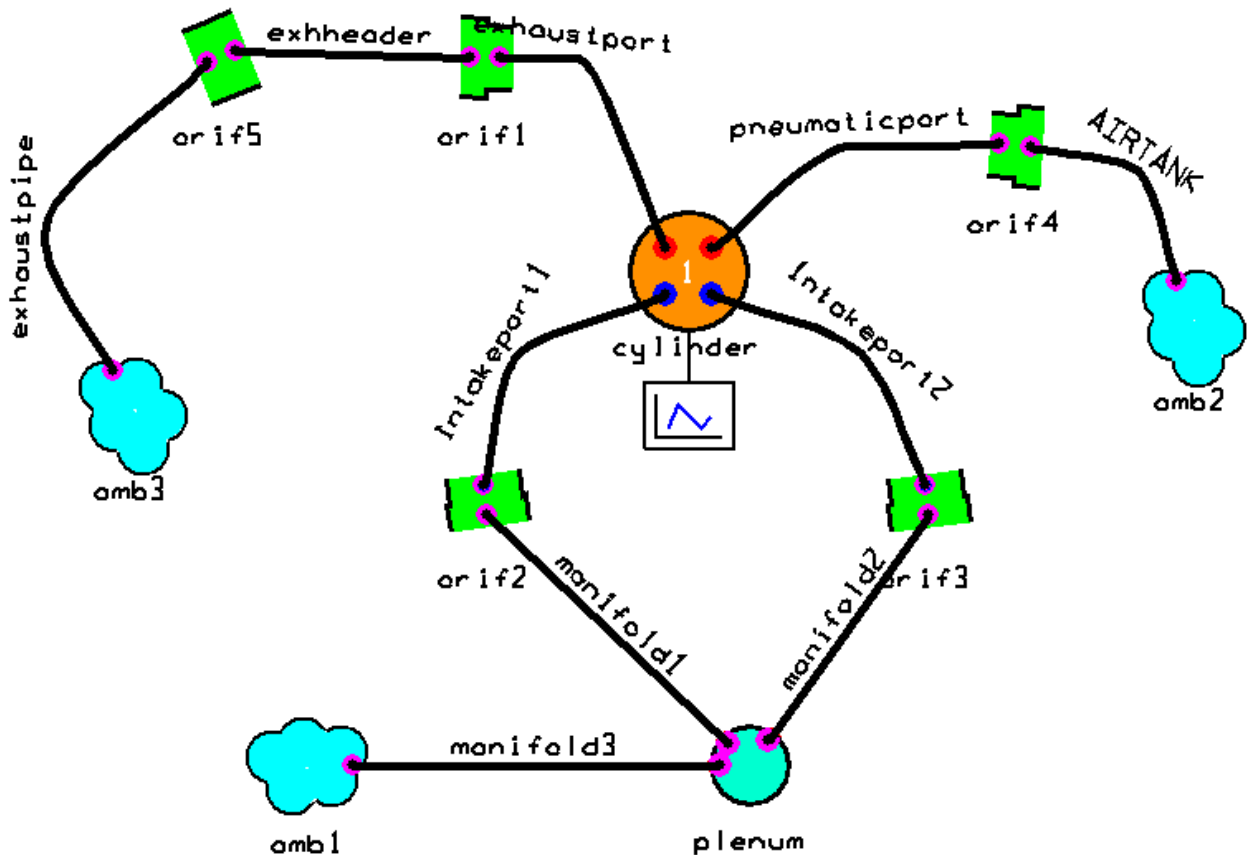


Figure 4.27: Model of air hybrid engine with FVVA.

Air mass flow, pressure and temperature plots are requested for the cylinder, shut-off valves, buffer chamber, airtank and intake manifold. Valve lift profile plots are also requested for engine intake and exhaust valves as well as shut-off valves. Imep, fmep, bmep and indicator diagram plots are requested for the engine cylinder in particular. The parameters defined for each of the model elements used are the same as those appear in Table 4.1 above. The dimensions of the model and the piping network, together with other characteristics, are summarized in Table 4.3. It should be noted that gas transfer valve and port have the same dimensions as for the exhaust, implying that one of the exhaust valves and port can be isolated and used for gas transfer, given that FVVA provides full independence to valve actuation.

Table 4.3: Model dimensions and characteristics.

Engine		Vavles		Manifolds	
Number of cylinders	1	Intake valve count	2	Intake header count	2
Cylinder bore	86mm	Diameter	23.5mm	Diameter	30mm
Piston stroke	86mm	Maximum lift	8mm	Length	300mm
Connecting rod length	160mm	Exhaust valve count	1	Volume	212cm ³
Displacement volume	500cm ³	Diameter	23.4mm	Runner count	1
Clearance volume	28.7cm ³	Maximum lift	8mm	Diameter	50mm
Total volume	528.7cm ³	Gas transfer valve count	1	Length	400mm
Compression ratio	18.4:1	Diameter	23.4mm	Volume	785cm ³
		Maximum lift	8mm	Plenum volume	65cm ³
		Other		Exhaust header count	1
Ports				Airtank volume	10 litre
Intake port count	2			Length	500mm
Volume	46cm ³			Volume	537cm ³
Exhaust port count	1			Runner count	1
Volume	53cm ³			Diameter	37mm
Gas transfer port count	1			Length	500mm
Volume	53cm ³			Volume	537cm ³

4.4.2. Valve timing optimization

FVVA system provides variable valve timing and lift, which means that for each individual engine valve the system deals with four variables: opening and closing points, opening and closing ramp durations. By assuming a constant valve velocity of 4.5 m/s throughout the entire engine speed range, as in the previous concept, ramp duration is fixed to 43° crank angle for 8 mm valve lift. The main advantage of FVVA is that the engine can be operated as a two-stroke air compressor or expander, while it can switch to normal four-

stroke firing engine during cruise. This feature is of interest here and is investigated below. Four-stroke air hybrid cycles are assumed to provide the same bmep as in two-stroke modes (but half the torque and power, according to Equations 4.3 and 4.4) and therefore systematic studies on four-stroke FVVA models have been omitted. It is also assumed that the valve lift allows enough clearance between the piston crown and the valve head when the later opens during upstrokes and hence there are no valve-to-piston clash issues.

Valve timing highly depends on the mode on which the engine is running, so investigation for air compressor (braking) and air expander (driving) modes must be separately undertaken. It is obvious that in normal firing mode gas transfer valve is deactivated and no gas exchange between the cylinder and the airtank takes place, while intake and exhaust valves are operated according to the conventional four-stroke cycle. The aims of the valve timing optimization for air compressor and air expander modes are:

- a) Minimum pumping losses between the cylinder and the airtank for air compressor.
- b) Unthrottled air intake of atmospheric air.
- c) Maximum bmep_a, ideally as high as average airtank pressure during the cycle.
- d) High torque output at very low engine speeds during driving (for engine start-up).
- e) Most importantly, allow 2-stroke air compressor and expander cycles to be implemented.

4.4.2.1. Valve timing for air compressor mode

As described in Chapter 3, intake valve opens during intake and gas transfer valve opens during compression period. IVO point can significantly influence the performance of the air compressor as it controls the blowdown pressure after TDC during early intake stroke and determines the mass of air that can be induced into the cylinder and therefore it needs to be optimized below in a systematic way. Advanced IVO, before TDC, lowers cylinder pressure during compression as compressed air expands to the atmosphere through the open intake valve. Retarded IVO, after TDC, increases cylinder pressure during the downstroke as compressed air trapped in the clearance volume expands back to the cylinder. IVC point is not of importance, given that the valve closes at BDC or shortly after BDC. Gas transfer valve opening (GVO) point is not of importance, given that the valve opens at BDC or shortly after BDC and after IVC. However, gas transfer valve closing (GVC) point can significantly influence the performance of the air compressor as it determines the mass of air that can be transferred to the airtank and therefore it needs to be

optimized below in a systematic way. Advanced GVC, before TDC, results in increased cylinder pressure towards the end of the compression period and during early intake. Retarded GVC, after TDC, lowers peak cylinder pressure and results to an intake curve of lower pressure. As airtank charging is a single-step process, air backflow during the cycle is inevitable and, in some cases, desirable.

Figure 4.28 presents the predicted sensitivity of $imep_b$ to IVO timing at 1000, 2000, 3000 and 4000 rpm. The results show that $imep_b$ is improved for slightly advanced valve opening (5° BTDC) at lower engine speeds, while it further increases with IVO advancing to 10° BTDC at high engine speeds. This is due to the gas dynamics of the intake system. $imep_b$ slightly descends for further IVO advancing, while it drops rapidly for retarded valve opening, especially after TDC. The predicted cylinder indicator diagrams at 2000 rpm engine speed for IVO at 20° BTDC, TDC and 20° ATDC, shown in Figure 4.29, not only validate the above conclusion, but they also provide a better understanding of the gas exchange process which takes place during the two-stroke air compressor cycle.

For advanced valve opening (blue line), the actual compression period ends before TDC, as compressed air escapes to the atmosphere through the open intake valve when cylinder pressure is just below 20 bar. As the piston approaching TDC, cylinder pressure drops to ambient at the end of the upstroke. This yields an important benefit to $imep_b$ as it lowers cylinder pressure during intake stroke. The indicator diagram, which rotates anti-clockwise, includes area A+B+D (blue line). When IVO is retarded, higher peak cylinder pressure is realized as air is compressed into the airtank for the full compression period. However, compressed air remaining trapped into the clearance volume expands back to the cylinder during intake and limits the area included by the indicator diagram to area A (green line). Finally, valve opening at TDC combines the benefits of low cylinder pressure during intake and high peak pressure during compression. The indicator diagram in that case includes area A+B+C (red line).

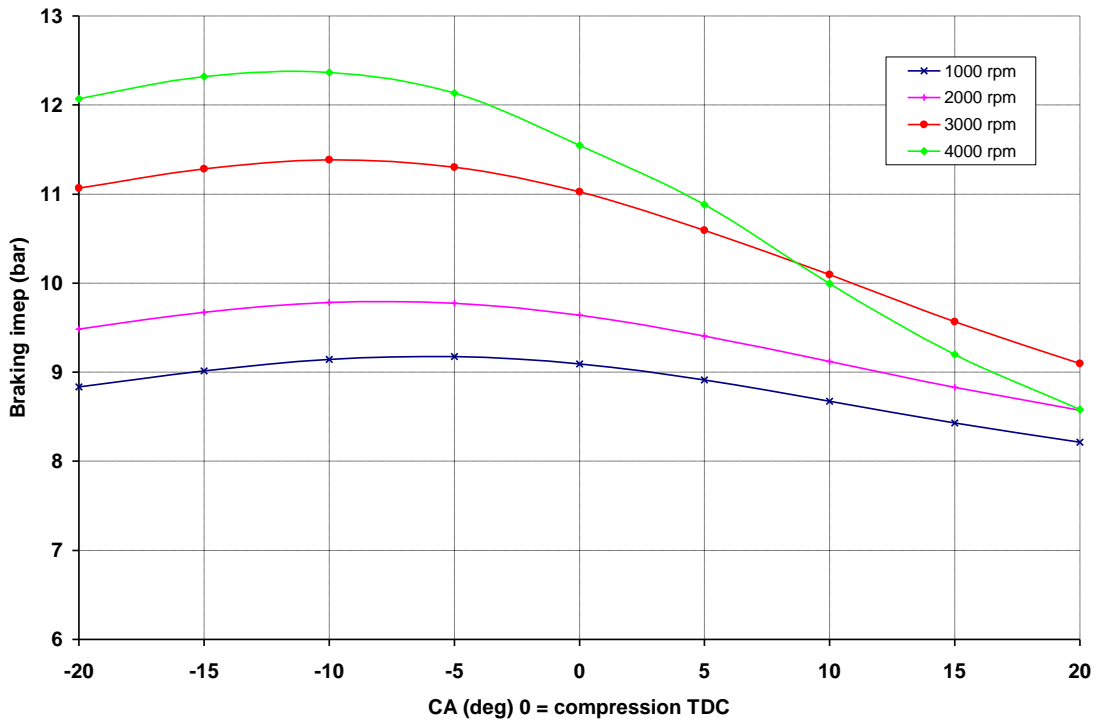


Figure 4.28: Predicted $imep_b$ against intake valve opening point for engine speed range between 1000 and 4000 rpm.

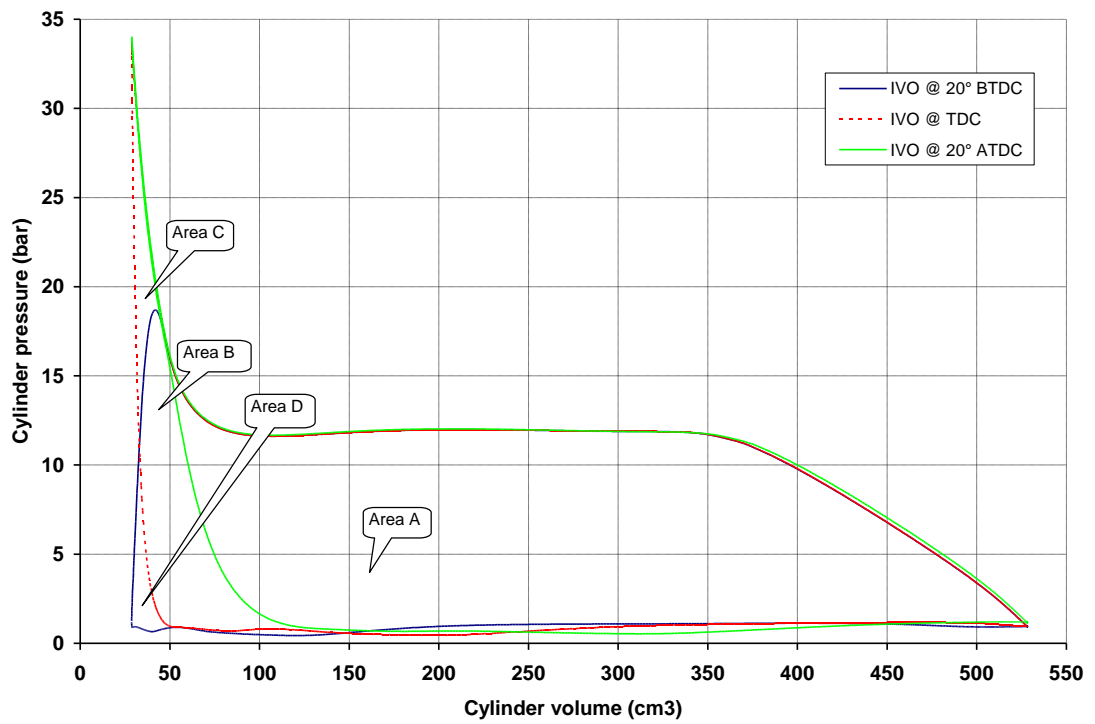


Figure 4.29: Indicator diagram at 2000 rpm for various intake valve opening points.

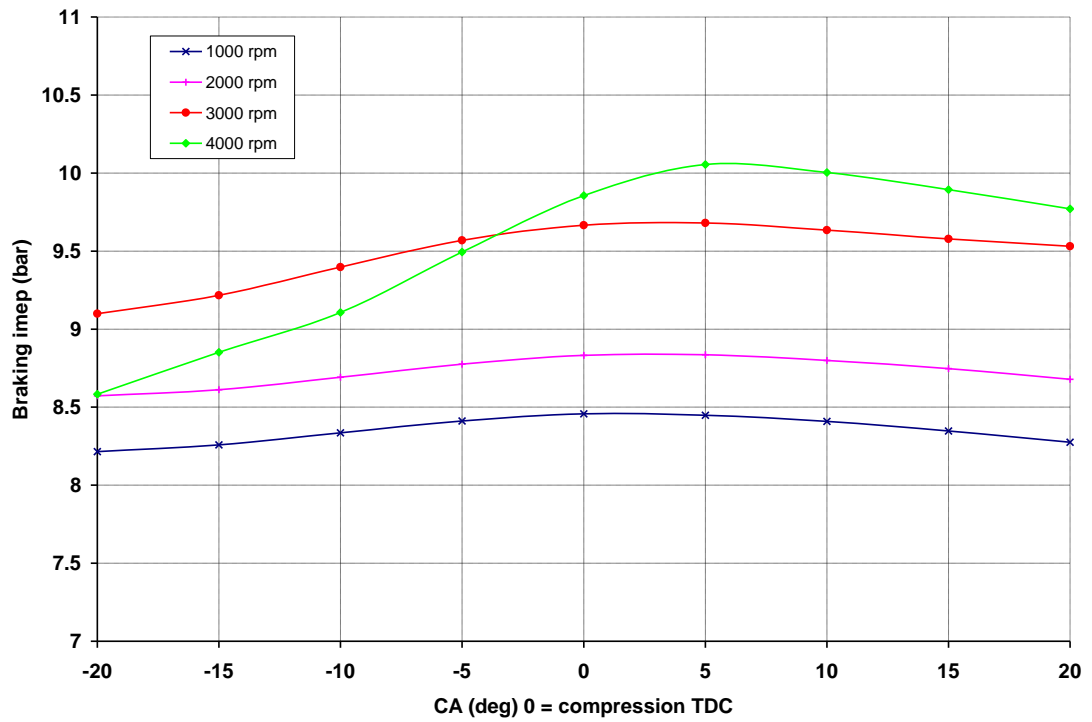
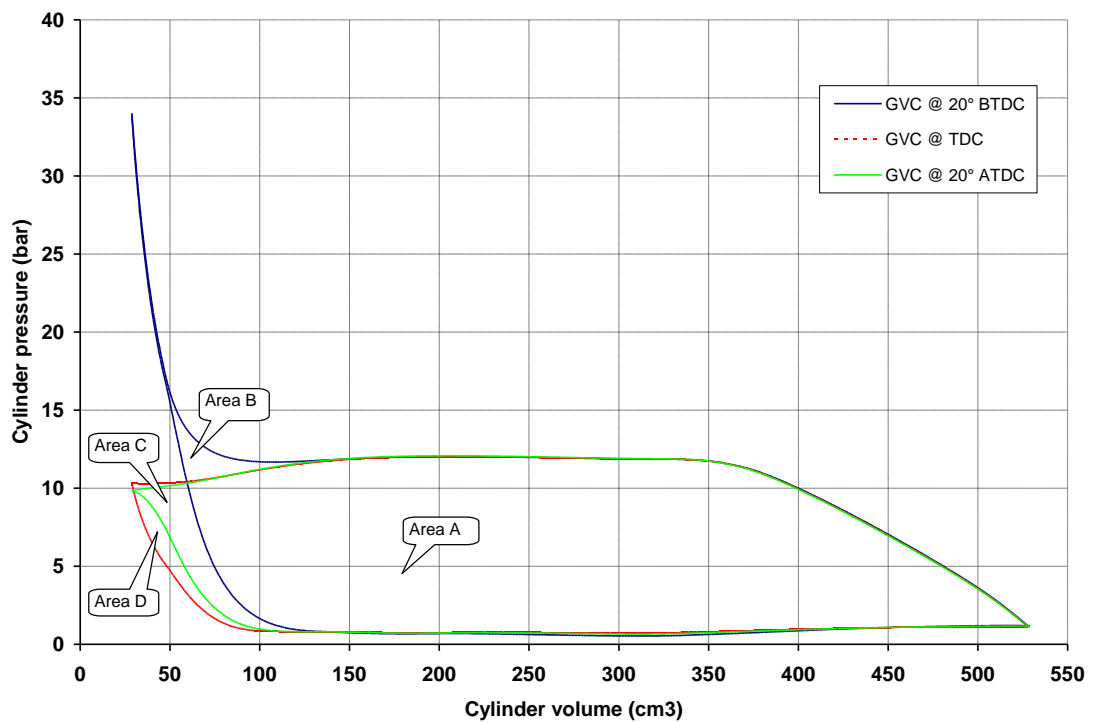


Figure 4.30: Predicted $imep_b$ against gas transfer valve closing point for engine speed range between 1000 and 4000 rpm.



4.31: Indicator diagram at 2000 rpm for various gas transfer valve closing points.

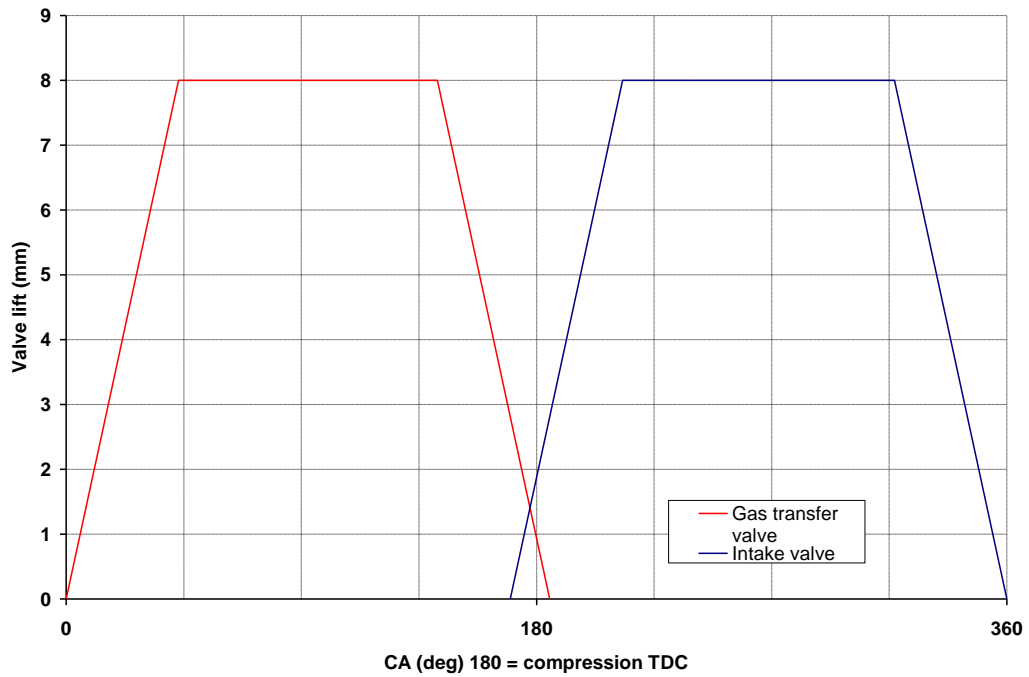


Figure 4.32: Optimal valve timing for two-stroke compressor mode.

Figure 4.30 presents the predicted sensitivity of $imep_b$ to GVC timing at 1000, 2000, 3000 and 4000 rpm. It is shown that $imep_b$ is improved for valve closing at TDC when the engine is operated at low speeds and for slightly retarded opening (5° BTDC) at higher engine speeds. $imep_b$ slightly descends for further GVC retarding, while it drops rapidly for advanced valve closing, especially before TDC. The predicted cylinder indicator diagrams at 2000 rpm engine speed for GVC at 20° BTDC, TDC and 20° ATDC, shown in Figure 4.31, not only validate the above conclusion, but they also provide a better understanding of the gas exchange process which takes place during the two-stroke air compressor cycle.

For advanced valve closing (blue line), cylinder pressure rises as the engine is not connected to the airtank after GVC. However, the air trapped in the clearance volume expands reversibly in the cylinder during the downstroke, limiting the area included by the indicator diagram to area A+B. Gas transfer valve closing at TDC limits peak cylinder pressure but eliminates flow reversibility, which yields benefits to $imep_b$, as shown in Figure 4.31 (red line, area A+C+D). Further retarding of GVC results in increased cylinder pressure during early intake stroke as there is air backflow from the airtank to the cylinder. The area included by the indicator diagram is then limited to area A+C.

It should be noted that $CATC_b$ is not affected by engine speed neither by valve timing. This is due to the deactivation of the exhaust valve, which in fact precludes the definition

of $CATC_b$ here, as no air mass is transferred through the exhaust valve and therefore $CATC_b$ equals the unit at all times. The influence of the gas dynamics of the intake (and hence the volumetric efficiency of the engine) to $imep_b$ in accordance with engine speed is also shown in Figures 4.28 and 4.30. According to the above investigation, optimal timing for intake and gas transfer valve is shown in Figure 4.32.

4.4.2.2. Valve timing for air expander mode

Similarly to the previous concept, a universal opening and closing ramp duration of 10° crank angle for all valves is assumed here. Unlike air compressor mode, it is assumed that engine speed (and hence gas velocity which is proportional to piston speed) in air expander mode is too low to govern important aspects of the air flow through nozzles, orifices, valves and restrictions and thus it does not importantly affect $imep_d$. However, $imep_d$ is a strong function of airtank pressure, as the latter governs cylinder pressure during expansion stroke.

As described in Chapter 3, intake valve is deactivated for two-stroke expander operation. Gas transfer valve open and close during the expansion period, while exhaust valve open and close during exhaust. GVO point is not of importance, given that the valve opens at TDC to release compressed air from the airtank into the cylinder. However, GVC is the key to efficient consumption of compressed air as it controls the blowdown pressure during expansion stroke. For light-load cycles, advanced GVC (before BDC) results in the elimination of the blowdown process, while compressed air is brought to ambient pressure at the end of the downstroke and maximum energy economy is realized. For heavier load conditions, blowdown becomes unavoidable due to valve closing at BDC, where maximum $imep_d$ is realized. Exhaust valve opens at BDC and closes at TDC.

Figure 4.33 presents the predicted $imep_d$ for various GVC timings, from 80° BBDC to BDC at an airtank pressure range between 5 and 25 bar with intervals of 5 bar. The results indicate that $imep_d$ is not influenced by advanced valve closing for timings up to 30° BTDC. Further retarding of GVC results in decreased $imep_d$ but it elevates compressed air economy. When very light load is demanded, GVC could be further advanced.

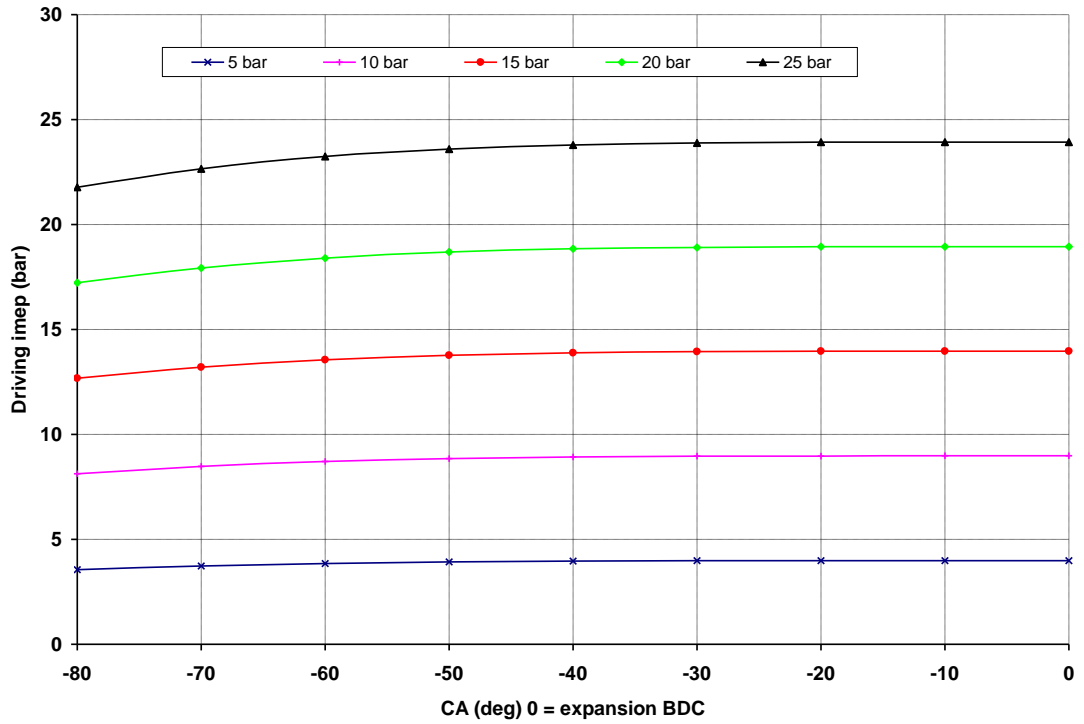


Figure 4.33: Predicted $imep_d$ against GVC timing for 5, 10, 15, 20 and 25 bar airtank pressure.

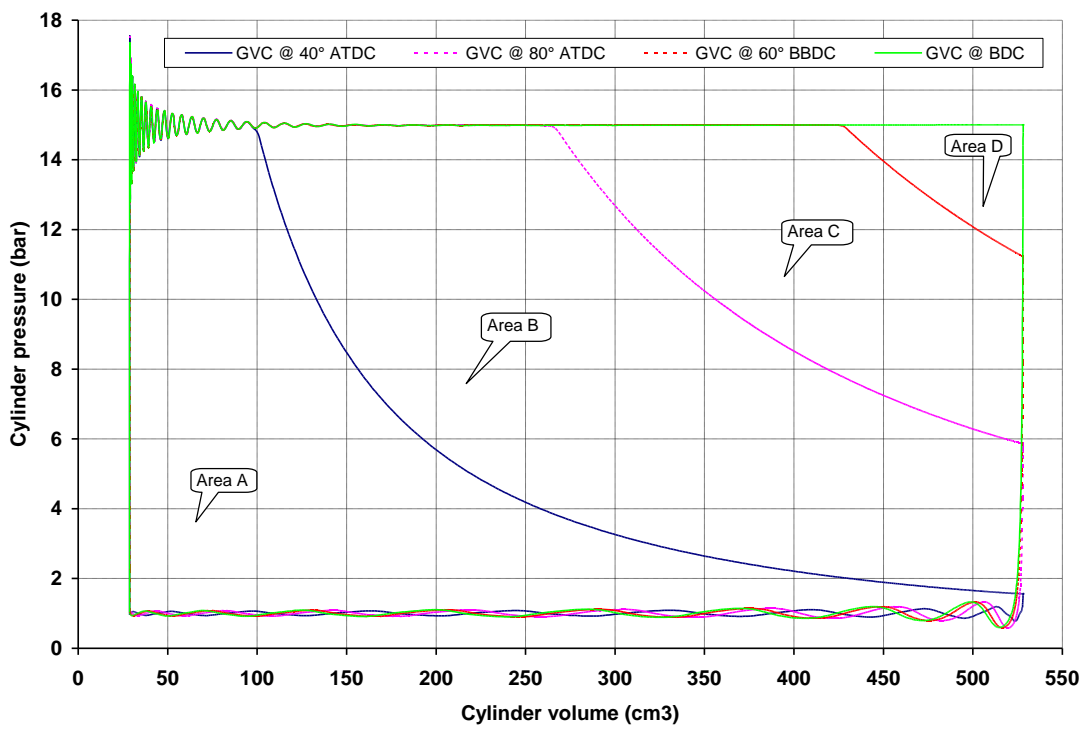


Figure 4.34: Indicator diagrams for various gas transfer valve closing points.

The predicted indicator diagrams for various GVC timings, presented in Figure 4.34, not only validate the above conclusions but they also provide a better understanding of the two-stroke air expander cycle. It is shown that when the valve close at 40° ATDC, minimum power and maximum energy economy are realized, as there is almost no blowdown at the end of expansion stroke, when exhaust valve opens (blue line – area A). As GVC point approaches BDC, $imep_d$ increases (magenta and red lines, which include areas A+B and A+B+C respectively), while on BDC an adiabatic expansion from nominal airtank pressure to ambient pressure is realized and maximum $imep_d$ is achieved (green line - area A+B+C+D), sacrificing air economy. According to the above investigation, optimal timing for intake and gas transfer valve is shown in Figure 4.35.

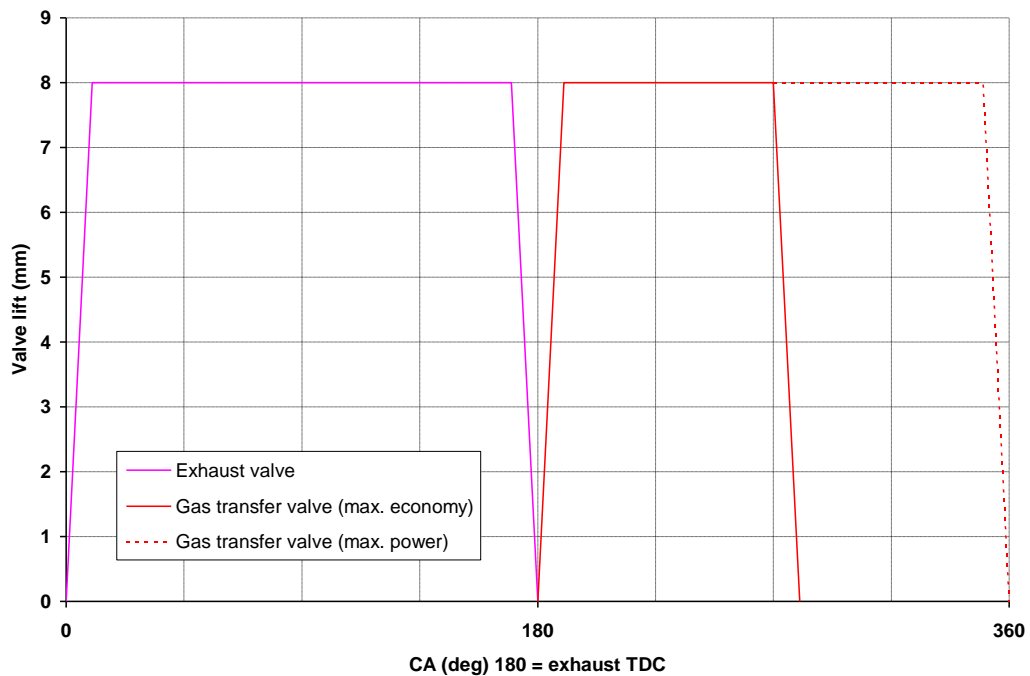


Figure 4.35: Optimal valve timing for two-stroke compressor mode.

4.4.3. Modeling results and discussion

Similar to section 4.3.3, the influence of a number of parameters (such as engine speed and number of cycles) on airtank pressure, bme_p and CATC for the two-stroke compressor and expander modes is examined and discussed here. It can be assumed that approximately half of the braking or driving torque and power is produced in four-stroke compressor and expander cycles. Although FVVA makes the four-stroke engine operation completely unnecessary, these cycles can be used where low braking or driving torque is demanded.

4.3.3.1. Airtank charging (air compressor mode)

Initially the model was used to determine the number of engine cycles required to charge the 10-litre airtank (roughly 1:20 cylinder to airtank volume) which was set at an initial pressure of 5 bar. The results are shown in Figure 4.36, where it can be seen that after 1000 engine cycles (1000 crankshaft revolutions) airtank pressure curve is approaching a limiting pressure of 19 – 21 bar at low engine speeds and 27 bar at higher engine speeds. Although airtank pressure is not a function of engine speed, the variation throughout the engine speed range can be explained by the different volumetric efficiencies that the engine realizes at different speeds because of the gas dynamics of the intake system. This affects the mass of air induced during the intake period and finally transferred to the airtank during compression. It is also shown that it takes 60 seconds to fully charge the airtank with the engine operating at 1000 rpm, 30 seconds at 2000 rpm, 20 seconds at 3000 rpm and 15 seconds at 4000 rpm. However, over 90% of this pressure can be achieved within 75% of the aforementioned times (within 500 engine cycles). The results for the intermediate engine speeds of 1500 rpm, 2500 rpm and 3500 rpm are omitted from the diagram.

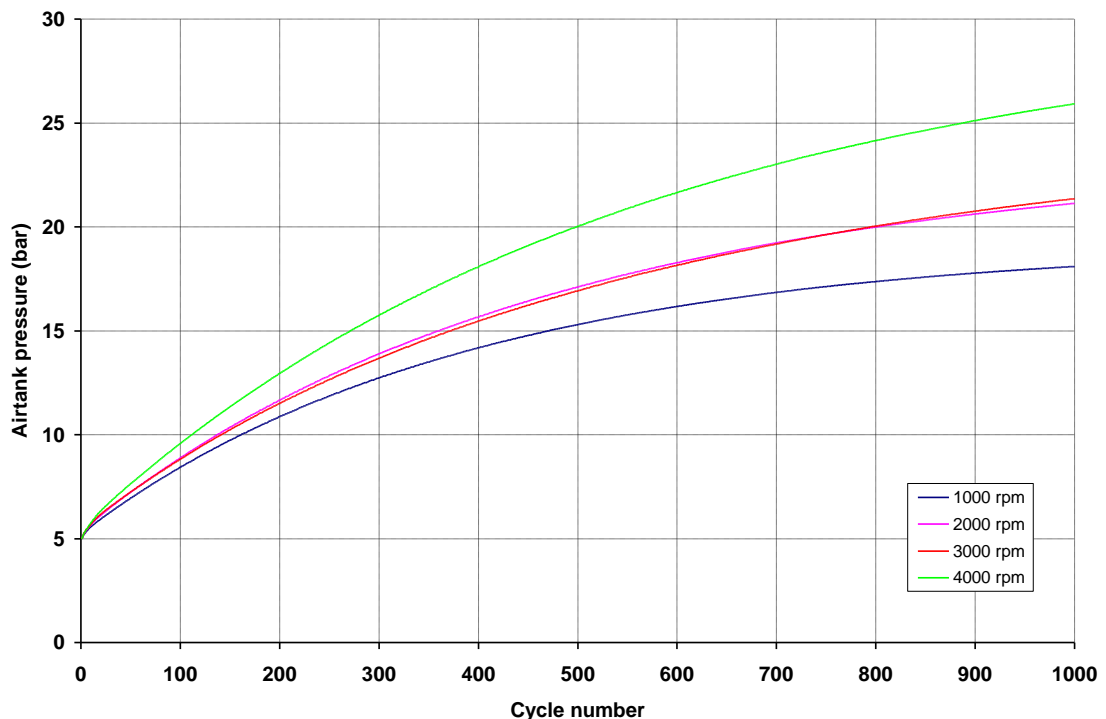


Figure 4.36: Airtank pressure throughout 1000 engine cycles (1000 crankshaft revolutions).

4.3.3.2. Braking bmep (air compressor mode)

Following from airtank pressure results, the model was used to study the sensitivity of $bmep_b$ to airtank pressure and engine speed. As shown in Figure 4.37, $bmep_b$ variation follows that of airtank pressure and therefore it is a strong function of it. At low engine speeds, where $fmep_b$ is very low and therefore $imep_b$ is very close to $bmep_b$, the later is almost equal to the average airtank pressure during the cycle. For higher engine speeds, $fmep_b$ increases significantly and results in elevated $bmep_b$ curves. It can be seen that the $bmep_b$ curve is displaced 0.5 – 0.7 bar higher on the diagram for engine speed increasing by 1000 rpm. This is because $fmep_b$ (which is engine-speed dependant) is added to $bmep_b$, according to Equation 4.21. It should be noted here that $bmep_b$ increases with increasing airtank pressure in a time (or cycle) basis, which makes braking power less predictable for the driver and suggests a drawback for the current concept.

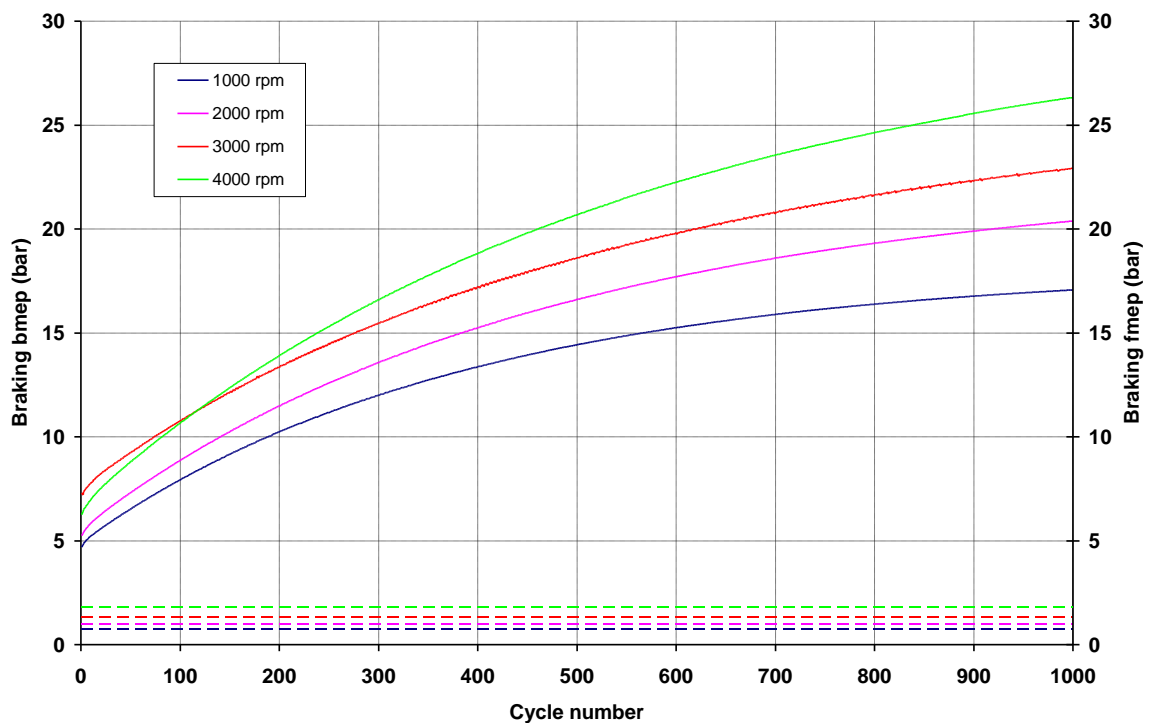


Figure 4.37: $Bmep_b$ (solid lines) and $fmep_b$ (dashed lines) throughout 1000 engine cycles (1000 crankshaft revolutions).

4.3.3.4. Airtank discharging (air expander mode)

The model was used to examine the rate of reduction of the airtank pressure during discharge, when compressed air is used to power the two-stroke air motor in order to primarily start the engine and secondarily propel the vehicle. The air reservoir is the same

10-litre airtank (roughly 1:20 cylinder to airtank volume) which has also been used for the air compressor modeling and was set at an initial pressure of 20 bar, similarly to the previous concept. The results are shown in Figure 4.38, where it can be seen that the minimum useable airtank pressure is 2 bar and below that limit no torque can be generated by the engine (see also Figure 4.40, which shows the variation of b_{mep_d} in regard to airtank pressure). This minimal airtank pressure is reached after 70 engine cycles (70 crankshaft revolutions) when an energy-saving valve timing strategy is adopted. At higher power demands, this period is limited to 50 engine cycles (50 crankshaft revolutions). Clearly, the larger the airtank the more sustainable the air expander torque but the longer the charging time. By the observation of Figure 4.38 it can be seen that engine speed does not affect the airtank discharging process.

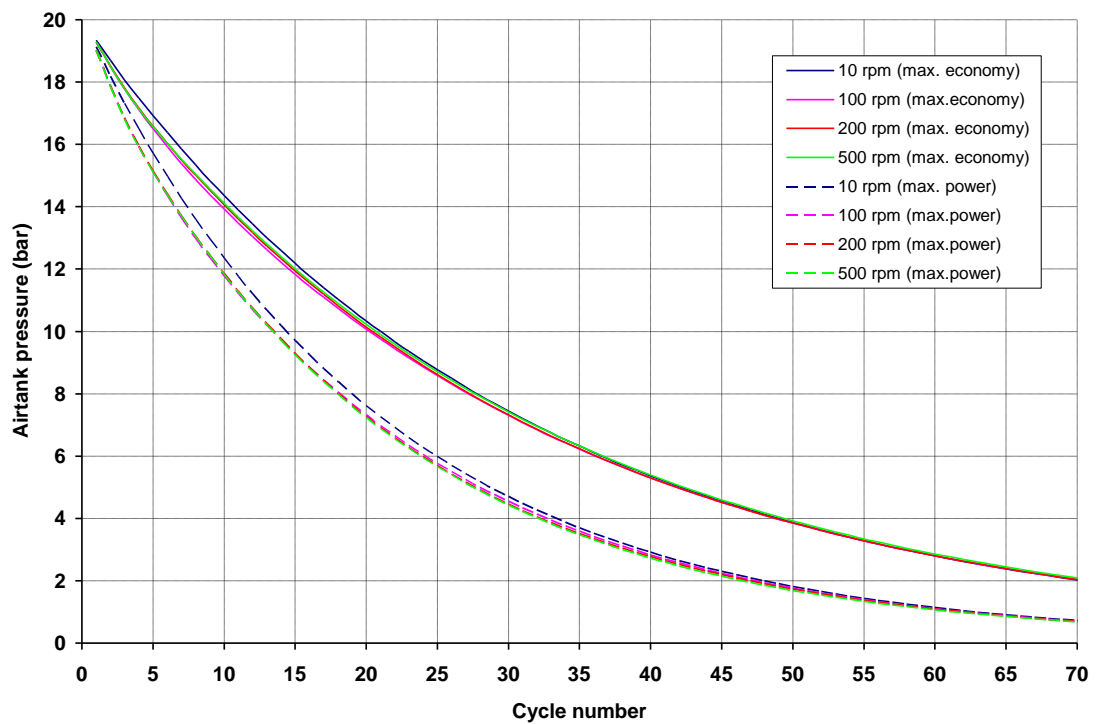


Figure 4.38: Airtank pressure throughout 70 engine cycles (70 crankshaft revolutions) at valve timing for maximum economy (solid lines) and maximum power (dotted lines).

4.3.3.5. Driving b_{mep} (air expander mode)

Following from airtank pressure results, the model was used to study the sensitivity of b_{mep_d} to airtank pressure and power demand (and thus valve timing strategy). As shown in Figure 4.39, b_{mep_d} remains unaffected by engine speed. However, it is proportional to airtank pressure and therefore the engine can provide driving torque for a limited number of cycles.

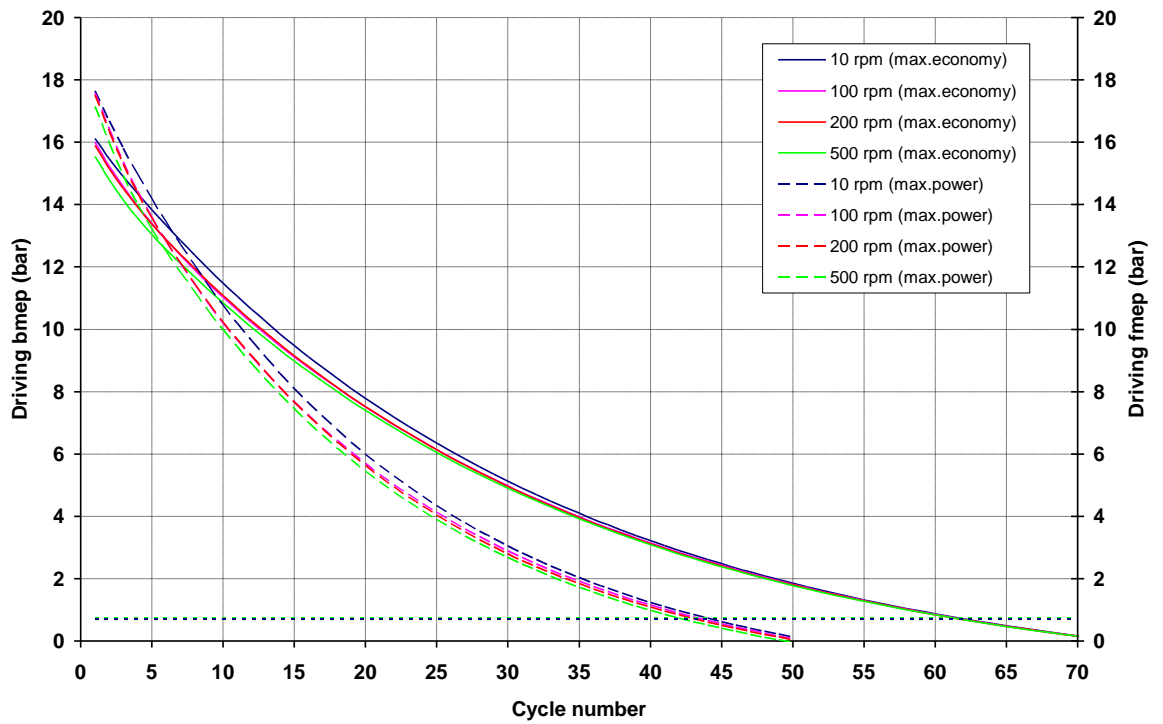


Figure 4.39: $Bmep_d$ and $fmep_d$ throughout 70 engine cycles (70 crankshaft revolutions) at valve timing for maximum economy (solid lines) and maximum power (dotted lines).

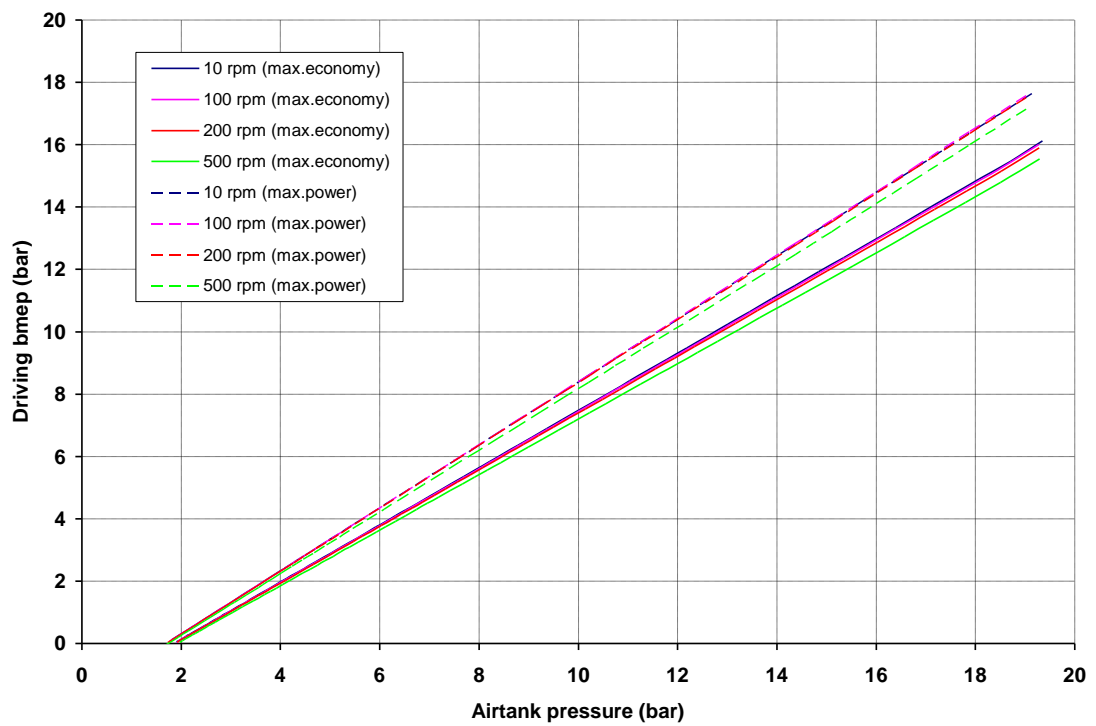


Figure 4.40: $Bmep_d$ against airtank pressure for maximum economy (solid lines) and maximum power (dashed lines).

It can be seen that for an initial airtank pressure of 20 bar, the engine can produce 16 bar of b_{mep_d} (and hence a starting torque of 63.7 Nm, according to Equations 4.6 and 4.7) at low-loads, when an energy-saving valve timing strategy is followed. It is also shown that b_{mep_d} can be elevated up to about 18 bar (and hence the engine can provide a starting torque of 71.6 Nm) at high power demands, with an unavoidable sacrifice to the airtank pressure reduction rate. B_{mep_d} drops down to zero after 70 engine cycles (70 crankshaft revolutions) under light-load conditions or after 50 engine cycles (50 crankshaft revolutions) under heavy-load conditions. It can be therefore concluded that the rate of reduction of the driving torque is significantly influenced by the torque demand.

The above results suggest that, similarly to the previous concept, the air expander should be used to start the engine and only for a limited time for the launch of the vehicle with lighter torque requirements, leading to longer periods of useable pressure availability from the airtank. The use of air expander to start the engine and launch the vehicle at the same time should be highlighted here as there is the additional benefit that the engine can be turned off when the vehicle is stationary.

4.5. Concept 3: Engine with reed valve inside the intake port

4.5.1. Model description

Figure 4.41 shows the simulation canvas of the present concept model. The modelled base engine has the same characteristics of the ones used in the above concepts (86mm bore, 86mm stroke and 500cm³ displacement volume). Intake and exhaust valve diameter is 23.5mm and 23.4mm respectively. The left intake port ("*intakeport1*") is directly linked to the intake manifold, whereas the right intake port ("*intakeport3*") is connected to the intake network through a non-return reed valve. This valve, labelled as "*REEDVALVE*", appears in the bottom end of the simulation canvas. Both intake ports are connected to the atmosphere ("*INamb*") through a simple 2-in-1 intake manifold which consists of two headers ("*manifold1*" and "*manifold2*"), the plenum ("*plenum*") and one runner ("*manifold3*"). The right intake port is connected to the Energy Control Valve ("*ECV*") through an auxiliary chamber ("*auxiliarychamber*"). The airtank ("*AIRTANK*"), which is modelled as duct of defined volume and initial pressure and it is connected to the ECV on one end and the ambient on the other end, which is used here to terminate the airtank

4.5.2. Valve timing optimization

As discussed in Chapter 3, the timing of the intake valve which is linked to the intake port containing the reed valve is controlled by a Cam Profile Switching (CPS) system, which enables the shifting of the valve lift profile. However, maximum lift and duration cannot be changed. As shown in Table 4.4, intake valves open at 20° BTDC and close at 60° ABDC while exhaust valves open at 60° BBDC and close at 35° ATDC, when the engine is operated at normal firing mode. Exhaust valve timing remains unaffected, regardless the engine mode (normal firing or air hybrid). However, the intake camshaft needs to be specially designed to deactivate the left intake valve during expander mode (EM) and shift the timing of the right intake valve during compressor mode (CM). ECV timing highly depends on the mode on which the engine is running, so investigation for air compressor (braking) and air expander (driving) modes must be separately undertaken. It is obvious that in normal firing mode ECV is deactivated and no gas exchange between the cylinder and the airtank takes place. The aims of the valve timing optimization for air compressor and air expander modes are:

- a) Reversible compression during braking at constant compression ratio.
- b) High Compressed Air Transfer Coefficient (CATC).
- c) Constant braking torque, regardless the state of charge of the air tank.
- d) Reversible expansion during driving at constant expansion ratio.
- e) High torque output at very low engine speeds during driving (for engine start-up).
- f) Lowest possible energy losses.

4.5.2.1. Valve timing for air compressor mode

The timing of the right intake valve during CM plays a significant role to the behavior and performance of the air compressor and it is examined below. The valve opens and closes during the compression stroke to enable compressed air from the cylinder to enter the intake port and the auxiliary chamber and therefore its timing must be retarded by approximately 180° CA. ECV opens at the end of the compression stroke. The opening point is of high importance and has a major effect on the efficiency of the air compressor and it needs to be optimized in a systematic way. ECV closing point is not of importance and does not affect the performance of the air compressor, as far as allows sufficient time for the compressed air to be transferred in the airtank.

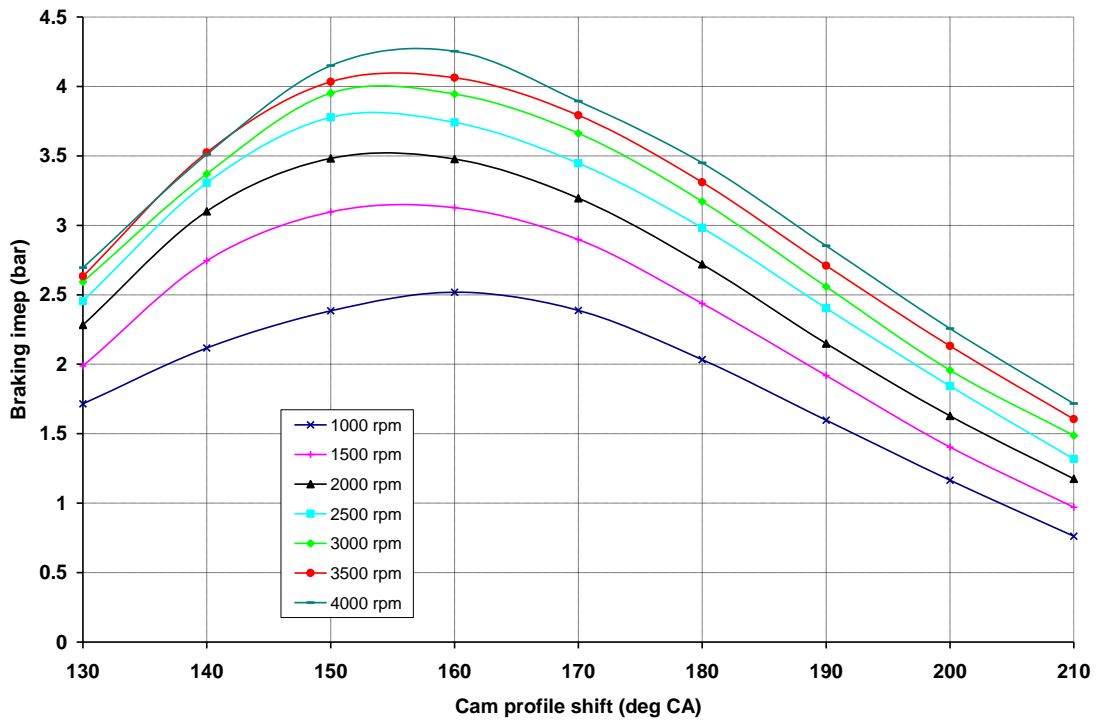


Figure 4.42: Predicted $imep_b$ against cam profile shift for engine speed range between 1000 and 4000 rpm.

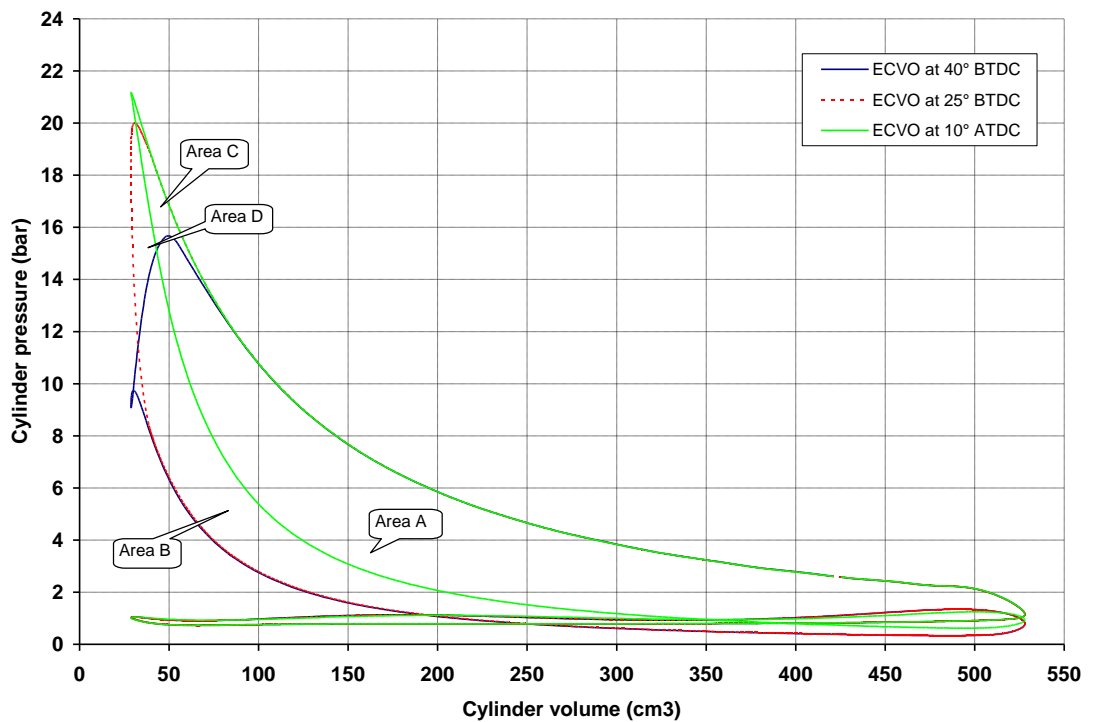


Figure 4.43: Indicator diagram at 2000 rpm for various cam profile shift angles.

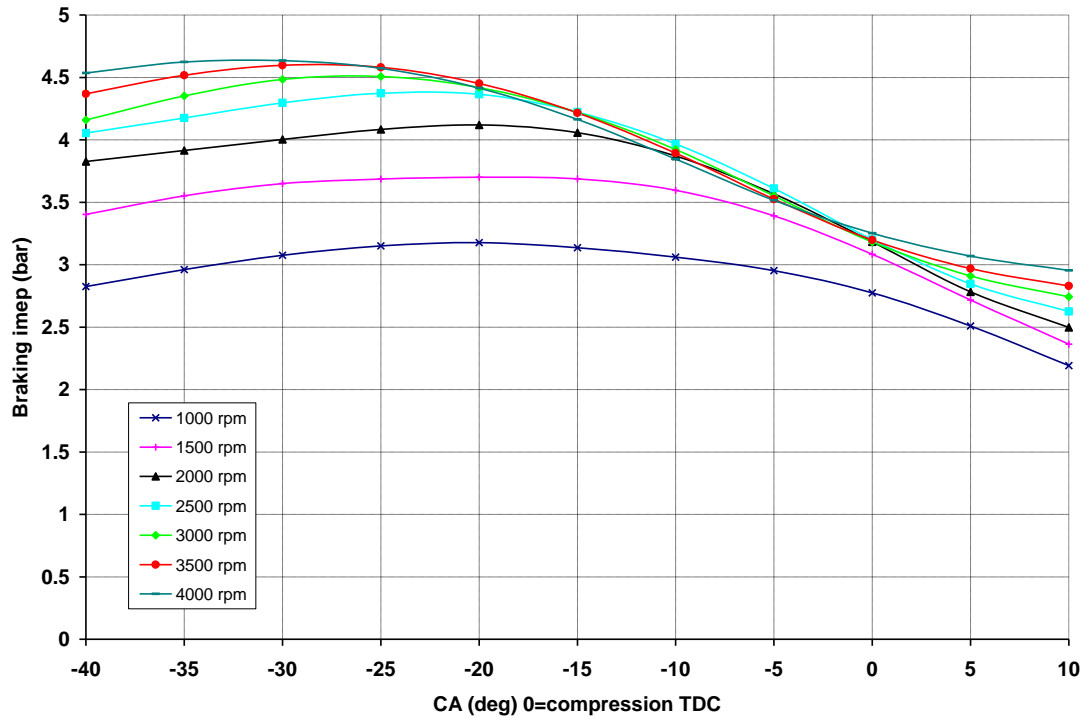


Figure 4.44: Predicted $imep_b$ against ECV opening timing for engine speed range between 1000 and 4000 rpm.

Figure 4.42 shows the predicted variation of $imep_b$ in regard to cam profile shift for the engine speed range between 1000 and 4000 rpm, at intervals of 500 rpm. It can be seen from the results that high braking performance is achieved for a valve profile shifting range of $150^\circ - 170^\circ$ CA, where increased $imep_b$ (and hence braking torque) is realized. $Imep_b$ drops rapidly for profile shifting out of the above range, while peak $imep_b$ is achieved at 160° CA, regardless the engine speed. This means that the intake camshaft must shift the lift profile of the right intake valve so that it opens 40° CA before the initiation of the compression stroke (30° BBDC) and closes 40° CA after the end of the stroke (50° ATDC). The predicted cylinder indicator diagrams for various valve lift profile shifts at 2000 rpm, which are shown in Figure 4.43, not only validate the above conclusion about the optimal cam shifting, but they also provide a better understanding of the gas exchange process which takes place during the air compressor cycle.

For 130° CA profile shifting, intake valve opens at 70° BBDC and there is sufficient time for the compressed air trapped into the auxiliary chamber at the end of the previous cycle to expand back into the cylinder. Because of advanced opening (and thus advanced closing, given that valve lift duration remains unaffected) of the intake valve, the later is half-closed towards the end of compression stroke, resulting in high peak cylinder pressure (blue line). The valve is fully closed at 10° ATDC so no air backflow from the auxiliary

chamber to the cylinder takes place during expansion stroke and the area enclosed by the indicator diagram is limited to area A+C. When the CPS intake valve profile is shifted by 160° CA, intake valve opens at 40° BBDC and there is enough time for the compressed air trapped into the auxiliary chamber at the end of the previous cycle to sufficiently expand into the cylinder. Part of that air mass escapes to the atmosphere through the partly-open left intake valve, which closes at 60° ATDC and therefore there is a 100-degree valve overlap. However, part of the compressed air is trapped into the cylinder after the left intake valve closes, which increases cylinder pressure during compression stroke (red line). CPS intake valve closes at 40° ATDC and there is limited backflow from the auxiliary chamber to the cylinder, which results in low cylinder pressure expansion stroke and elevates imep_b (area A+B+D).

Finally, for 210° CA profile shifting (green line), intake valve opens at 10° ABDC and compressed air trapped into the auxiliary chamber at the end of the previous cycle expands into the cylinder during compression stroke. This has an effect to cylinder pressure during the compression stroke, similarly to the previous case. However, the retarded closing of the valve, at 90° ATDC, results in excessive air backflow from the auxiliary chamber to the cylinder during expansion which raises cylinder pressure during expansion stroke and limits the area enclosed by the indicator diagram to area D.

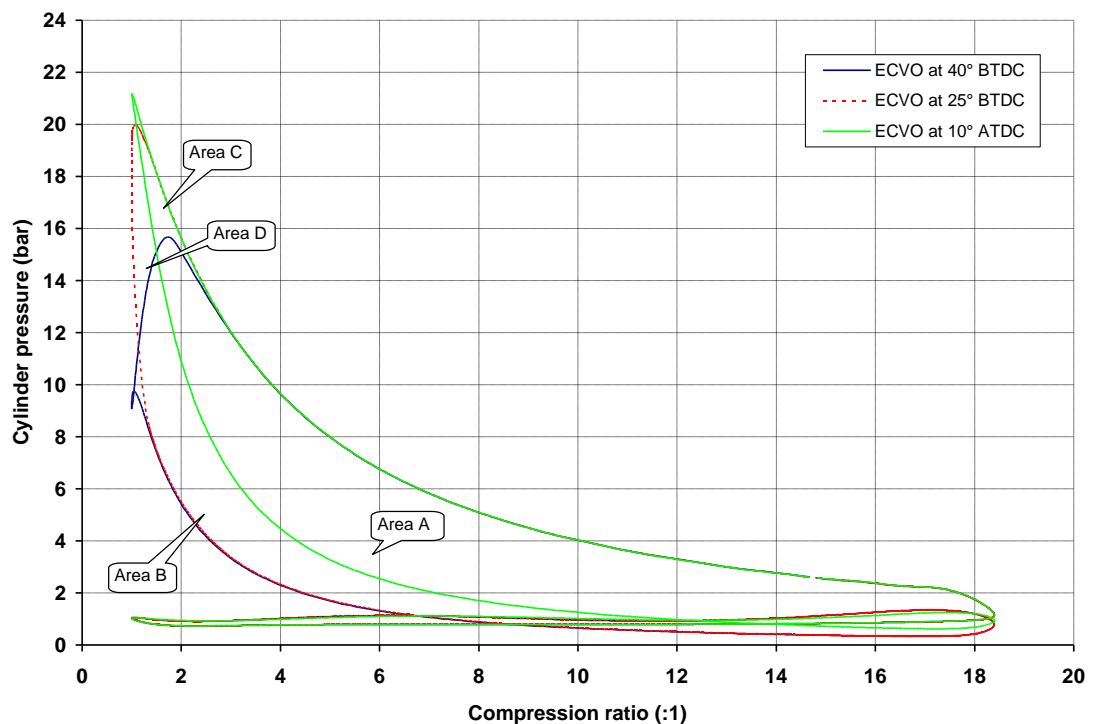


Figure 4.45: Indicator diagram at 2000 rpm for various ECV opening points.

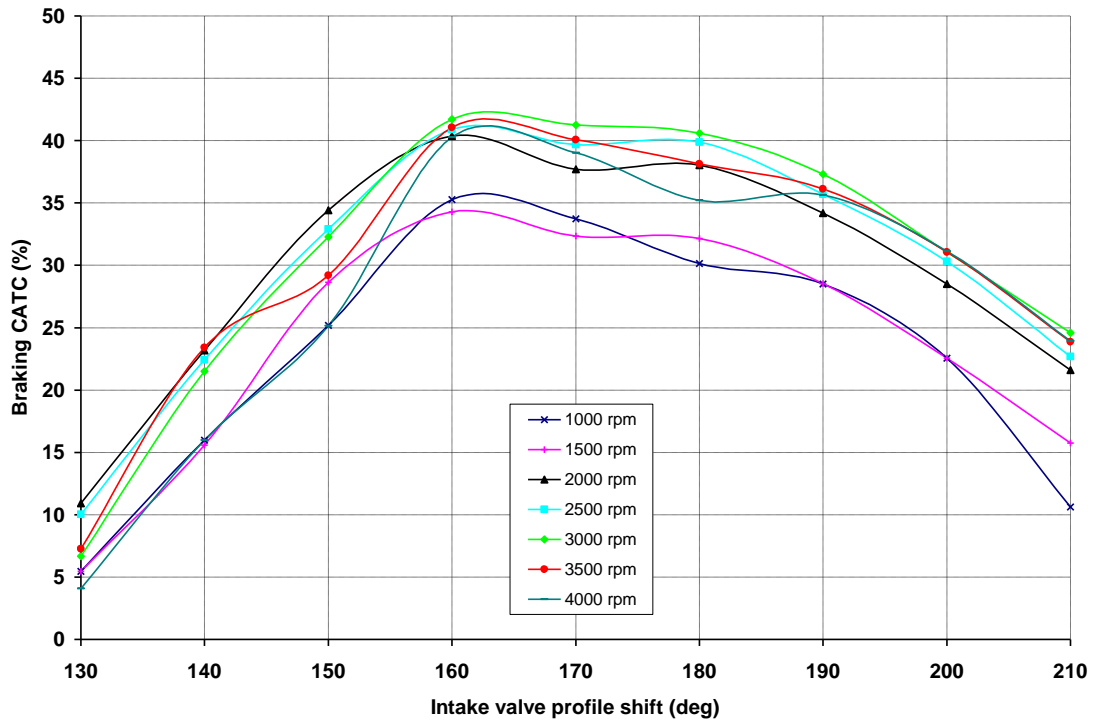


Figure 4.46: Predicted $CATC_b$ against intake valve profile shift for engine speed range between 1000 and 4000 rpm.

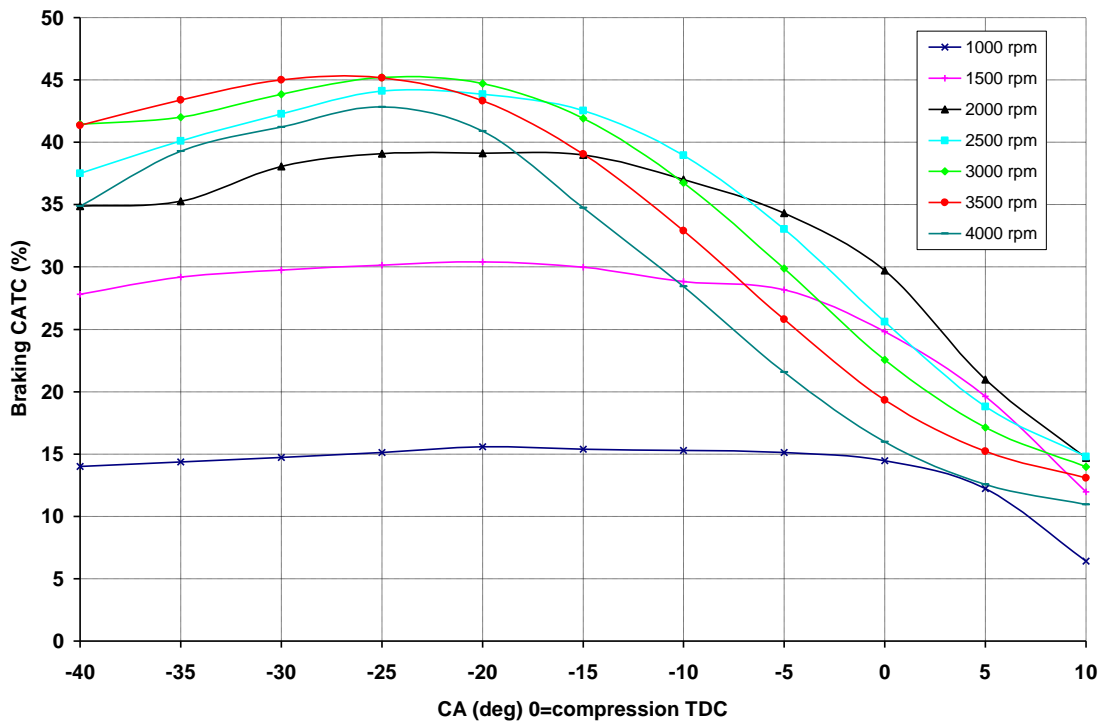


Figure 4.47: Predicted $CATC_b$ against ECV opening point for engine speed range between 1000 and 4000 rpm.

Following from profile shifting optimization for the right intake valve, the model was used to determine the optimal ECV timing. It can be seen in Figure 4.44 that the engine demonstrates increased imep_b for advanced ECV openings, $20^\circ - 25^\circ$ BTDC. For more advanced timings imep_b is slightly decreased, while it drops rapidly for opening points after 20° BTDC. Given that CPS intake valve closes at 40° ATDC, it can be concluded that a valve overlap of $60^\circ - 65^\circ$ CA has a positive effect on air compressor performance. Reduced imep_b is realized at low engine speeds due to the gas dynamics of the intake system, which influence the volumetric efficiency of the engine. The effect of advanced opening of ECV can be better perceptible by the means of the cylinder indicator diagrams for various ECV timings at 2000 rpm, which are shown in Figure 4.45.

According to those diagrams, compressed air expands back into the cylinder from the high-pressure auxiliary chamber through the partly-closed CPS intake valve during expansion stroke for retarded ECV opening, which increases cylinder pressure and confine the area included by the indicator diagram to area A+C (green line). For advanced ECV opening at 25° BTDC (red line), there is limited air backflow because the auxiliary chamber expands into the airtank (and therefore the air pressure in the auxiliary chamber drops) earlier. This allows for low-pressure expansion strokes to be realized, resulting to larger areas included by the indicator diagram (area A+B+C+D). When the ECV opening point is further advanced, peak cylinder pressure is decreased as it tends to equalise the airtank pressure and the indicator diagram is limited to area A+B (blue line).

Although CATC_b depends on the gas dynamics of the intake system and the auxiliary chamber, it is can be seen in Figure 4.46 that maximum CATC_b is realized by shifting the CPS intake valve by 160° CA regardless, the engine speed. This is because the maximum port area is achieved during compression stroke for the aforementioned timing and air flow from the cylinder to the auxiliary chamber is not restricted. Furthermore, intake valve closing at 40° ATDC prevents backflow of the compressed air, providing maximum air transfer efficiency. CATC_b drops rapidly for timings before 160° CA, while it is kept in high levels for timings up to 180° CA. Furthermore, figure 4.47 indicates that CATC_b drops rapidly for ECV opening timings after 20° BTDC, similarly to imep_b . This is because there is a limited period of valve overlap and thus not enough time for compressed air to be transferred into the airtank, in conjunction with high auxiliary chamber pressure, which pushes air back into the cylinder. However, CATC_b is not significantly affected by ECV timing at speeds up to about 2000 rpm. Depending on the volumetric efficiency of the engine, CATC_b is lower at low engine speeds.

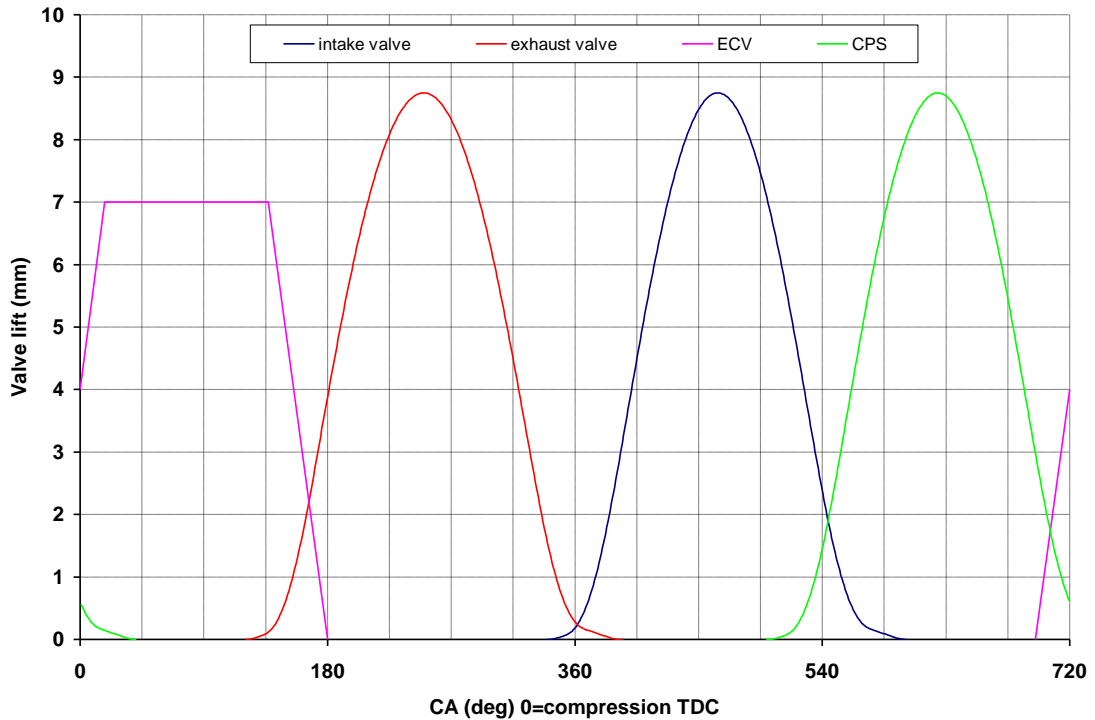


Figure 4.48: Optimal ECV and CPS timing in respect to engine valve timing for air compressor mode.

According to the above investigation, optimal intake CPS and ECV timing is shown in the same diagram together with engine valve timing in Figure 4.48. Similar to the previous concepts, a valve lift ramp of 43° CA is adopted for the trapezoidal ECV profile and for all engine speeds at the present simulation for simplicity reasons, assuming lower valve velocities for lower engine speeds according to Equation 4.32.

4.5.2.2. Valve timing for air expander mode

The objective of optimal CPS and ECV timing for the air expander cycle is the same as in the previous concepts; it should primarily enable the engine to start without the aid of the electric starter and ideally propel the vehicle from stop until the engine is switched to normal firing mode. The engine speed range of interest for expander mode is very low (between 0 rpm and idle speed) and therefore opening and closing ramp duration for ECV can be reduced to 10° crank angle here, assuming the same valve velocity as in air compressor mode (4.5 m/s). It is also assumed that engine speed (and hence gas velocity which is proportional to piston speed) is too low to govern important aspects of the air flow through nozzles, orifices, valves and restrictions and thus it does not importantly affect $imep_d$. However, $imep_d$ is a strong function of airtank pressure, as the latter governs cylinder pressure during the power stroke.

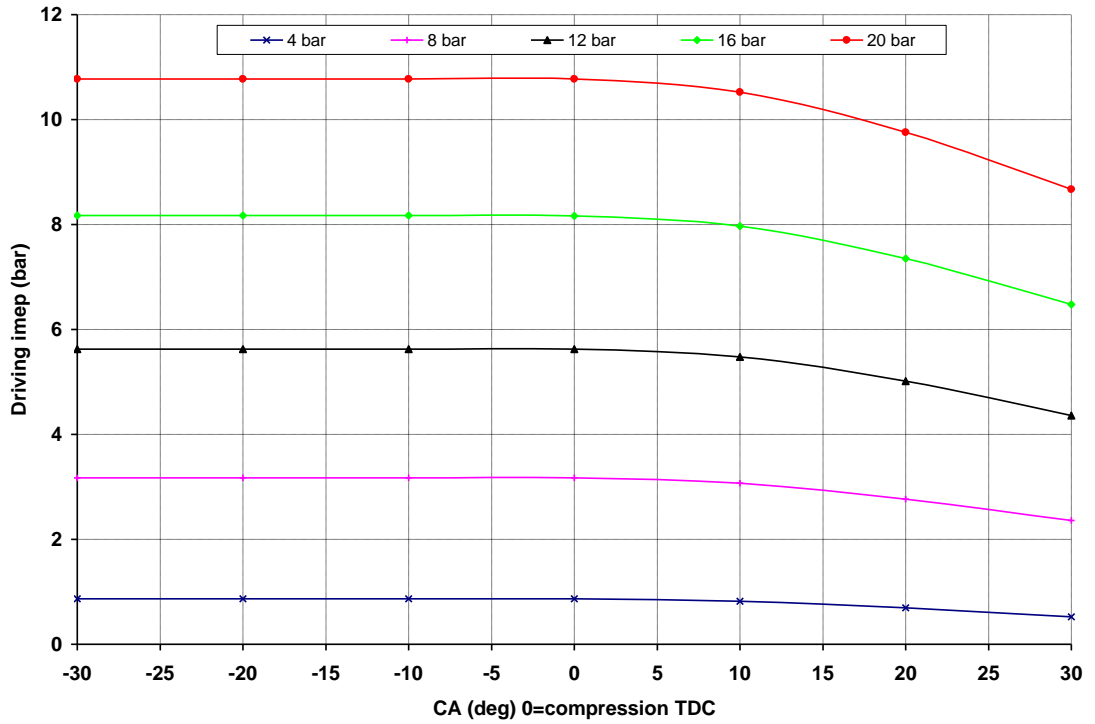


Figure 4.49: Predicted imep_d against ECV opening point for airtank pressure range between 4 and 20 bar.

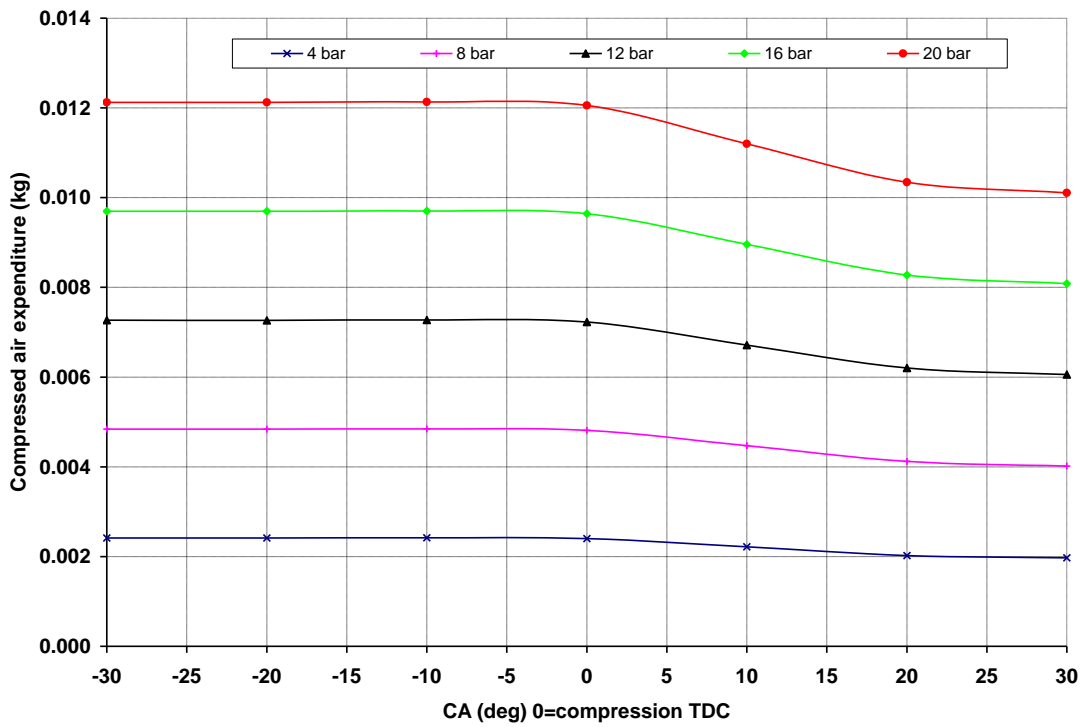


Figure 4.50: Compressed air expenditure against ECV opening point for airtank pressure range between 4 and 20 bar.

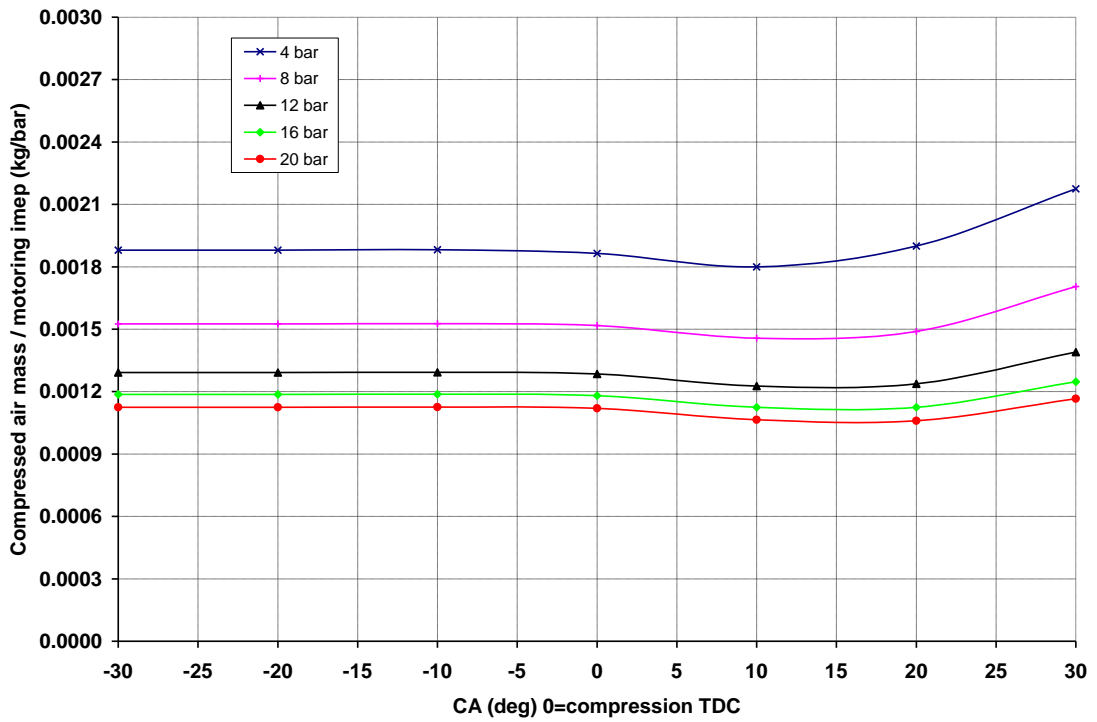


Figure 4.51: Compressed air expenditure to imep_d ratio against ECV opening point for airtank pressure range between 4 and 20 bar.

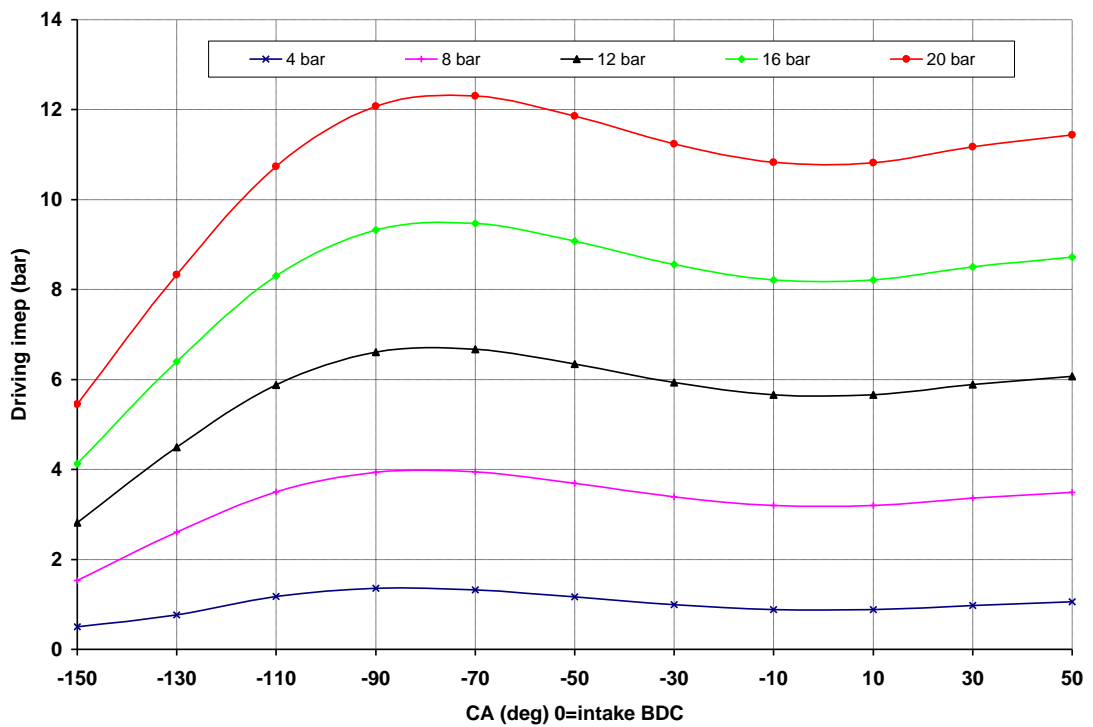


Figure 4.52: Predicted imep_d against ECV closing point for airtank pressure range between 4 and 20 bar.

The intake stroke is the power stroke here, as compressed air from the airtank is released into the cylinder during this period. As a result, the piston is forced downwards, generating driving torque on the crankshaft. The right intake valve, which plays the role of the gas transfer valve in AM mode, must open and close during the intake period. Therefore, the profile shifting system is deactivated and the valve events are the same as in normal firing mode. The left intake valve must be deactivated in order to prevent compressed air from escaping to the atmosphere. A separate cam deactivation system, which would only work when the engine is switched to AM mode, is therefore required here.

The gas transfer process is controlled by ECV timing and thus the performance of the air expander is greatly influenced by ECV opening and closing events. Figure 4.49 shows the sensitivity of the predicted $imep_d$ to ECV opening point for various airtank pressures. It can be seen that $imep_d$ is a strong function of airtank pressure and proportional to it. $imep_d$ drops for retarded ECV openings (ATDC), while it is not influenced by advanced openings (BTDC). It should be noted that $CATC_b$ is not affected by engine speed neither by valve timing. This is due to the deactivation of the left intake valve, which in fact precludes the definition of $CATC_b$ here, as the mass of air released into the cylinder is transferred to the atmosphere through the exhaust valves and therefore $CATC_b$ equals the unit at all times.

Figure 4.50 shows the sensitivity of predicted mass of air transferred during one engine cycle to ECV opening point for various airtank pressures. It is shown that compressed air expenditure is maximized for advanced opening points (BTDC) while it slightly drops for retarded closing points (ATDC) and therefore some energy economy can be achieved at these timings. However, the ratio of compressed air expenditure to $imep_d$, which practically represents the efficiency of the air expander and it is shown in Figure 4.51 for various airtank pressures and ECV opening points, indicates that compressed air is more efficiently consumed when ECV opens at TDC or shortly before TDC.

Figure 4.52 shows the sensitivity of the predicted $imep_d$ to ECV closing timing for various airtank pressures. It can be seen that $imep_d$ increases for advanced ECV closing (BBDC) and is maximized for valve closing at 80° BBDC. Further advancing of closing event results in rapidly decreasing $imep_d$, while retarded valve closing (at BDC or after BDC) also lowers $imep_d$, although the later is not greatly influenced by retarded ECV closing.

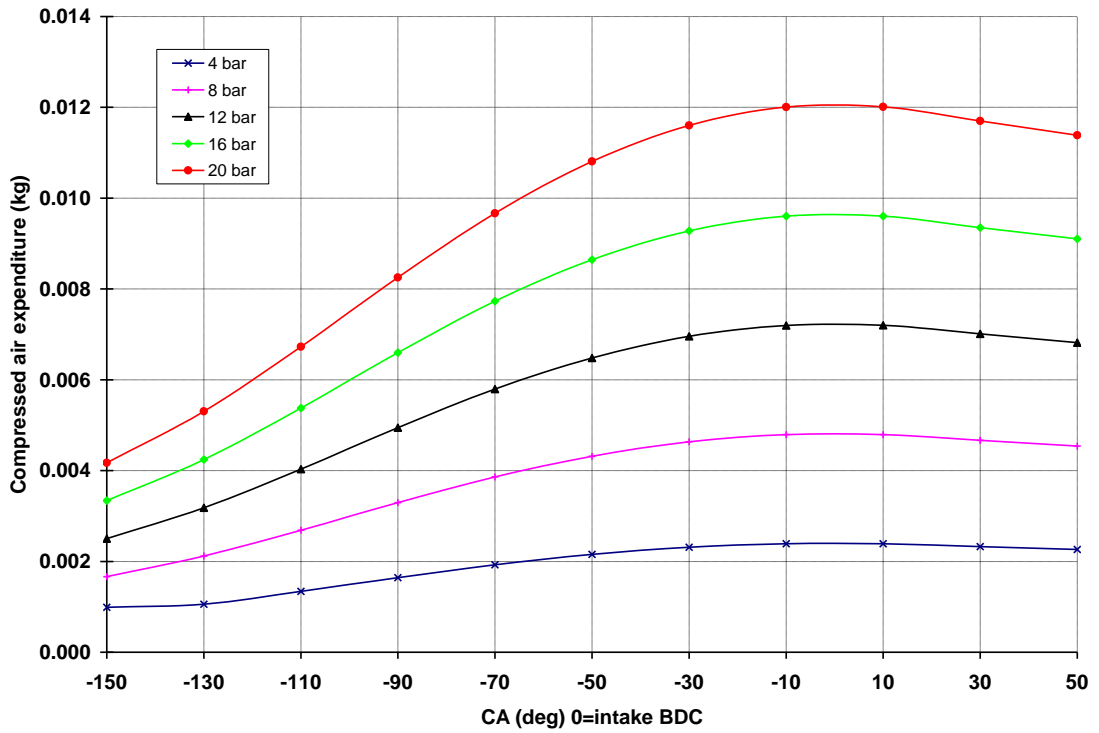


Figure 4.53: Compressed air expenditure against ECV closing point for airtank pressure range between 4 and 20 bar.

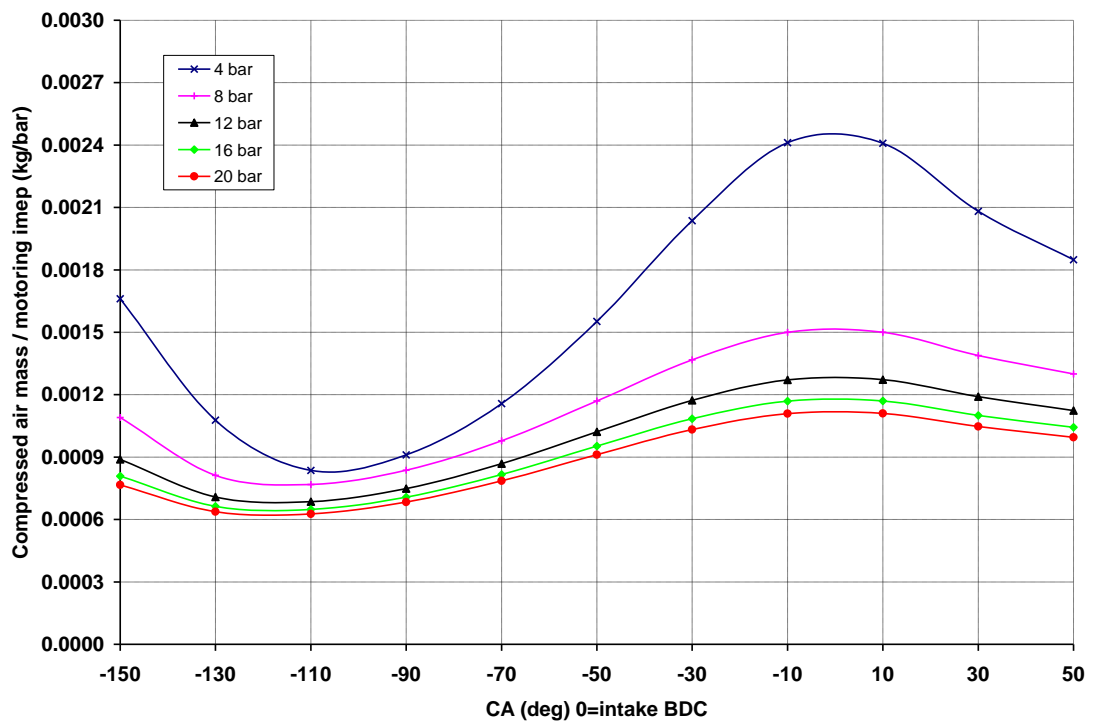


Figure 4.54: Compressed air expenditure to imep_d ratio against ECV closing point for airtank pressure range between 4 and 20 bar.

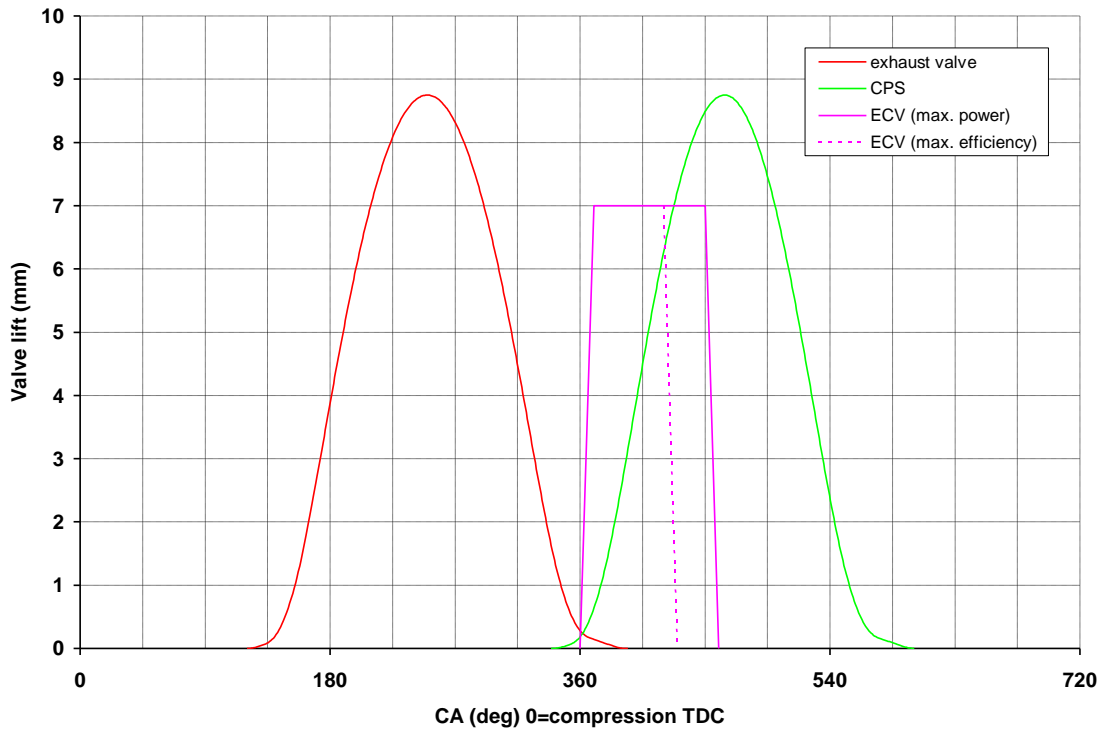


Figure 4.55: Optimal ECV timing in respect to engine valve timing for air expander mode.

Figure 4.53 shows the air mass past the CPS intake valve during one engine cycle against ECV closing point for various airtank pressures. It is shown that the expenditure of compressed air is maximized for valve closing at BDC and it drops with advanced valve closing (BBDC). For retarded ECV closing (ABDC), air expenditure remains at high levels, although it drops slightly. It can be therefore concluded that the more advanced ECV closing the more sustainable the air expander torque.

However, it can be seen in Figure 4.54 that the ratio of compressed air expenditure to imep_d , which practically represents the efficiency of the air expander, is optimal for ECV closing at $100^\circ - 110^\circ$ BBDC. Therefore, depending on the torque demand, two ECV closing timings are possible: For light engine loads the valve can close at 110° BBDC, while when full power is needed, ECV closing at 80° BBDC could provide the extra driving torque.

Finally, Figure 4.55 shows the optimal ECV timing according to the above investigation. Exhaust and CPS intake valve timings are also shown in the same diagram. ECV closing appears in the diagram between two extreme points; for maximum power (solid line) and for maximum efficiency (dotted line).

4.5.3. Modeling results and discussion

4.5.3.1. Airtank charging (air compressor mode)

Initially the model was used to determine the rate of increase of the airtank pressure in respect to the number of engine cycles (or time). The capacity of the airtank is 10 litres (roughly 1:20 cylinder to airtank volume) and was set at an initial pressure of 5 bar. The results are shown in Figures 4.56 and 4.57, where it can be seen that after 1000 cycles (2000 crankshaft revolutions) airtank pressure reaches a pressure of 19 bar at low engine speeds, while it drops to 18 and 17 bar at 3000 and 4000 rpm respectively. This pressure variation is due to the gas dynamics of the auxiliary chamber, ECV and intake system which influence the volumetric efficiency of the engine, which in turn has an effect on the pressure of the compressed air reaching the airtank at the end of each cycle. The airtank pressure curve is asymptotically approaching a pressure of 20 bar at low engine speeds, while it drops to 19 and 18 bar at 3000 and 4000 rpm respectively. It should be noted that over 75% of the maximum achievable pressure is realized within approximately 550 engine cycles (1100 crankshaft revolutions), which in terms of time is 66 seconds at 1000 rpm, 33 seconds at 2000 rpm, 22 seconds at 2000 rpm and 16.5 seconds at 4000 rpm.

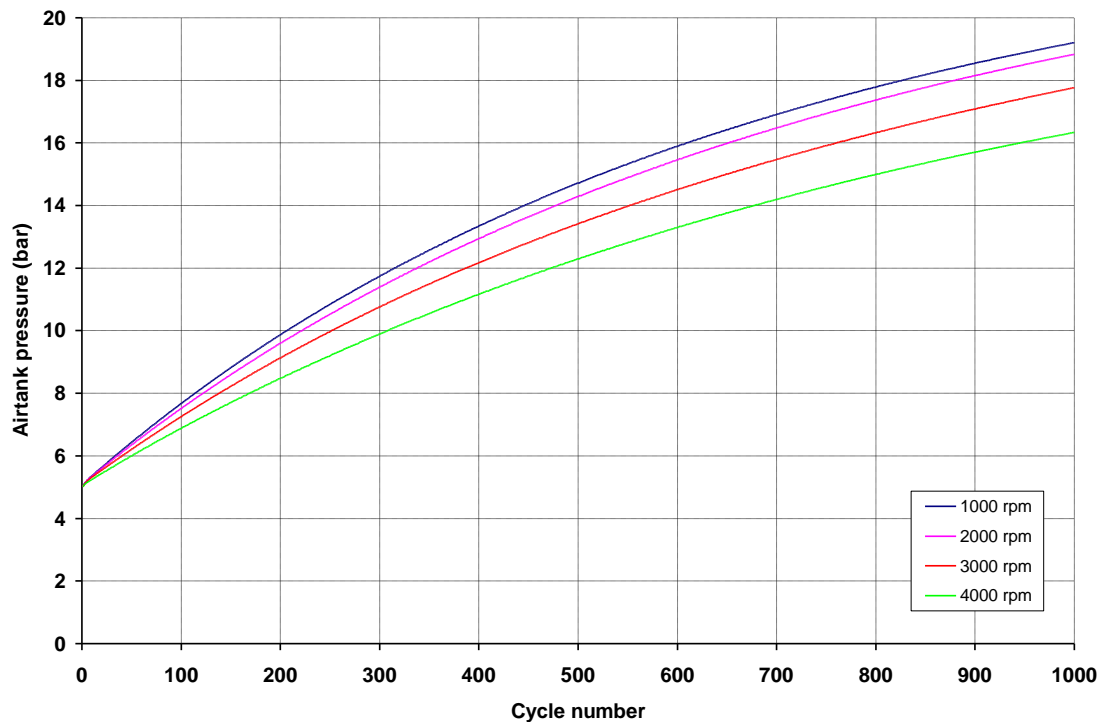


Figure 4.56: Airtank pressure through 1000 engine cycles (2000 crankshaft revolutions) for auxiliary chamber volume equal to 100% of engine clearance volume (28.7 cm^3).

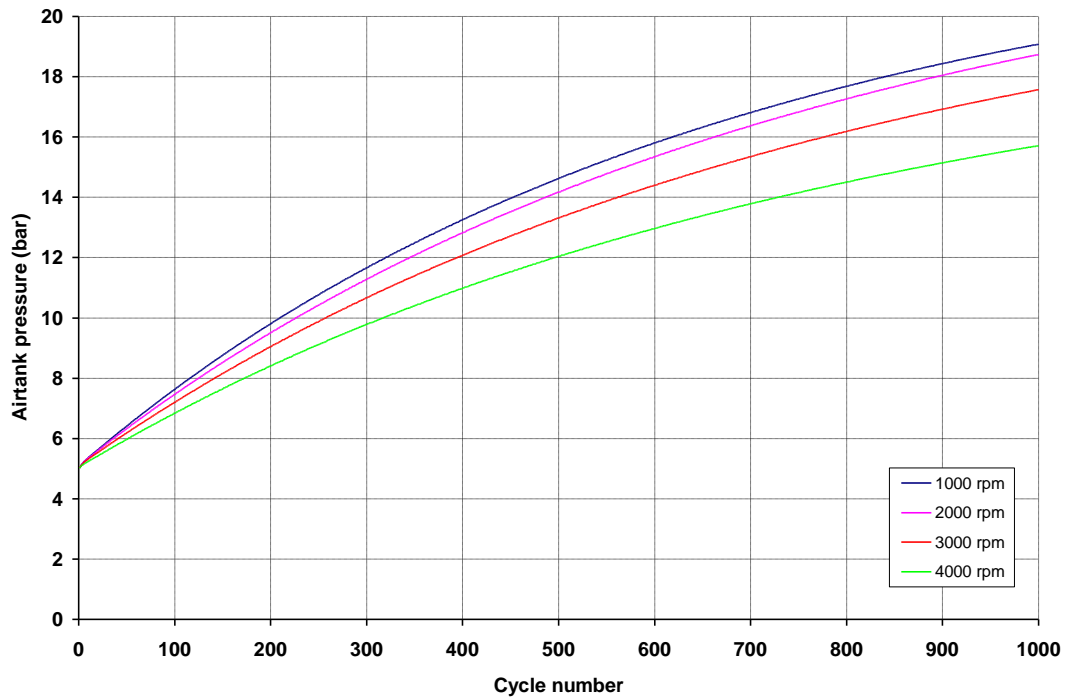


Figure 4.57: Airtank pressure through 1000 engine cycles (2000 crankshaft revolutions) for auxiliary chamber volume equal to 50% of engine clearance volume (14.4 cm^3).

Finally, the comparison of the diagrams in Figures 4.56 and 4.57 shows that the volume which connects the cylinder and the airtank (i.e. auxiliary chamber volume) does not affect the tank filling process, as the pressure curves are identical in both diagrams. The results for the intermediate engines speeds of 1500 rpm, 2500 rpm and 3500 rpm are omitted from the diagrams for simplicity reasons.

4.5.3.2. Braking bmep (air compressor mode)

Following from airtank pressure results, the model was used to study the sensitivity of bmep_b to airtank pressure, engine speed and auxiliary chamber volume. As shown in Figures 4.58 and 4.59, bmep_b remains unaffected by auxiliary chamber volume. Although compression ratio is increased by 16% by reducing auxiliary chamber volume by 50%, the comparison of the two diagrams shows that there is no variation to bmep_b values throughout the 1000 engine cycles. By the observation of bmep_b sensitivity to airtank pressure, it can be concluded that bmep_b is not a strong function of airtank pressure. For airtank pressure increase by 280% (i.e. from 5 bar to 19 bar – Figure 4.56), bmep_b is increased by only 164% (i.e. from 4.2 bar to 6.7 bar – Figure 4.58). Finally, it can be seen that initially bmep_b slightly increases with engine speed because of fmep_b (see Equation 4.21). However, after approximately 500 engine cycles, bmep_b curves in both diagrams converge.

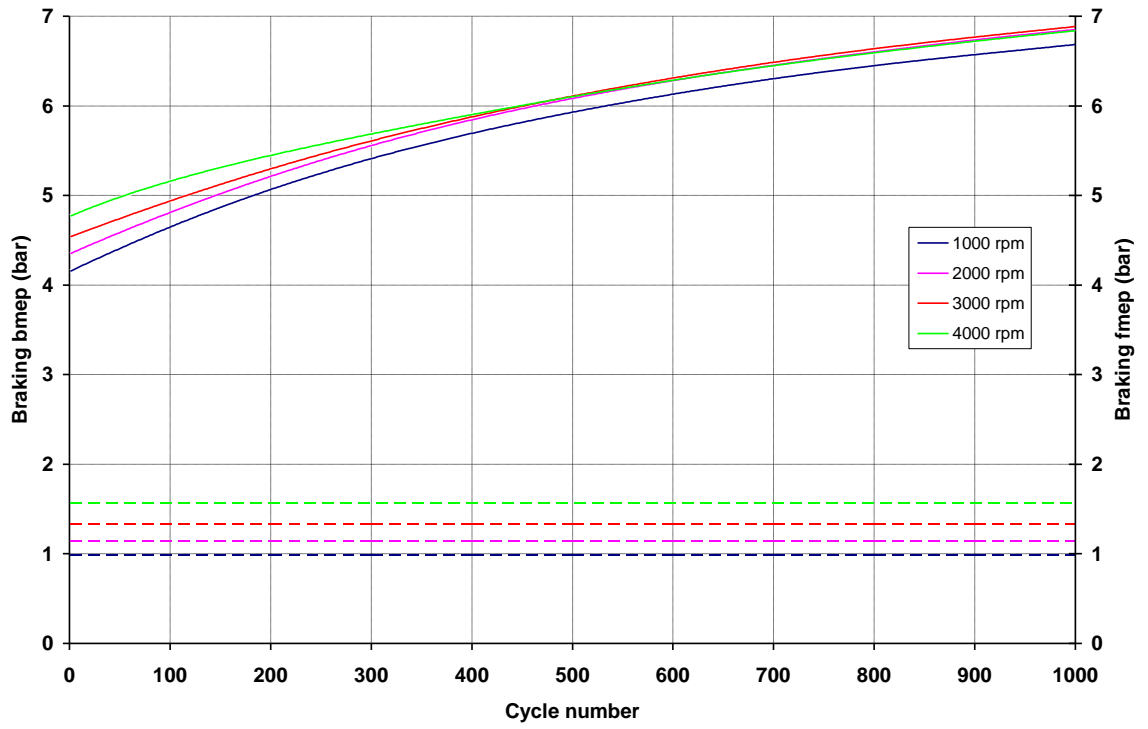


Figure 4.58: $Bmep_b$ through 1000 engine cycles (2000 crankshaft revolutions) for auxiliary chamber volume equal to 100% of engine clearance volume (28.7 cm^3).

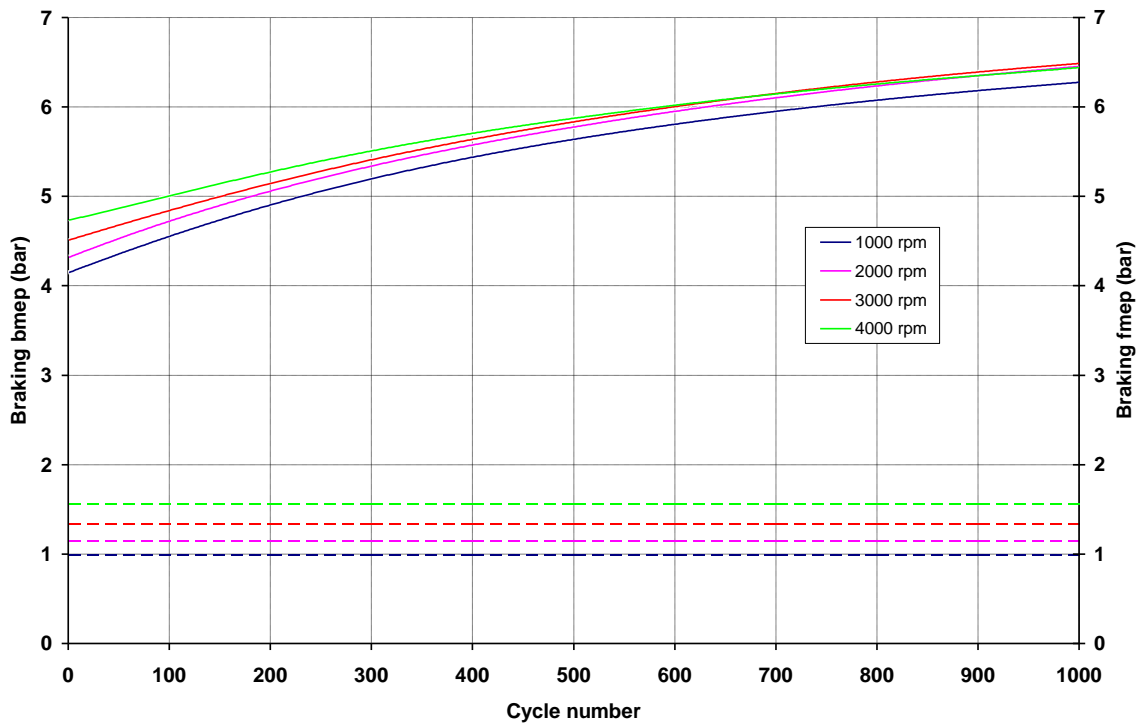


Figure 4.59: $Bmep_b$ through 1000 engine cycles (2000 crankshaft revolutions) for auxiliary chamber volume equal to 50% of engine clearance volume (14.4 cm^3).

4.5.3.3. Air mass transfer (air compressor mode)

Figures 4.60 and 4.61 show the sensitivity of air mass which is transferred from the cylinder to the airtank at the end of each cycle against time (i.e. number of cycles, at given engine speeds). It is shown that when the state of charge (SOC) of the airtank is low and the pressure difference between the airtank and the auxiliary chamber is high, there is an air flow as high as 0.00025 - 0.0003 kg per cycle through the ECV at low engine speeds and 0.0002 – 0.00025 kg per cycle at high engine speeds. This is due to the gas dynamics of the intake system, which affect the mass of air induced during the intake period and finally transferred to the airtank during compression. The above quantities are reduced by 50% after 500 engine cycles (1000 crankshaft revolutions). After 1000 engine cycles (2000 crankshaft revolutions) the transferred air mass curves are asymptotically approaching a value of 0.00005 kg per cycle due to the high SOC of the airtank. Finally, it should be noted that auxiliary chamber volume does not affect air flow, as the flow curves in Figures 4.60 and 4.61 are identical.

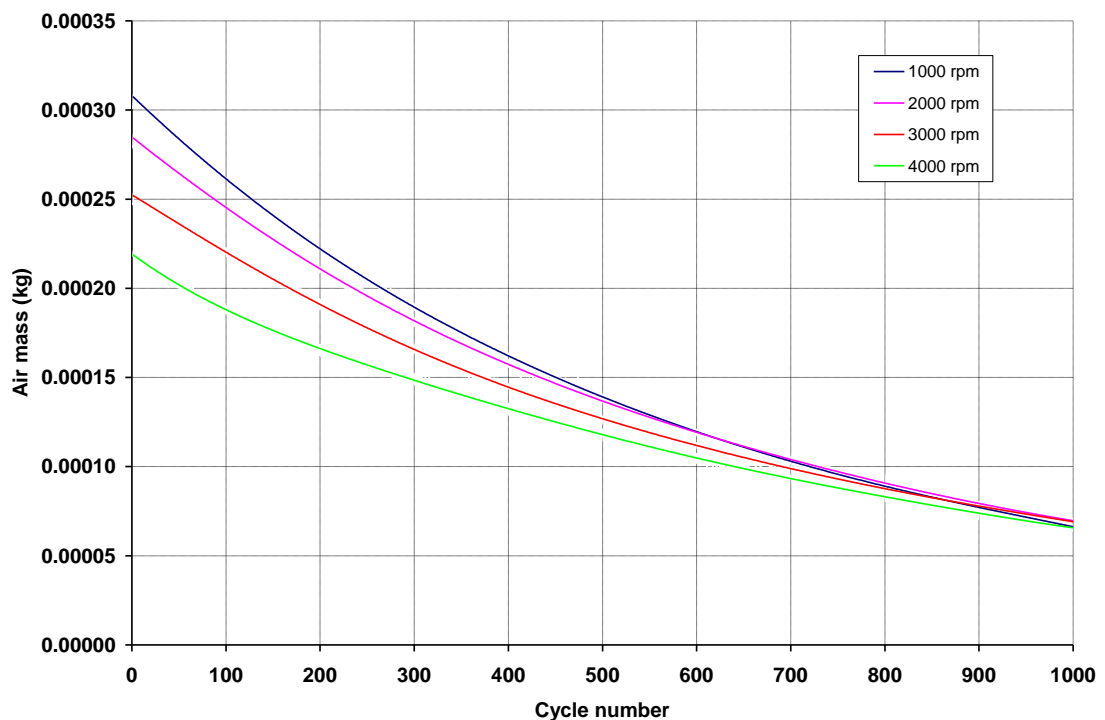


Figure 4.60: Air mass transferred from the cylinder to the airtank per cycle for auxiliary chamber volume equal to 100% of engine clearance volume (28.7 cm^3).

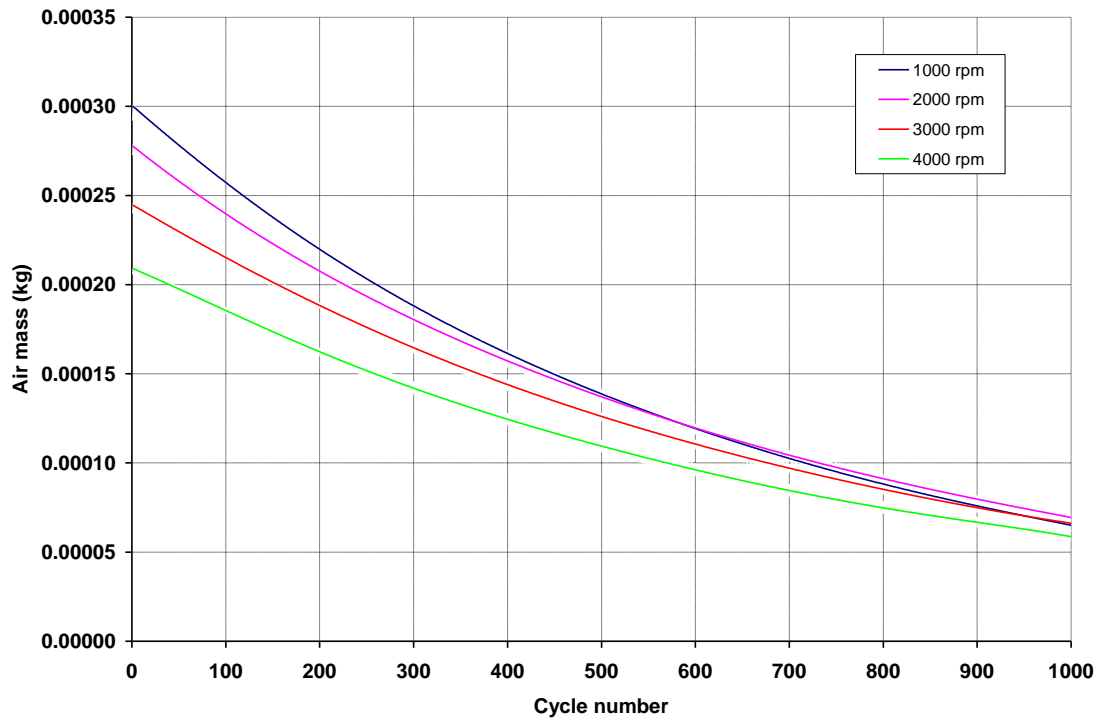


Figure 4.61: Air mass transferred from the cylinder to the airtank per cycle for auxiliary chamber volume equal to 50% of engine clearance volume (14.4 cm^3).

4.5.3.4. Airtank discharging (air expander mode)

The model was used to examine the rate of reduction of the airtank pressure during discharge, when compressed air is used to power the air motor. The air reservoir is the same 10-litre airtank (roughly 1:20 cylinder to airtank volume) which has also been used for the air compressor modeling. The airtank is assumed to be pre-charged at an initial pressure of 20 bar. The results are shown in Figures 4.62 and 4.63, where it can be seen that the minimum useable airtank pressure is 3 bar. Below that limit no torque can be generated by the engine, so the airtank pressure must not drop below that pressure (see also Figure 4.66, which show the variation of bmep_d in regard to airtank pressure). The minimal airtank pressure is reached after approximately 70 engine cycles (140 crankshaft revolutions) when ECV is timed for maximum efficiency (and therefore energy economy). For higher engine torque demands, this period is limited to 50 engine cycles (100 crankshaft revolutions). Clearly, the larger the airtank the more sustainable the air expander torque but the longer the charging time. By the observation of Figures 4.62 and 4.63 it can be concluded that the airtank discharging process is not influenced by factors such as engine speed and auxiliary chamber volume, as the curves in both Figures are almost identical.

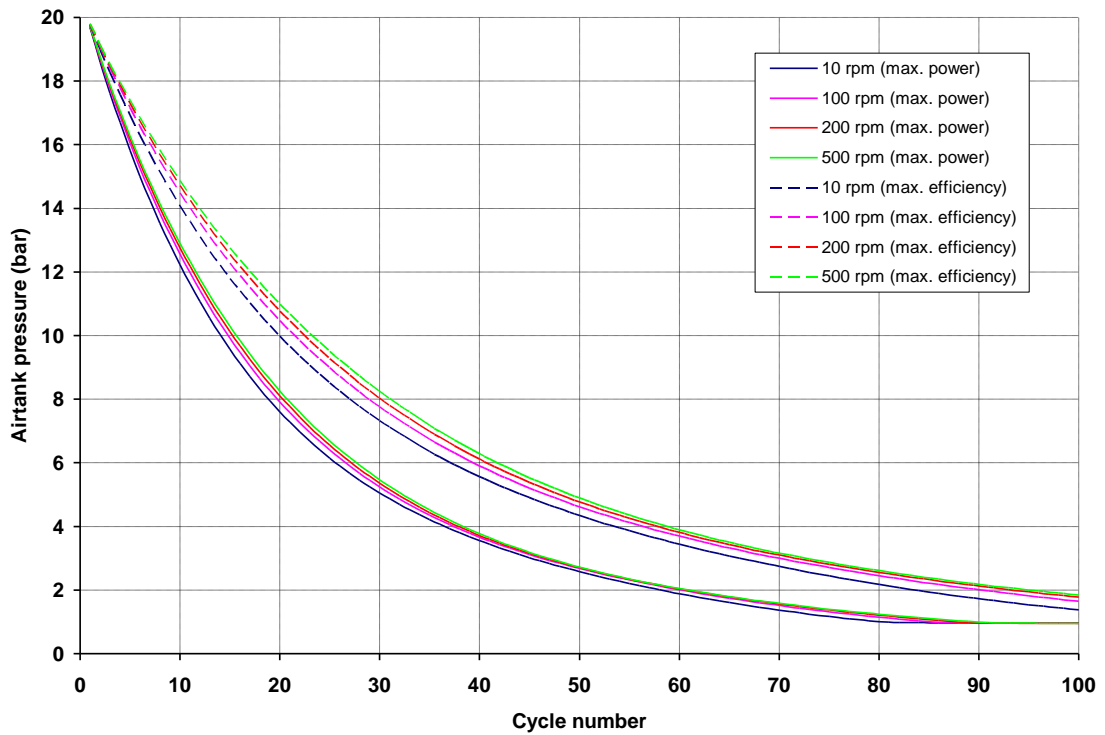


Figure 4.62: Airtank pressure through 60 engine cycles (120 crankshaft revolutions) for auxiliary chamber volume equal to 100% of engine clearance volume (28.7 cm^3).

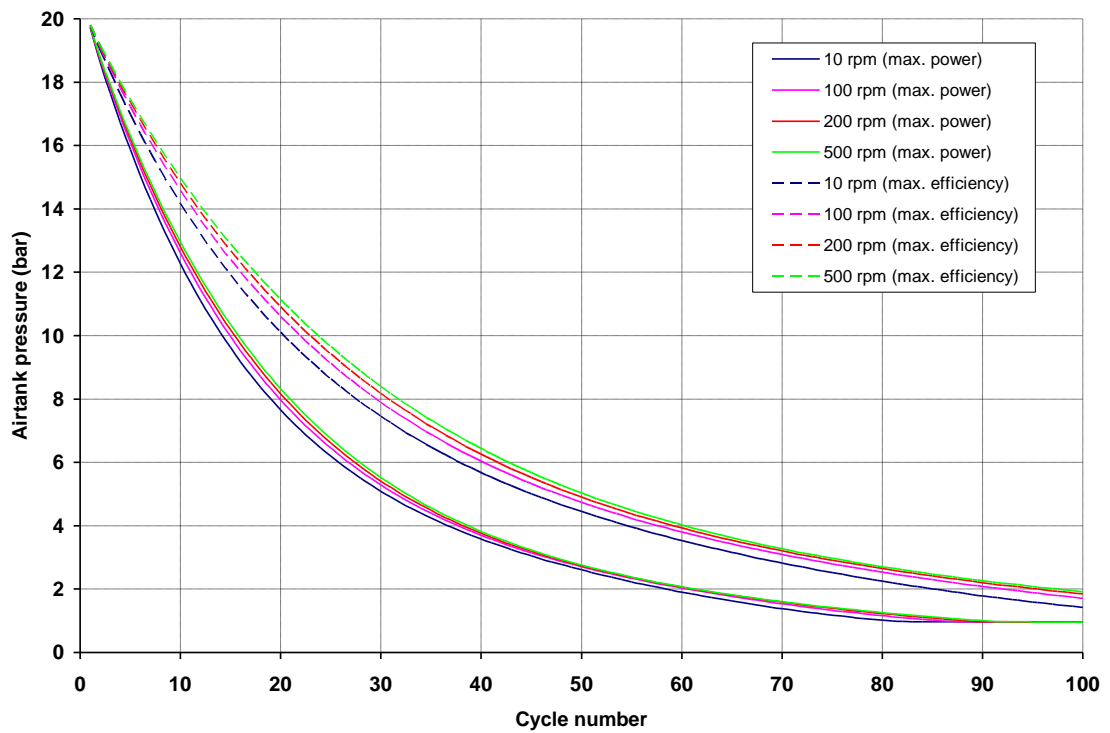


Figure 4.63: Airtank pressure through 60 engine cycles (120 crankshaft revolutions) for auxiliary chamber volume equal to 50% of engine clearance volume (14.4 cm^3).

4.5.3.5. Driving bmep (air expander mode)

Similarly to air compressor mode, the model was used to study the sensitivity of $bmep_d$ to airtank pressure, engine speed and auxiliary chamber volume. As shown in Figures 4.64 and 4.65, $bmep_d$ is not influenced by auxiliary chamber volume and engine speed. However, it is a strong function of airtank pressure and therefore the engine can provide driving torque for a limited number of cycles, given that the airtank is at a high SOC. It can be seen that for an initial airtank pressure of 20 bar, the engine is capable of producing approximately 11 bar of $bmep_d$ (and hence a starting torque of 43.68 Nm, according to Equations 4.6 and 4.7). $Bmep_d$ drops down to zero after 50 engine cycles (100 crankshaft revolutions). A further factor which influences the rate of reduction of the driving torque is the torque demand. Figures 4.64 and 4.65 show that driving torque, similarly to airtank pressure, is more sustainable at a lower torque demand (i.e. when ECV is timed for maximum efficiency), as the mass transfer per cycle from the airtank to the cylinder is restricted by ECV closing. For lighter power demand, initial $bmep_d$ is slightly lower (9 bar), providing a starting torque of 35.77 Nm which is more sustainable. It can be seen that $bmep_d$ at maximum power descends rapidly and drops lower than at maximum efficiency after 15 engine cycles.

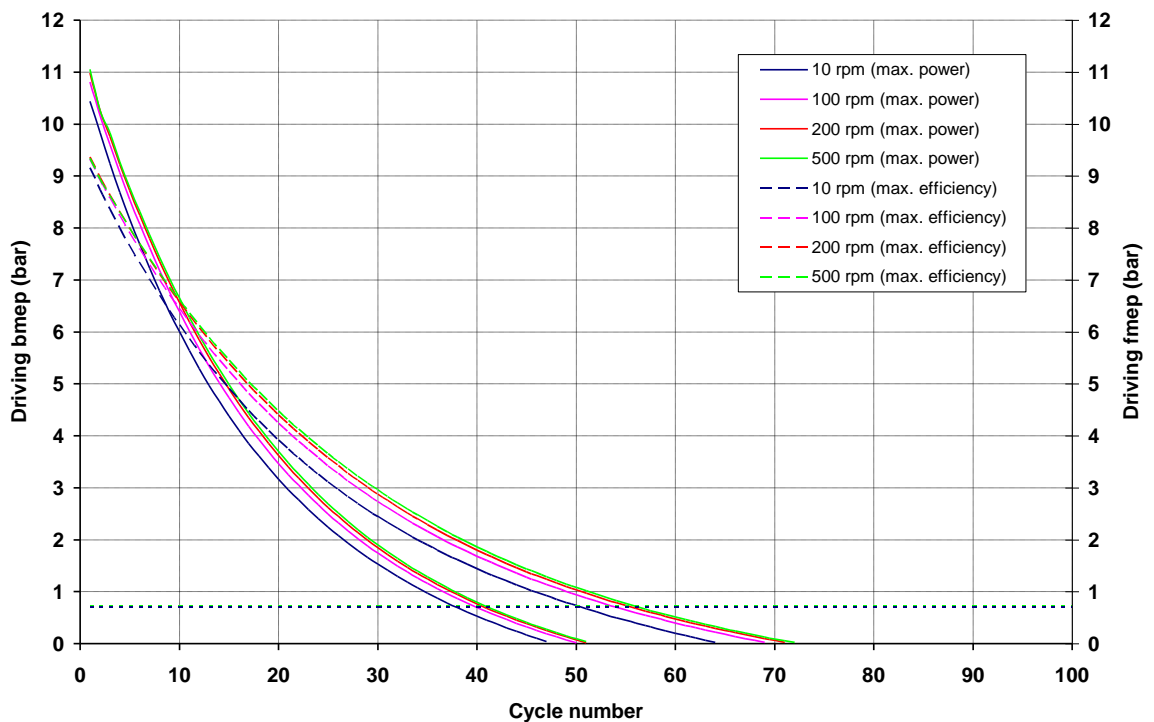


Figure 4.64: $Bmep_d$ and $fmep_d$ throughout 60 engine cycles (120 crankshaft revolutions) for auxiliary chamber volume equal to 100% of engine clearance volume (28.7 cm^3).

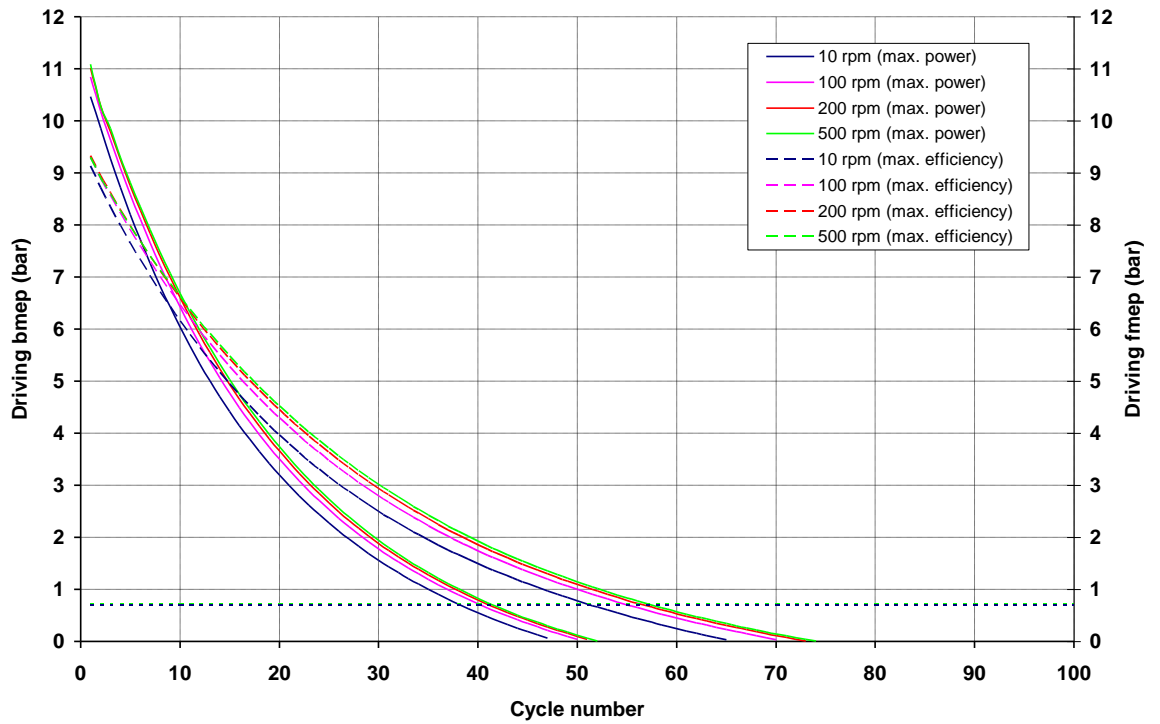


Figure 4.65: $Bmep_d$ and $fmep_d$ throughout 60 engine cycles (120 crankshaft revolutions) for auxiliary chamber volume equal to 50% of engine clearance volume (14.4 cm^3).

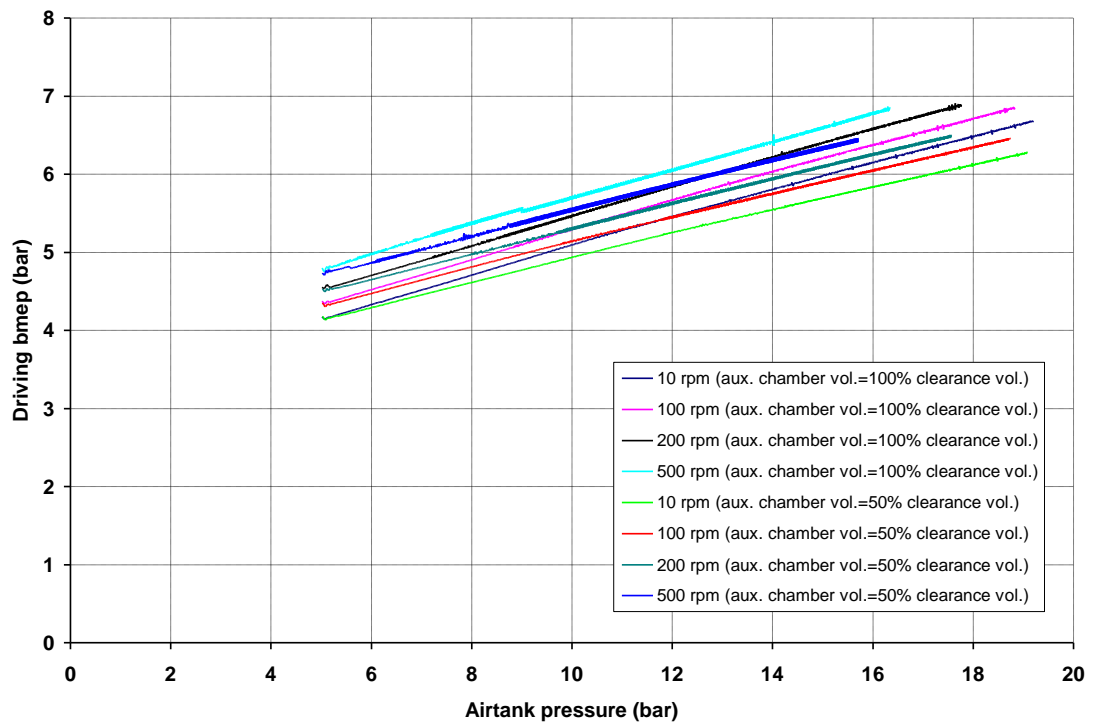


Figure 4.66: $Bmep_d$ against airtank pressure for various engine speeds and for auxiliary chamber volume equal to 100% clearance volume (solid lines) and auxiliary chamber volume equal to 50% clearance volume (dashed lines).

4.5.3.6. Air mass transfer (air expander mode)

Finally, Figures 4.67 and 4.68 show the sensitivity of air mass which is transferred from the airtank to the cylinder at the end of each cycle against the number of cycles. It is shown that initially, when the SOC of the airtank is high and therefore the pressure difference between the airtank and the auxiliary chamber is also high, there is a flow of compressed air as high as 0.008 - 0.009 kg per cycle through the ECV for high torque demand. For lighter loads, the flow is restricted by the advanced closing of ECV and it drops down to 0.0055 – 0.0065 kg per cycle. The rate of reduction of the air mass flow is shown in Figures 4.67 and 4.68, where it can be seen that the later is proportional to the rate of decrease of airtank pressure. As airtank pressure builds drops, the mass of compressed air transferred to the cylinder decreases because of the decreasing pressure difference between the airtank and the cylinder. It can also be seen that engine speed (and hence gas velocity which is proportional to piston speed) is too low to govern important aspects of the air flow through nozzles, orifices, valves and restrictions and thus it does not importantly affect the transferred air mass during EM. The later is not influenced by the volume of the auxiliary chamber, as it can be seen in Figures 4.67 and 4.68 that the air flow curves are identical.

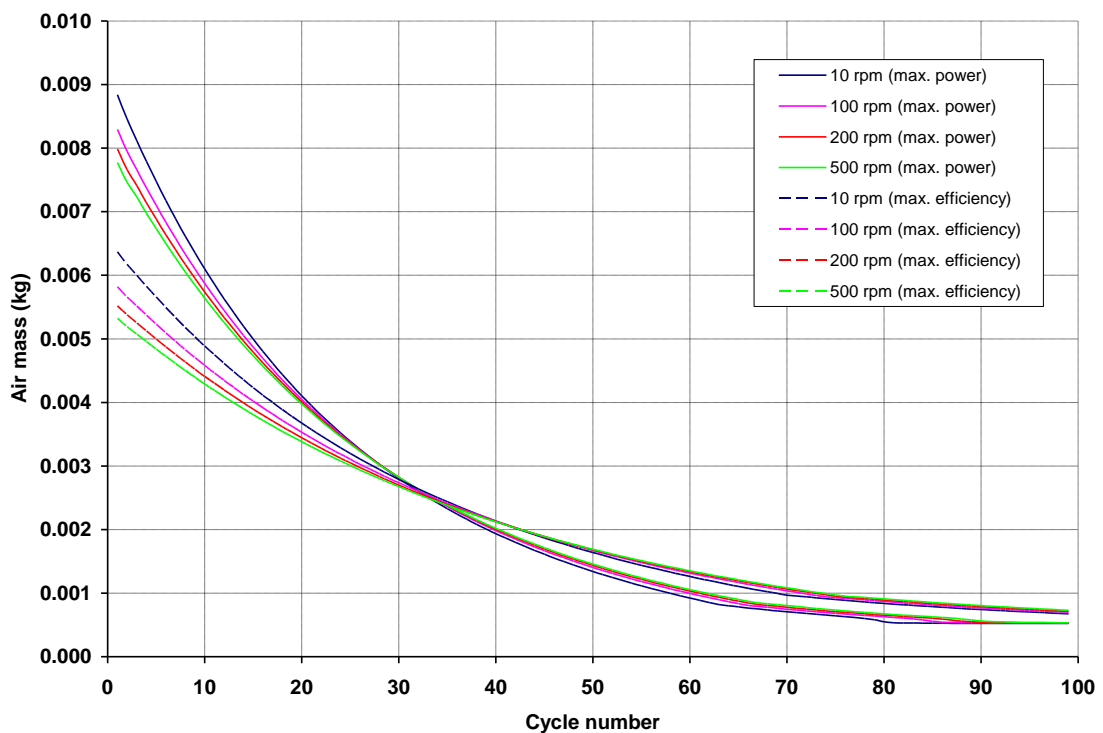


Figure 4.67: Air mass transferred from the cylinder to the airtank per cycle for auxiliary chamber volume equal to 100% of engine clearance volume (28.7 cm³).

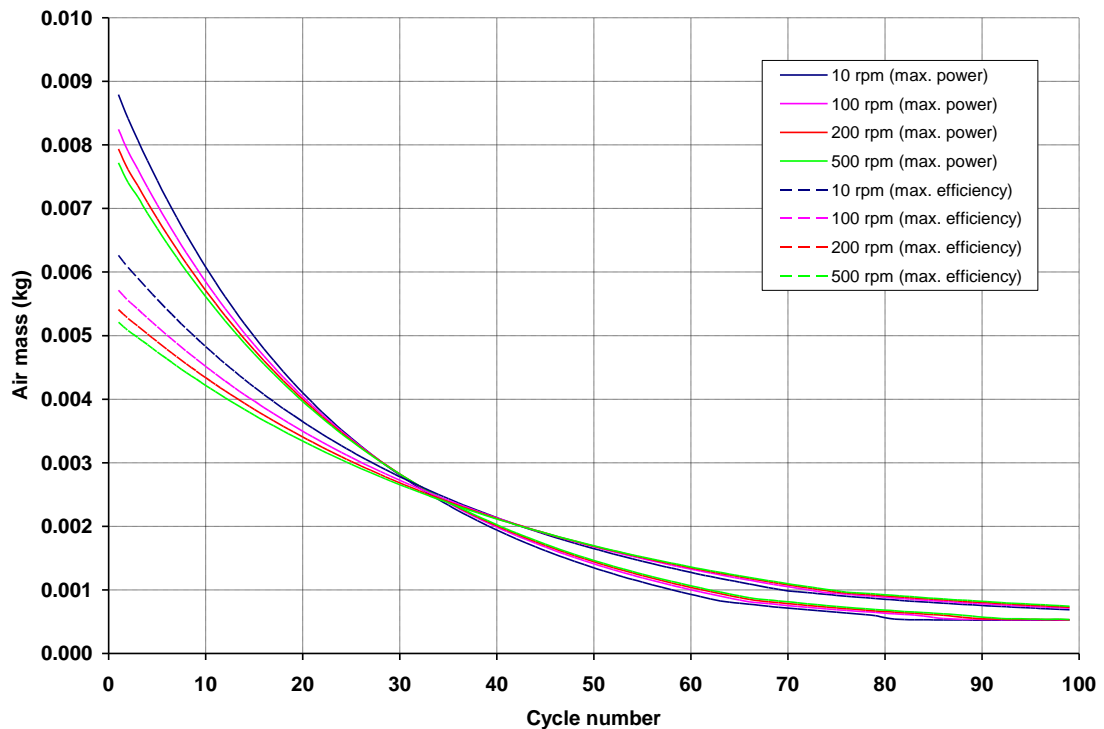


Figure 4.68: Air mass transferred from the cylinder to the airtank per cycle for auxiliary chamber volume equal to 50% of engine clearance volume (14.4 cm³).

4.5.4. Alternative actuation of intake valve 6

As discussed in Chapter 3, section 3.4.2, intake valve 6 may be actuated by a hydraulic lifter in order to be kept jam open during expansion stroke and therefore augment the performance of a hybrid engine when the later is operated as an air expander. One of the advantages of this alternative valve actuation mechanism is that the power stroke takes place during the expansion instead of the intake stroke. This allows for intake valve 5 to be operated normally, according to the conventional four-stroke cycle and eliminated the need of an additional valve deactivation system. Consequently, no modification is required to the valvetrain of intake valve 5 and therefore conventionality is enhanced. Similar to section 5.4.3, ECV timing controls the air expenditure (and thus the produced driving torque) while intake valve 6 opens towards the end of the compression stroke and closes after expansion BDC. It is obvious that the more time ECV is open the more the produced torque and the more the air expenditure. Figure 4.69 shows the predicted variation of $bmep_d$ throughout engine cycles (crankshaft revolutions) at various engine speeds. It is shown that for an initial airtank pressure of 20 bar, the engine is capable of producing approximately 13.5 bar of $bmep_d$ when high torque output is demanded (and hence a starting torque of 53.5 Nm, according to Equations 4.6 and 4.7).

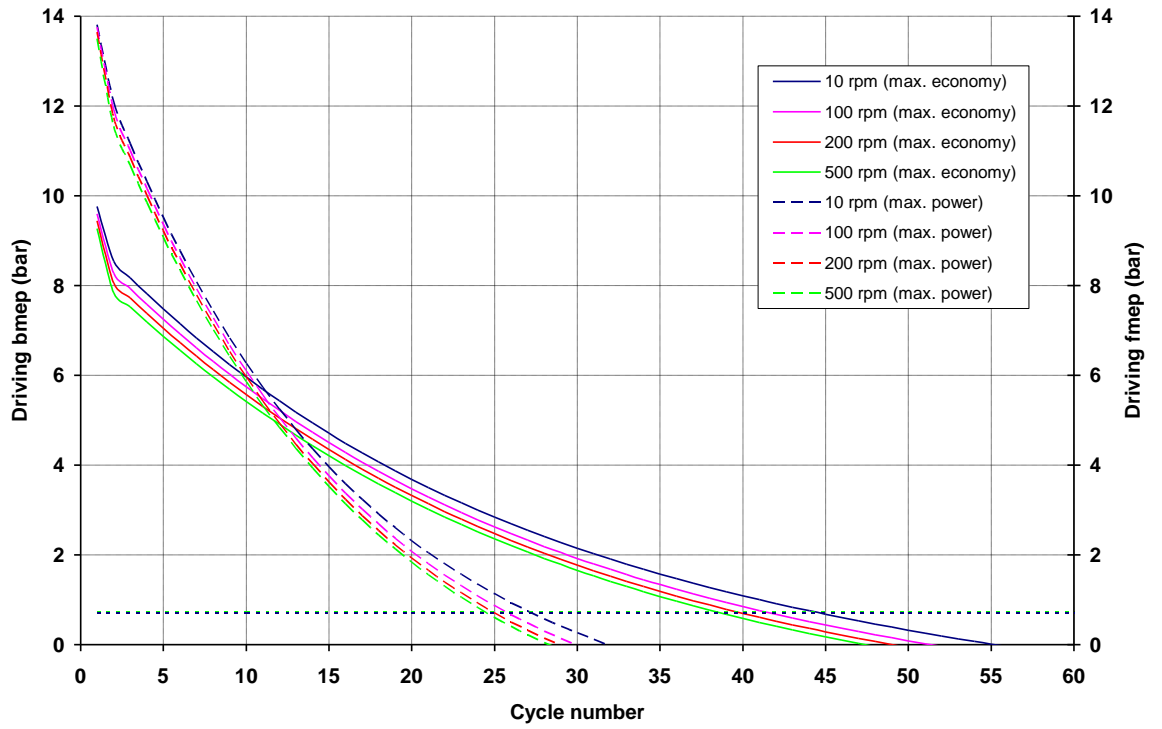


Figure 4.69: Predicted $bmep_d$ and $fmepe_d$ variation at various engine speeds, for maximum economy (solid lines) and maximum power (dashed lines).

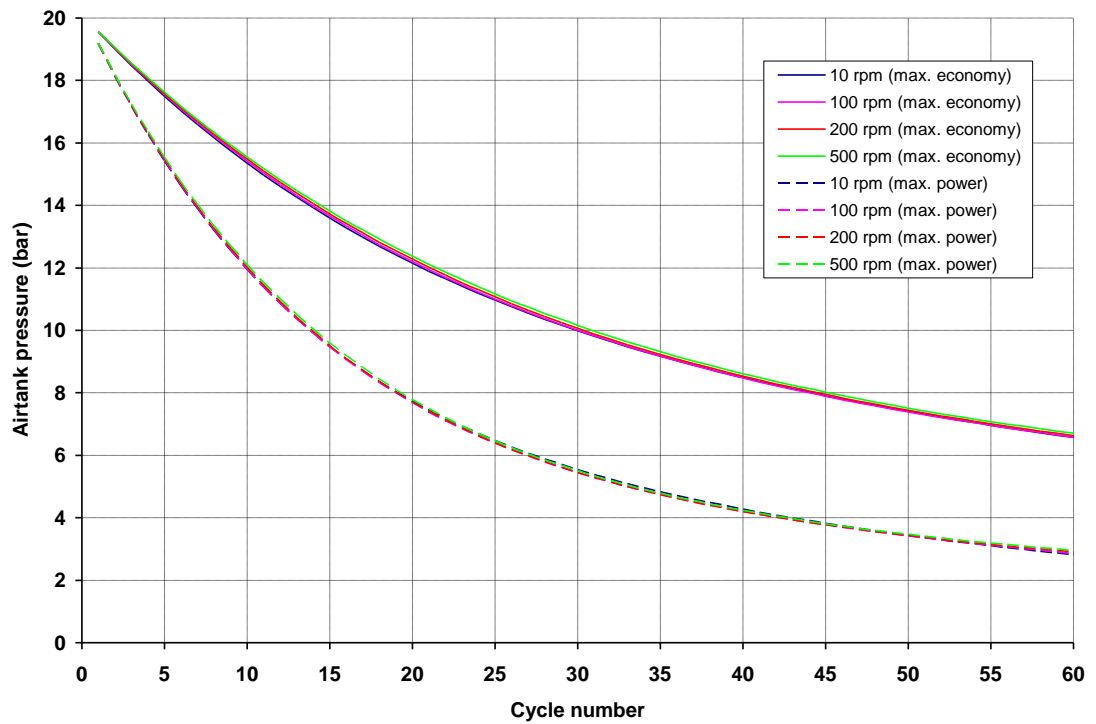


Figure 4.70: Predicted airtank pressure variation at various engine speeds, for maximum economy (solid lines) and maximum power (dashed lines).

The comparison between Figures 4.64 and 4.69 reveals that b_{mep_d} can be increased by 23% by adopting this alternative valve operation strategy, compared to the concept examined in section 4.5. However, b_{mep_d} is sustainable for only 30 engine cycles (60 crankshaft revolutions), while the model originally displayed a b_{mep_d} sustainable for 50 engine cycles (100 crankshaft revolutions). Similar to airtank pressure presented in section 4.5.3.4, minimum useable airtank pressure is 3 bar and no driving torque can be generated below that limit, as shown in Figure 4.70.

When the power demand is low, advanced closing of ECV (before EVO) can improve the compressed air expenditure. However, b_{mep_d} is decreased down to approximately 9.5 bar, resulting to a starting torque of 37.65 Nm, according to Equations 4.6 and 4.7. Again, b_{mep_d} is approximately 5% higher than in section 4.5.3.5 but less sustainable, as the comparison of Figures 4.64 and 4.69 reveals.

4.6. Summary

Three air hybrid engine concepts, which are described in Chapter 3, are modelled, analyzed and compared here. The modelling tool employed is Ricardo's Wave engine simulation software, a computer-aided engineering code specifically designed for both steady state and transient simulations, where all cycle-averaged quantities are changed from one engine cycle to the other, and can be used to model the complete IC engine.

Firstly, the optimal valve timing had to be determined by taking into account the specific features of each concept and carrying out systematic studies on various valve opening and closing events. Compromises had to be made in some cases between braking or driving torque output and compressed air economy or air transfer efficiency. After having defined the optimal valve timing for all three concepts and for CM and EM at a wide engine speed range (1000 – 4000 rpm), the effect of other operating parameters on the performance of the air hybrid engine, such as buffer (or auxiliary) chamber volume, airtank volume and pressure, etc, was examined. The intake and exhaust systems of the engine were not optimized in any systematic way and the standard, untuned intake and exhaust arrangement were used instead.

Following from the model optimization, the model was used to simulate the CM and EM for the three concepts. In contrast to the qualitative results used for optimizing various

operating parameters, the modeling results are quantitative in order to enable the comparison between the concepts and to give an actual prediction of the variation of quantities of interest, such as bmep, airtank pressure, CATC, etc. It can be concluded that the concept that uses the ERV has the major advantage over the other two concepts of producing constant and predictable braking torque, independent of the state of charge (SOC) of the energy storage tank. The later is not directly connected to the engine but it communicates with the cylinder in two stages. Braking torque in the other concepts is directly linked to airtank pressure and therefore requires a dedicated system to distribute the braking demand between engine brake and friction brake in order to improve drivability. The volume of the buffer chamber not only dictates the compression and expansion ratio but it also lowers it. As a result, maximum achievable airtank pressure is limited to 15 – 18 bar and bmep_b is limited to 2.5 – 4 bar, which is the main drawback of the concept.

The second concept, which uses a state-of-the-art FVVA system, overcomes the aforementioned disadvantages of the concept with the ERV, but it imports an extra degree of complexity. However, the extra degree of flexibility which it offers, allows for two-stroke air compressor and air expander cycles to be implemented and the highest braking and driving torque to be realized, compared to the other concepts. The airtank can be charged up to 25 bar, while the two-stroke cycle in accordance with the optimized, fully variable valve timing allows for bmep_b and bmep_d as high as the airtank pressure (25 bar).

Finally, the last concept focuses on the employment of well known and widely used technologies for camshaft shifting in conjunction with a robust reed valve placed in one of the engine intake ports. It is similar to the first concept, with the reed valve and the ECV creating a two-stage transfer valve. The operation of ECV and CPS, combined with intake valve deactivation, governs the air compressor and air expander modes, while in normal firing mode the engine operates as a conventional IC engine, with the reed valve opening to allow air flow from the atmosphere to the cylinder during intake. However, the volume of the intake port, together with the volume included by the ECV and the reed valve, is included in the engine clearance volume when the engine is operated in air compressor or air expander mode. The resulting low compression and expansion ratio leads to low maximum achievable airtank pressure, which is limited to 18 bar, as well as low bmep_b (4 – 6.5 bar). Table 4.5 below summarizes the dependency of each one of the examined variables to various engine operating parameters. Finally, Table 4.6 displays a comparison

between the three air hybrid engine concepts, in regards to the performed b_{mep_b} and b_{mep_d} .

Table 4.5: Dependency of examined variables to engine operating parameters.

Concept of engine with Energy Recovery Valve					
	valve timing	engine speed	number of cycles	airtank pressure	buffer chamber vol.
$imep_b$	*	*	*	#	#
$imep_d$	*	#	*	*	#
b_{mep_b}	*	*	*	#	#
b_{mep_d}	*	#	*	*	#
$CATC_b$	*	*	*	*	*
$CATC_d$	#	#	*	*	#
airtank pressure	*	#	*	-	#

Concept of engine with reed valve inside the intake port					
	valve timing	engine speed	number of cycles	airtank pressure	auxiliary chamber vol.
$imep_b$	*	*	*	*	#
$imep_d$	#	#	*	*	#
b_{mep_b}	*	*	*	#	#
b_{mep_d}	*	#	*	*	#
$CATC_b$	*	*	*	*	#
$CATC_d$	#	#	*	*	#
airtank pressure	*	*	*	-	#

Concept of engine with Fully Variable Valve Actuation					
	valve timing	engine speed	number of cycles	airtank pressure	<u>key</u> * high dependency # no dependency - not applicable
$imep_b$	*	*	*	*	
$imep_d$	*	#	*	*	
b_{mep_b}	*	*	*	*	
b_{mep_d}	*	#	*	*	
airtank pressure	*	*	*	-	

Table 4.6: Comparison of braking and driving performance among the three concepts.

Concept 1 (4-stroke)		Concept 2 (2-stroke)		Concept 3 (4-stroke)		Alternative to Concept 3
b_{mep_b}	b_{mep_d}	b_{mep_b}	b_{mep_d}	b_{mep_b}	b_{mep_d}	B_{mep_d}
2 - 4 bar	12 - 0 bar	5 - 26 bar	18 - 0 bar	4 - 7 bar	11 - 0 bar	14 - 0 bar
0 - 1000 cycles	0 - 55 cycles	0 - 1000 cycles	0 - 70 cycles	0 - 1000 cycles	0 - 70 cycles	0 - 55 cycles
1000 - 4000 rpm	10 - 500 rpm	1000 - 4000 rpm	10 - 500 rpm	1000 - 4000 rpm	10 - 500 rpm	10 - 500 rpm

Chapter 5: Experimental Test Facility

5.1. Introduction

The present Chapter comprises the experimental part of this Thesis. An experimental test facility was set up and commissioned so that the experimental work described in this thesis could be undertaken. The test rig consists of a base engine, a dynamometer, a data acquisition and logging system and a power pack. The engine is supplied with a specially designed cylinder head, which accommodates four electro-hydraulically actuated valves. A detailed description regarding the role and function of each component used in the present test facility is given below. The testing scenarios examined, as well as the experimental methodology followed are also described in detail in the current Chapter.

5.2. Single cylinder base engine and valve actuation system

Table 5.1: Ricardo Hydra engine characteristics

Number of cylinders	1
Bore	81 mm
Stroke	88.9 mm
Displacement volume	458.1 cm ³
Total volume	527.3 cm ³
Clearance volume	69.2 cm ³
Connecting rod length	158 mm
Compression ratio	7.5:1
Maximum permissible speed	90 rps (5400 rpm)
Valve arrangement	overhead
Intake valve count	2
Intake valve diameter	31.2 mm
Exhaust valve count	2
Exhaust valve diameter	27.5 mm
Airtank volume	11.3 litre
Airtank working pressure	20 bar

The base engine, which is a Ricardo Hydra, is shown in Figure 5.1 in its original form (before the modifications described below). The engine is of the single-cylinder, four-stroke type with a normal speed range between 660 and 5400 rpm, although the speed range of the experiments described below was between 1000 and 4000 rpm. The hardened

cast-iron cylinder liner placed inside the cylinder block has a bore of 81 mm with a Mahle flat-top piston of the corresponding diameter reciprocating in it. The crankshaft has a stroke of 88.9 mm. The aforementioned geometry gives a displacement volume of 458.1 cm³. The connecting rod has a bronze-alloy bearing at its small end to support the piston pin and it is 158 mm in length. Table 5.1 summarizes the engine test cell characteristics.

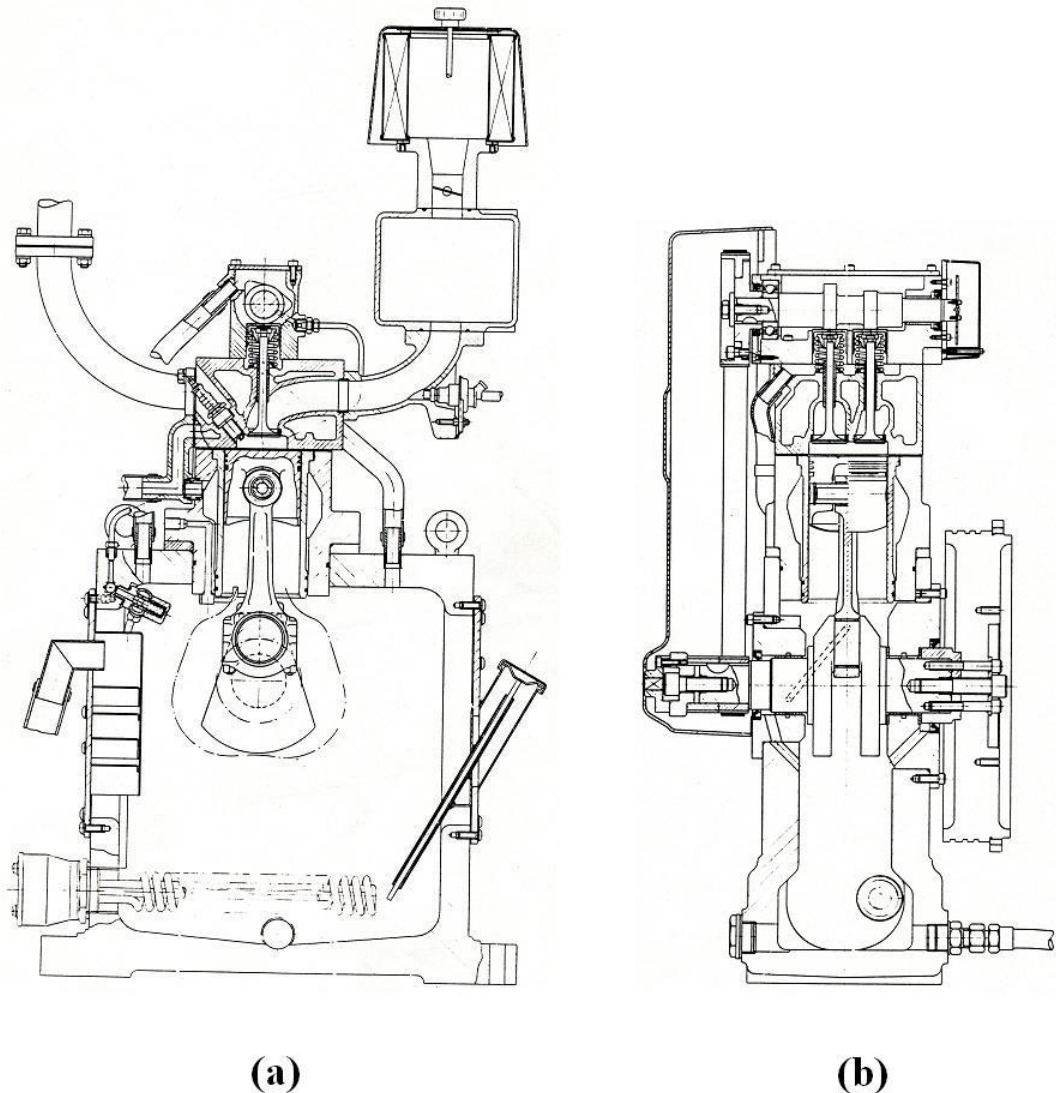


Figure 5.1: Cross section (a) and longitudinal section (b) of the Ricardo Hydra engine.

The engine is versatile for experimental purposes because the valve lift profile and timing are fully variable, which allows for two-stroke and four-stroke air expander and air compressor cycles to be realized, apart from the conventional four-stroke IC engine cycle (normal firing mode). This is achieved by means of a state-of-the-art camless valve control system which is installed on the specially designed cylinder head. This valvetrain, which is designed and manufactured by Lotus and it is called Active Valve Train (AVT), is extensively described and analyzed below. There are steel spacers on the lower face of the

cylinder in order to adjust the height of the cylinder head relative to the crankshaft and therefore vary the compression ratio of the engine.

5.2.1. Intake and exhaust systems

Air passes directly to the engine from the atmosphere through the 2-in-1 intake system made of steel pipes (shown in Figure 5.2) and it is connected to a resonator via a 2-meter rubber hose. One of the exhaust valves is used as the gas transfer valve. Beyond the exhaust ports, the exhaust gases are divided into two separate and isolated streams. The exhaust stream passes through a rubber hose connected to the exhaust port via a convenient adapter and connector. Exhaust then passes through a silencing box before released to the atmosphere. The compressed air stream passes through a metal pipe connected directly to the airtank by means of a specially designed flange to ensure sufficient air impermeability at high temperature and pressure conditions (shown in Figure 5.2). There are several features fitted to the pneumatic pipe to facilitate the measurement of compressed air pressure and temperature.

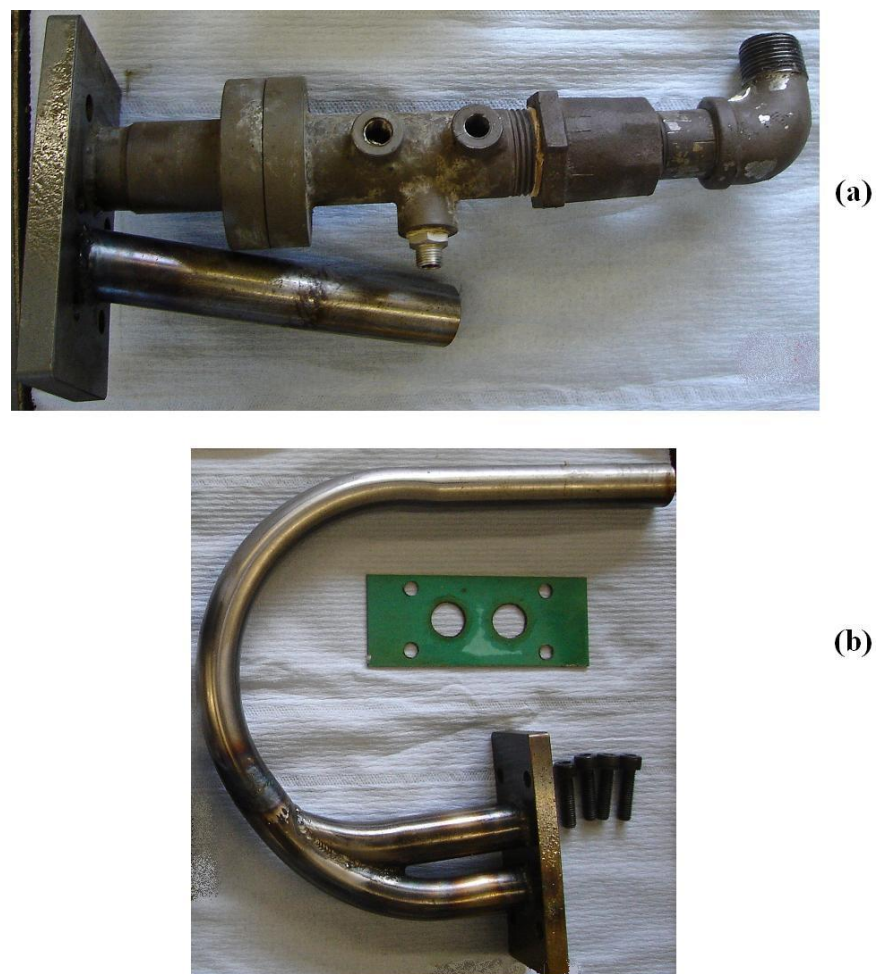


Figure 5.2: Exhaust and compressed air pipes (a) and intake pipes (b).

5.2.2. Combustion chamber geometry

The geometry of the combustion chamber is shown in Figure 5.3. It is cylindrical in shape with the ends being formed by the flat surfaces of the cylinder head, piston, and intake and exhaust valves. A 5mm aperture, which is not shown in Figure 5.3 and is situated on the side of the cylinder head, accommodates a pressure transducer which monitors the in-cylinder pressure. There is no aperture for the spark plug or diesel injector, as the cylinder head is not designed for combustion but it can only be used to operate the engine in air compressor or air expander modes. It can be seen that the distance between the piston head and the upper face of the cylinder is 3.52 mm. The thickness of the cylinder head gasket (when the later is compressed) was measured 1.46 mm and the gasket diameter is 83.74 mm.

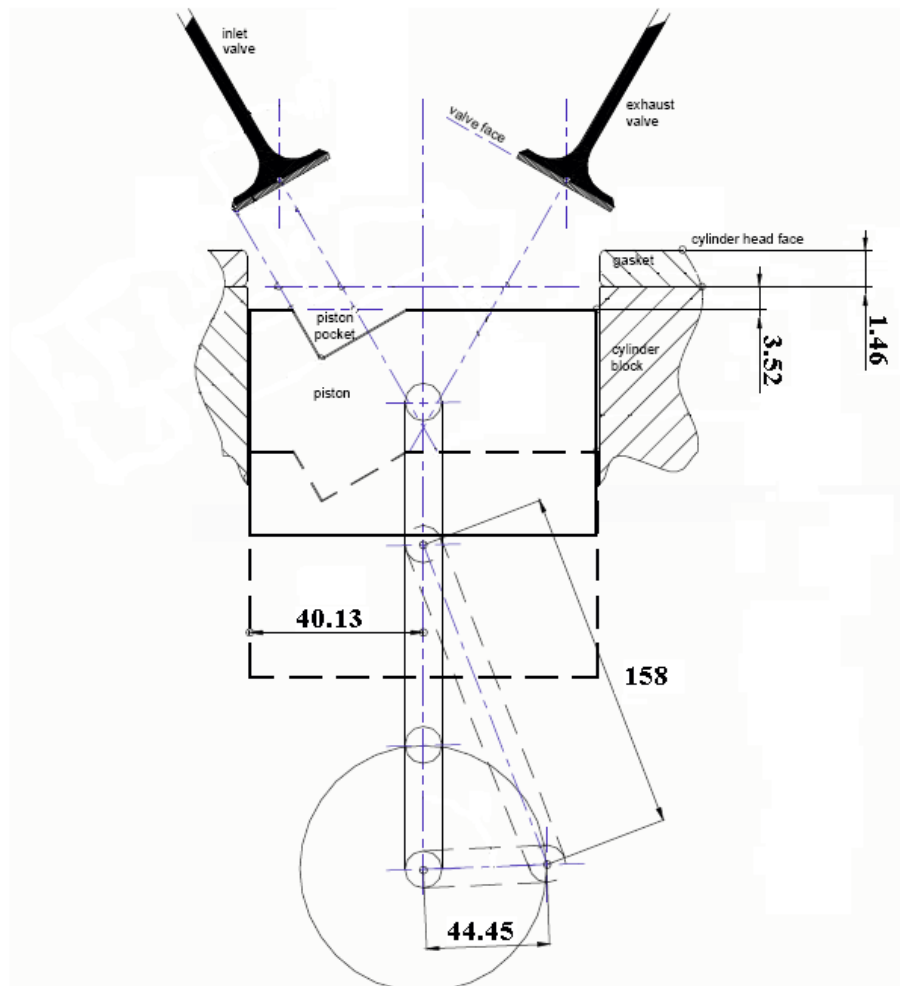


Figure 5.3: Cylinder and combustion chamber geometry.

The combustion chamber volume in the cylinder head was measured and found to be 43 cm³. The clearance volume of the engine is the volume included between the piston crown

and the combustion chamber. This therefore includes the volume enclosed between the upper face of the cylinder and the piston crown, the volume enclosed by the cylinder head gasket and the volume enclosed between the cylinder head face and the combustion chamber. Clearance volume is algebraically given by Equation 5.1. Consequently, the geometric compression ratio of the engine equals the total volume over the clearance volume and is given by Equation 5.2.

$$V_c = \frac{\pi \cdot 8.1^2 \cdot 0.352}{4} + \frac{\pi \cdot 8.374^2 \cdot 0.146}{4} + 43 = 69.2 \text{ cm}^3 \quad \text{Equation 5.1}$$

$$R_c = \frac{V_c + V_d}{V_c} = \frac{69.2 + 458.1}{69.2} = 7.62:1 \quad \text{Equation 5.2}$$

5.2.3. Airtank

A BOC cylinder, type BA, is used as a compressed air storage tank. The air bottle is 0.43 m in height and 0.27 m in diameter and it weights 9 kg when it is empty. It is made of welded steel and is intended for storage of environmentally friendly hydrocarbon refrigerants, such as Ammonia (R717) and Refrigerant grade CO₂ (R744). Welded steel cylinders are used for low pressure liquefiable gases so the maximum fill pressure is 20 bar. Maximum airtank pressures that normally occurred during the experimental work described in this Thesis do not exceed the region of 20 bar, so the rated pressure is adequate for all testing requirements. The volume of the airtank is 11.3 litre. The air container is connected to the compressed air piping by means of a ½” thread which is located on the top of the air bottle.

5.3. Dynamometer control panel and test bed

5.3.1. Test bed

The engine is mounted on a 450 kg flexibly supported cast-iron block. The suspension system under the block helps to effectively reduce the amplitude of the vertical vibratory forces excited by the engine’s rotating and reciprocating masses. It also helps to counteract torque reaction. This mounting block is attached to a rigid welded base frame by four rubber mountings which minimize the transmitted disturbance to the base frame of the test

bed. The cooling module, which was not used during the experimental work described below, is bolted on to the base frame to the rear of the engine mounting block. The remaining part of the base frame is occupied by the dynamometer assembly, whose rearing housings are supported on subframes mounted on supporting feet which stand on the base frame. An ancillary pillar is also mounted in front of the engine mounting block, on the top face of the base frame. It accommodates an emergency stop button as well as components of the spark ignition system and thermocouple plug blocks which were not used during the experimental work undertaken.

5.3.2. Dynamometer

The dynamometer is an electrical shunt wound type DC machine with separate excitation, manufactured by McClure. It is rated at 400 V, 70 A and 30 kW continuous absorbing. The maximum permissible rotational speed of the dynamometer rotor is 6000 rpm. The later is mounted on trunnion bearings which are supported by pedestals. The unit is force ventilated by an electrically driven fan attached on the base frame adjacent to the dynamometer. The dynamometer carries two torque arms, each of which has a weight that can be adjusted in its slotted mounting hole in order to achieve static balance. The right-hand torque arm, as viewed from the engine, is connected through a load limiting device to a 20 kg load cell mounted on a stand from the baseplate. The electrical signal from the load cell provides a continuous display of torque at the dynamometer control panel. Since the dynamometer can both brake and motor the engine, a weight hanger is provided on each torque arm so that the load cell can be calibrated for both clockwise and anti-clockwise torque reaction. The effective torque arm radius is fixed at 407.8 mm so that a calibration mass of 12 kg represents a torque of 48 Nm. The load limiting device contains a helical coil compression spring which is pre-compressed such that the device will extend or compress at a predetermined load, allowing the torque arm to contact the adjustable stop screws without overloading the load cell. However, the driving or braking torque output is not directly obtained from the control panel instruments but it is calculated through the engine indicator diagram.

The dynamometer is operated through a KTK thyristor converter unit so that it can act as an electrical DC motor to drive the engine during starting and driving operations (when the engine is operated as an air compressor) or as a DC generator during braking operations (when the engine is operated as an air expander). During engine braking, the DC power from the dynamometer is converted to 3-phase AC power by the converter unit and fed

back into the mains supply. A tachogenerator is mounted on the dynamometer shaft in order to provide a speed signal to the closed loop speed control system so that the speed selected by the user at the control panel is maintained by automatic adjustments to the driving or braking torque.

5.3.3. Control panel

The control panel is a free standing cubicle which houses the torque, speed and ignition/injection rack, the automatic control unit rack, the remote control rack and the power supply unit. Access is provided at the rear of the console by a lockable door. The control panel is shown in Figure 5.4. The range of the analogue and digital torque indicators is between 0 and 50 Nm. The digital indicator also displays the “+” prefix when the engine drives the dynamometer, or the “-“ prefix when the dynamometer drives the engine. The analogue and digital torque indicators have a range of 0 – 120 rps (0 – 7200 rpm). The last instrument in the torque, speed and ignition/injection rack is can be switched between ignition advance timing indicator (70° BTDC to 20° ATDC) and static fuel injection timing (TDC to 40° BTDC). The last instrument was not used during the experimental work described below, as the engine was operated only in air compressor and air expander modes and not in normal firing mode.

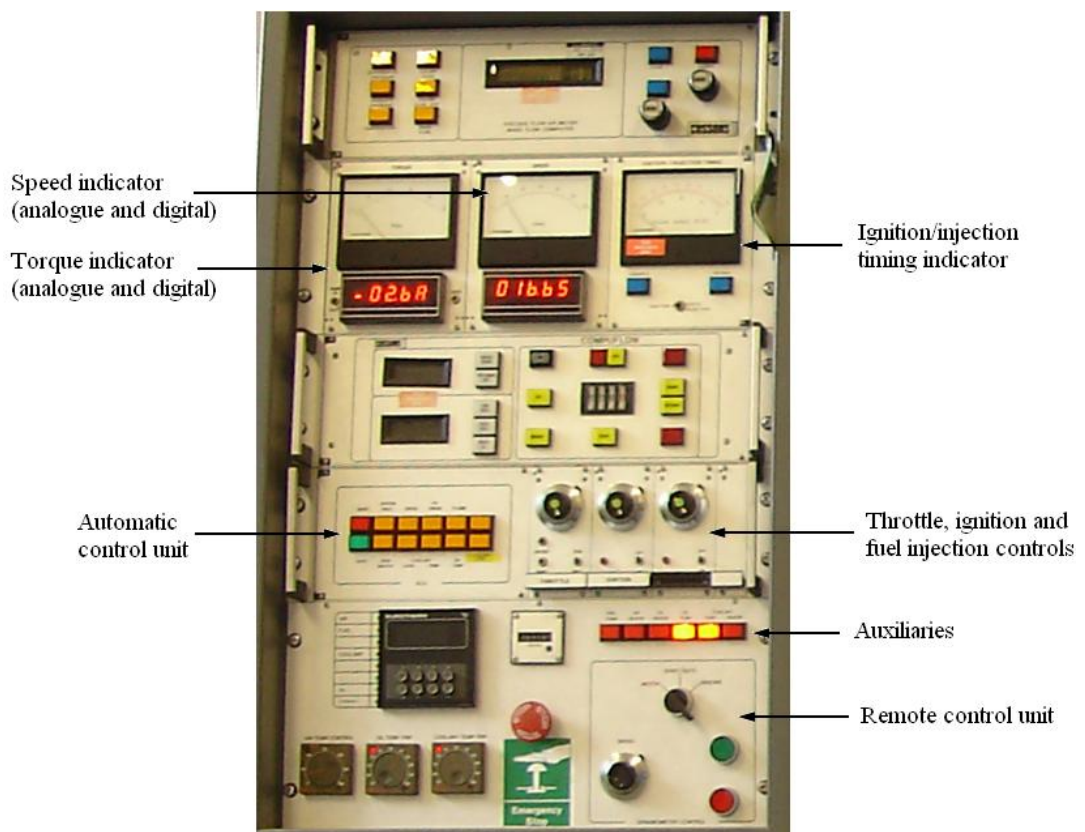


Figure 5.4: Control panel.

The automatic control unit is a safety trip system designed to protect the equipment and/or the operator. The cluster monitors several operating parameters, including a general system fault trip which is triggered when a dynamometer fault occur, a speed trip which is triggered when engine speed drops below 720 rpm or rise above 5520 rpm, an oil pressure trigger which is triggered when oil pressure drops below 15 psi (1.05 bar), etc. Finally, the remote control rack includes the dynamometer controls and it is used to switch the dynamometer between absorb, motor and start/auto modes. The dynamometer only absorbs power in absorb mode. The set speed is not maintained if engine power output is below pumping and friction losses. The dynamometer only motors the engine in motor mode, while fueling is inhibited. In start/auto mode, the dynamometer automatically changes from motor to brake mode to maintain the required speed setting, which can be adjusted by a multi turn dial.

5.4. Lotus AVT system

The Active Valve Train (AVT) system is an electronically controlled, hydraulically operated system that facilitates control of individual valve lift profiles. Lotus has produced this system as a research and development tool over the past ten years. It allows the user to specify the desired valve lift profiles via a PC based software and without the need to change the intake and exhaust camshafts physically. The AVT system does not use camshafts. It consists of several components, described in detail below, which were installed on the aforementioned Ricardo Hydra test single cylinder engine.

5.4.1. Cylinder head

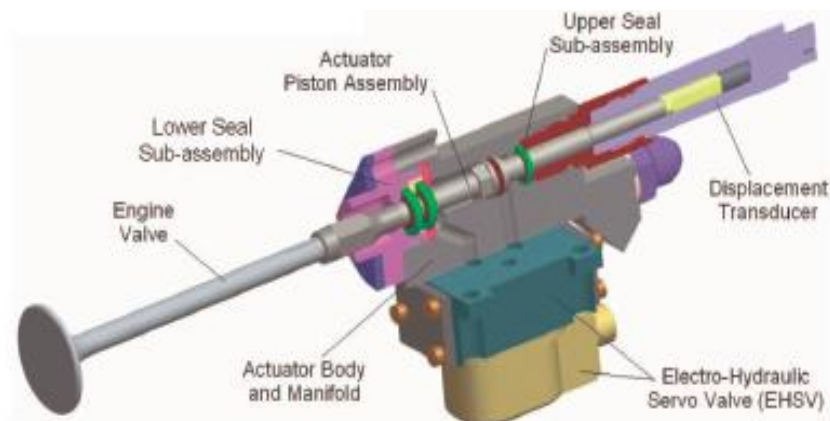


Figure 5.5: Engine valve, EHSV and displacement transducer assembly [78].

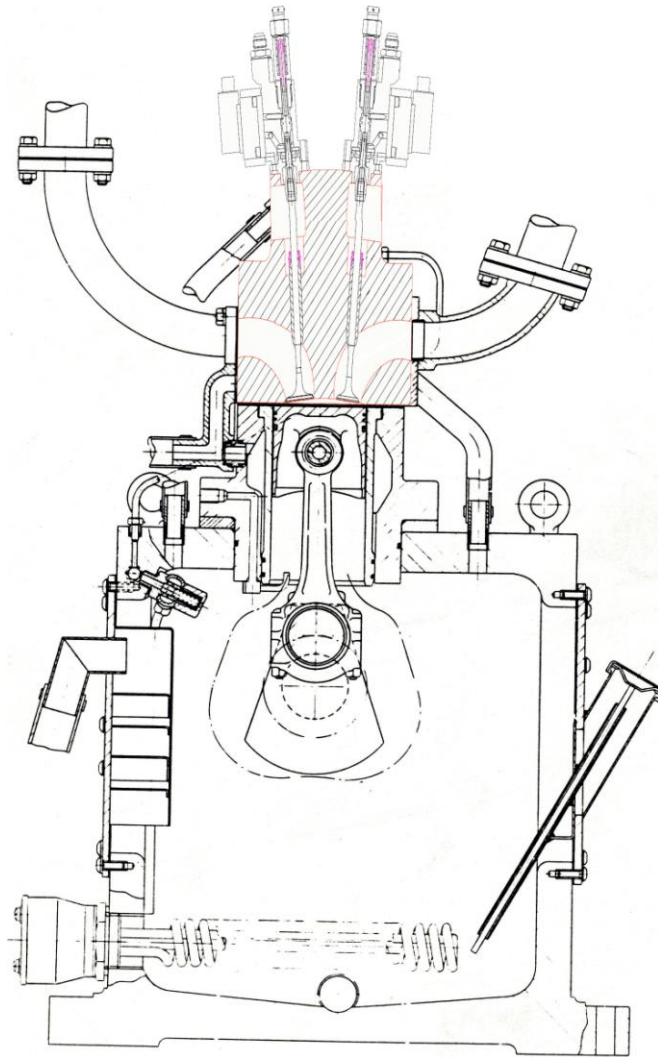


Figure 5.6: Cross section of the Ricardo Hydra engine with the AVT cylinder head installed on it.

The standard Ricardo Hydra cylinder head was replaced by an aluminium-alloy cylinder head which houses four poppet valves and it is manufactured by Lotus. The cylinder head is mounted on the cylinder block by means of four M12 allen bolts. The standard Ricardo head gasket was used. Four double-acting hydraulic actuators – one for each valve - are fixed on the cylinder head. A hydraulic piston, located coaxial to each actuator, is mounted directly on the top of the otherwise standard engine valve by means of a M7 fine thread coupling. A fast-response, variable inductor, non-contact, shock-resistant displacement transducer is connected to the top of each piston, enabling the poppet valve position to be monitored with high accuracy. The displacement transducer provides a voltage output that is proportional to the valve displacement and it is the only electrical part of the system that requires regular calibration (zeroing) through the user interface software.

The proportional control electro-hydraulic servo valves (EHSV), manufactured by Moog Controls Ltd., actuate the poppet valves in the engine. They are electromagnetic devices with internal arrangements which permit hydraulic fluid to be proportioned to either end of the valve's shuttle. The movement of the shuttle can be controlled accurately and therefore the mass of a component such as the engine poppet valve can be operated very rapidly, providing that sufficient hydraulic pressure is available. Figure 5.5 shows the engine valve, EHSV and displacement transducer assembly, while Figure 5.6 illustrates the cylinder head installed on the otherwise standard Ricardo hydra engine.

5.4.2. Hydraulic Power Pack (HPP)

A remote Hydraulic Power Pack (HPP) supplies hydraulic fluid at high pressure and high flow rate to EHSV via two high-pressure rubber hoses – one pressure (P) hose and one return (R) hose. The HPP is powered by a 3-phase star/delta electric 30 kW motor which drives a variable displacement hydraulic pump. Hydraulic oil is stored in a 200-litre reservoir which is mounted on the frame of the HPP. In order to prevent the hydraulic oil from overheating, a liquid-to-liquid, mains-water fed heat exchanger is used.



Figure 5.7: Hydraulic Power Pack (HPP).

There is a mechanical pressure relief valve which is set so that the hydraulic pump only gives the maximum system pressure. An electronically controlled pressure relief valve is also present in order to regulate the working pressure specified by the operator. Finally, a 3 micron non-bypass filter is fitted to each one of the pressure and return lines in order to capture the harmful debris and foreign bodies which may be introduced inadvertently during assembly or servicing and maintenance procedures contained in the hydraulic oil

and can easily damage and reduce the working life of the AVT seals and the EHSVs. Figure 5.7 shows the HPP arrangement.

5.4.3. User interface software

The control parameters of the system are accessed via a user interface software implemented in a personal computer (PC) that communicates with the Lotus AVT controller. The controller uses a closed loop feedback system coupled with a slower adaptive phase correction control strategy to detect and correct automatically the actual displacement towards achieving the desired displacement. The software, which is developed by Lotus, allows the user to download the control parameters of the system, such as valve lift profiles, profile offsets, hydraulic oil working pressure, etc, as well as calibrations and permissible performance limits to the controller. It is possible to vary the opening point and closing point of a valve lift profile in increments of one degree of crank angle. The maximum lift is adjustable to any valid figure between 0.01mm and the maximum travel of the actuator piston. Each valve is controlled individually. The software is also capable of accessing and displaying data from the system transducers by using the AVT graphical user interface, which is effectively a front end to the Matlab control system design software.

5.4.4. Uninterruptible Power Supply (UPS)

The UPS is used to supply AC mains to the PC and to the linear power supply that provides DC power to the AVT controller. It is intended to maintain the operation of the system in the event of an AC mains failure for long enough to allow the system to be shut down safely and in a controlled manner. It also provides the PC and the AVT controller with isolation from mains-borne interference and voltage spikes.

5.4.5. AVT controller

The AVT controller, shown in Figure 5.8, is the heart of the system and distributes power to the sensors and transducers that require it. It is a dual Texas TMS320C32 32 bit processor operating at 15 Mhz. Among its numerous functions, it monitors the hydraulic pressure and the position of each individual valve, it controls the pressure output by the HPP and it can shut the system down if a system malfunction is detected. Essentially, the controller performs a closed loop Proportional- Integral-Differential (PID) control of the valve lift versus crank angle. It is capable of storing up to 256 valve profile arrays in flash

memory which can be applied to individual valves. Figure 5.9 shows a simplified schematic diagram of the Lotus AVT system.



Figure 5.8: Lotus AVT controller.

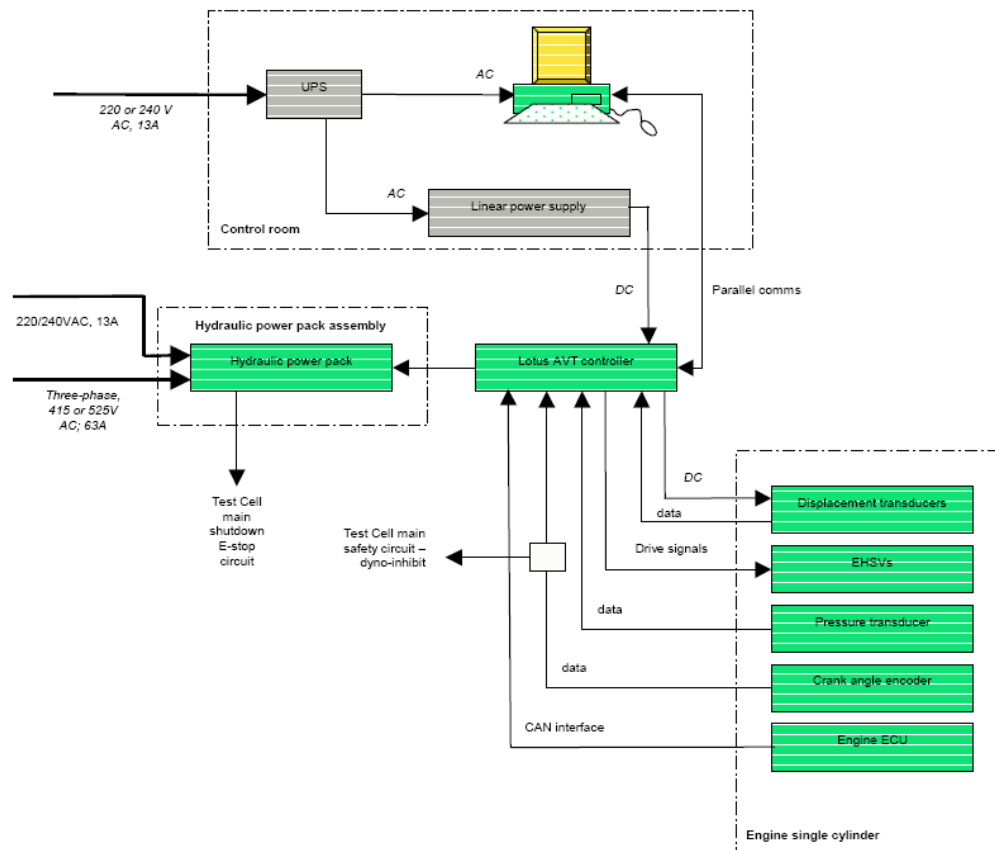


Figure 5.9: Lotus AVT system schematic diagram [78].

5.4.6. Crankshaft encoder

The incremental shaft encoder is attached to the end of the engine crankshaft and provides a TTL level pulse output signal of 360 pulses per revolution (ppr) for crankshaft angle resolution, as well as a separate 1 ppr signal (trigger) of the crankshaft at the TDC position of the piston. The shaft encoder, type RSI 503, is an optical angle encoder manufactured by Leine and Linde AB. The crankshaft encoder signal is read by the AVT controller in order to calculate the crank position, which in turn sends the appropriate driving signal through the digital-to-analogue converter (DAC) to the servo valve.

5.4.7. Hydraulic fluid

The hydraulic fluid used in the Lotus AVT system is Castrol's Brayco Micronic 882. It is a red-coloured, synthetic hydrocarbon based, fire resistant hydraulic fluid developed for aircraft, ordnance and industrial use. Unlike conventional hydraulic fluids, it is not subject to polymer breakdown under high shear conditions and it has high flash and fire points, low propagation and an exceptionally high auto ignition point, according to its manufacturer's specifications. Its properties also include controlled rubber swell for long seal life, low foaming, excellent anti-wear and good corrosion and oxidation stability. Brayco Micronic 882 hydraulic fluid is designed to operate in the -45 to +204 °C temperature range. When used in the Lotus AVT system, the recommended operating temperature of the fluid when measured at the HPP bulk tank temperature should be between +30 and +50 °C [78].

5.5. Pressure and temperature measurement instrumentation

5.5.1. Compressed air temperature measurement

An RS thermocouple temperature sensor, type K, was located on the pipe connecting the exhaust port to the airtank and used for sensing the temperature of the air charge entering the airtank. The thermocouple consists of two dissimilar conductors; Nickel-Chromium (Ni-Cr) for the positive leg and Nickel-Aluminium (Ni-Al) for the negative leg. The temperature range for the thermocouple is between 0 and 1100 °C. The output voltage of the thermocouple is fed to a Digitron TM-22 industrial differential digital thermometer

with cold junction compensation function which is used to monitor the compressed air temperature by means of an LCD display.

5.5.2. In-cylinder pressure measurement

A Kistler piezoelectric pressure transducer type 7061 is mounted in the side of the cylinder head via an access hole and it is used for monitoring and tracing real time in-cylinder pressure. The transducer output, measured in electrical charge units (picocoulombs – pC), is proportional to the force acting on the transducer's quartz crystals and thus to the cylinder pressure. In spite of the fact that changes in temperature affect the transducer output by varying the resonant frequency of the quartz crystals and by causing expansion or contraction to the transducer diaphragm and housing, Kistler claims that the sensitivity remains largely constant for temperatures between –50 and 350 °C [79]. Although the transducer could be water-cooled, no water cooling lines were connected on it as the temperatures realized during the experiments were much lower because the engine was only used for driving and braking, as an air expander and compressor respectively, and thus no combustion took place inside the engine cylinder.

A Kistler charge amplifier type 5011 is used to convert the electrical charge yielded by the piezoelectric sensor to a voltage signal. A low-pass filter in the charge amplifier with 300 kHz cut off frequency is used to filter out the high frequency noise. A long time constant is selected according to Lancaster et al, who note that charge amplifier time constants should be set to give the longest system time with minimal signal drift [80]. The time constant of a piezoelectric system is a measure of the time for a given signal to decay, not the time it takes the system to respond to an input. The transducer's sensitivity (pC/bar) is inputted to the charge amplifier as appears in the calibration sheet provided by Kistler for the specific transducer. Finally, the output sensitivity (bar/V) is calibrated such that the numerical voltage output from the amplifier corresponds to a predetermined cylinder pressure level. The inputted value of 10 bar/V is verified together with the linearity of the transducer by means of an oil-filled dead weight tester and an oscilloscope; known pressures are applied to the transducer and in the meantime the charge amplifier output voltage is adjusted so that it corresponds to 10 bar/V, over a range of 10 V (100 bar). Maximum in-cylinder pressures that normally occurred during the experimental work do not exceed the region of 20 bar, so the calibrated range is adequate for all testing requirements.

Piezoelectric pressure transducers produce a charge relative to change in pressure levels and therefore a method is required to peg recorded pressure data to absolute levels. The charge amplifier output, E , is in volts. The relationship between the output voltage and the actual pressure is defined at any crank angle θ by Equation 5.3:

$$E(\theta) = \frac{p(\theta)}{C} + E_b \quad \text{Equation 5.3}$$

Where E_b is the bias voltage with zero pressure and C (bar/V) is the gain (calibration) factor of the system [81]. Randolf describes a number of methods for pegging absolute cylinder pressures. The two main types of pegging described are setting a point within the engine cycle to a known or estimated pressure and fitting the compression to a polytropic process [82,83]. The method used here, which is the most often used one and it is a very accurate procedure in untuned intake systems or at low speeds at tuned systems, is referencing at inlet BDC (IBDC), which involves setting the cylinder pressure at IBDC equal to manifold absolute pressure (map). The absolute pressure can then be determined from the output voltage at any crank angle according to Equation 5.4:

$$p = C \cdot (E - E_{IBDC}) + p_{IBDC} \quad \text{Equation 5.4}$$

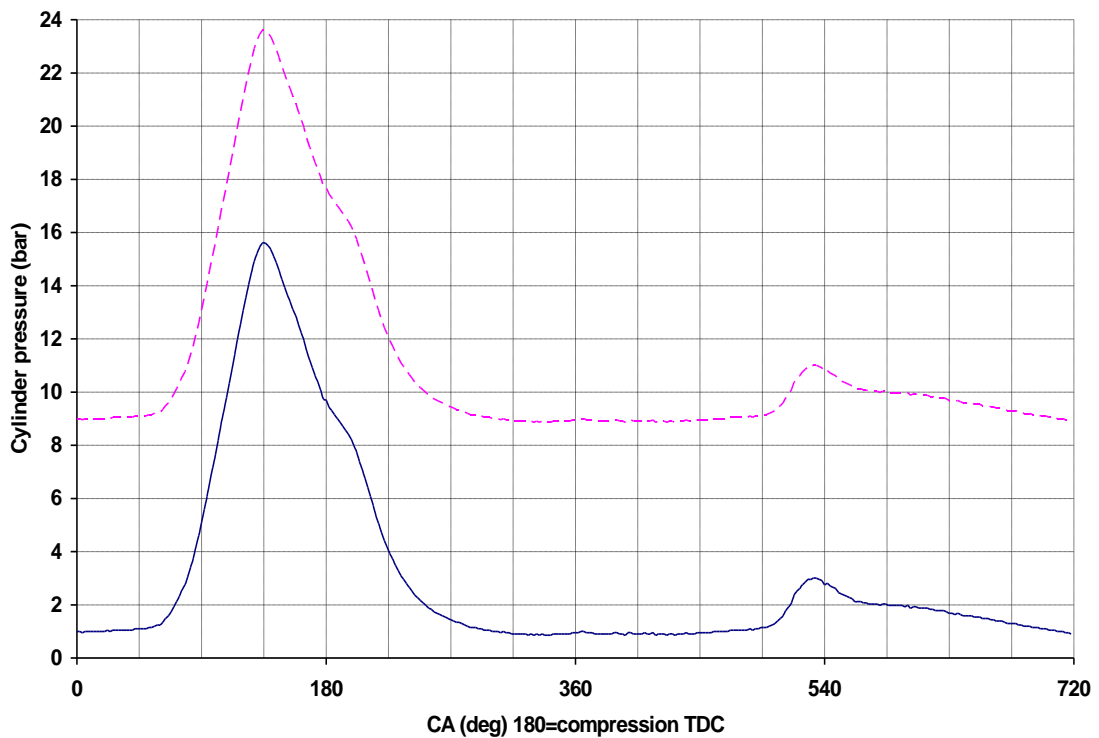


Figure 5.11: Cylinder pressure diagram before pegging (dashed magenta line) and after pegging (solid blue line).

Randolf also notes that determination of IMEP, variability in IMEP, PMEP, maximum rate of pressure rise and location of peak pressure do not require pegged data. It is only absolute metrics, such as peak pressure, that require pegged data. Figure 5.10 shows a typical cylinder pressure reading before and after pegging.

As mentioned before, the transducer output is very small (within the range of pC) and it is therefore important that all connections between the charge amplifier and transducer be degreased with contact cleaner. This is because low insulation resistance in the transducer or cables and connection causes drift of the charge amplifier output. It is also mandatory to use a highly-insulating, low-noise coaxial cable to connect the pressure transducer to the charge amplifier.

5.5.3. Airtank pressure measurement

A Kistler piezoresistive pressure transducer type 4045A50 is used for monitoring and tracing compressed air pressure inside the storage tank. A silicon measuring cell with pressure-sensitive resistors diffused in and interconnected to form a fully active Wheatstone bridge is used as the sensing element [84]. The effective pressure measuring range is 0 – 50 bar absolute pressure.

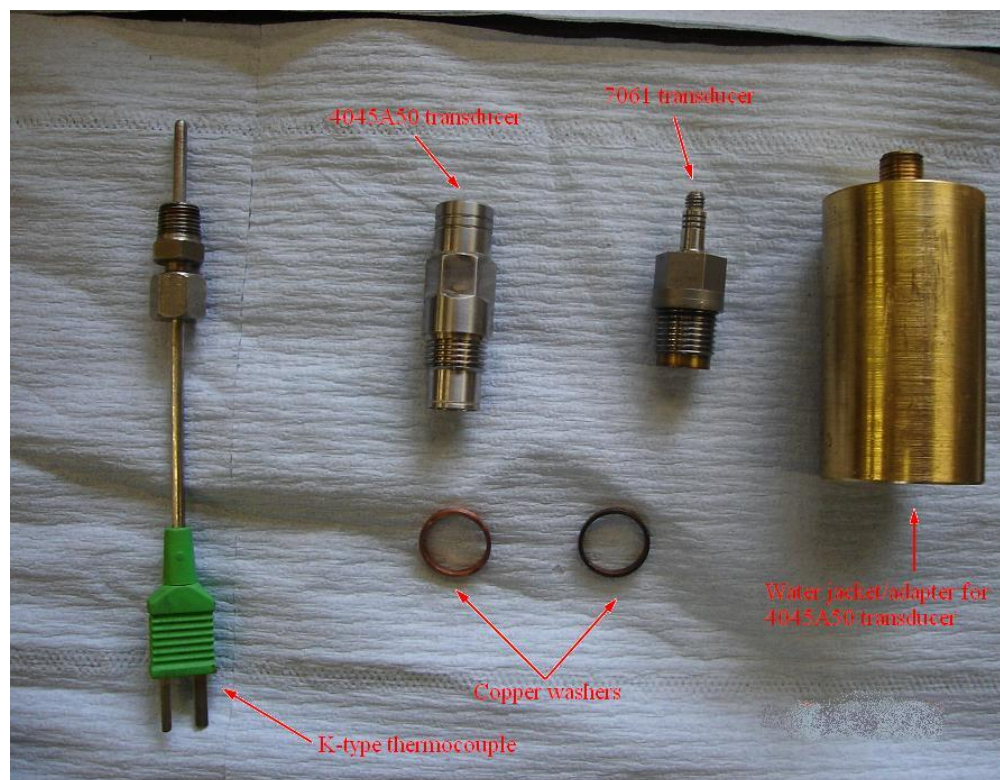


Figure 5.11: From left to right; Thermocouple, airtank pressure transducer, cylinder pressure transducer and water jacket/adaptor.

Providing that maximum airtank pressures that normally occurred during the experimental work do not exceed the region of 20 bar, the sensing range is adequate for all testing requirements. The working temperature range of the piezoresistive transducers is generally narrower than that of the piezoelectric pressure transducers, as the resistance of the Wheatstone bridge is influenced by extreme temperature conditions. Therefore, the temperature range of the 4045A50 transducer is between 20 and 120 °C. In order to maintain the above temperature limits, a specially designed adapter is manufactured in order to mount the pressure transducer onto the metal pipe connecting the cylinder to the airtank. The adapter is made of bronze for better thermal conductivity and it is machined in such a way that it incorporates a water jacket, shown in Figure 5.11, in order to sufficiently absorb and reject the heat. Finally, a Kistler voltage amplifier type 4618A0 was used to convert the low-voltage signals to a level suitable for the recording by the data acquisition system. The amplifier was powered by a RS 18 - 30V, 250mA adjustable voltage power source.

5.5.4. Data acquisition (DAQ) system

The data acquisition system operates as a real-time displaying, measuring, and logging device for both the in-cylinder and airtank pressure readings. It comprises a National Instruments' PCI data acquisition card type AT-MIO-16E-1 with a 68-pin connector block type CB-68LP installed in a PC and it is operated with the National Instruments Labview software from which real-time data analysis software can be developed for specific data acquisition requirements. As shown in Figure 5.12, sampling of both charge and voltage amplifier outputs is controlled by the crank angle signal from the aforementioned encoder attached to the end of the engine crankshaft. Therefore, four input signals are required for correct operation: the charge amplifier output, the voltage amplifier output, the clock signal (360 ppr), and the trigger signal (1 ppr). The clock and trigger signals are required by the DAQ system so that both pressure outputs can be sampled at regular intervals and its phasing relative to the four-stroke cycle can be established. The clock and trigger signals are transferred to the DAQ system via an electronic interface in the computer.

There are four charts on the main screen that are updated in real-time on a cyclic basis during the data acquisition process, as the airtank and cylinder pressure signals are sampled. The first chart shows the in-cylinder pressure (P_c) versus crank angle. Using the trigger signal, the software displays the full engine cycle with TDC on the compression stroke phased so that it occupies the centre of the chart. The next chart shows the indicator

diagram (i.e. cylinder pressure versus cylinder volume). Cylinder volume is calculated directly from the clock signal by the means of Equations 5.5 and 5.6 [85]:

$$V = V_c + \frac{\pi \cdot D^2}{4} \cdot (l + a - s) \quad \text{Equation 5.5}$$

$$s = a \cdot \cos\theta + \sqrt{(l^2 - a^2 \sin^2 \theta)} \quad \text{Equation 5.6}$$

where V_c is the clearance volume, D is the cylinder bore diameter, l is the connecting rod length, a is the crank radius, s is the distance between the crank axis and the piston pin axis, θ is the crank angle.

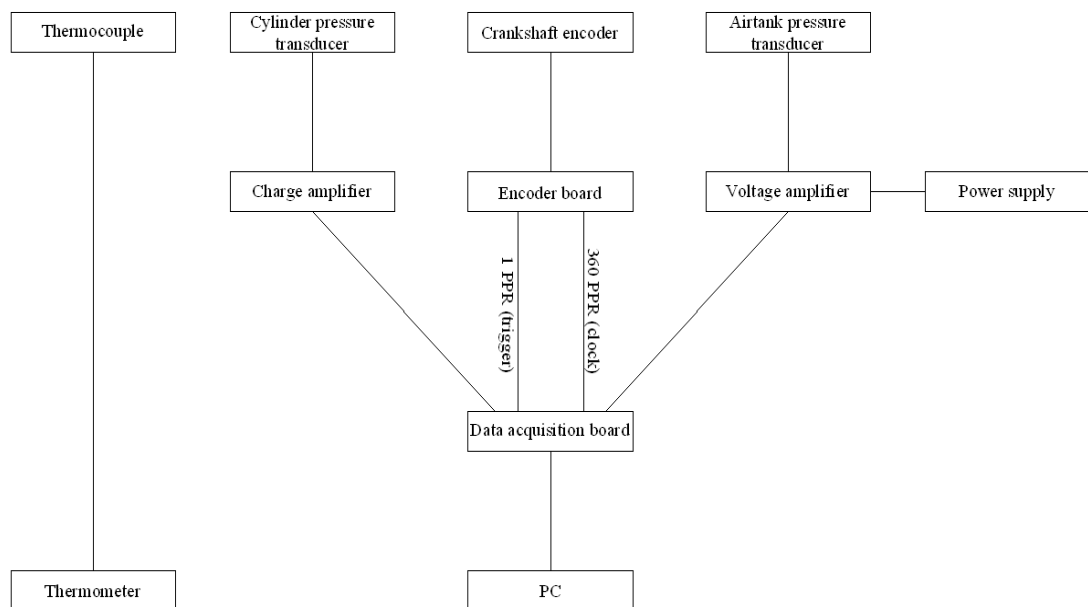


Figure 5.12: Schematic diagram of the data acquisition system.

The program is capable of recording all of the outputs described above in tabular form. In theory, the number of successive cycles that can be recorded is unlimited. However, computing power, memory resources, buffer size and data storage capacity limit the practical operation. Tests have proved that the storage of 1000 cycles takes approximately 15 - 60 seconds, depending on the engine speed and pressure sampling frequency. The size of the output files amount to 2 MB for pressure sampling at every 1 °CA. Storage in an ASCII format allows quick data access and manipulation by employing packages such as Corel Quattro Pro.

5.6. Experimental work

The experimental work undertaken can be divided into three discrete test cases, where imep and airtank pressure variations were examined for a number of cycles and for various valve timings and engine speeds:

1. Four-stroke air compressor (braking) mode. The non-firing engine is motored by the dynamometer while it is operated according to the conventional four-stroke cycle with dual intake and single exhaust valves of conventional lift profiles and a single gas transfer valve of trapezoidal lift profile.
2. Two-stroke air compressor (braking) mode. The non-firing engine is motored by the dynamometer while it is operated according to the two-stroke cycle described by Turner et al [64,65] with dual intake and single gas transfer valves of trapezoidal lift profile. The single exhaust valve is deactivated.
3. Four-stroke air expander (driving) mode. The dynamometer brakes the non-firing engine while later is operated according to the conventional four-stroke cycle with dual intake and single exhaust valves of conventional lift profiles and a single gas transfer valve of trapezoidal lift profile.

In test cases 1 and 2 the engine speed range is between 1000 and 4000 rpm at intervals of 500 rpm. Engine speed for test case 3 is 1000 rpm. Valve timing step is 5°CA. To this end, all other engine variables are fixed to the values shown in Table 5.1. The measured or dependant variables (airtank pressure, in-cylinder pressure, compressed air temperature) can be either time-averaged or cycle-averaged and are obtained during testing using the DAQ system and the thermometer. Thus, each measured variable forms a surface over the two-dimensional engine speed and valve timing range. One of the objectives of these tests is to define the two-dimensional region in which the air compressor or air expander can be efficiently operated. The range of the independent variables (engine speed and valve opening and closing points) are summarized in Table 5.2.

Table 5.2: Values of independent variables used for each test case.

Test case 1	1000 rpm	1500 rpm	2000 rpm	2500 rpm	3000 rpm	3500 rpm	4000 rpm
GVO @ 15° BIVC	GVC @ TDC						
GVO @ 10° BIVC							
GVO @ 5° BIVC							
GVO @ IVC							
GVO @ 15° BIVC	GVC @ 5° ATDC						
GVO @ 10° BIVC							
GVO @ 5° BIVC							
GVO @ IVC							
GVO @ 15° BIVC	GVC @ 10° ATDC						
GVO @ 10° BIVC							
GVO @ 5° BIVC							
GVO @ IVC							
GVO @ 15° BIVC	GVC @ 15° ATDC						
GVO @ 10° BIVC							
GVO @ 5° BIVC							
GVO @ IVC							

Test case 2	1000 rpm	1500 rpm	2000 rpm	2500 rpm	3000 rpm	3500 rpm	4000 rpm
GVO @ 15° BTDC	IVC @ 15° BTDC						
GVO @ 15° BTDC	IVC @ 10° BTDC						
GVO @ 10° BTDC							
GVO @ 15° BTDC	IVC @ 5° BTDC						
GVO @ 10° BTDC							
GVO @ 5° BTDC							
GVO @ 10° BTDC	IVC @ TDC						
GVO @ 5° BTDC							
GVO @ TDC							
GVO @ 5° BTDC	IVC @ 5° ATDC						
GVO @ TDC							
GVO @ 5° ATDC							
GVO @ TDC	IVC @ 10° ATDC						
GVO @ 5° ATDC							
GVO @ 10° ATDC							
GVO @ 5° ATDC	IVC @ 15° ATDC						
GVO @ 10° ATDC							
GVO @ 15° ATDC							

Test case 3	1000 rpm
GVO @ 10° BTDC	GVC @ 10° BEVO
GVO @ 10° BTDC	GVC @ 5° BEVO
GVO @ 5° BTDC	
GVO @ 10° BTDC	GVC @ EVO
GVO @ 5° BTDC	
GVO @ TDC	
GVO @ 5° BTDC	GVC @ 5° AEVO
GVO @ TDC	
GVO @ 5° ATDC	
GVO @ TDC	GVC @ 10° AEVO
GVO @ 5° ATDC	
GVO @ 10° ATDC	

5.6.1. Conventional 4-stroke cycle - air compressor mode

In test case 1 the engine is operated as a four-stroke air compressor. The dynamometer is switched to motor mode and therefore motors the engine. A mass of air is sucked into the cylinder during the intake stroke. When the intake valves close, at the beginning of compression stroke, the gas transfer valve opens and the trapped mass of air is pushed by the piston into the airtank. At the end of compression stroke the gas transfer valve closes and the residual compressed air trapped inside the cylinder clearance volume expands during the expansion stroke until the exhaust valve opens, when it is pushed by the piston and escapes to the atmosphere during exhaust stroke. Provided that lift and timing for intake and exhaust engine valves are fixed, only the opening and closing events of the gas transfer valve can be changed and therefore are tested here. The valve lift diagram in Figure 5.13 describes the corresponding valve operation strategy.

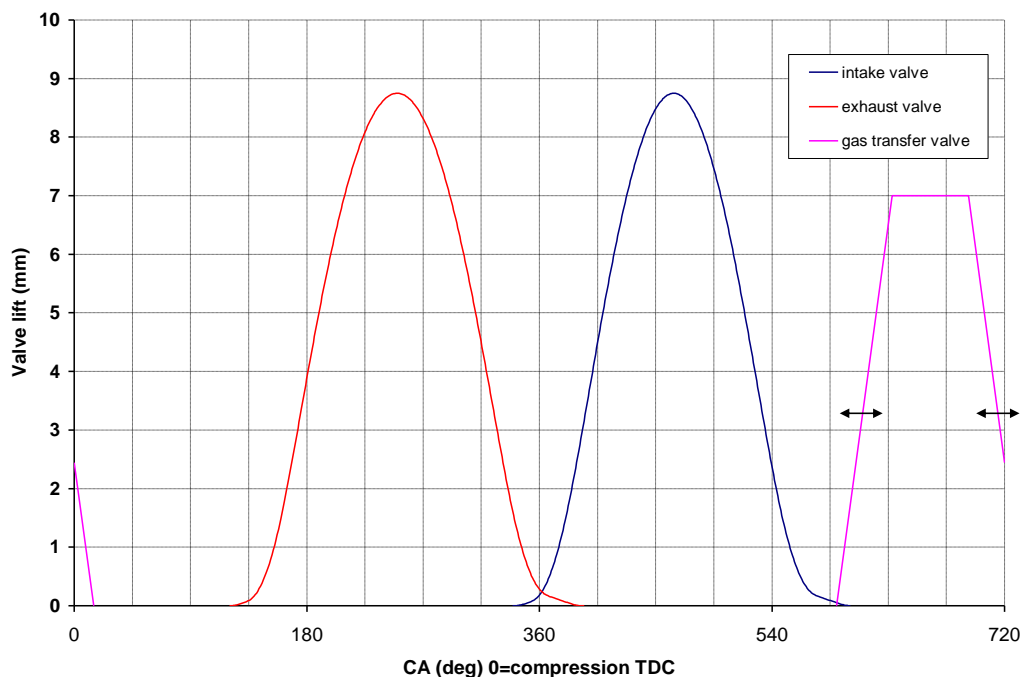


Figure 5.13: Valve lifts for test case 1.

5.6.1.1. Airtank pressure

Figure 5.14 shows the maximum airtank pressure, achieved after 1000 engine cycles for each one of the four GVO timings and seven engine speeds examined. The variation of airtank pressure after 1000 air compressor cycles (2000 crankshaft revolutions) indicates that advanced GVO (at 10° BIVC) results to increased airtank pressure, compared to other GVO timings. Further advancing of the GVO point results in air backflow from the airtank

to the cylinder and then from the cylinder to the atmosphere through the open intake valves. It can be seen that retarding of the GVO point does not greatly influence airtank pressure. However, a small decrease is realized due to the gas dynamics of the intake and gas transfer piping.

Figure 5.15 shows the maximum airtank pressure, achieved after 1000 cycles for each one of the four GVC timings and seven engine speeds examined. The variation of airtank pressure after 1000 air compressor cycles (2000 crankshaft revolutions) indicates that retarded GVC (at 15° ATDC) results to increased airtank pressure, compared to other gas transfer valve timings. Further retarding of the GVC point results in air expansion back to the cylinder (and therefore lowering $CATC_b$). Advancing of the GVC point at TDC or shortly before TDC, lowers airtank pressure as it limits the air flow from the cylinder to the airtank towards the end of the compression stroke.

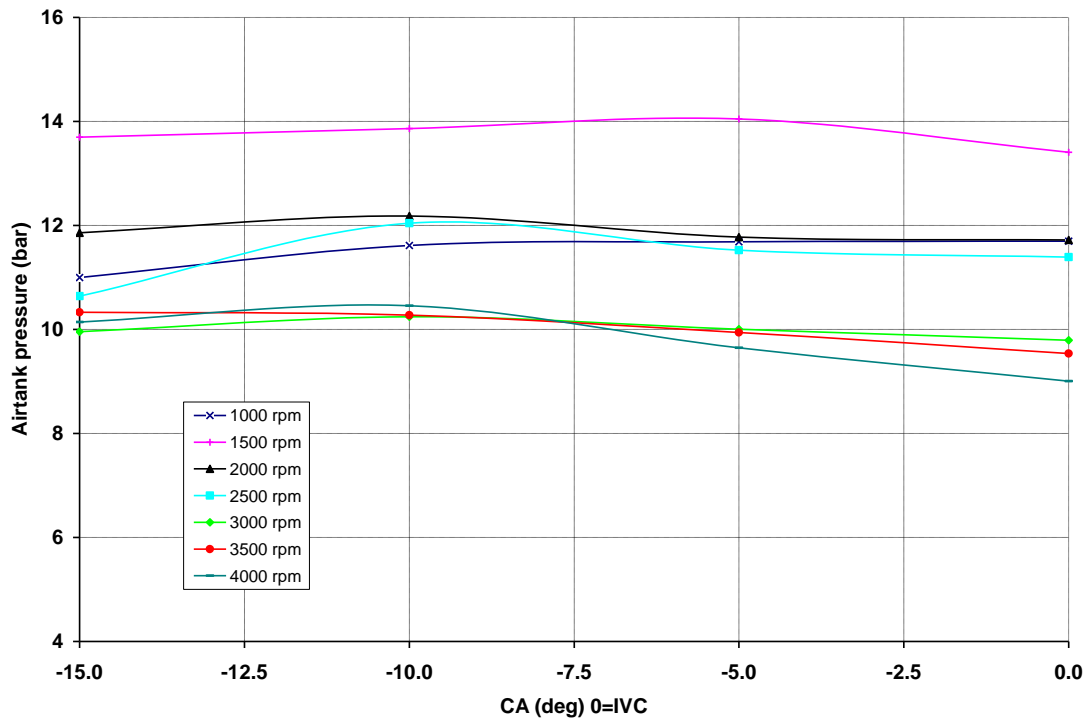


Figure 5.14: Airtank pressure after 1000 engine cycles (2000 crankshaft revolutions) for various GVO timings at different engine speeds.

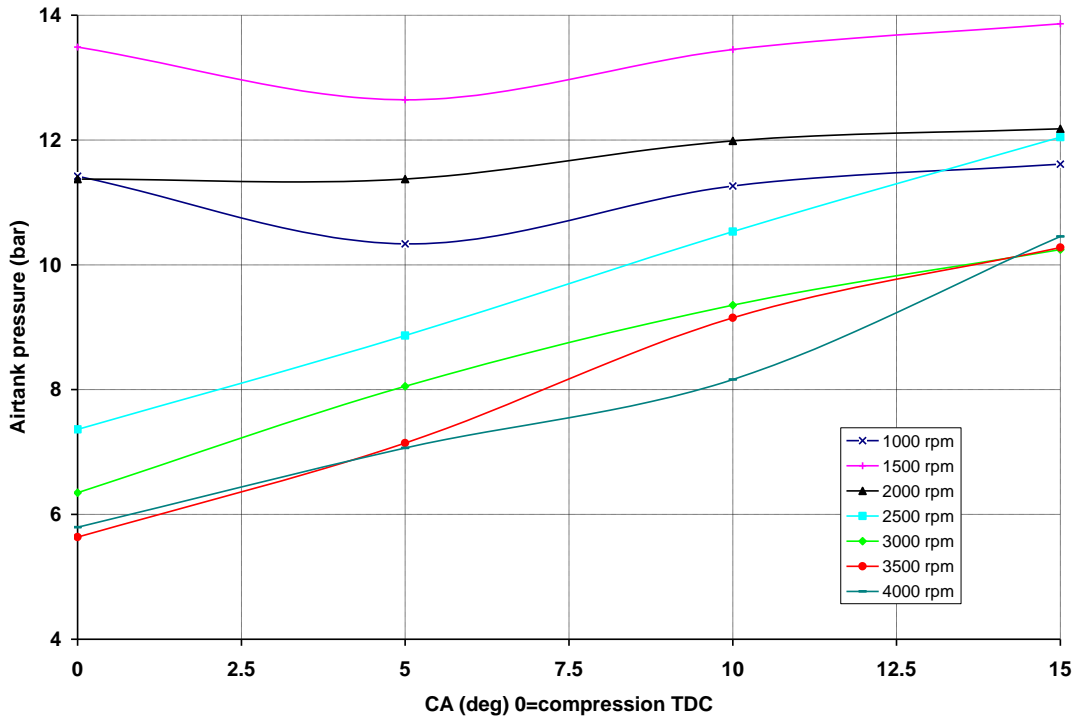


Figure 5.15: Airtank pressure after 1000 engine cycles (2000 crankshaft revolutions) for various GVC timings at different engine speeds.

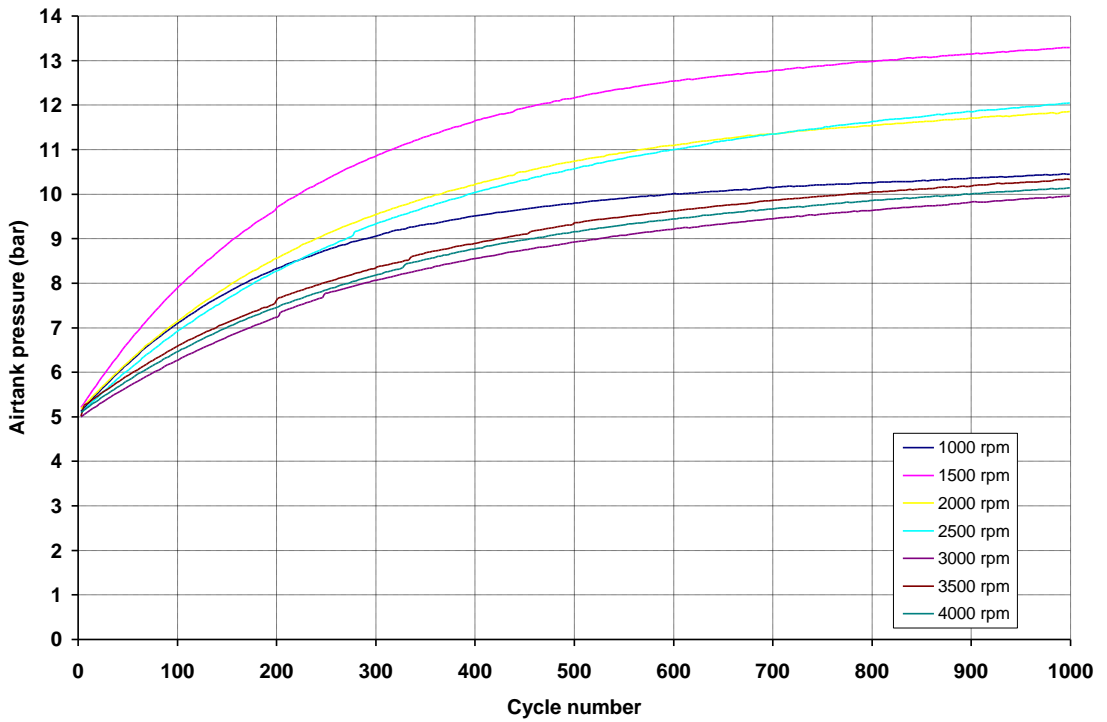


Figure 5.16: Airtank pressure throughout 1000 engine cycles (2000 crankshaft revolutions) at various engine speeds.

Figure 5.16 shows the variation of airtank pressure throughout 1000 engine cycles (2000 crankshaft revolutions) at various engine speeds. The airtank was precharged at an initial pressure of 5 bar. Maximum airtank pressure is indicative of the volumetric efficiency of the engine; the more air is induced into the cylinder, the more air is pushed into the airtank and increases its pressure. It can be seen that the pressure curve of the airtank is asymptotically approaching a limiting pressure of 11 bar for both high and low ends of the engine speed range. However, airtank pressure is 18 - 27% higher (13 - 14 bar) for mid-range speeds (1500 – 2500 rpm). It is also shown that it takes 120 seconds to fully charge the airtank with the engine operating at 1000 rpm, 60 seconds at 2000 rpm, 40 seconds at 3000 rpm and 30 seconds at 4000 rpm. However, over 90% of this pressure can be achieved within 50% of the aforementioned times (within 500 engine cycles).

5.6.1.2. Braking imep_b, fimep and bimep

Figures 5.17 and 5.18 show the variation of maximum imep_b, realized after 1000 engine cycles (2000 crankshaft revolutions) for the examined GVO and GVC points respectively. It can be seen that the GVO event does not affect imep_b importantly, provided that the valve opens after BDC. However, further retarding of the GVC event results in air backflow from the airtank to the cylinder and therefore increasing cylinder pressure during the expansion stroke and consequently decreasing imep_b. The comparison between Figures 5.14 and 5.17, reveals that maximum imep_b is realized for the same GVO timing as that for the highest airtank pressure (at 10° BIVC). Similarly, the comparison between Figures 5.15 and 5.18 indicates that maximum imep_b is realized for the same GVC timing as that for the highest airtank pressure (at 15° ATDC).

Figure 5.19 shows the variation of imep_b throughout 1000 engine cycles (2000 crankshaft revolutions) at various engine speeds. It can be seen that imep_b curve is asymptotically approaching a limiting value of 4 – 5.5 bar for low and medium engine speeds, resulting to an indicated braking torque of 14.6 – 20 Nm (see Equations 4.2, 4.3 and 4.4). It is also shown that energy storage efficiency drops with increasing engine speed, resulting to reduced imep_b. This is because of the gas dynamics of the intake, exhaust and compressed air transfer piping, which restrict the gas exchange between the cylinder, the airtank and the atmosphere. It should be noted at this point that imep_b variation follows that of airtank pressure, especially at low engine speeds, as the comparison of Figures 5.16 and 5.19 reveals.

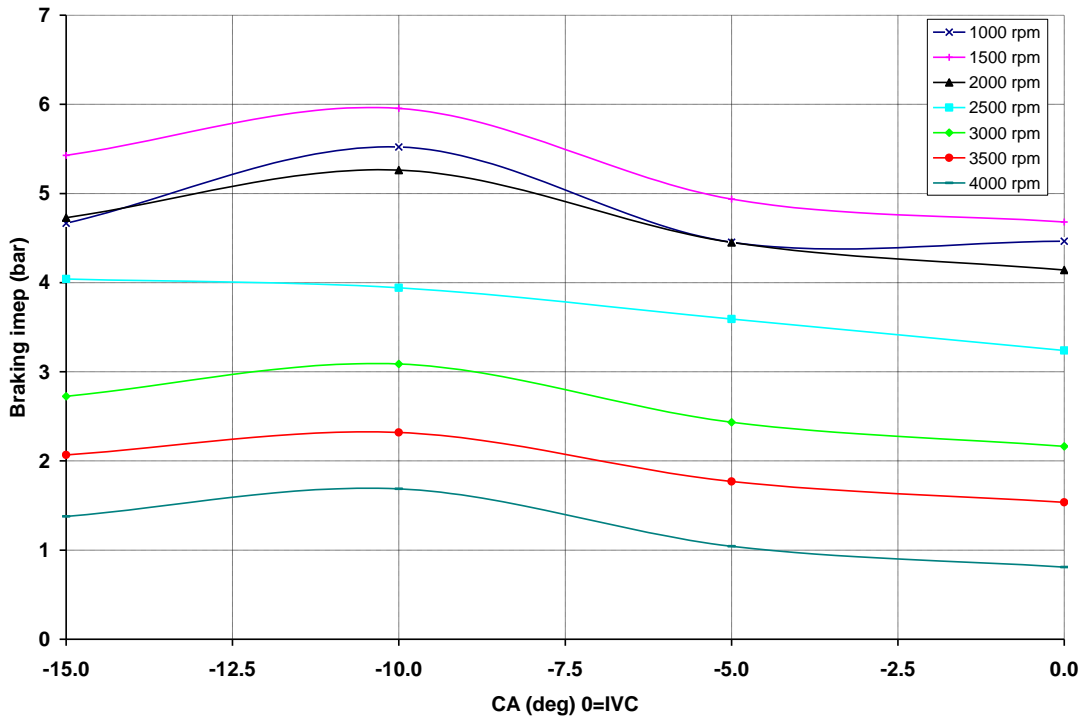


Figure 5.17: $Imep_b$ after 1000 engine cycles (2000 crankshaft revolutions) for various GVO timings at different engine speeds.

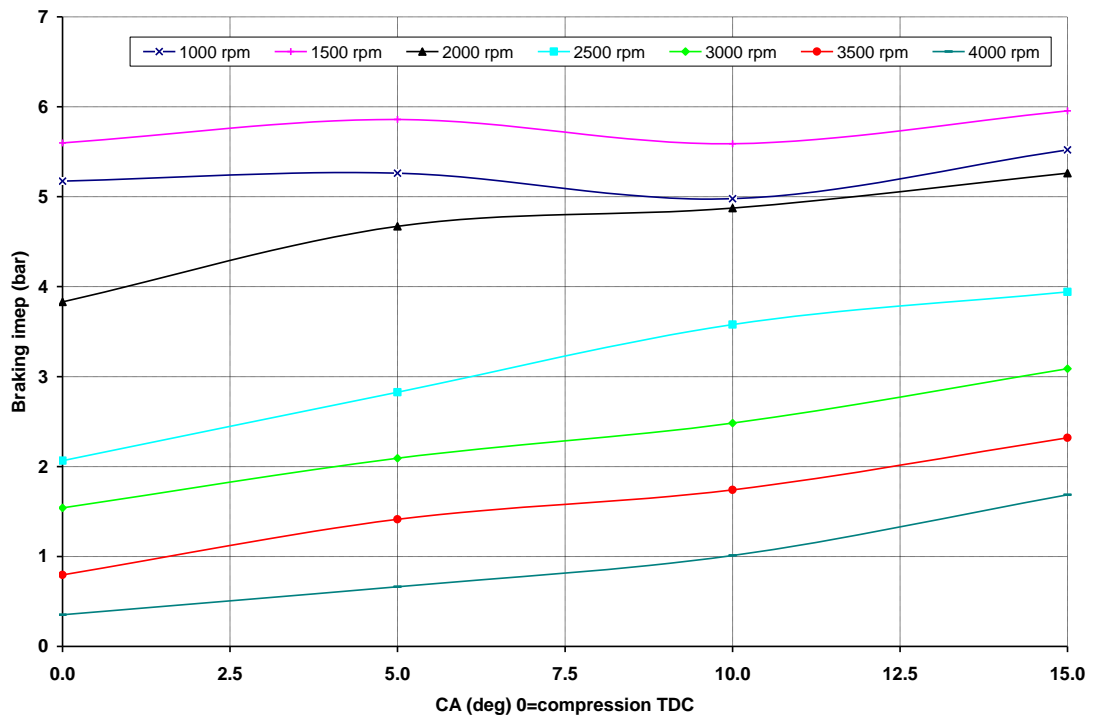


Figure 5.18: $Imep_b$ after 1000 engine cycles (2000 crankshaft revolutions) for various GVC timings at different engine speeds.

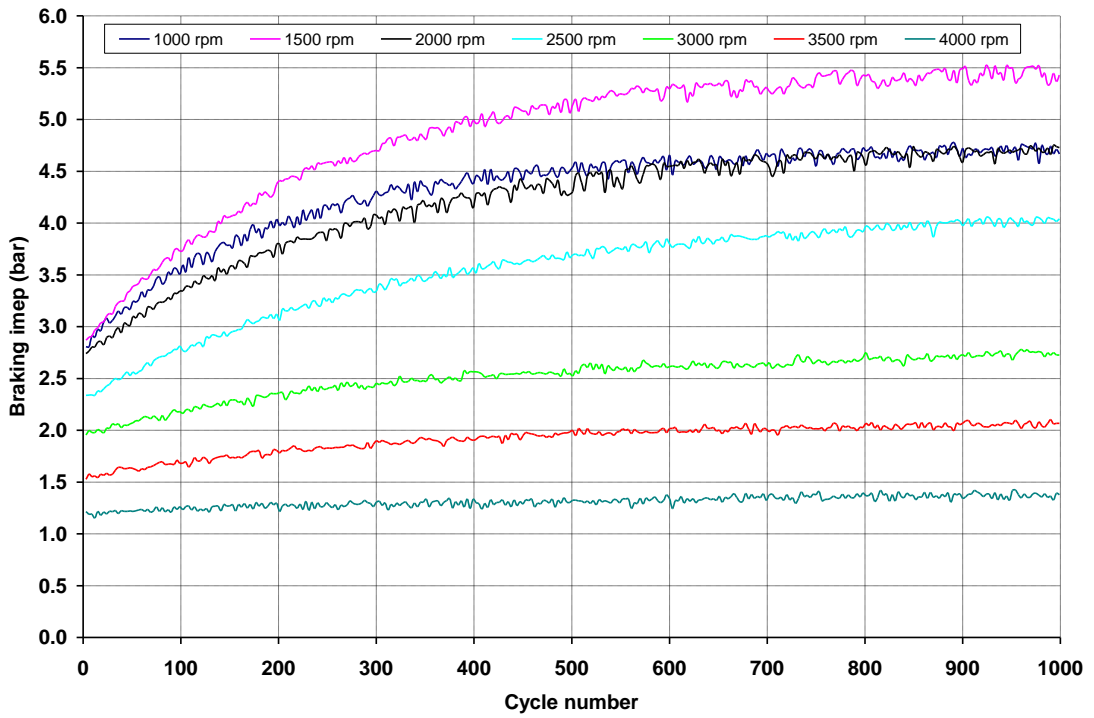


Figure 5.19: $Imep_b$ throughout 1000 engine cycles (2000 crankshaft revolutions) at various engine speeds.

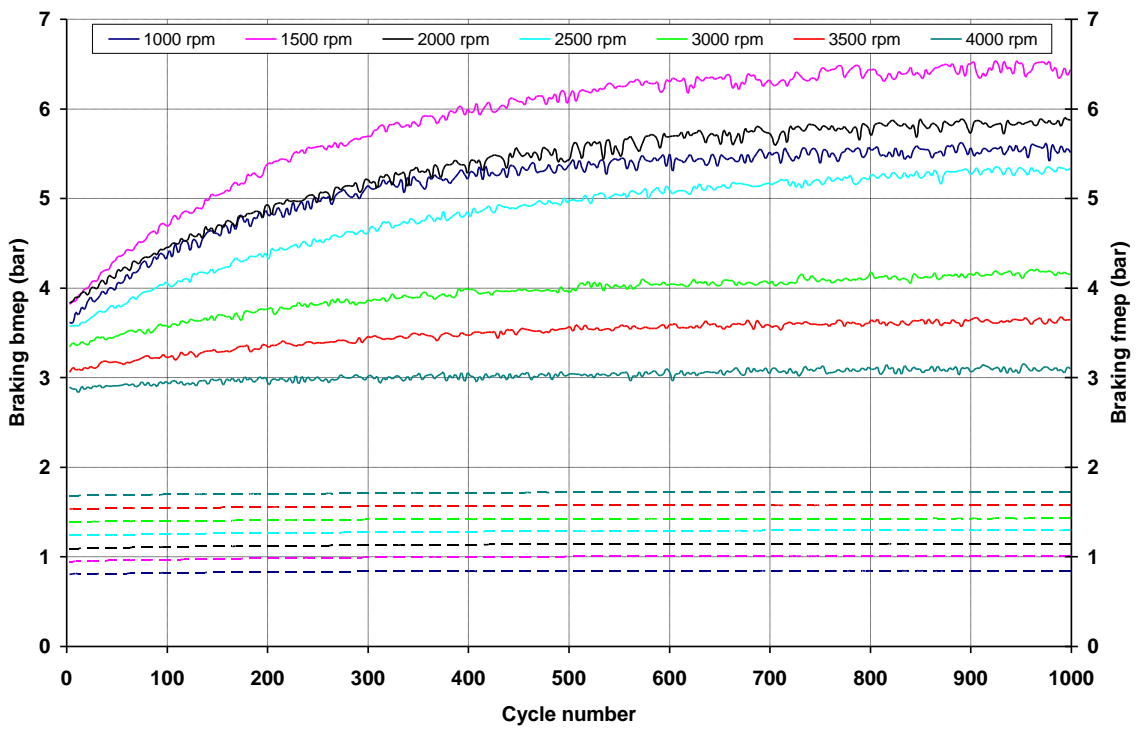


Figure 5.20: $Bmep_b$ and $fmep_b$ throughout 1000 engine cycles (2000 crankshaft revolutions) at various engine speeds.

F_{mep_b} derives from the measured maximum cylinder pressure and engine speed and can be calculated according to Equation 4.11. B_{mep_b} can therefore be computed according to Equation 4.21. The results are shown in Figure 5.20, where it can be seen that b_{mep_b} is slightly elevated, compared to i_{mep_b} , because of the frictional losses of the engine. Finally, Figure 5.21 shows the in-cylinder pressure throughout the four-stroke cycle for various numbers of cycles (and therefore various airtank pressures). It is shown that peak cylinder pressure increases with increasing airtank pressure and the area included by the indicator diagram (and thus i_{mep_b}) increases accordingly.

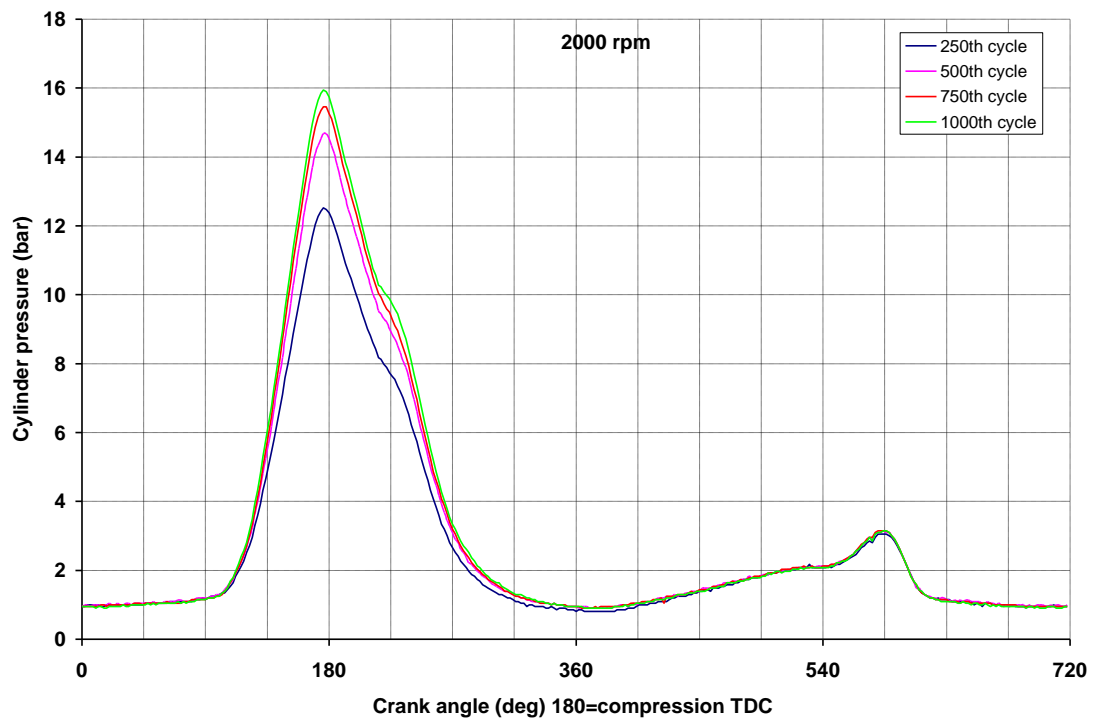


Figure 5.21: Cylinder pressure at the 250th, 500th, 750th and 1000th cycle at 2000 rpm.

5.6.2. 2-stroke engine cycle - air compressor mode

Following from test case 1, the engine is operated as a two-stroke air compressor. Similarly to test case 1, the dynamometer is switched to motor mode and therefore motors the engine. The cycle consists of an upstroke (compression) and a downstroke (intake). Intake valves open and a mass of air is sucked into the cylinder during the intake stroke. During compression, the trapped mass of air is pushed into the airtank through the open gas transfer valve. The engine exhaust valve is deactivated throughout the cycle. The performance of the air compressor is influenced by IVC and GVO points. The amount of mass of air which is transferred from the cylinder to the airtank at the end of each cycle depends on valve timing and overlap at TDC. Therefore, several IVC and GVO points are

examined here. The valve lift diagram in Figure 5.17 describes the corresponding valve operation strategy.

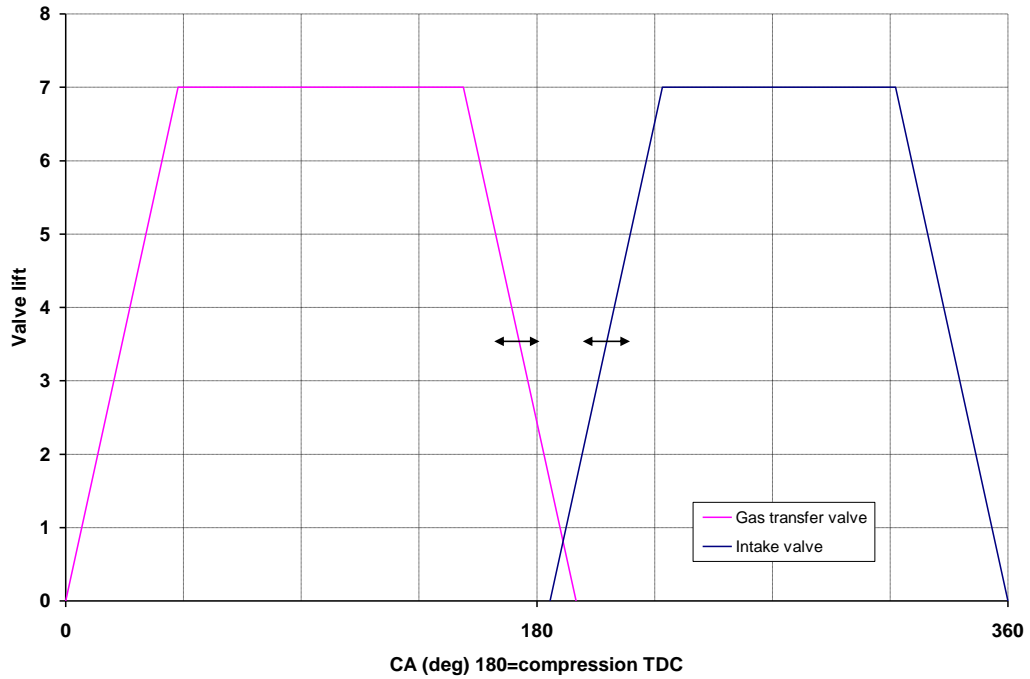


Figure 5.22: Valve lifts for test case 2.

5.6.2.1. Airtank pressure

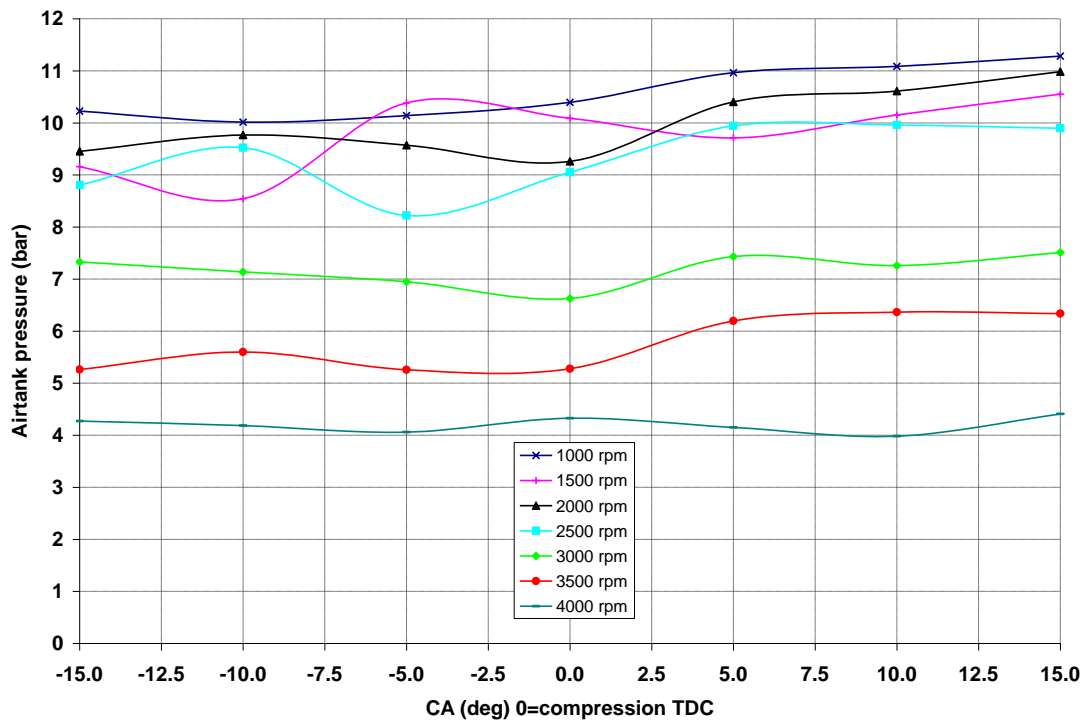


Figure 5.23: Airtank pressure after 1000 engine cycles (1000 crankshaft revolutions) for various IVO timings at different engine speeds.

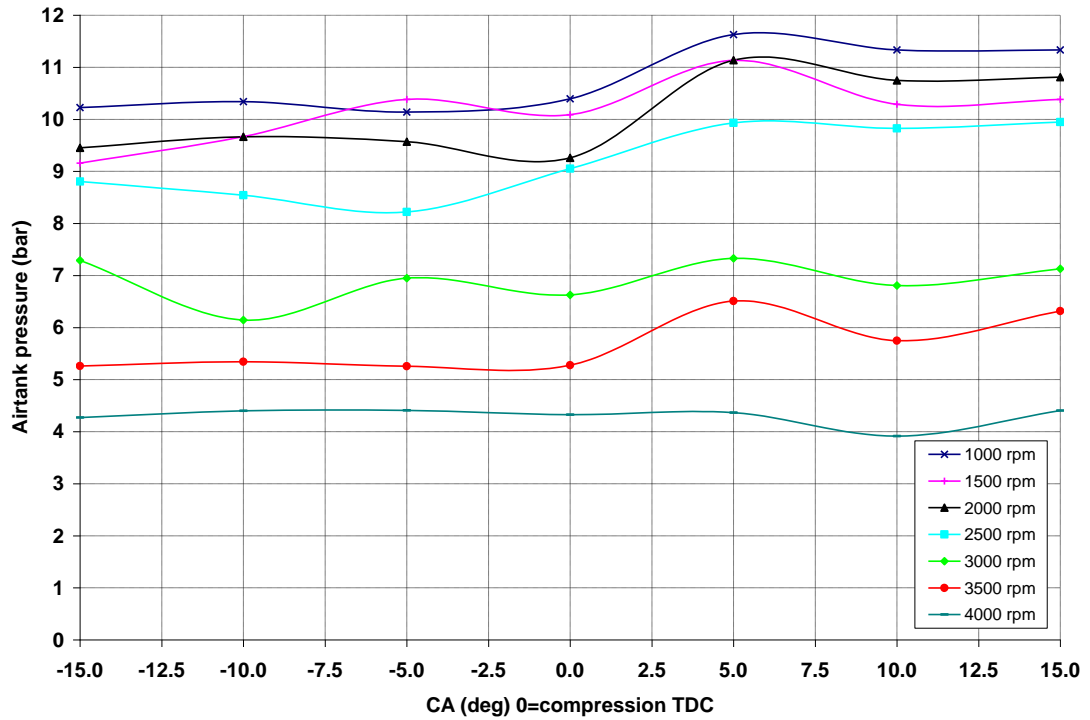


Figure 5.24: Airtank pressure after 1000 engine cycles (1000 crankshaft revolutions) for various GVC timings at different engine speeds.

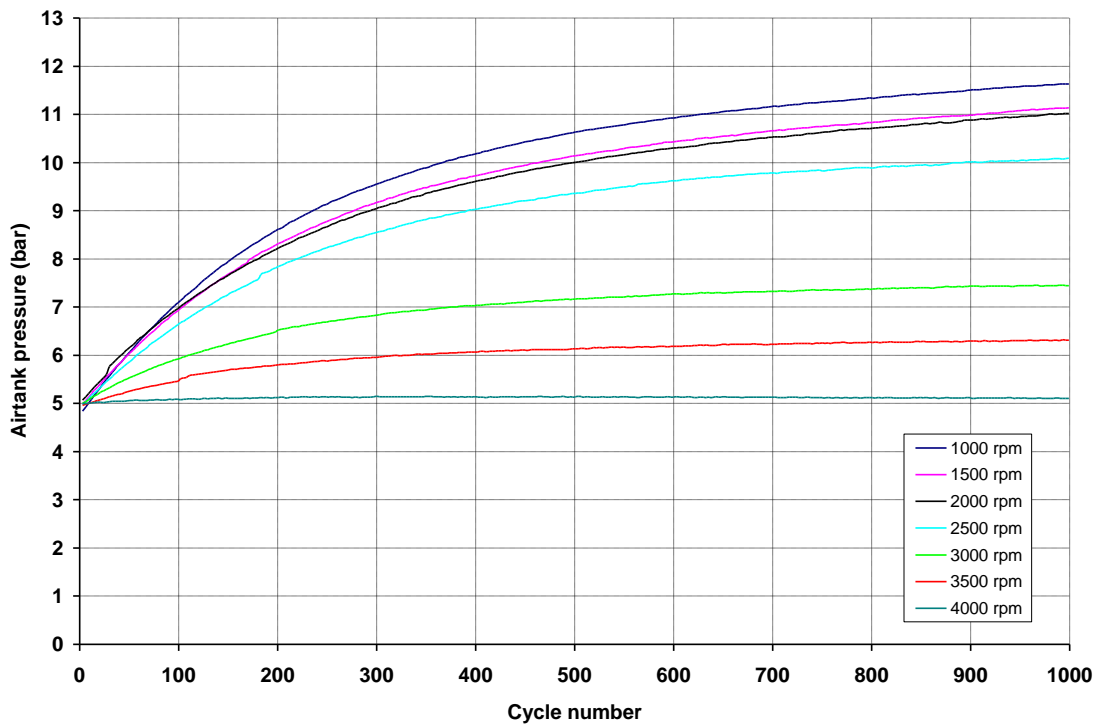


Figure 5.25: Airtank pressure throughout 1000 engine cycles (1000 crankshaft revolutions) at various engine speeds.

Figure 5.23 shows the maximum airtank pressure, achieved after 1000 engine cycles for each one of the seven IVO timings and seven engine speeds examined. The variation of airtank pressure after 1000 air compressor cycles (1000 crankshaft revolutions) indicates that retarded IVO (at 15° ATDC) results to increased airtank pressure, compared to other intake valve timings. Further retarding of the IVO point results in air expansion back to the cylinder as the cylinder volume increases because of the downwards motion of the piston during the intake stroke. Furthermore, advancing of the IVO point at TDC or shortly before TDC, lowers airtank pressure as it limits the air flow from the cylinder to the airtank towards the end of the compression stroke and results to compressed air escaping to the atmosphere.

Figure 5.24 shows the maximum airtank pressure, achieved after 1000 cycles for each one of the seven GVC timings and seven engine speeds examined. The variation of airtank pressure after 1000 air compressor cycles (2000 crankshaft revolutions) indicates that slightly retarded GVC (at 5° ATDC, which gives a valve overlap of 10° CA) results to increased airtank pressure, compared to other GVC timings. Further retarding of the GVC point increases the overlap between the intake and gas transfer valves and therefore lowers airtank pressure, as compressed air escapes to the atmosphere. Advanced IVO points, at TDC or shortly before TDC, limit the available time for the compressed air to be transferred from the cylinder to the airtank at the end of the compression stroke.

Figure 5.25 shows the variation of airtank pressure throughout 1000 engine cycles (1000 crankshaft revolutions) at various engine speeds. The airtank was precharged at an initial pressure of 5 bar. This pressure can be barely maintained at 4000 rpm, while it is increased only by 20 - 35% at 3500 and 3000 rpm respectively. At lower engine speeds, the pressure curve of the airtank is asymptotically approaching a limiting pressure of 10.5 - 12 bar. Maximum airtank pressure is indicative of the volumetric efficiency of the engine; the more air is induced into the cylinder, the more air is pushed into the airtank and increases its pressure. It is also shown that it takes 60 seconds to fully charge the airtank with the engine operating at 1000 rpm, 30 seconds at 2000 rpm, 20 seconds at 3000 rpm and 15 seconds at 4000 rpm. However, over 90% of this pressure can be achieved within 50% of the aforementioned times (within 500 engine cycles). It should be mentioned at this point that advancing or retarding of IVO and GVC points does not greatly affect airtank pressure. However, the gas dynamics of the intake and gas transfer systems influence airtank pressure at high engine speeds. Subsequently, the airtank does not reach a satisfactory state of charge (SOC) at engine speeds exceeding 3000 rpm.

5.6.2.2. Braking imep, bmep and fmep

Figures 5.26 and 5.27 show the variation of maximum imep_b, realized after 1000 engine cycles (1000 crankshaft revolutions) for the examined IVO and GVC points respectively. The comparison between Figures 5.23 and 5.26 reveals that maximum imep_b is realized for the same IVO timing as that for the highest airtank pressure (at 15° ATDC). Similarly, the comparison between Figures 5.24 and 5.27 indicates that maximum imep_b is realized for the same GVC timing as that for the highest airtank pressure (at 5° ATDC).

Figure 5.28 shows the variation of imep_b throughout 1000 engine cycles (1000 crankshaft revolutions) at various engine speeds. It can be seen that imep_b curve is asymptotically approaching a limiting value of 4 – 5 bar for low and medium engine speeds, resulting to an indicated braking torque of 29.2 – 36.4 Nm (see Equations 4.2, 4.3 and 4.4). At high engine speeds (above 3000 rpm), imep_b drops to approximately 2.5 bar, resulting to an indicated braking torque of 18.2 Nm. It should be noted at this point that imep_b does not increase with increasing cycle number at high engine speeds, although airtank pressure slightly rises. Imep_b drops down to approximately 1.1 bar at 4000 rpm and therefore the corresponding indicated torque is too low to decelerate the vehicle sufficiently. In case of the four-stroke air compressor with valves of trapezoidal lift profile, described by Turner et al [64,65], the above indicated braking torque values are anticipated to be reduced by 50%. It is also shown that energy storage efficiency drops with increasing engine speed, resulting to reduced imep_b, similar to test case 1. This is because of the gas dynamics of the intake, exhaust and compressed air transfer piping, which restrict the gas exchange between the cylinder, the airtank and the atmosphere. It should be noted at this point that imep_b variation follows that of airtank pressure, especially at low engine speeds, as the comparison of Figures 5.25 and 5.28 reveals.

Fmep_b derives from the measured maximum cylinder pressure and engine speed and can be calculated according to Equation 4.11. Bmep_b can therefore be computed according to Equation 4.21. The results are shown in Figure 5.29, where it can be seen that bmep_b is slightly elevated, compared to imep_b, because of the frictional losses of the engine. Finally, Figure 5.30 shows the in-cylinder pressure throughout the two-stroke cycle for various numbers of cycles (and therefore various airtank pressures) in respect to crank angle. It is shown that peak cylinder pressure increases with increasing airtank pressure and the area included by the indicator diagram (and thus imep_b) increases accordingly.

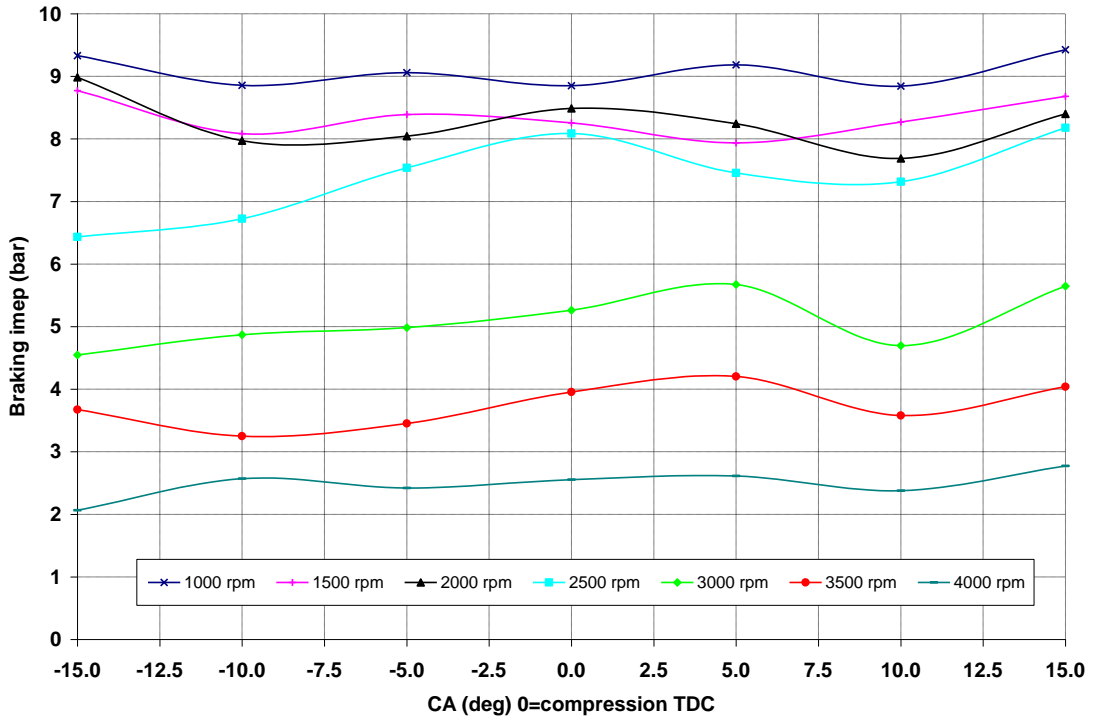


Figure 5.26: $Imep_b$ after 1000 engine cycles (1000 crankshaft revolutions) for various IVO timings at different engine speeds.

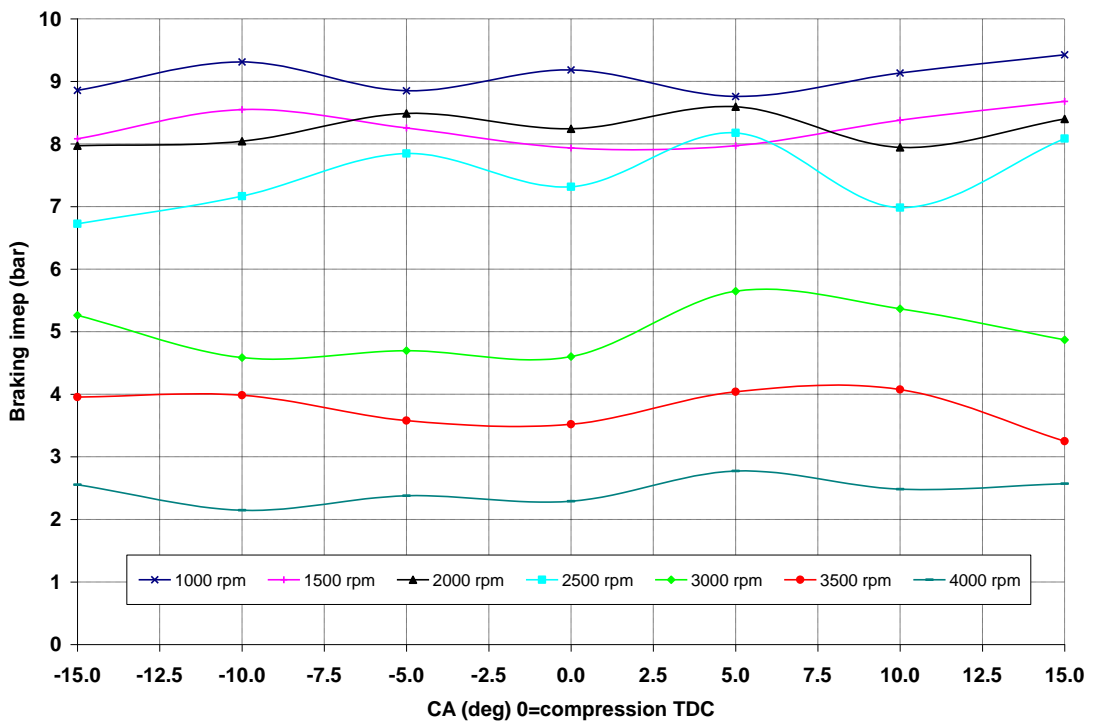


Figure 5.27: $Imep_b$ after 1000 engine cycles (1000 crankshaft revolutions) for various GVC timings at different engine speeds.

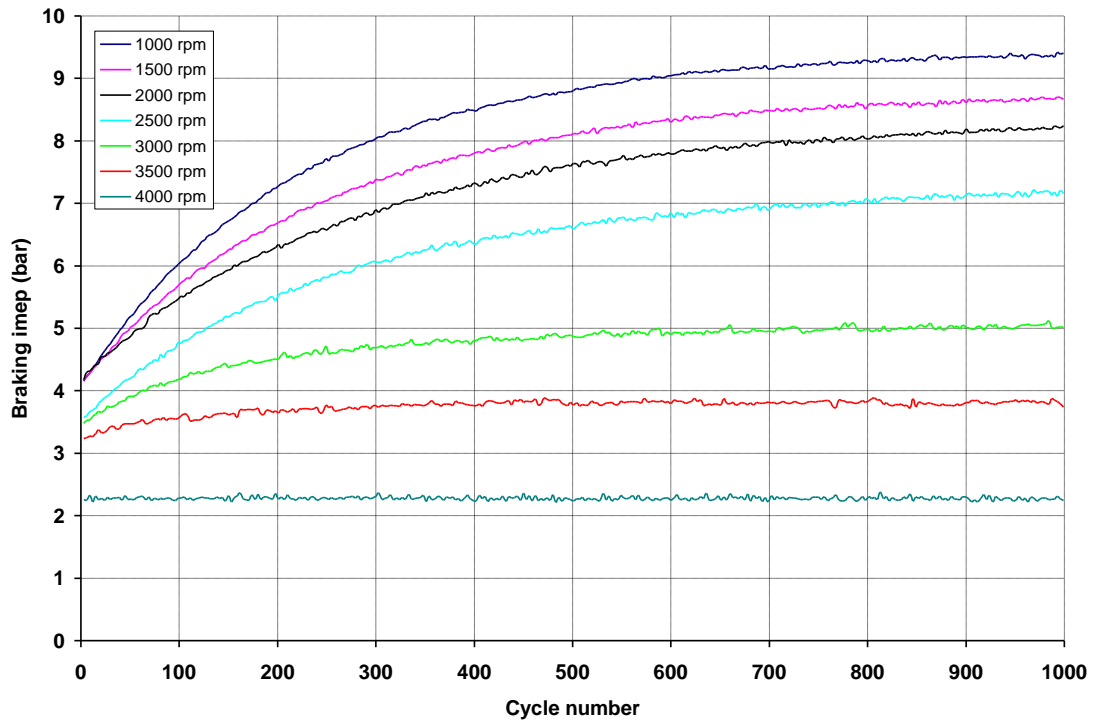


Figure 5.28: $Imep_b$ throughout 1000 engine cycles (1000 crankshaft revolutions) at various engine speeds.

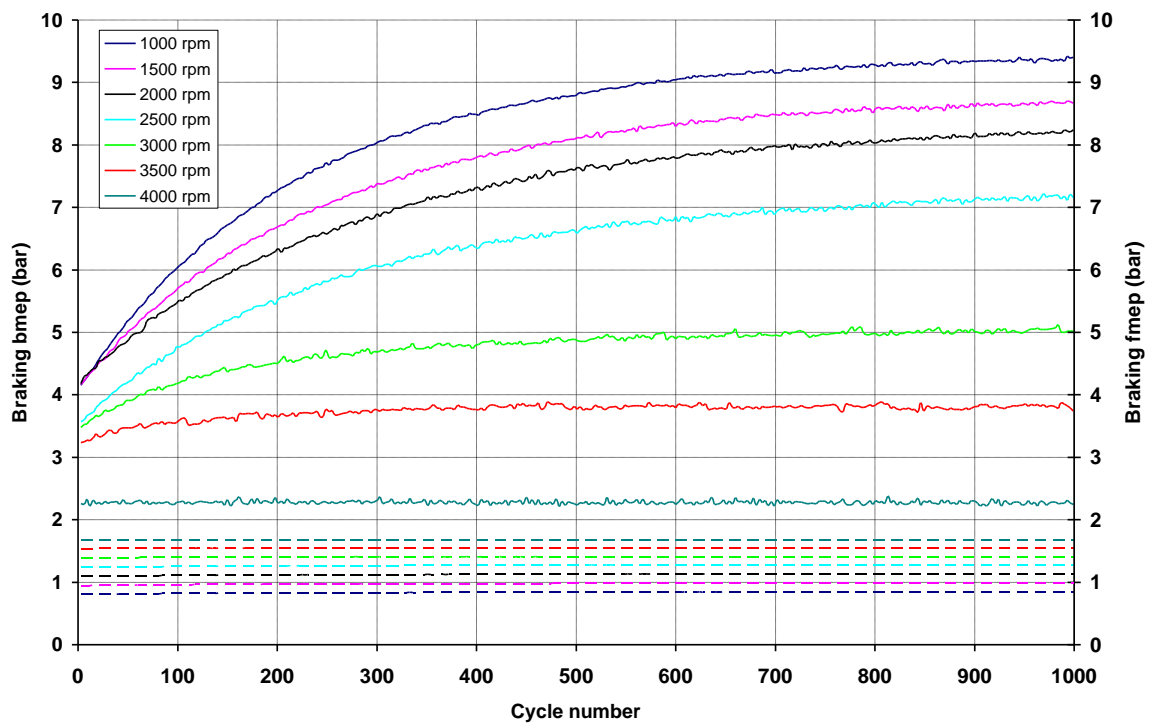


Figure 5.29: $Bmep_b$ and $fmep_b$ throughout 1000 engine cycles (1000 crankshaft revolutions) at various engine speeds.

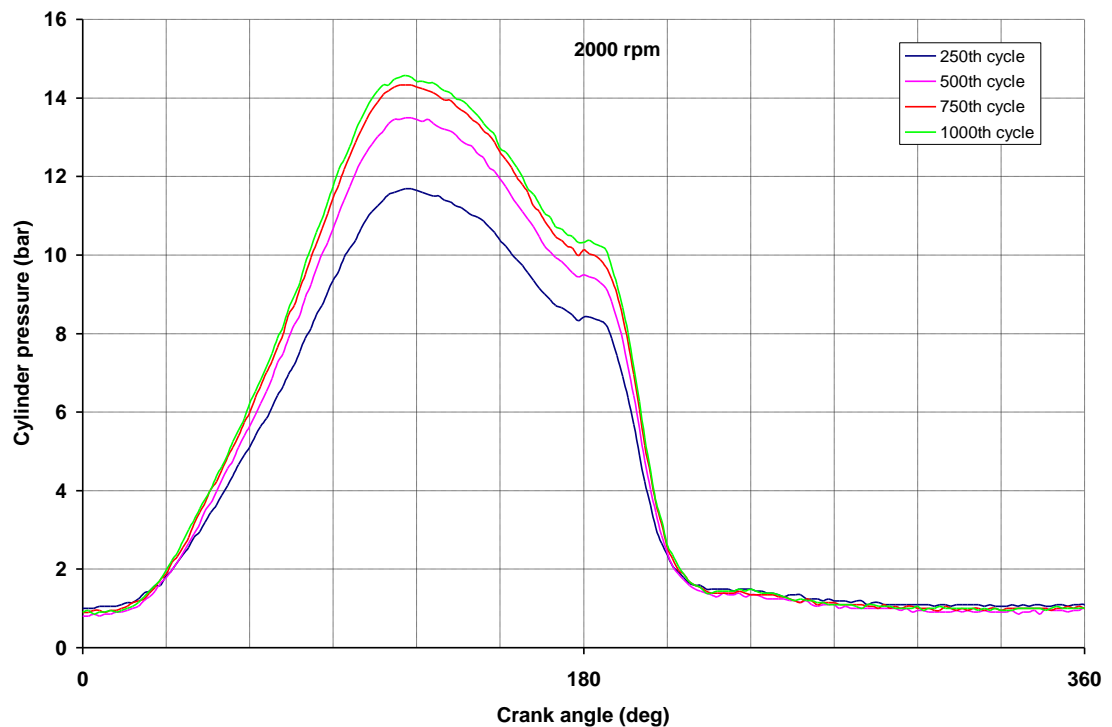


Figure 5.30: Cylinder pressure at the 250th, 500th, 750th and 1000th cycle at 2000 rpm.

5.6.3. Conventional 4-stroke cycle - air expander mode

In test case3 the engine is operated as a four-stroke air expander. Intake valves open and air charge is sucked into the cylinder during the intake stroke. Cylinder pressure increases during the compression stroke, when all valves are closed. The gas transfer valve opens during the expansion stroke, at TDC or shortly after TDC, and compressed air is released into the cylinder, enhancing the cylinder pressure during the downstroke. Therefore, the region included by the indicator diagram is increased and $imep_d$ is augmented. The valve closes at EVO or shortly after EVO to prevent excessive compressed air expenditure. The residual air is pushed to the atmosphere through the open exhaust valve during the expansion stroke. The valve lift diagram in Figure 5.31 describes the corresponding valve operation strategy.

The objective of the experimentation on the air expander is to explore the potential of providing enough torque to overcome frictional and pumping losses and start the engine without the aim of the electric starter. Ideally, the driving torque should be sufficient to propel the vehicle from stop until the engine is switched to normal firing mode. The engine

speed range of interest is therefore very low (between 0 rpm and idle speed). However, the AVT controller shifts to fail-safe mode when the crankshaft encoder reading is below 750 rpm. Furthermore, the speed trip of the dynamometer control panel is triggered when engine speed drops below 720 rpm. Consequently, the experiments took place at 1000 rpm in order to make use of the valve control parameters and AVT settings used for the air compressor test cases at the specific engine speed. This eliminates the need for further adjustments and modifications to the engine test cell and AVT system.

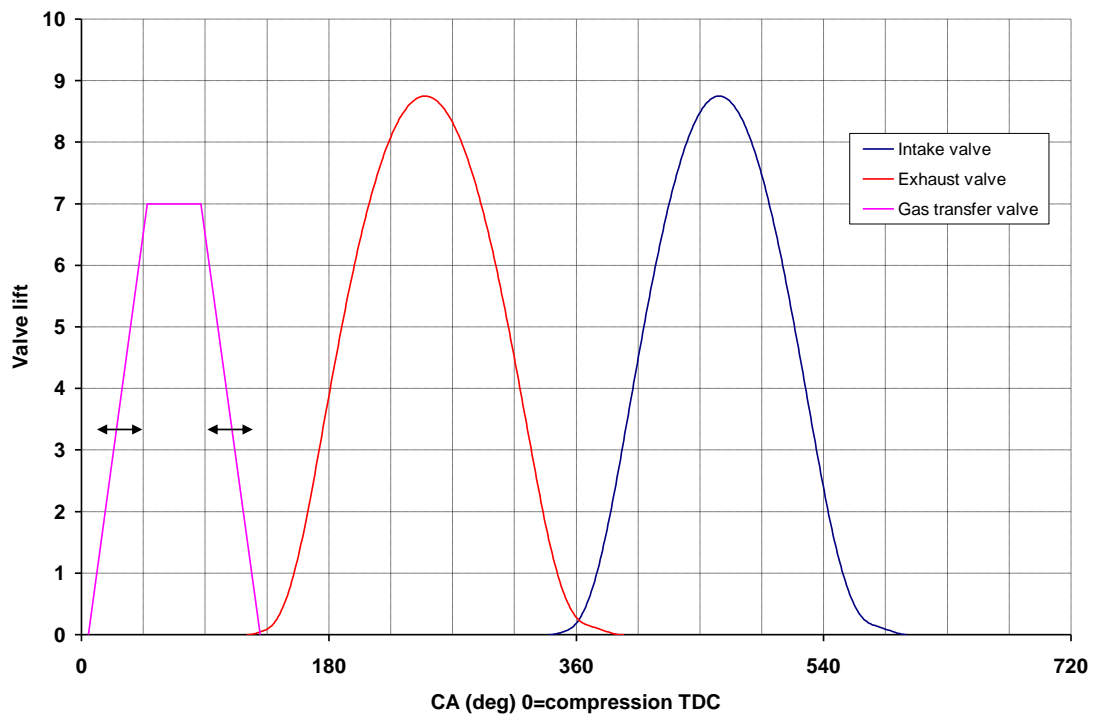


Figure 5.31: Valve lifts for test case 3.

The dynamometer is switched to start/auto mode, and therefore it automatically changes from motor to brake mode to maintain the required speed setting. In contrast to air compressor test cases, where the optimal valve timing was found through maximum achieved airtank pressure and $imep_b$ after a number of engine cycles, here optimal valve timing is found through the investigation of compressed air discharge efficiency, which is expressed as the averaged ratio of the realized $imep_d$ to airtank pressure at the end of each cycle, over a number of cycles, as described by Equation 5.7:

$$\eta_{air} = \frac{\sum_{i=0}^n \frac{imep_{m_i}}{P_{t_i}}}{\sum_{i=0}^n i} \quad \text{Equation 5.7}$$

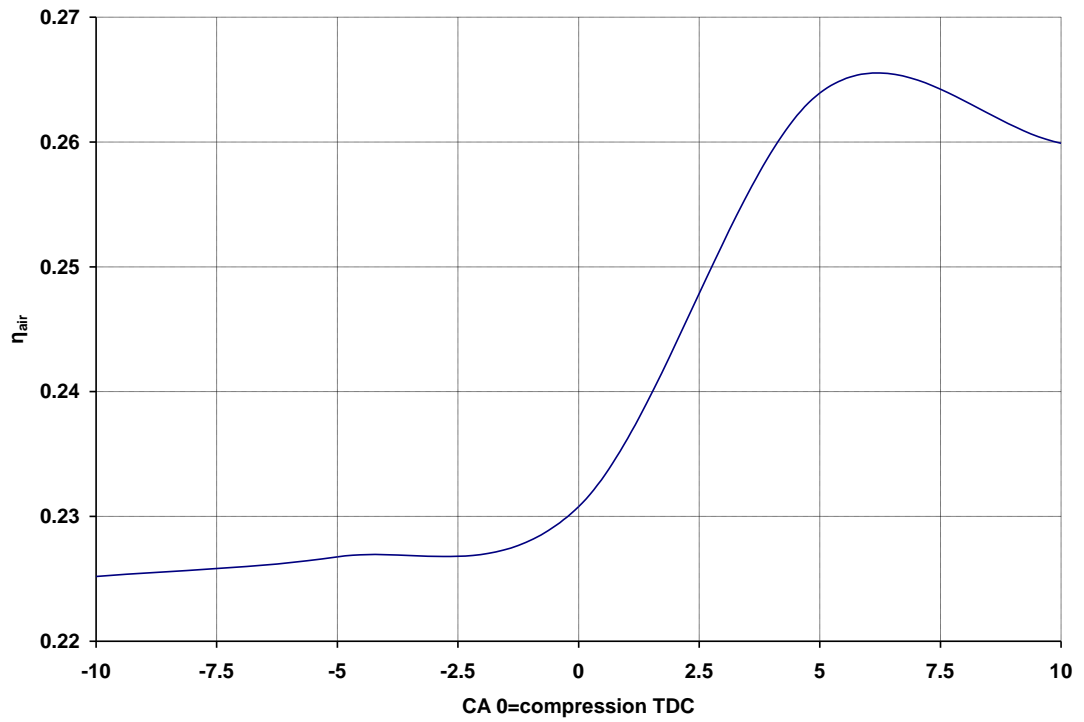


Figure 5.32: Averaged ratio of the realized $imep_d$ to airtank pressure against various GVO points.

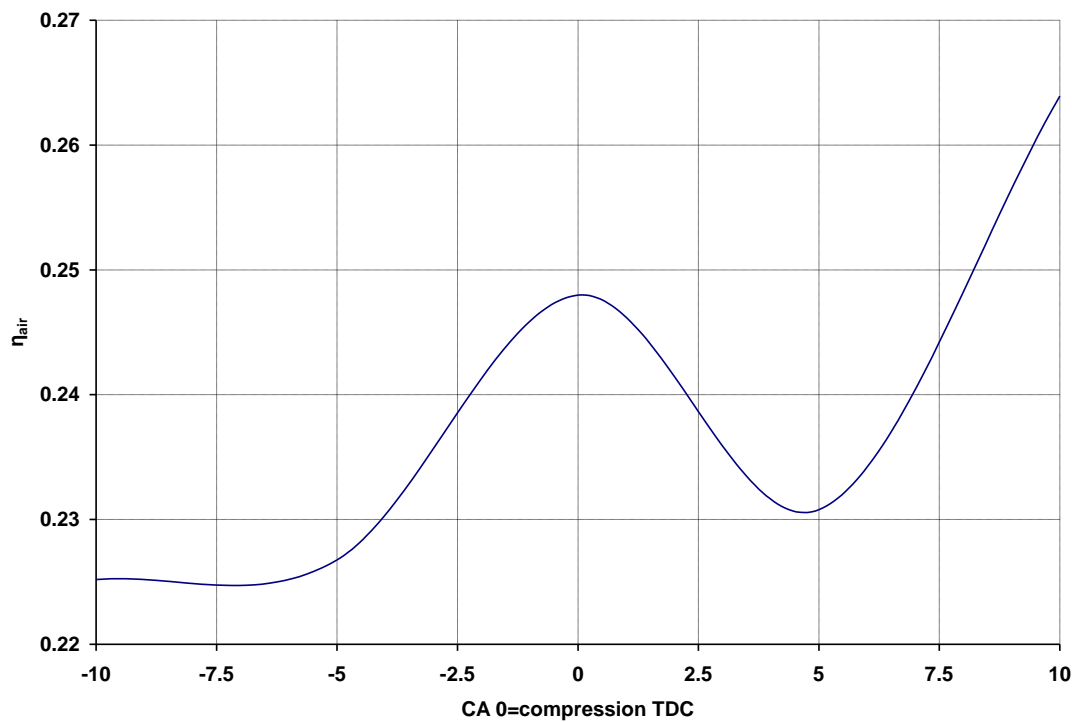


Figure 5.33: Averaged ratio of the realized $imep_d$ to airtank pressure against various GVC points.

Figures 5.32 and 5.33 show the $imep_d$ to airtank pressure ratio sensitivity to GVO and GVC timings respectively. It can be seen that maximum compressed air discharge efficiency is realized for slightly retarded GVO point (at 5° ATDC) in conjunction with retarded GVC point (at 10° AEVO).

5.6.3.1. Airtank pressure

Prior to air expander mode, the engine is operated as an air compressor in order to precharge the airtank to a pressure as high as 11 bar, which is regarded as the initial pressure for every air expander experiment. Once the airtank is charged, the valve lift profile is switched to four-stroke air expander and the experiment initiates.

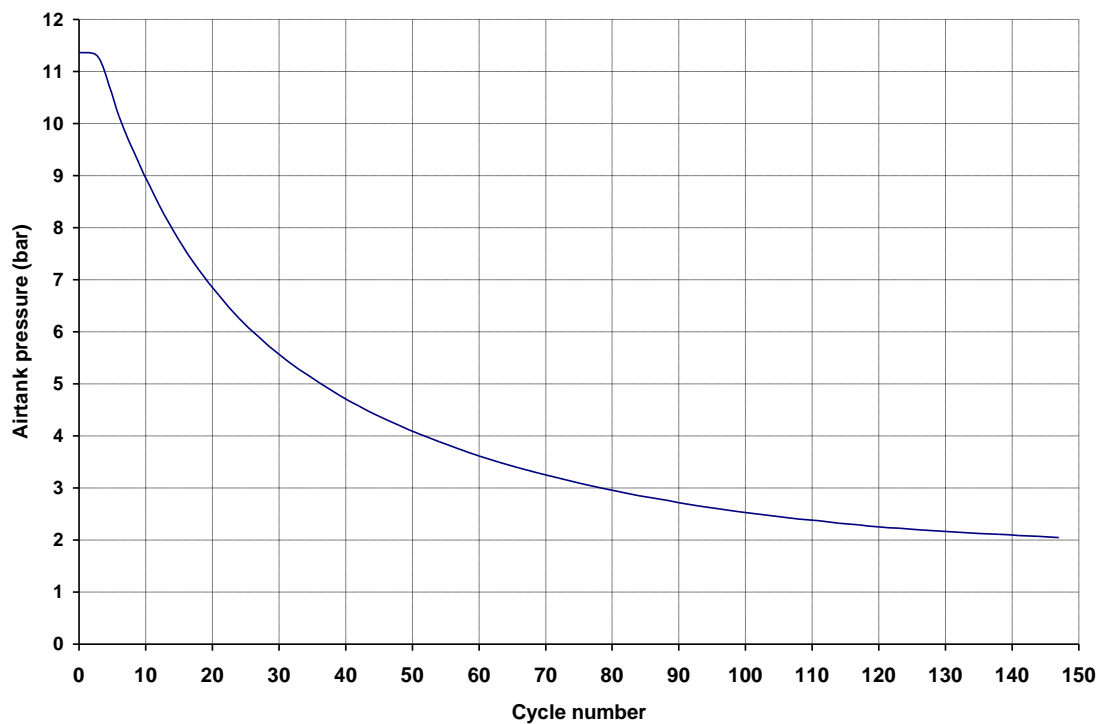


Figure 5.34: Airtank pressure variation throughout 150 engine cycles (300 crankshaft revolutions).

Figure 5.34 shows the variation of airtank pressure throughout 150 engine cycles (300 crankshaft revolutions). It is shown that the average rate of reduction of airtank pressure during the twenty first cycles is approximately 0.22 bar per cycle. From cycle 20 to cycle 40 the aforementioned rate is reduced by 50% (0.11 bar per cycle), while for cycles 40 through 60 it is further reduced by 50% (0.05 bar per cycle). Finally, the average rate of reduction of airtank pressure is 0.03 bar per cycle from cycle 60 to cycle 100, while it drops down to 0.009 bar per cycle during the last 50 cycles. The above variation reveals

that the pressure curve is approaching a limiting pressure of 2 bar and therefore the system reaches a pressure equilibrium between the cylinder and the airtank after approximately 150 bar, as shown in the diagram.

5.6.3.2. Driving imep, bmep and fmep

Following from airtank pressure results, the engine was used to study the sensitivity of $imep_d$ to airtank pressure and number of operating cycles. It is shown in Figure 5.35 that initially the realized driving torque output of the engine is 4.7 bar, giving a compressed air discharge efficiency coefficient as high as 0.42 for an initial airtank pressure of 11 bar. The resulting indicated driving torque is 17 Nm, according to Equations 4.2, 4.3 and 4.4). The aforementioned coefficient is reduced to 0.27 after 20 engine cycles, when $imep_d$ is decreased by approximately 61% (1.85 bar). After 40 cycles, η_{air} is reduced to 0.15, as $imep_d$ drops to 0.735 bar, resulting in an indicated driving torque of 2.6 Nm. After 57 engine cycles, $imep_d$ drops to zero and therefore it can be concluded that there is no indicated driving torque output for airtank pressures lower than 3.7 bar. Below that pressure, the SOC of the airtank is too low to power the engine. The above indicated driving torque values are anticipated to be doubled (increased by 100%) when the engine is operated as a two-stroke air expander, in the way described by Turner et al [64,65]. Similar to the previous test cases, $fmep_d$ derives from the measured maximum cylinder pressure and engine speed and can be calculated according to Equation 4.11. $Bmep_d$ can therefore be computed according to Equation 4.28. The results are shown in Figure 5.35, where it can be seen that $bmep_d$ is decreased, compared to $imep_d$, because of the frictional losses of the engine.

Finally, Figure 5.36 displays the in-cylinder pressure for various numbers of cycles (and therefore various airtank pressures) in respect to crank angle. It is shown that peak cylinder pressure is as high as 16.5 bar regardless the cycle number, as the conventional intake and compression strokes are unaffected in air expander mode. The pressure drop caused by the downwards motion of the piston is compensated by the expansion of compressed air during the expansion stroke. Accordingly, the area included by the indicator diagram (and thus $imep_d$) is varied in respect to airtank pressure.

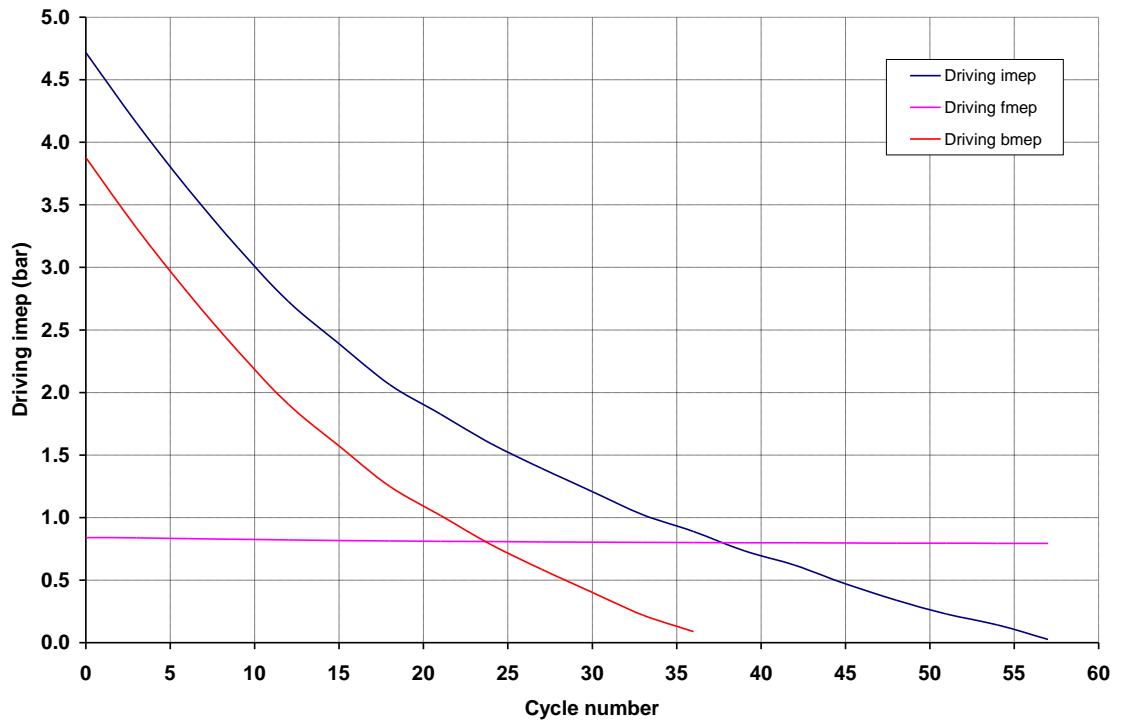


Figure 5.35: $Imep_d$ throughout 60 engine cycles (120 crankshaft revolutions).

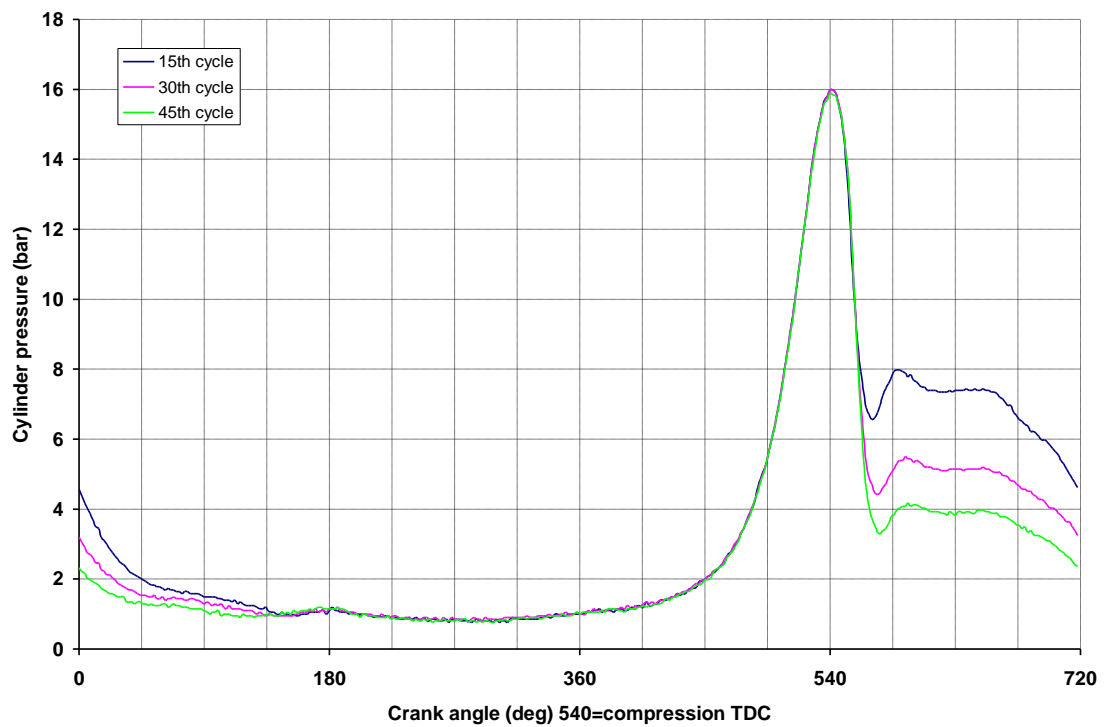


Figure 5.36: Cylinder pressure at the 15th, 300th and 45th cycle.

5.7. Comparison between predicted and experimental results

Following from the experimental work, a comparison between the experimental and predicted results is made in order to examine whether they converge or not and discuss the similarities and differences between the numerical and the experimental methods. Figure 5.37 shows the predicted b_{mep_b} for the air compressor concept with the two-stage ERV (concept 1), the predicted b_{mep_b} for the air compressor concept with the reed valve (concept 3) and the measured b_{mep_b} for the air compressor concept with conventional camshaft profiles (test case1). All the above cycles are four-stroke cycles. Although the compression ratio in concept 1 is close to that in test case 1, the presence of the two-stage ERV results in invariable b_{mep_b} throughout the whole braking period, dissimilar to test case 1, where the presence of the one-stage gas transfer valve results to an increasing b_{mep_b} trend over the braking period. The same trend is realized in concept 3. However, the predicted b_{mep_b} is slightly higher than in test case 1 because of the higher compression ratio. In addition, the airtank and piping in concepts 1 and 3 were regarded to be thermally isolated (and thus the compression of the air in the airtank was regarded adiabatic), while during the experimental work there was no thermal isolation and therefore a significant amount of reusable thermal energy was dissipated to the atmosphere.

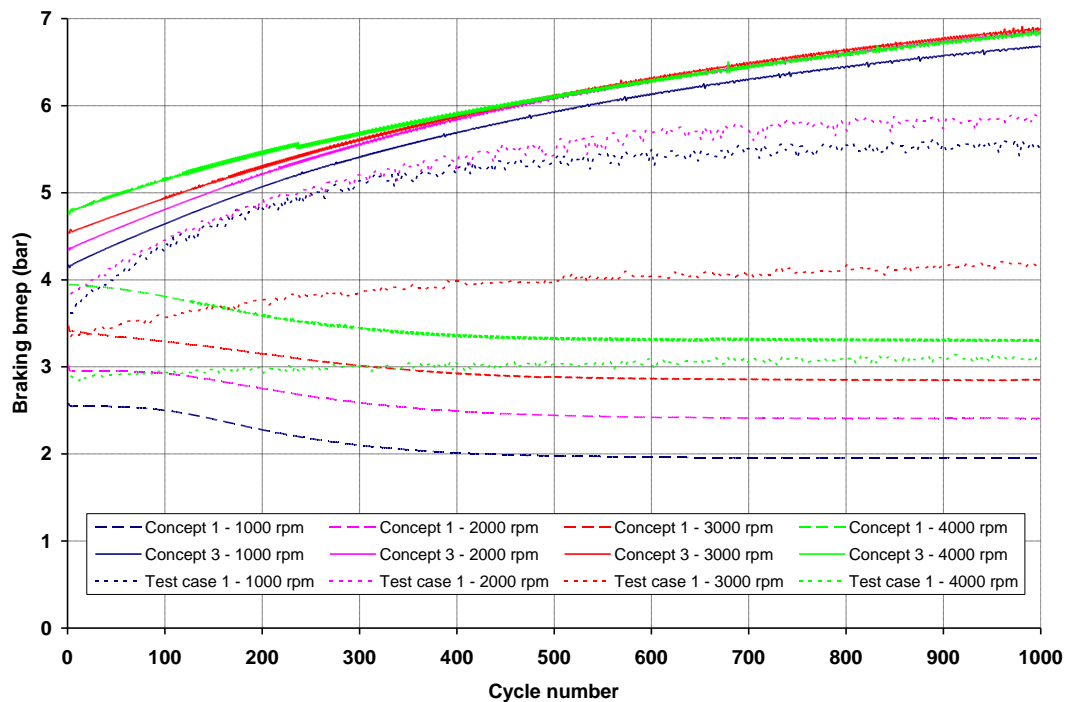


Figure 5.37: Predicted b_{mep_b} results for concepts 1 and 3 (dashed and solid lines respectively) and experimental b_{mep_b} results for test case 1 (dotted lines) at various engine speeds.

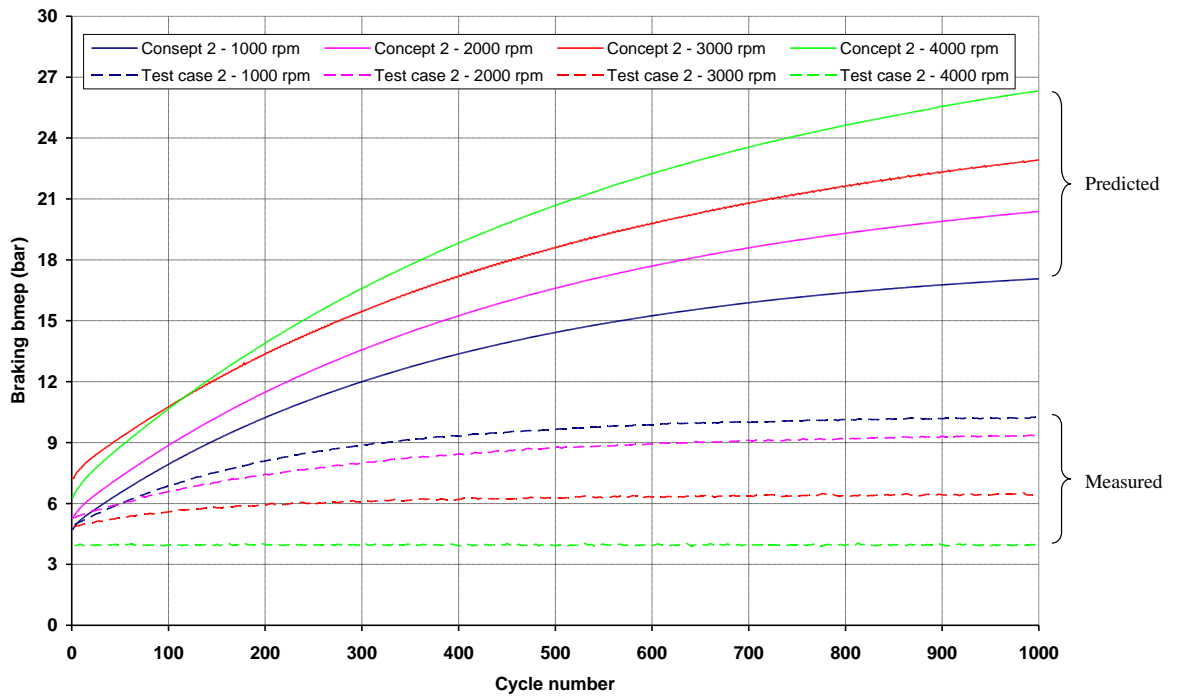


Figure 5.38: Predicted $bmep_b$ results for concept 2 (solid lines) and experimental $bmep_b$ results for test case 2 (dashed lines) at various engine speeds.

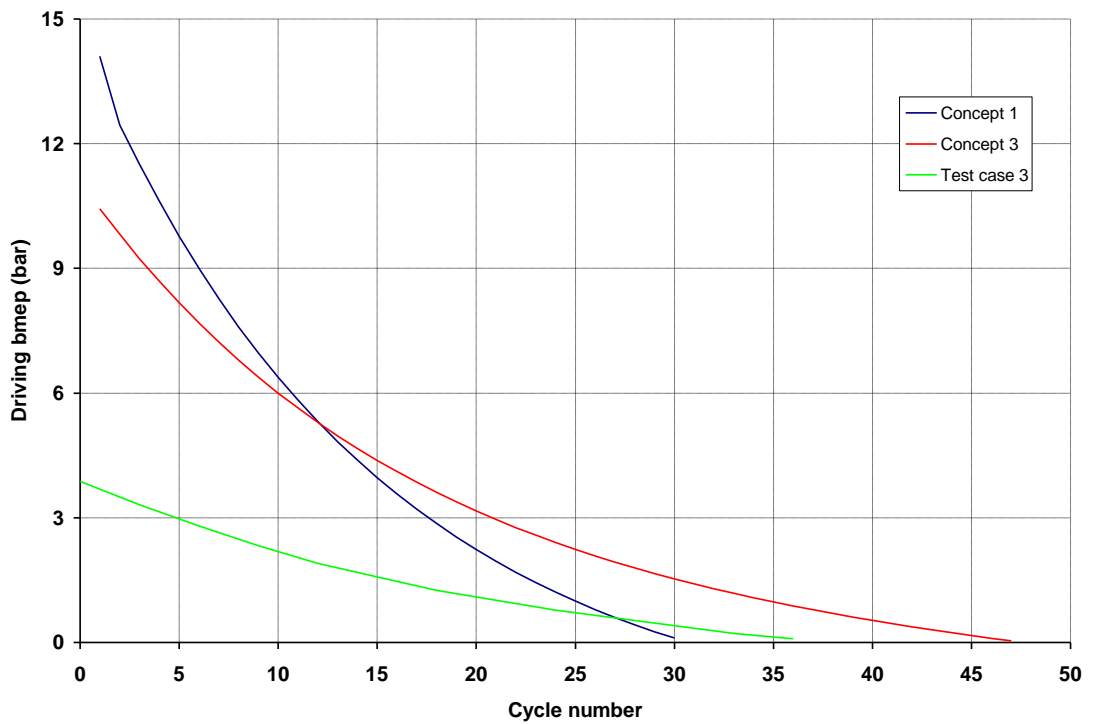


Figure 5.39: Predicted $bmep_d$ results for concepts 1 and 3 and experimental $bmep_d$ results for test case 3.

The comparison between the predicted bmep_b for the two-stroke air compressor (concept 2) and the measured bmep_b for the two-stroke air compressor (test case 2), shown in Figure 5.38, reveals that bmep_b follows the same trend (i.e. it is increasing until it reaches an asymptote). However, the compression ratio of the experimental engine is approximately 2.5 times lower than that of the modelled engine. This has an effect on the absolute values of realized imep_b (and thus bmep_b), as shown in the above diagram. Furthermore, it can be seen that the produced bmep_b for the modelled engine is rising with increasing engine speed, as a result of the growing fmep_b which is added on the produced imep_b . On the other hand, the intake, exhaust and gas transfer systems of the experimental engine were not optimized and therefore the volumetric efficiency of the engine dropped significantly at high engine speeds, decreasing the efficiency of the gas transfer process and consequently decreasing bmep_b .

One last comparison has to be made between the predicted and measured bmep_d for the four-stroke air expander. As shown in Figure 5.39, bmep_d in concepts 1 and 3, as well as in test case 3, follows the same decreasing trend, although it drops more rapidly in the modelled concepts than in the experimental case. However, the experimentally realized bmep_d is lower than the predicted one. The significantly reduced expansion ratio of the test engine and the reduced initial airtank pressure are the two main reasons for the low levels of the produced bmep_d . Initial airtank pressure in test case 3 (11 bar) is only 55% of the initial pressure of the modelled airtank in concepts 1 and 3 (20 bar). Furthermore, the cylinder of the modelled engine has a capacity (and thus a displacement volume) of 500 cm^3 , which is more than 8% larger than the displacement volume of the test engine 458 cm^3 , resulting in higher realized imep_d (and thus bmep_d). Finally, it can be seen that bmep_d in concepts 1 and 3, as well as in test case 3, is sustainable for approximately the same number of engine cycles.

5.8. Summary

Details of the single cylinder research engine and the Lotus AVT system that was used for all of the experimental tests have been presented in the current Chapter. Significant upgrades to the cylinder head and valve actuation system, which have been undertaken in order to ensure precise control of engine valves and therefore enable the realization of air compressor and air expander cycles in four strokes and in two strokes, were also described

in detail. The aforementioned modifications included the connection of the twin exhaust ports with two separate pipes; one for exhaust and one for gas transfer. In-cylinder and airtank pressure, as well as transferred air temperature measurement systems were installed in order to accurately record the effects of changing the intake and gas transfer valve timings, as well as engine speed. The investigation eventuated in the realization of the optimal valve timing for each one of the three test cases.

The acquired data were processed in order to monitor the variation of airtank pressure and imep throughout a number of engine cycles. The comparison between airtank pressure and imep variation indicated that they both are strong functions of cycle number (and thus time). In addition, imep is greatly influenced by airtank pressure. Another important conclusion that derives from the comparison of the experimental results of test cases 1 and 2 is that there is no compressed air transfer from the cylinder to the airtank at high engine speeds when the engine is operated as a two-stroke air compressor. However, the airtank can be charged efficiently at high engine speeds when the engine is operated as a four-stroke air compressor. Additionally, the comparison between two-stroke and four-stroke air compressor modes in regards to the variation of imep_b reveals that in both cases there no significant imep_b variation throughout a number of engine cycles at high engine speeds (3000 – 4000 rpm).

It should be also noted at this point that imep_b values are similar in both test cases. However, indicated braking torque is approximately doubled in the case of the two-stroke air compressor, as the developed imep_b is realized within 360° crank angle (one crankshaft revolution). The experimental results from test case 3 (air expander mode) indicated that an airtank of 11.3 litre, charged at 11.5 bar, is only sufficient to power the engine for a limited number of cycles. Compressed air of less than 3.7 bar pressure has proved not to be useable. Table 5.3 summarizes the experimental results and displays a comparison between the three test cases in regards to the performed bmep_b and bmep_d.

Table 5.3: Comparison of braking and driving performance among the three test cases.

4-stroke air compressor	2-stroke air compressor	4-stroke air expander
bmep _b	bmep _b	Bmep _d
3 - 6.5 bar	2.5 - 9.5 bar	4 - 0 bar
0 - 1000 cycles	0 - 1000 cycles	0 - 37 cycles
1000 - 4000 rpm	1000 - 4000 rpm	1000 rpm

Finally, a comparison between the predicted and the experimental results was made. It was concluded that experimentally realized braking and driving bmep was lower than the predicted. This is not only due to the different valve operation strategies followed and the various operational restrictions that the experimental engine could not overcome, but also due to the different cylinder capacities and thermodynamic properties between the modeled and the experimental engine.

Chapter 6: Vehicle Simulation

6.1. Introduction

It has been discussed in Chapter 4 that the overall efficiency of conventional IC engines can be calculated from the thermodynamic cycles and the properties of the working fluid. However, the operating mode of a hybrid engine must be switched between air expander and air compressor in order to achieve maximum overall efficiency, as well as optimal airtank refilling and compressed air expenditure over a specific driving cycle. The selection of the current operating mode for each one of the engine cylinders (normal firing, compressor, expander) is performed by the engine controller. Therefore, overall efficiency not only depends on the thermodynamic cycle but also on the driving cycle itself and the engine control strategy.

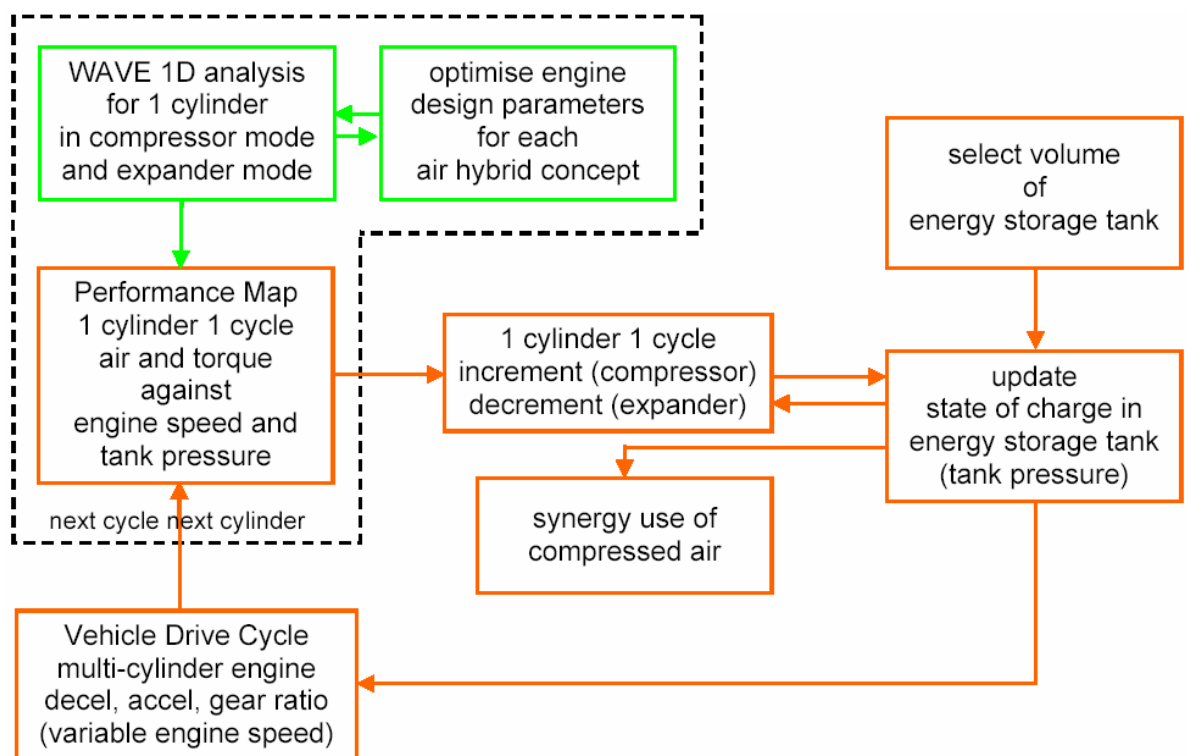


Figure 6.1: Schematic diagram of the procedure tree used for vehicle simulation.

The diagram in Figure 6.1 shows the connection between the tasks comprising the present vehicle simulation. It describes how the engine modelling results (in the form of performance maps for one engine cylinder and one cycle) are used in the driving cycles. The procedure is discussed in details below.

6.2. Driving cycles

A driving cycle is a standardized driving pattern which is described by means of a velocity – time table. The track that is to be covered is divided into time-steps, mostly seconds. Consequently, vehicle speed during a time step is a linear function of time. Provided that speed and acceleration are known for each point of time, the required mechanical power as a function of time can be determined by means of mathematic equations, which are discussed in section 6.3 below. This function integrated over the duration of the driving cycle produces the mechanical energy needed for the specific driving cycle. Apart from driving the vehicle in actual driving conditions, a driving cycle may be simulated on a rolling road. In the case of ICE-driven vehicles, the fuel consumption and emissions are directly measured. The same holds for the fuel conversion system of hybrid-engine driven vehicles, where primary energy can be calculated from the fuel consumption. The overall efficiency of the driving system is determined by dividing the mechanical energy output by the primary energy supplied to the vehicle. There are three main driving cycles used worldwide:

- i) European driving cycles
- ii) US driving cycles
- iii) Japanese driving cycles

6.2.1 European driving cycles

6.2.1.1. ECE 15

This driving cycle belongs to the modal cycles and represents urban driving. This means that there are parts within the cycle where vehicle speed is constant. Modal cycles do not represent real driving patterns. It is characterized by low vehicle speed (maximum 50 km/h), low engine load and low exhaust gas temperature. The cycle pattern can be seen in Figure A6 in the Appendix.

6.2.1.2. EUDC

This driving cycle also belongs to the modal cycles and describes a suburban route. At the end of the cycle the vehicle accelerates to highway speed. Both speed and acceleration are higher than the ECE 15 but it still is a modal cycle. The cycle pattern can be seen in Figure A7 in the Appendix.

6.2.1.3. EUDCL

The EUDCL is a suburban cycle for low-powered vehicles. It is similar to the EUDC but maximum vehicle speed is 90 km/h. The cycle pattern can be seen in Figure A8 in the Appendix.

6.2.1.4. NEDC

This is a combined cycle consisting of four ECE 15 cycles followed by an EUDC or EUDCL cycle. It represents the typical usage of a car in Europe and it is used, among other purposes, to assess the emission levels of car engines. The NEDC is also referred as ECE cycle and it is the official driving cycle used in the EU for light duty vehicles. The cycle pattern can be seen in Figure A9 in the Appendix.

6.2.1.5. HYZEM

The cycles mentioned above are stylistic cycles, which means that they can not represent real driving patterns. The HYZEM cycle is a transient cycle. The parts at which the speed is constant are much smaller than in modal cycles. The HYZEM cycle is derived from real driving patterns throughout Europe. Therefore, it is a better representation for driving conditions than the standard European cycles. The HYZEM cycle is often used but it is not official. It consists of an urban cycle, an extra-urban cycle, and a highway cycle and it is nearly similar to FTP-75 cycle below.

6.2.2. US driving cycles

These driving cycles are transient and they give a better representation of real driving patterns than the modal cycles. The following subdivision can be made:

6.2.2.1. NYCC

This cycle represents an urban route through the city of New York and it is characterized of low average vehicle speed. The cycle pattern can be seen in Figure A10 in the Appendix.

6.2.2.2. FTP-72

In the early seventies this cycle has been developed to describe an urban route. The cycle consists of a cold start phase. This phase is followed by a transient phase with many speed

peaks which start from rest. The FTP-72 is often referred as FUDS, UDDS or LA-4. The cycle pattern can be seen in Figure A11 in the Appendix.

6.2.2.3. LA-92

The LA-92 represents an urban route, similar to the FTP 72. The LA-92 has been developed in 1992, because the existing FTP 72 turned out to be a non-realistic representation of urban driving patterns. For example the LA-92 has a higher average speed. The cycle pattern can be seen in Figure A12 in the Appendix.

6.2.2.4. US-06

This is the so called aggressive driving cycle. It is developed to describe a driving pattern with high engine loads. The cycle pattern can be seen in Figure A13 in the Appendix.

6.2.2.5. FTP-75

The FTP 75 is similar to FTP-72 with an extra third phase. This phase is identical to the first phase of the FTP-72 but is performed with a hot engine. The FTP 75 is the official driving cycle used in the USA. The cycle pattern can be seen in Figure A14 in the Appendix.

6.2.3. Japanese driving cycles

6.2.3.1. 10 Mode

This driving cycle belongs to the modal cycles and represents an urban driving route. The cycle pattern can be seen in Figure A15 in the Appendix.

3.3.3.2 15 Mode

This is a combination of an urban and an extra-urban route. The maximum speed is 70 km/h. The cycle pattern can be seen in Figure A16 in the Appendix.

3.3.3.3 10-15 Mode

This is a combination of five cycles. First the 15-Mode, then three times 10-Mode and at last again the 15 Mode. The 10-15 Mode is the official driving cycle used in Japan. The cycle pattern can be seen in Figure A17 in the Appendix.

6.3. Vehicle and driveline model

In order to calculate the engine braking torque (during decelerations) or driving torque (during accelerations) demand throughout a driving cycle, a dynamic vehicle model has to be used. The balance of the forces that control the motion of the vehicle can be expressed by the following Equation, which is an application of the second Newtonian law:

$$\sum \vec{F}_x = \vec{F}_r + \vec{F}_a + \vec{F}_w + \vec{F}_b = m_v \times \vec{a} \quad \text{Equation 6.1}$$

where m_v is the vehicular mass, a is the vehicle acceleration, F_r is the rolling drag force, F_a is the aerodynamic drag force, F_w is the wheel force and F_b is the brake force. Each one of the above terms is analyzed in detail below.

6.3.1. Acceleration

The acceleration of the vehicle during each time step of the driving cycle is assumed to be constant. It is calculated by the average vehicle speed during the corresponding time step, as described by Equation 6.2:

$$\vec{a} = \frac{d\vec{u}}{dt} = \frac{\vec{u}_2 - \vec{u}_1}{t_2 - t_1} \quad \text{Equation 6.2}$$

where u is the vehicle speed in metres and t is time in seconds. It is obvious that is positive during accelerations (when the vehicle speed difference $u_2 - u_1$ is positive) and negative during decelerations (when the vehicle speed difference $u_2 - u_1$ is negative).

6.3.2. Rolling drag force

The friction developed by a rolling tire is caused by the bonding between the tire tread and the aggregate in the road surface. In other words, in a molecular level, the rubber tends to flow into and over the “peaks and valleys” on the road surface. The resulting rolling drag force, developed by the tires’ rolling friction to the road is computed by Equation 6.3:

$$\vec{F}_r = m_v \cdot \vec{g} \cdot C_r \quad \text{Equation 6.3}$$

where m_v is the vehicular mass in kg, g is the gravitational acceleration and C_r is the rolling resistance coefficient, which is defined according to the following Equation:

$$C_r = u^5 \cdot C_5 + u^4 \cdot C_4 + u^3 \cdot C_3 + u^2 \cdot C_2 + u \cdot C_1 + C_0 \quad \text{Equation 6.4}$$

where $C_0, C_1, C_2, C_3, C_4, C_5$ are the coefficients which define the tire rolling resistance via a curve-fitted, 5th order polynomial. Typical values are $2 \cdot 10^{-14}$, $2 \cdot 10^{-12}$, $8 \cdot 10^{-11}$, $4 \cdot 10^{-6}$, $6 \cdot 10^{-5}$ and 0.011 respectively, based on vehicle speed in km/h [86].

6.3.3. Aerodynamic drag force

The aerodynamic drag is caused as viscous air flows past and over a moving vehicle and is defined as in Equation 6.5:

$$\vec{F}_a = \frac{1}{2} \cdot \rho_a \cdot \vec{u}^2 \cdot A_v \cdot C_D \quad \text{Equation 6.5}$$

where C_D is the aerodynamic drag coefficient, which is a measure of the effectiveness of a streamline aerodynamic body shape in reducing the resistance of the air to the forward motion of a vehicle. The typical range of C_D is between 0.22 and 0.4 for passenger cars [87]. A_v is the vehicle frontal area and ρ_a is the density of air, which is dependent on the air pressure and temperature, as described by the following Equation:

$$\rho_a = \frac{P}{R \cdot T} \quad \text{Equation 6.6}$$

where p is the air pressure, T is the air temperature and R is the universal gas constant and equals $287.05 \left[\frac{J}{kg \cdot K} \right]$. Therefore, dry air has a density of 1.168 kg/m^3 at standard ambient temperature and pressure ($25 \text{ }^\circ\text{C}$ and 10^5 Pa respectively).

6.3.4. Wheel force

The driving force acting on the wheels is applied perpendicular to the wheel radius at the point of contact with the road. The direction of the force depends on whether the vehicle is accelerating (where the engine propels the drivetrain) or decelerating (where the drivetrain motors the engine). Therefore, the engine brake work depends on the direction of the power flow. Power losses in drivetrains, associated principally with tooth friction, must be taken into account at this point. The frictional losses are strongly dependent on the arrangement of the gear train and the reduction ratios, gear size, as well as the assumed

average value of the coefficient of friction, which is based on the materials involved and the lubricant. Wheel force is given by Equation 6.7:

$$\vec{F}_w = \frac{k_g \cdot k_{fd} \cdot \eta_g \cdot \eta_{fd}}{2 \cdot \pi \cdot r_w} \cdot \vec{W}_b \quad \text{Equation 6.7}$$

where k_g is the ratio of the selected gear, k_{fd} is the ratio of the final drive, η_g is the mechanical efficiency of the selected gear and η_{fd} is the mechanical efficiency of the final drive. Typical values of mechanical efficiency have been the subject of considerable investigation by many researchers and are 0.95 for final drives and 0.97 for transmission gears [88-91]. W_b is the brake work produced by the engine and r_w the wheel radius, measured from the centre of the wheel to the tyre circumference.

6.3.5. Brake force

The brake force, produced by the mechanical brake system of the vehicle, is an unsteady term which only exists to close the balance of the forces acting on the vehicle in case of strong deceleration, when engine braking is insufficient.

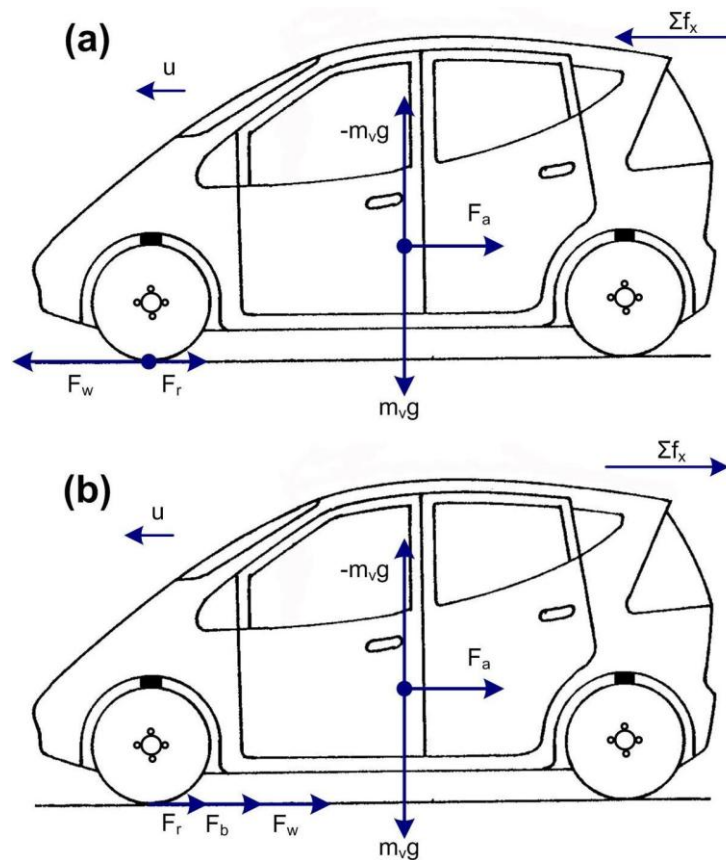


Figure 6.2: Free body diagram of a vehicle under acceleration (a) and deceleration (b).

When a vehicle is under acceleration, as shown in Figure 6.2a, the balance of the forces acting on the vehicle is described by Equation 6.8. When a vehicle is under deceleration, as shown in Figure 6.2b, the balance of the forces acting on the vehicle is described by Equation 6.9.

$$F_w - F_r - F_a = m_v \cdot a \quad \text{Equation 6.8}$$

$$F_w + F_r + F_a + F_b = -m_v \cdot a \quad \text{Equation 6.9}$$

As already mentioned in paragraph 4.3, the term “braking” is used to express the flow of energy from the vehicle to the engine and therefore means that the engine is being motored when the vehicle is braking (compression brake). The term “driving” is used to express the flow of energy from the engine to the vehicle and therefore means that the engine drives the vehicle when the later is coasting or accelerating. Subsequently, the terms “braking torque” and “driving torque” refer to the engine brake torque (measured at the engine shaft) during braking and driving respectively. Because all quantities are given here in respect of the vehicle (the vehicle is used as the reference rather than the engine), all driving terms are positive, while all braking terms are negative.

6.4. Airtank pressure and temperature model

In order to sufficiently predict the behaviour of the air hybrid engine throughout the driving cycle, the numerical model of mass and energy transfer between the cylinder and the airtank needs to be defined. Although ambient air is not an ideal gas, its properties are assumed to be very close to those of ideal gases and therefore are regarded to follow the ideal gas law, which is the equation of state of a hypothetical ideal gas. The state of an amount of gas is determined by its pressure, volume, and temperature according to Equation 6.10:

$$p \cdot V = m \cdot R \cdot T \quad \text{Equation 6.10}$$

where p is the absolute pressure, V is the volume, m is the mass and T is the temperature of the gas. Subsequently, airtank pressure at the end of each braking and driving engine operation is described by Equations 6.11 and 6.12 respectively:

$$p_t = \frac{(n_t + m_c) R \cdot T_t}{V_t} \quad \text{Equation 6.11}$$

$$p_t = \frac{(n_t - m_c) R \cdot T_t}{V_t} \quad \text{Equation 6.12}$$

where m_c is the mass of the transferred air charge, m_t is the mass of compressed air stored in the airtank, V_t is the airtank volume and T_t is the compressed air temperature inside the airtank.

The thermodynamic processes that take place in the airtank and the engine cylinders are of unsteady state. The airtank and cylinders can be assumed to constitute a closed system. Because the airtank volume is much larger than the cylinder volume, the variation of the cylinder volume can be ignored to simplify the calculations. The cylinder volume is therefore included to the airtank volume. It is also assumed that the whole system (airtank, piping and engine cylinder) is thermally isolated. Consequently, during the airtank charging process, the energy equation for the airtank can be written as follows, by assuming that the process is adiabatic:

$$dm_c \cdot h_c = m_{t_2} \cdot u_{t_2} - m_{t_1} \cdot u_{t_1} \quad \text{Equation 6.13}$$

where m_c and h_c are the mass and the specific enthalpy of the air charge transferred to the airtank respectively, m_{t_2} and u_{t_2} are the mass and the specific internal energy of the compressed air inside the airtank at the end of the compression process (final state) and m_{t_1} and u_{t_1} are the mass and the specific internal energy of the compressed air inside the airtank in the beginning of the compression process (initial state).

Since the mass is conserved, $m_{t_2} - m_{t_1} = dm_c$ and hence Equation 6.13 can be written as:

$$\begin{aligned} dm_c \cdot C_p \cdot T_c &= m_{t_2} \cdot C_v \cdot T_{t_2} - (m_{t_2} - dm_c) \cdot C_v \cdot T_{t_1} \\ \Leftrightarrow (C_p \cdot T_c - T_{t_1}) \cdot dm_c &= m_{t_2} \cdot (C_{t_2} - T_{t_1}) \cdot dT_t \\ \Leftrightarrow T_t &= \int \frac{\gamma \cdot T_c - T_{t_1}}{m_t} dm_t \end{aligned}$$

$$T_t = \int \frac{\gamma \cdot T_c - T_{t_1}}{m_t} dm_t \quad \text{Equation 6.14}$$

where C_v is the specific heat capacity at constant volume, C_p is the specific heat capacity at constant pressure, T_c is the average temperature of the air charge during compression, m_t is the mass of the compressed air in the airtank, T_{t1} is the initial tank temperature (at the beginning of the compression process) and T_{t2} is the final tank temperature (at the end of the compression process).

Similarly, during the airtank discharging process, the energy equation for the airtank is given by Equation 6.15:

$$dm_c \cdot h_c = m_{t1} \cdot u_{t1} - m_{t2} \cdot u_{t2} \quad \text{Equation 6.15}$$

Since the mass is conserved, $m_{t1} - m_{t2} = dm_c$. Considering that the air charge temperature is equal to the airtank temperature at the initial stage of the expansion process ($T_c = T_{t1}$), Equation 6.15 can be written as:

$$T_c \cdot \gamma \cdot dm_c = m_{t2} \cdot T_{t1} + dm_c \cdot T_{t1} - m_{t2} \cdot T_{t2} + dm_c \cdot C_p \cdot T_{t2}$$

$$\Leftrightarrow dT_t = \left(\gamma \cdot T_c - T_{t1} \right) \frac{dm_c}{m_t}$$

$$\Leftrightarrow T_t = \int \frac{\left(\gamma - 1 \right) T_{t1}}{m_t} dm_t$$

$$T_t = \int \frac{\left(\gamma - 1 \right) T_{t1}}{m_t} dm_t \quad \text{Equation 6.16}$$

6.5. Response maps

As it can be seen in Figure 6.1, engine response maps are used to feed the numerical models of the driveline and the airtank with engine torque (T), transferred air mass (m), air charge pressure (p) and air charge temperature (t) values for an instantaneous airtank pressure and engine speed, in order to update the state of the engine and the airtank for a given time instance. Airtank pressure and engine speed between two time instants are assumed to be constant. Table 6.1 shows two different templates of a response map. The upper map is for the air compressor mode (CM), while the lower map is for air expander mode (EM). The difference between the two maps relies on the engine speed range, as the air expander is operated at a lower engine speed range than the air compressor. Four

different maps are required for each one of the operating modes; an engine torque map (driving or braking), a compressed air charge mass map, a compressed air charge average pressure map and a compressed air charge average temperature map. Therefore, eight maps are required to fully feed the numerical models of the engine and the airtank; a set of four maps for air CM and another set of four maps for air EM. Each map has 7 engine speed points (x-axis) and 5 airtank pressure points (y-axis). Therefore, there are 35 $f_{(x,y)}$ grid elements. For intermediate x and y points, $f_{(x,y)}$ can be calculated by means of interpolation. The response maps are generated by running steady-state simulations of the modelled engine in Ricardo's WAVE software for predefined engine speeds and airtank pressures and arranging the results of interest in tables.

Table 6.1: Response map template for air compressor mode (upper) and air expander mode (lower).

		Engine speed (rpm)						
		1000	1500	2000	2500	3000	3500	4000
Airtank pressure (bar)	5							
	10	Grid of engine torque (T) / transferred air mass (m) / air charge pressure (p) / air charge temperature (t)						
	15							
	20							
	25							

		Engine speed (rpm)						
		10	20	50	100	200	500	1000
Airtank pressure (bar)	5							
	10	Grid of engine torque (T) / transferred air mass (m) / air charge pressure (p) / air charge temperature (t)						
	15							
	20							
	25							

6.6. Vehicle simulation

The driving cycles, the response maps, as well as the driveline and airtank models are linked together to a Matlab-based vehicle simulation code in order to define the optimal strategy for switching from normal firing mode to air hybrid mode (air compressor or air expander). Individual cylinder deactivation or mode switching is also possible, provided that it is allowed by the engine's hardware. Therefore, the amount of energy (and thus fuel) which can be conserved by means of engine hybridization can be estimated for a specific driving cycle. In addition, further fuel economy improvement is achieved by means of stopping the engine when the vehicle is stationary (i.e. while idling in front of a traffic

light). Although no energy can be stored and regenerated during periods of engine idling, fuel saving and exhaust gas emission reduction is significant, especially in congested urban driving conditions, where idling periods suggest an important percentage of the total driving cycle period [92].

The vehicle simulation code is divided into four routines:

- a. Definition of the gear shift pattern for each driving cycle, as well as definition of the engine hybridization strategy.
- b. Acquisition of user-defined inputs.
- c. Data process
- d. Extraction of the simulation results

6.6.1. Gear shift pattern and simulation decision diagram

The gear shift pattern that is adopted for the vehicle simulation is predetermined, as shown in Figures 6.3a and 6.3b below. It is also assumed that the clutch disengages the engine from the transmission when vehicle is stopped or when the vehicle speed is too low (<7 km/h) to obtain the minimum (idle) engine speed with the first gear selected to the gearbox. Each one of the aforementioned inputs is stored within the Matlab code as a separate variable and can be changed each time that the simulation runs.

The mode under which the engine should be operated, as well as the number of engine cylinders to be used for normal firing mode, CM or EM (where individual cylinder operation and/or cylinder deactivation is applicable) are defined in such a way that the following equality is satisfied:

$$\sum_{\text{firing cylinders}} W_{b, \text{ firing}} + \sum_{\text{compressor cylinders}} W_{b, \text{ braking}} + \sum_{\text{exp ander cylinders}} W_{b, \text{ driving}} = W_{b, \text{ required}} \quad \text{Equation 6.17}$$

where $W_{b, \text{ firing}}$ is the brake work produced by each firing cylinder, $W_{b, \text{ braking}}$ is the braking work produced by each cylinder operated in CM, $W_{b, \text{ driving}}$ is the driving work produced by each cylinder operated in EM and $W_{b, \text{ required}}$ is the brake work required on the engine shaft, which is calculated through Equation 6.1.

The simulation strategy followed to control the hybridization of the engine throughout a driving cycle is shown in Figure 6.4. It can be seen that primarily the vehicle kinetics is examined by looking at the vehicle speed and acceleration at each time instant:

- a. If $a = 0$ and $u = 0$ then the vehicle is stopped
- b. If $a = 0$ and $u > 0$ then the vehicle is coasting
- c. If $a < 0$ and $u > 0$ then the vehicle is decelerating
- d. If $a > 0$ and $u > 0$ then the vehicle is accelerating

In case a, where the vehicle is stopped, the engine is switched off. This yields important benefits to fuel economy. In case b, where the vehicle is coasting at constant speed, only normal firing mode can be used for all cylinders. Here, cylinder deactivation could be possible. However, this would create serious engine balancing problems. In case c, where the vehicle is decelerating, the torque demand on the wheel shaft is examined. Due to aerodynamic and rolling forces acting on the vehicle, engine driving power may be still needed during mild decelerations. If this is the case, the engine continues to operate in normal firing mode. However, during rapid decelerations, where braking work is required (the torque demanded on the wheel shaft is negative), the engine is operated in CM to satisfy the condition of the Equation 6.17, provided that the required braking work is higher than the minimum achievable by one engine cylinder. The frictional work of the deactivated cylinders is also taken into consideration. If the resulting braking torque on the wheel shaft is not enough to meet the braking demand, a small part of the braking work is done by the mechanical brakes which are applied by the driver in order for the forces to reach the equilibrium described in Equation 6.1. Finally, in case d, where the vehicle is accelerating, the state of charge (SOC) of the airtank is examined. It has been mentioned in Chapter 4 that no driving torque can be produced if the SOC of the airtank has reached a minimum limit (2 – 5 bar, depending on the hybrid engine concept). If the SOC of the airtank is too low to start the engine and power the vehicle, then normal firing mode is used. However, if there is sufficient airtank pressure available, one or more engine cylinders can be used in EM to meet the driving torque requirement. If the produced driving torque is lower than the demanded, then a part of the driving work is done by the firing cylinders in order to satisfy the condition described in Equation 6.17. The aforementioned decision diagram is used at each time instant of the driving cycle in order to update the operational mode of the engine.

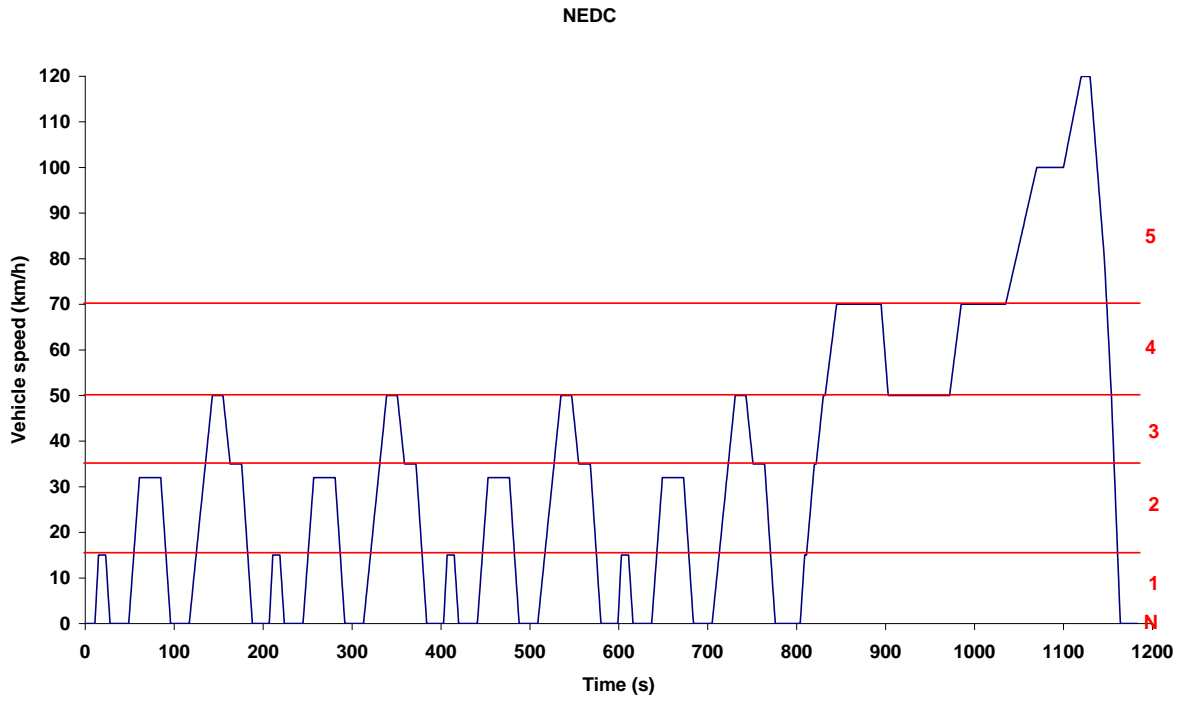


Figure 6.3a: Gear shift pattern for the EUDC [93-95].

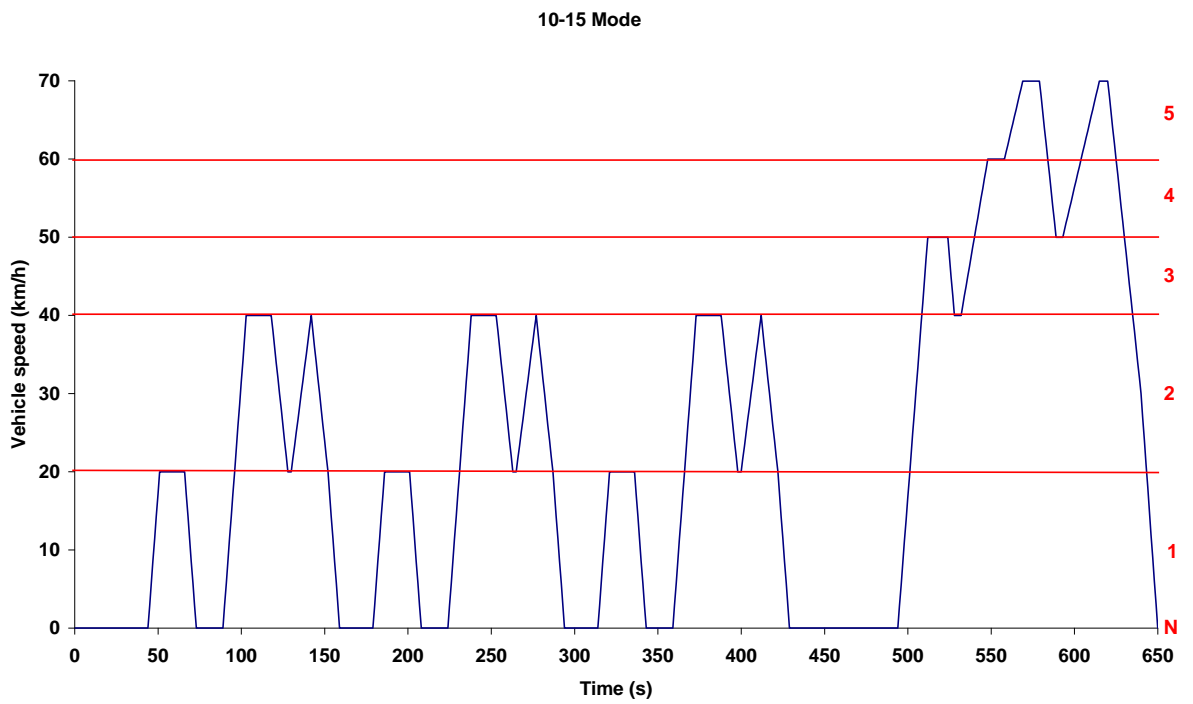


Figure 6.3b: Gear shift pattern for the 10-15 Mode driving cycle [93-95].

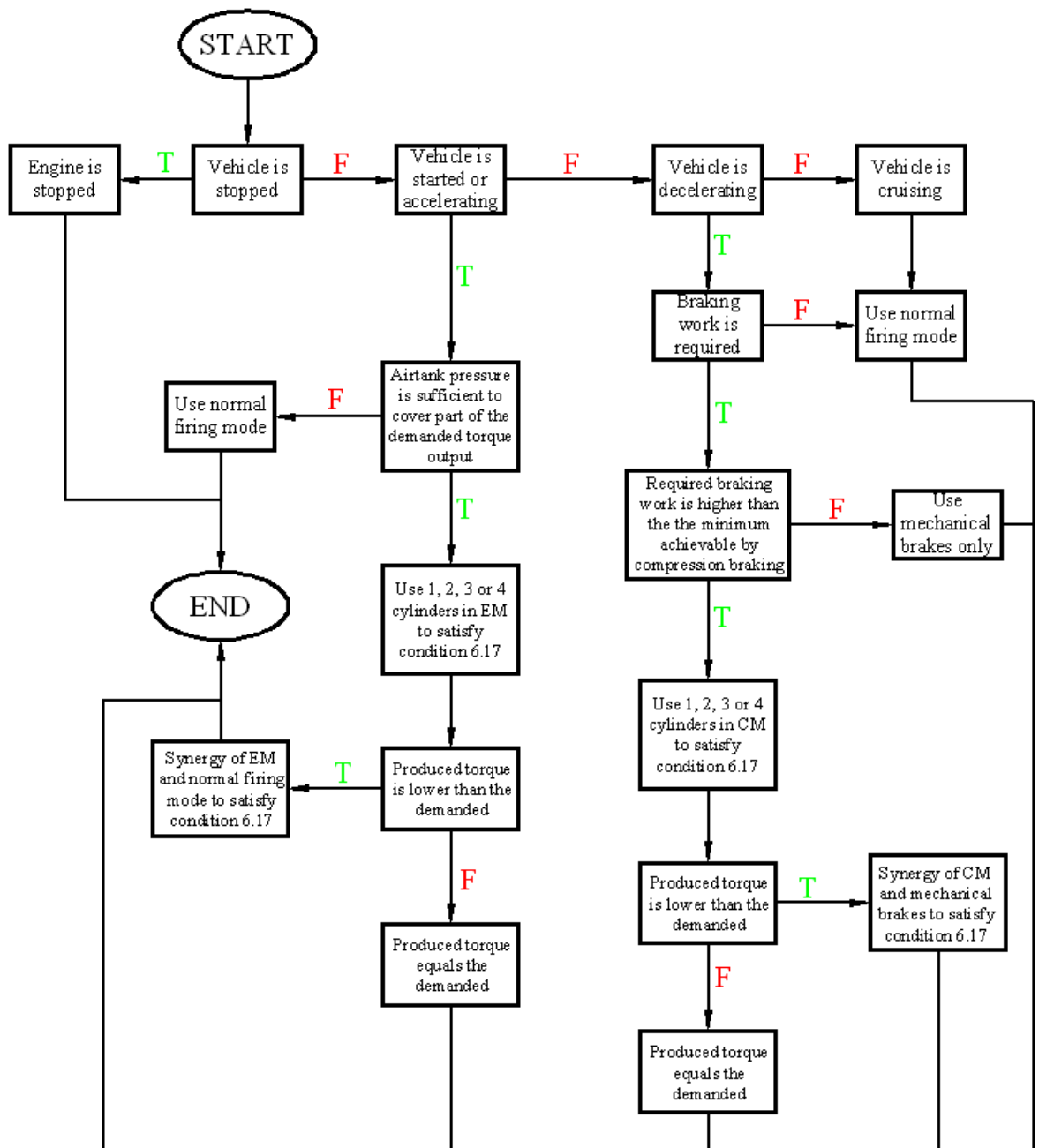


Figure 6.4: Decision diagram.

6.6.2. Acquisition of user-defined inputs

Initially, the user defines the driving cycle to be followed. The available driving cycles to choose from are listed in section 6.2. Only one driving cycle can be loaded by the code per time. The time-speed data points for each driving cycle, contained in a separate Microsoft Excel file, are loaded in a Matlab table of 2 columns and i rows (where i is the number of time-speed data points comprising the driving cycle). Two modal cycles were selected for the present study; the European NEDC and the Japanese 10-15 Mode. The response maps for braking and driving modes need to be specified by the user at this point. Each one of the 8 response maps required for describing the variables of interest in CM and EM is

contained in a separate Microsoft Excel file, which is loaded in an 8x6 Matlab table. The first row and first column contain the engine speed and airtank pressure points respectively, while the leftmost upper cell is empty as shown in Table 6.1. Ambient temperature and pressure, as well as initial airtank temperature and pressure, vehicular mass, vehicle frontal area, aerodynamic drag coefficients, air density, gear ratios, final drive ratio, gear mechanical efficiency, final drive mechanical efficiency and tyre radius are also need to be defined.

Table 6.2: Engine, vehicle and driveline parameters.

Engine		Vehicle		Driveline		
No. of cylinders	4	Mass	1250 kg		Ratio	Efficiency
Displacement	2000 cm ³	Frontal area	2 m ²	1 st gear	3.55	0.97
Geometric compression ratio	18.4:1	Drag coefficient	0.35	2 nd gear	2.16	0.97
Speed range	1000-4000 rpm			3 rd gear	1.48	0.97
Airtank				4 th gear	1.12	0.97
Airtank volume	40 l			5 th gear	0.89	0.97
Initial temperature	300 °K			Final drive	3.55	0.95
Initial pressure	10 bar			Wheel radius	0.284 m	

A 2-litre, four-cylinder engine was assumed for the vehicle simulations described below. The engine has the same operating characteristics and parameters (such as geometry and compression ratio) as modelled in Chapter 4. Thus, the displacement volume of each cylinder is 0.5 litre. Therefore, the airtank is assumed to have a capacity of 40 litres (four times larger than modelled in Chapter 4) in order to comply with the modelled air hybrid concepts where the response maps are derived from. Here, an initial airtank pressure and temperature of 10 bar and 300 °K respectively are assumed throughout all the implemented simulations. The vehicle is assumed to be a light-duty passenger car with a mass of 1250 kg. The engine, vehicle and driveline parameters used for the present simulation are summarized in Table 6.2 above.

6.6.3. Data processing

Initially, the code calculates the engine speed at each point of time, taking into account either the predefined gear shift pattern or the gear shift strategy described above.

$$N = u_v \cdot \frac{k_g \cdot k_{fd}}{2 \cdot \pi \cdot r_w} \cdot slip \quad \text{Equation 6.18}$$

where *slip* is the coefficient of friction between the tyre and the road, which must be taken under consideration at this point. It is related to tyre's resistance to wheel spin or slip and it is typically close to 0.8 for wheel slip and 1.15 for wheel spin [90,96].

Following from the calculation of engine speed, the code computes the acceleration of the vehicle at each time interval, according to Equation 6.2. Deceleration is regarded as negative acceleration. Rolling drag force and aerodynamic drag force throughout the cycle are also determined according to Equations 6.3 and 6.5 respectively in order to calculate the force on the wheels. Consequently, the braking or driving work (and thus torque) required from the engine is also determined according to Equation 6.7.

Unlike the aforementioned variables, which are updated on a time basis, airtank pressure and temperature are updated on a cycle basis according to Equations 6.11 or 6.12 and 6.14 or 6.16 respectively. In order to transform the cyclic duration into temporal duration for these two variables, Equation 6.19 is used [97].

$$n = \frac{1}{n_R \cdot 60} \cdot \int_{t_1}^{t_2} N(t) dt \quad \text{Equation 6.19}$$

where n is the number of cycles realized within a time period between t_1 and t_2 , N is the engine rotational speed and n_R the number of crank revolutions for each power stroke per cylinder. That is 1 for two-stroke and 2 for four-stroke engines.

6.6.4. Extraction of the simulation results

The output of the simulation is a Matlab table of 19 columns and i rows (where i is the number of time-speed data points comprising the driving cycle). The columns contain data for the following variables: time, vehicle speed, engine speed, selected gear, vehicle acceleration, rolling drag force, aerodynamic drag force, wheel force, mechanical brake force (if applicable), required engine brake torque, number of firing cylinders, brake torque of each firing cylinder, number of cylinders operated in CM, braking torque of each compressor cylinder, number of cylinders operated in EM, driving torque of each expander cylinder, airtank pressure, airtank temperature and CATC. A subroutine transforms cycle-averaged variables to time-averaged variables in order to properly fit in the table in such a way that all variables are ready to be plotted against time. A second subroutine exports the aforementioned data to a Microsoft Excel file in order to make the spreadsheet easily accessible and simplify the calculation of the fuel consumption improvement.

6.7. Simulation results and discussion

6.7.1. Engine speed

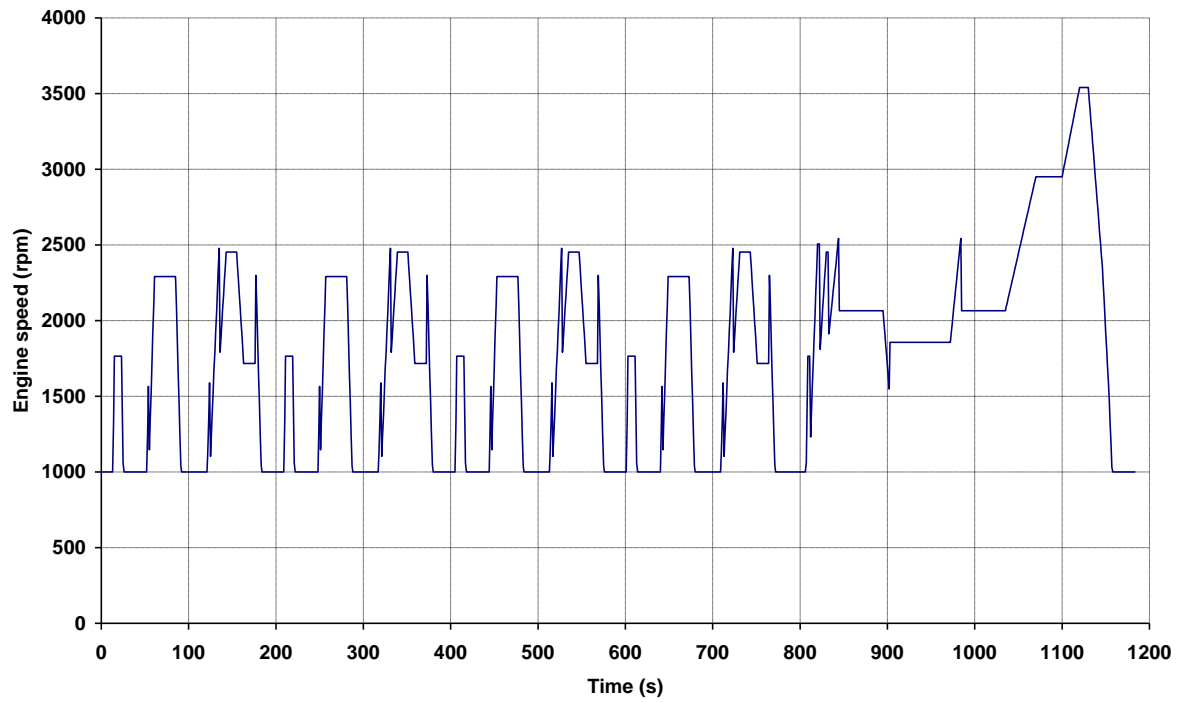


Figure 6.5a: Engine speed throughout the NEDC.

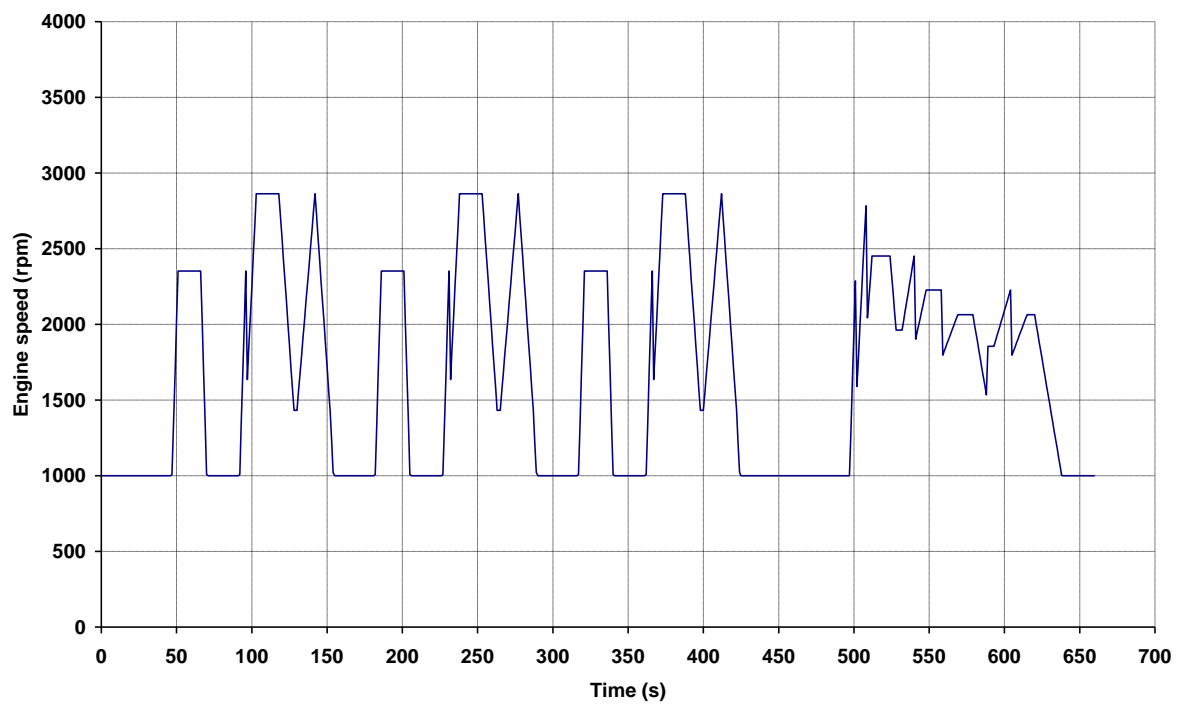


Figure 6.5b: Engine speed throughout the 10-15 Mode driving cycle.

Initially the simulation code was used to determine the engine speed by means of combining the given vehicle speed and the selected gear ratio (according to the gear shift strategy shown in Figures 6.3a and 6.3b) at each point of the NEDC and 10-15 Mode time scale, as in Equation 6.18. The results are shown in Figures 6.5a and 6.5b respectively. It can be observed that the gear shift pattern followed throughout the NEDC limits the maximum operating engine speed at 2500 rpm for the urban driving and 3500 rpm for the extra-urban driving. However, the gear shift pattern followed throughout the 10-15 Mode driving cycle sets the operating engine speed limit close to 2750 rpm for the urban driving and around 2250 rpm for the extra-urban driving conditions.

6.7.2. Torque, power and energy demand

Following from the engine speed, the simulation code was used to determine the required brake torque output (braking or driving) when the vehicle is driven throughout the NEDC and 10-15 Mode driving cycle. The results are shown in Figures 6.6a and 6.6b respectively. It can be seen that, for the NEDC cycle, 74% of the total brake torque demand throughout the cycle is driving torque and 26% is braking torque.

This is due to high vehicle speeds (up to 120 km/h) realized mainly at the extra-urban part of the cycle and the increased aerodynamic and rolling resistance forces that occur. Furthermore, NEDC cycle includes rapid vehicle accelerations and smooth decelerations that require more driving torque and less braking torque.

On the other hand, for the 10-15 Mode cycle, 64% of the total brake torque demand throughout the cycle is driving torque and 36% is braking torque. This is due to the limited vehicle speeds (up to 70 km/h) realized throughout the driving cycle. Furthermore, 10-15 Mode cycle includes smooth vehicle accelerations and rapid decelerations that require less driving torque and more braking torque.

The simulation code was also used to compute the demanded braking and driving power, which is given in respect of braking and driving torque demand, as well as engine speed, as in Equations 6.20 and 6.21 respectively. The results are shown in Figures 6.7a and 6.7b. It can be seen that, for the NEDC cycle, 80% of the total brake power demand throughout the cycle is driving power and 20% is braking power. On the other hand, for the 10-15 Mode cycle, 70% of the total brake power demand throughout the cycle is driving power and 30% is braking power.

$$P_{b, braking} = 2 \cdot \pi \cdot N \cdot T_{b, braking} \quad \text{Equation 6.20}$$

$$P_{b, driving} = 2 \cdot \pi \cdot N \cdot T_{b, driving} \quad \text{Equation 6.21}$$

Finally, the braking and driving energy is computed by integrating the power – time diagrams shown in Figures 6.7a and 6.7b (Equations 6.22 and 6.23). The results indicate that 1210 kJ of braking energy and 4843 kJ of driving energy are required throughout the NEDC, while 719 kJ of braking energy and 1706 kJ of driving energy are required throughout the 10-15 Mode driving cycle.

$$E_b = \sum \int P_{b, braking} dt \quad \text{Equation 6.22}$$

$$E_d = \sum \int P_{b, driving} dt \quad \text{Equation 6.23}$$

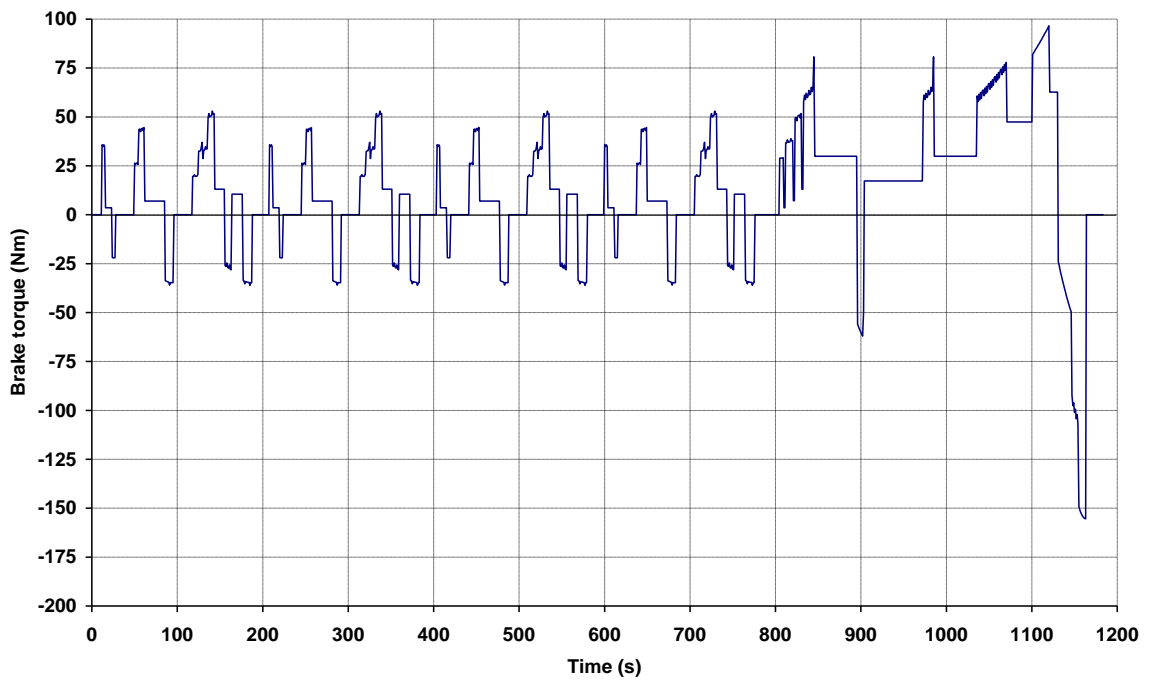


Figure 6.6a: Brake torque output demand throughout the NEDC. Braking torque is negative, while driving torque is positive.

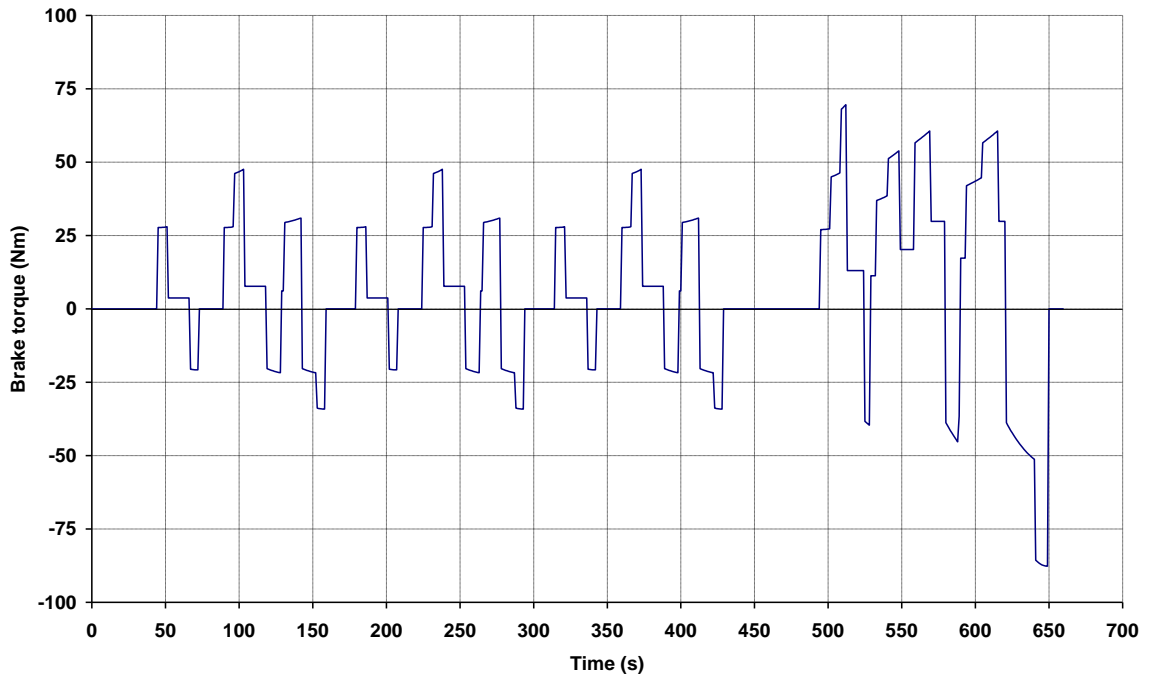


Figure 6.6b: Brake torque output demand throughout the 10-15 Mode driving cycle.
Braking torque is negative, while driving torque is positive.

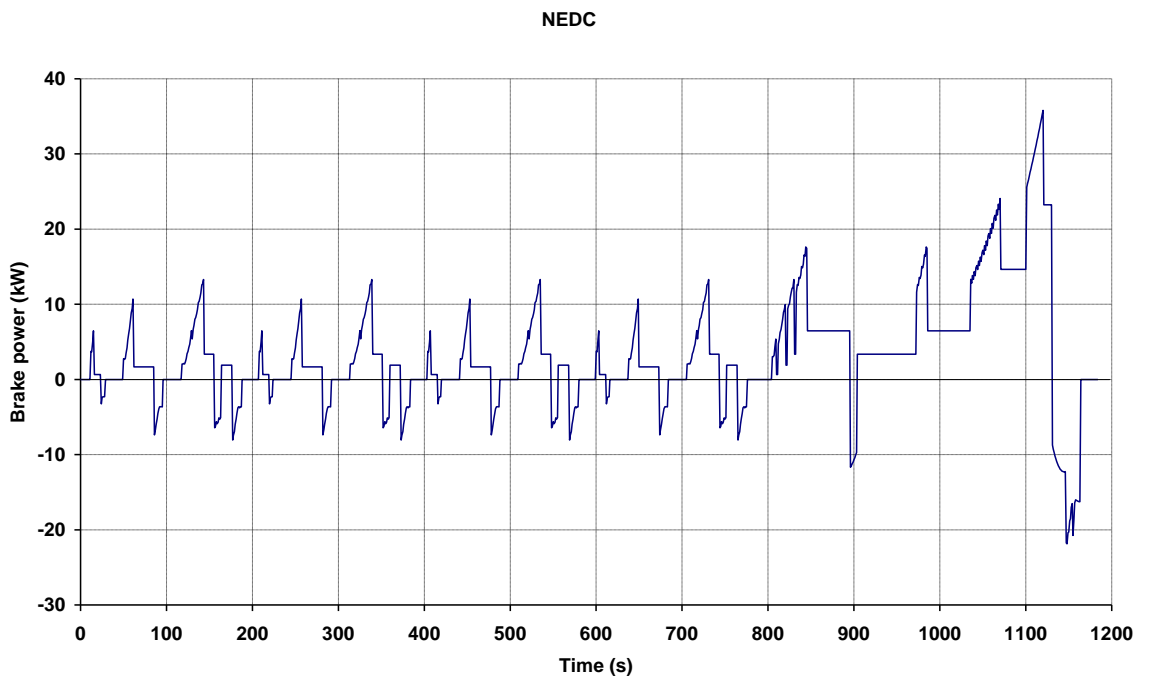


Figure 6.7a: Brake power demand throughout the NEDC. Braking power is negative, while driving power is positive.

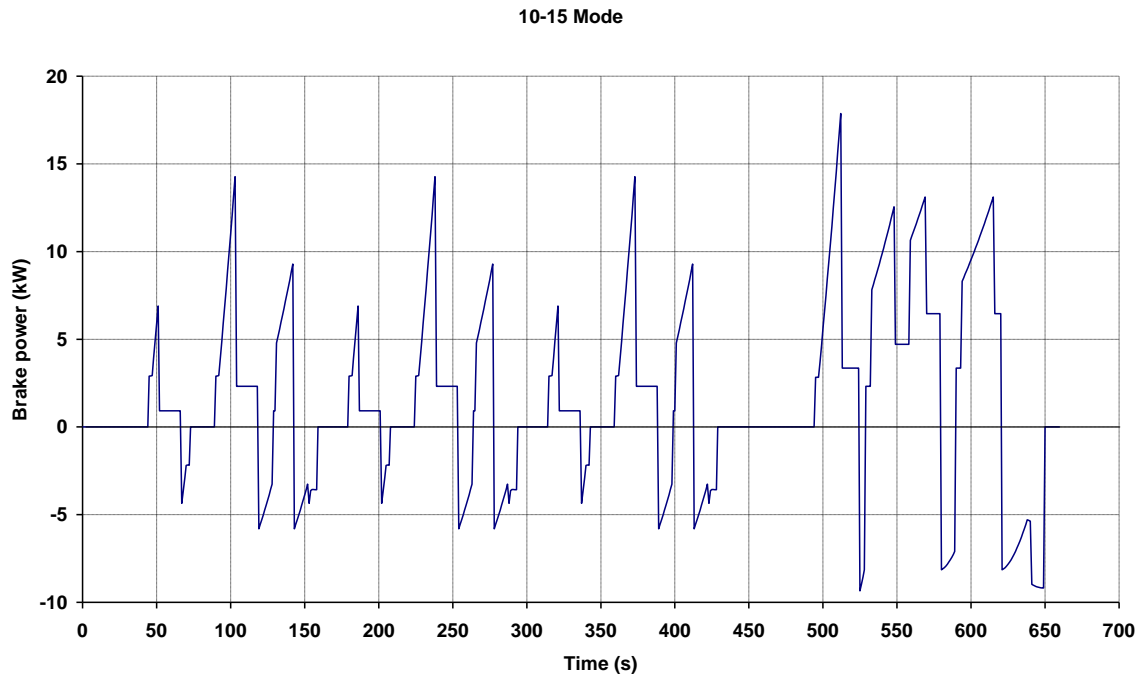


Figure 6.7b: Brake power demand throughout the 10-15 Mode driving cycle. Braking power is negative, while driving power is positive.

6.7.3. Braking energy recovered and driving energy generated

Figures 6.8a, 6.8b and 6.8c show the results of the application of engine hybridization on the braking and driving torque throughout the NEDC. It is shown that the air hybrid engine of concept 1 can more efficiently capture braking energy due to the low braking torque output of each cylinder that allows for fine adjustments to be made to the produced braking torque of the engine in order to match the required braking torque as closely as possible. This can also be seen in Table 6.3 below, where it is shown that more than one cylinders in air compressor mode (CM) to recover 69.08% of the total braking energy demand, while only 46.52% and 57.51% of the total braking energy demand is recovered by multi-cylinder operation in concepts 2 and 3 respectively.

Furthermore, it is shown that the air expander mode is used for a small period of the acceleration phase (1.56% – 3.72%). However, the stored compressed air has sufficient energy to start the engine without the use of the electric starter during start ups throughout the NEDC. The worst braking efficiency throughout the NEDC is realized by the air hybrid engine of concept 2, while the worst driving efficiency is realized by concept engine 3. On the other hand, the best braking efficiency throughout the NEDC is realized by the air hybrid engine of concept 3, while the best driving efficiency is realized by concept engine 1.

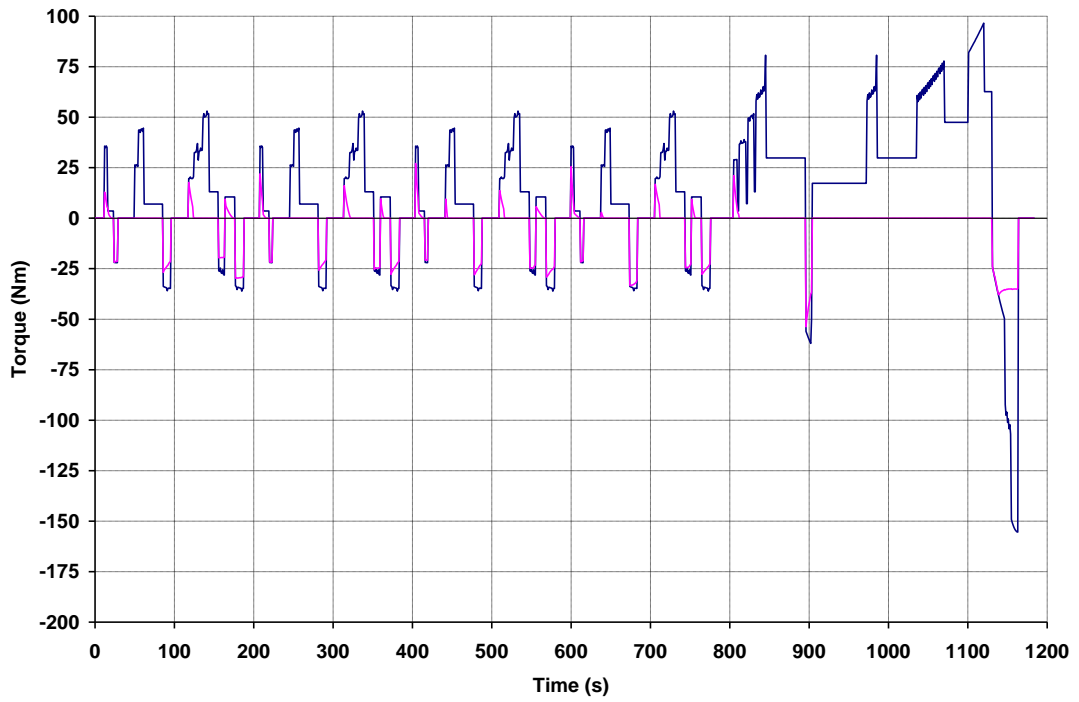


Figure 6.8a: Air hybrid engine braking and driving torque output in comparison with the required brake torque throughout the NEDC (concept 1).

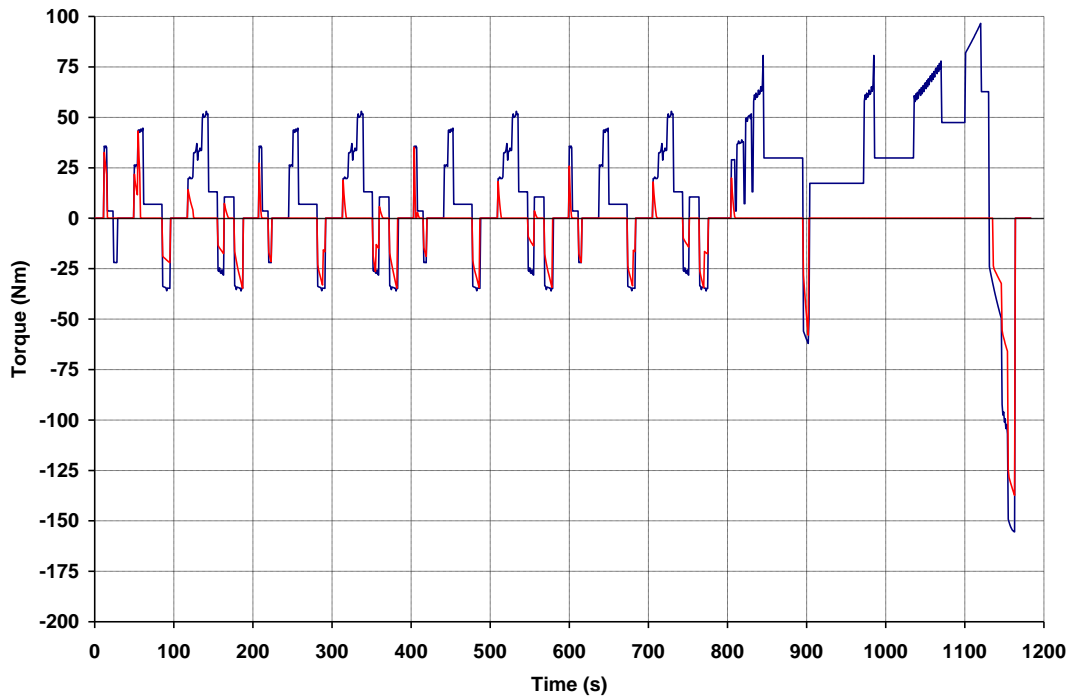


Figure 6.8b: Air hybrid engine braking and driving torque output in comparison with the required brake torque throughout the NEDC (concept 2).

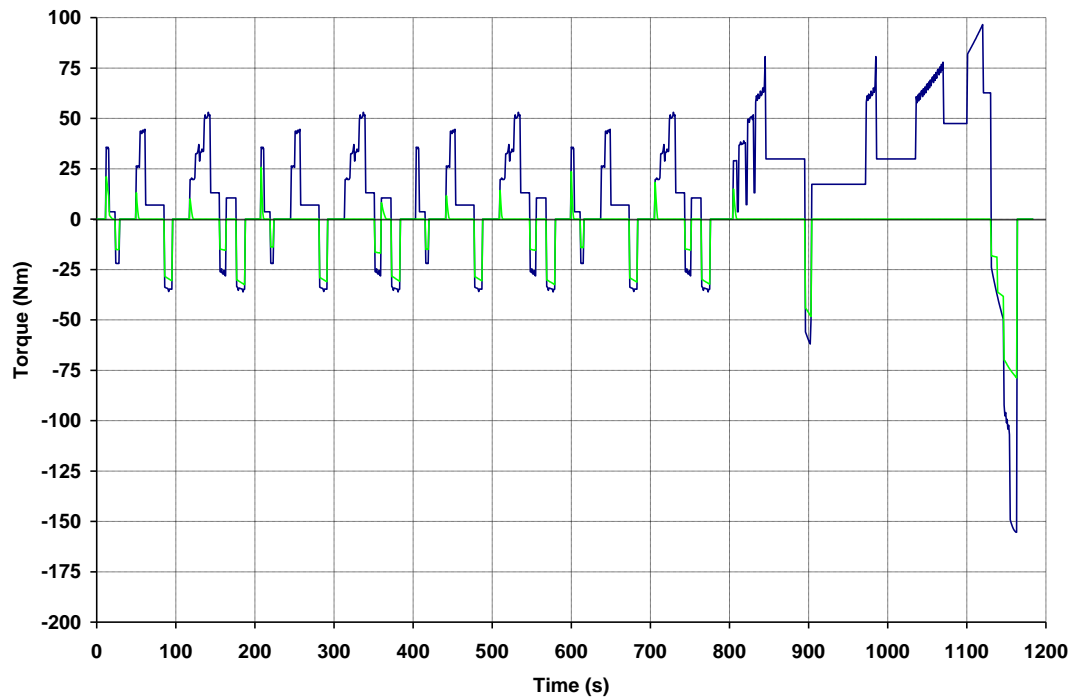


Figure 6.8c: Air hybrid engine braking and driving torque output in comparison with the required brake torque throughout the NEDC (concept 3).

Figures 6.8d, 6.8e and 6.8f show the results of the application of engine hybridization on the braking and driving torque throughout the 10-15 Mode driving cycle. Similar to NEDC, it is shown that the air hybrid engine of concept 1 can more efficiently capture braking energy due to the low braking torque output of each cylinder that allows for fine adjustments to be made to the produced braking torque of the engine in order to match the required braking torque as closely as possible. This can also be seen in Table 6.3 below, where it is shown that more than one cylinders in air compressor mode (CM) to recover 80.41% of the total braking energy demand, while only 14.5% and 40.49% of the total braking energy demand is recovered by multi-cylinder operation in concepts 2 and 3 respectively. It should be noted at this point that throughout the 10-15 Mode driving cycle, where the total braking energy demand is significantly lower than that of the NEDC, one or two cylinders are used in CM mode to recover more than 50% of the total braking energy demand.

Again, it is shown that the compressed air is sufficient to start the engine without the use of the electric starter during start ups throughout the 10-15 Mode driving cycle. The total driving energy reimbursed to the vehicle by the air expander is 92.166 – 55.708 kJ, about 1.5 to 5 times less than that realized throughout the NEDC. The period of the air motor operation is about 3.27% – 5.4% of the total acceleration period throughout the 10-15

Mode driving cycle. Similar to the NEDC, worst braking efficiency here is realized by the air hybrid engine of concept 2, while the worst driving efficiency is realized by concept engine 3. On the other hand, the best braking efficiency throughout the 10-15 Mode driving cycle is realized by the air hybrid engine of concept 1, while the best driving efficiency is realized by concept engine 2.

The most significant disadvantage of the air hybrid engine of concept 2 is that the minimum achievable braking torque per cylinder is too high, compared to concept engines 1 and 3. Consequently, only one engine cylinder can be used for most of the decelerations, as shown in Table 6.3. It can be seen that the engine uses one cylinder in CM throughout the urban driving part of the cycle to recover part of the braking energy more than concepts 1 and 3 do. However, the engine demonstrates a relatively high driving torque output and it can therefore propel the vehicle for longer periods of time, compared to the air hybrid engine of concept engine 3. Therefore, a valve timing other than the one used here, that allows for lower braking torque outputs to be realized, would yield significant benefits to the application of concept engine 2 on NEDC and 10-15 Mode driving cycles.

It should be also noted at this point that in addition to the energy reimbursed to the vehicle during periods of cruising or accelerations, the stop-and-start capability of the air hybrid engine during idling periods of the driving cycle (which is the 25.2% of the NECD total running time and the 32.6% of the 10-15 Mode driving cycle total running time) suggests a significant improvement in fuel economy, and thus energy saving. It is estimated that for a four-cylinder gasoline engine, where the fuel consumption is approximately as high as 0.46 kg/h at idle speed, a mass of 0.038 kg of fuel is burnt during periods of idling throughout the NEDC (298 s), while a mass of 0.027 kg of fuel is burnt during periods of idling throughout the 10-15 Mode driving cycle (215 s). For a fuel calorific value of 44.8 MJ/kg, there are 1702 kJ and 1210 kJ saved due to engine stopping during idling, which is the 26% and 41.5% of the total energy consumption throughout the NEDC and 10-15 Mode driving cycle respectively. Previous studies have shown that cylinder deactivation and/or engine shutdown could improve fuel economy by 30% to 66% [98-101].

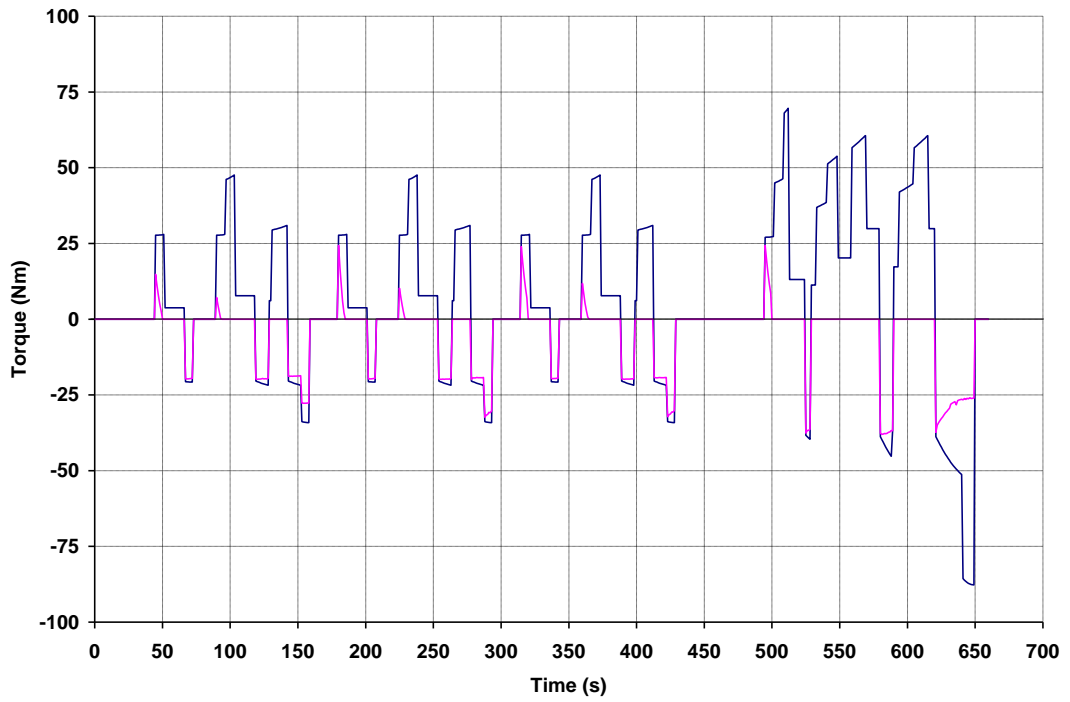


Figure 6.8d: Air hybrid engine braking and driving torque output in comparison with the required brake torque throughout the 10-15 Mode driving cycle (concept 1).

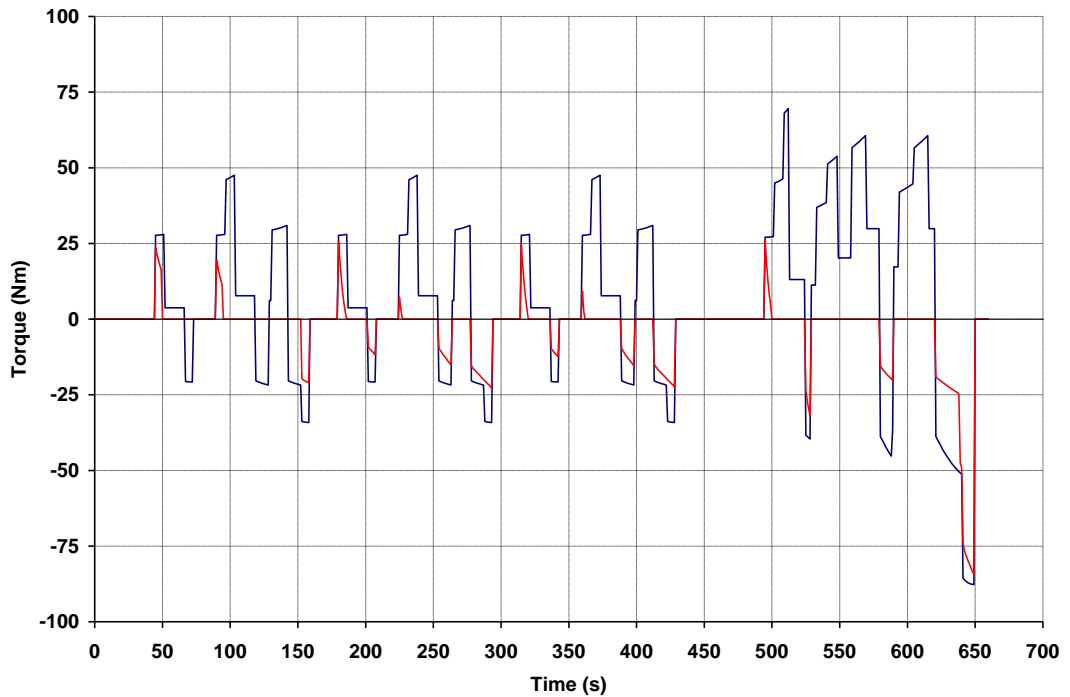


Figure 6.8e: Air hybrid engine braking and driving torque output in comparison with the required brake torque throughout the 10-15 Mode driving cycle (concept 2).

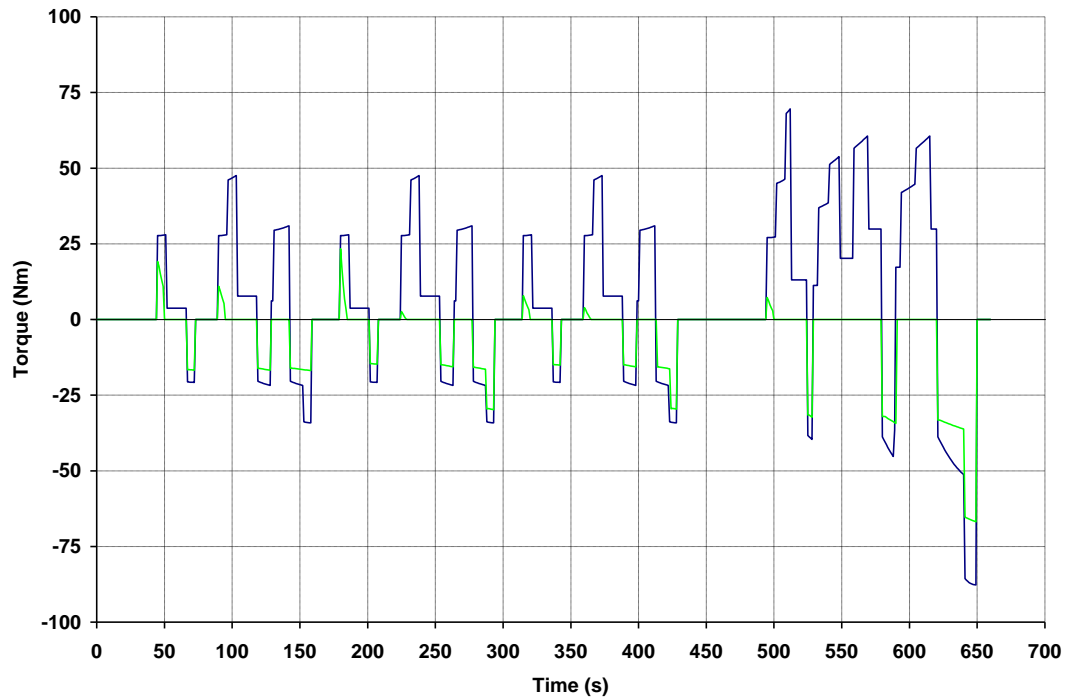


Figure 6.8f: Air hybrid engine braking and driving torque output in comparison with the required brake torque throughout the 10-15 Mode driving cycle (concept 3).

6.7.4. Airtank pressure

Finally, the simulation code was used to determine the SOC of the airtank for the three concept engines throughout the driving cycles. The results are shown in Figures 6.9a and 6.9b. As discussed above, the airtank is assumed to have a volume of 40 liters and to be pre-charged to 10 bar. It is shown that airtank pressure can be maintained within the range of 6 – 11 bar only in concept 1. This is because the minimum achievable driving torque of the air hybrid engine of concept 1 is realized at 6 bar of airtank pressure. Concept engines 2 and 3 can be operated in lower pressures. Therefore, airtank pressure for concepts 2 and 3 is maintained within the range of 2 bar and 5.5 bar. It should be also noted here that throughout the extra-urban driving part of the cycle, where the engine can be solely operated in CM and the braking torque demand is high, the SOC of the airtank reaches its initial level and therefore the airtank is fully recharged. It can be seen that airtank pressure at the end of the cycle is between 75% and 150% of the initial pressure.

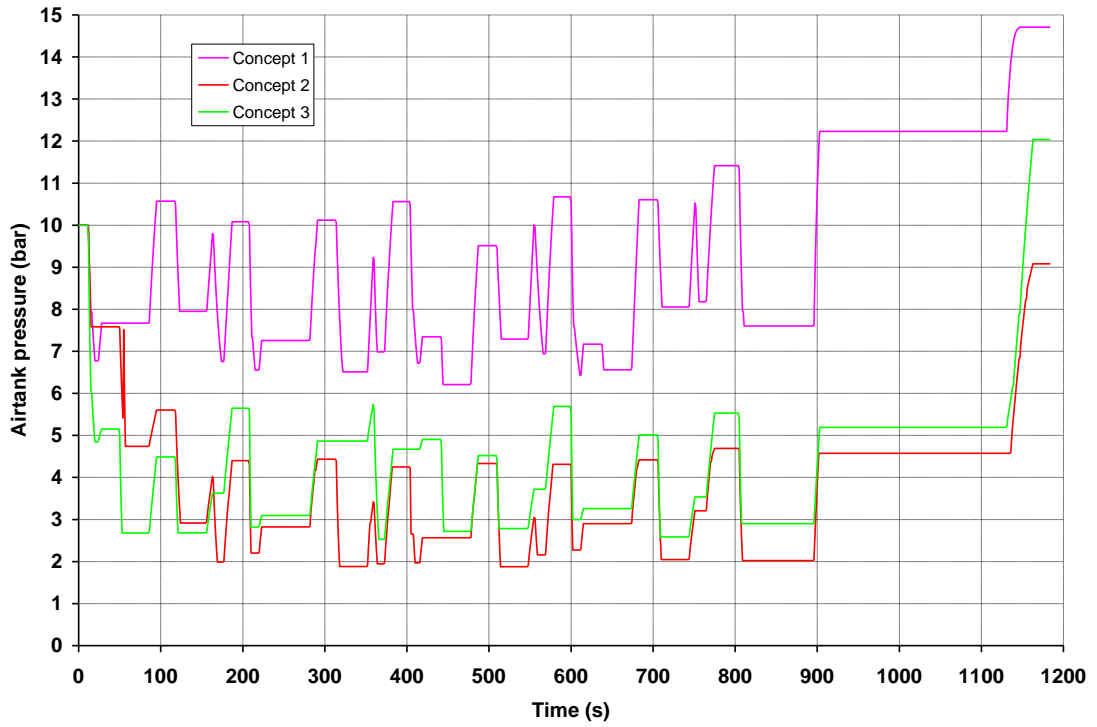


Figure 6.9a: Airtank pressure variation throughout the NEDC.

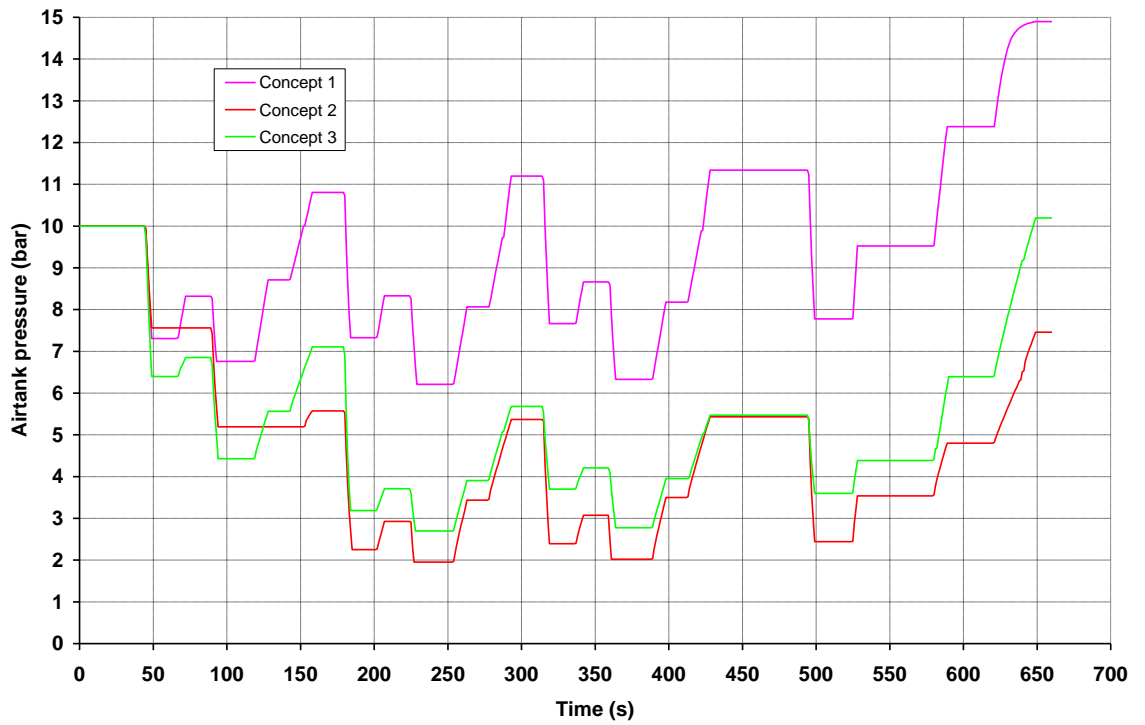


Figure 6.9b: Airtank pressure variation throughout the 10-15 Mode driving cycle.

Table 6.3: Braking energy recovery and driving energy reimbursement.

NEDC	Concept 1		Concept 2		Concept 3	
	kJ	% of the total braking demand	kJ	% of the total braking demand	kJ	% of the total braking demand
braking energy recovered by CM	835.893	69.08%	778.032	64.30%	882.163	72.91%
from hybridization of 1 engine cylinder	0.000	0.00%	214.995	17.77%	186.350	15.40%
from hybridization of 2 engine cylinders	430.894	35.61%	385.788	31.88%	447.673	37.00%
from hybridization of 3 engine cylinders	161.072	13.31%	54.616	4.51%	65.968	5.45%
from hybridization of 4 engine cylinders	243.927	20.16%	122.633	10.13%	182.172	15.06%
	kJ	% of the total driving demand	kJ	% of the total driving demand	kJ	% of the total driving demand
driving energy reimbursed by EM	360.794	3.72%	163.934	3.38%	75.390	1.56%
from hybridization of 1 engine cylinder	72.230	0.75%	31.737	0.66%	26.109	0.54%
from hybridization of 2 engine cylinders	221.923	2.29%	106.976	2.21%	21.458	0.44%
from hybridization of 3 engine cylinders	61.731	0.64%	17.841	0.37%	27.824	0.57%
from hybridization of 4 engine cylinders	4.909	0.05%	7.380	0.15%	0.000	0.00%
10-15 Mode	Concept 1		Concept 2		Concept 3	
	kJ	% of the total braking demand	kJ	% of the total braking demand	kJ	% of the total braking demand
braking energy recovered by CM	578.155	80.41%	387.735	53.93%	548.009	76.22%
from hybridization of 1 engine cylinder	0.000	0.00%	283.526	39.43%	256.857	35.72%
from hybridization of 2 engine cylinders	302.644	42.09%	33.275	4.63%	229.954	31.98%
from hybridization of 3 engine cylinders	89.250	12.41%	70.935	9.87%	0.000	0.00%
from hybridization of 4 engine cylinders	186.262	25.91%	0.000	0.00%	61.198	8.51%
	kJ	% of the total driving demand	kJ	% of the total driving demand	kJ	% of the total driving demand
driving energy reimbursed by EM	70.735	4.15%	92.166	5.40%	55.708	3.27%
from hybridization of 1 engine cylinder	0.000	0.00%	40.485	2.37%	43.583	2.55%
from hybridization of 2 engine cylinders	58.823	3.45%	51.681	3.03%	12.125	0.71%
from hybridization of 3 engine cylinders	11.912	0.70%	0.000	0.00%	0.000	0.00%
from hybridization of 4 engine cylinders	0.000	0.00%	0.000	0.00%	0.000	0.00%
NEDC			10-15 Mode			
Total cycle duration	1184 s		Total cycle duration	660 s		
Total idling duration	298 s		Total idling duration	215 s		
Total braking demand	1210 kJ		Total braking demand	719 kJ		
Total driving demand	4843 kJ		Total driving demand	1706 kJ		

6.8. Summary

A numerical model of an air hybrid vehicle driven throughout the NEDC and the 10-15 Mode driving cycle is realized by means of a Matlab-based simulation code. Each of the three air hybrid engine concepts, presented in Chapters 3 and 4, is included in the present vehicle simulation studies. Details of the driveline and vehicle model, as well as a brief description of the driving cycles are presented. The analysis of the results indicates that all the concept engines have the potential of braking energy storage and regeneration. It is clear that the regenerative braking force, and thus the regenerative braking energy, is closely related to the deceleration demand, vehicle speed (and therefore engine speed) and the adhesive coefficient of tire-ground contact.

Each of the three air hybrid engine concepts is shown to be able to provide all the braking power required, as well as to start the engine after each stop. However, the braking energy recovered could be significantly improved by optimizing the valve timing to achieve best regenerative braking efficiency. Finally, it is concluded that the application of the air hybrid concept engine on vehicles with small engine displacement to vehicular mass ratio would significantly elevate the efficiency of energy storage and regeneration, as well as fuel economy due to engine downsizing.

Chapter 7: Conclusions and Recommendations for Further Work

7.1. Conclusions

A number of different versions of a novel air hybrid powertrain concept, based on a conventional IC engine, are modelled by means of Ricardo's WAVE one-dimensional simulation package in this Thesis. Three of these versions have also been implemented in the laboratory, where an experimental test facility was commissioned. Finally, a vehicle simulation has been set up in order to investigate the influence of regenerative braking on energy (and thus fuel) savings.

7.1.1. Modelling work

7.1.1.1. Concept 1

The air hybrid engine of concept 1 combines a conventional IC engine with a pneumatic energy converter and storage subsystem in such a way that there is no need of major changes to the base engine, in order to lower the production cost and weight of the system and stay with the well-known technologies which are already in production. As the standard camshaft-operated valvetrain remains in use, the need of adopting fully flexible valve actuation which adds to the system's complexity is eliminated.

- I. First shut-off valve opening event does not influence the performance of the air compressor. However, first shut-off valve closing point affects $imep_b$. Maximum $imep_b$ (and thus maximum $bmep_b$ and T_b) is achieved for valve closing at 20° ATDC. However, this timing can be either advanced or retarded by 10° CA in order to lower the realized $imep_b$ by approximately 17% in order to meet lower braking torque requirements, when the optimal charging of the airtank is not the first priority. On the other hand, $CATC_b$ is significantly influenced by engine speed and therefore first shut-off valve closing must be varied between 15° ATDC and 25° ATDC, depending on the engine speed, when optimal airtank charging is of high importance.
- II. Second shut-off valve closing event does not influence the performance of the air compressor. However, second shut-off valve opening point affects $imep_b$. Maximum $imep_b$ (and thus maximum $bmep_b$ and T_b) is achieved for valve opening at TDC.

- III. First shut-off valve opening and closing events does not have significant effects on $imep_d$ (and thus $bmep_d$ and T_d) or $CATC_d$.
- IV. However, the performance of the air expander is affected by second shut-off valve opening point and airtank pressure. Maximum $imep_d$ is achieved for valve opening at 50° BTDC when the airtank is at a low SOC. For increasing airtank pressure, second shut-off valve opening point must be retarded up to 10° BTDC. Furthermore, $CATC_d$ is only influenced by airtank pressure and therefore second shut-off valve opening event does not affect it.
- V. It has been also found that $imep_d$ increases with retarded second shut-off valve closing. However, $CATC_d$ drops due to excessive air expenditure and therefore a compromise may be necessary between the desired driving torque output and the air expenditure. Maximum compressed air economy is achieved by closing the second shut-off valve at 60° BEVO, while maximum torque output is realized when the valve closes at 40° AEVO.
- VI. Realized $bmep_b$ is within the range of 2 – 4 bar, at 1000 – 4000 rpm and 5 – 18 bar of airtank pressure, for a 10-litre airtank volume. $Bmep_d$ is within the range of 12 – 0 bar, at 10 – 500 rpm and 20 – 4 bar of airtank pressure, for the same airtank capacity as above. The driving torque is sustainable for 55 engine cycles (110 crankshaft revolutions).

7.1.1.2. Concept 2

The air hybrid engine of concept 2 is an IC engine with camless valve actuation. One of the engine valves connects the cylinder to the airtank and it is operated as a gas transfer valve. This design eliminates the need of control over additional shut-off valves and does not alter the cylinder head characteristics in any way (clearance volume, etc). The greatest advantage of the present concept lies on the fact that two-stroke air compressor and expander cycles can be realized, which improves hybrid performance.

- I. IVC and GVO events do not influence the performance of the two-stroke air compressor, provided that they take place at BDC or around BDC.
- II. However, IVO significantly influences $imep_b$. Maximum achievable $imep_b$ (and thus optimal airtank charging) is realized when the intake valve opens at 10° BTDC.

Advancing of the IVO point by 10° CA results in a reduction in imep_b by approximately 4%. Retarding of the IVO point by 10° CA results in a drop in imep_b decrease by 7% – 15%, depending on the engine speed. Consequently, IVO can be varied in order to meet lower braking torque requirements, when the optimal charging of the airtank is not the first priority.

- III. Similarly to IVO, GVC event influences imep_b . Maximum imep_b is realized when the gas transfer valve closes at 5° ATDC. Retarded GVC causes a slight drop to the imep_b curve. Advanced GVC (up to 20° BTDC) causes a drop in imep_b by 3% – 14%, depending on the engine speed.
- IV. The thermodynamic process that takes place inside the cylinder of the two-stroke air expander is very close to the adiabatic expansion. Provided that the gas exchange process takes place at very low engine speeds, only the GVC event is of importance for the performance of the air expander. Similar to the air expander cycle of concept 1, a compromise may be necessary between the desired driving torque and the air expenditure. Maximum compressed air economy is achieved by closing the gas transfer valve at 80° BBDC, while maximum torque output is realized when the valve closes at BDC.
- V. The two-stroke air hybrid engine has a predicted bmep_b within the range of 5 – 26 bar, while maximum achievable bmep_d is 18 bar. Similarly to the air expander cycle of concept 1, bmep_d is only sustainable for a limited number of engine cycles.

7.1.1.3. Concept 3

Two well established technologies are used in air hybrid engine concept 3; valve deactivation, Variable Valve Timing (VVT) and/or Cam Profile Switching (CPS). As a conventional, camshaft-operated variable valvetrain is used, the need of adopting fully variable valve actuation is eliminated and thus only minor modifications to the engine architecture are required. However, the function of the engine is not altered in any way when operating in normal firing mode.

- I. The performance of the air compressor is influenced by cam profile shift and ECV opening events. ECV closing does not significantly affect bmep_b .

- II. An intake valve profile shift of 160° CA leads to the realization of maximum bmep_b . Less than 150° CA or more than 170° CA in the valve profile shift causes a significant drop to the predicted bmep_b . CATC_b curve follows the same pattern; it reaches a maximum for an intake valve profile drift of 160° CA and it drops rapidly for other CPS timings.
- III. ECV opening at 25° BTDC allows for an optimal gas exchange process. Therefore, the air compressor displays maximum bmep_b and CATC_b for the aforementioned timing. There is also a small degree of dependency of ECV timing on engine speed.
- IV. Provided that the cam profile of the gas exchange valve follows the conventional intake valve timing, the performance of the air expander entirely depends on the ECV opening and closing events. ECV opening does not importantly affect bmep_d . For ECV opening timing within the range of 30° BTDC and 10° ATDC, bmep_d is unaffected, while it is slightly decreased for further retarded ECV opening timing (after 10° ATDC). However, ECV closing timing has a greater impact on bmep_d . Maximum bmep_d is achieved for ECV closing at 70° BBDC. Advancing or retarding the ECV closing event causes a slope to the bmep_d curve.
- V. The expenditure of compressed air is increased with increased bmep_d . Therefore, the measurement of the consumed energy per unit work is expressed as the compressed air mass expenditure to driving imep ratio. It has been concluded that optimal (lowest) air expenditure is achieved for ECV opening at 10° ATDC and ECV closing at 70° ATDC. Therefore, ECV may close at 70° ATDC where maximum efficiency (and thus optimal energy expenditure) is required, while its closing may be retarded up to 70° BBDC where high levels of driving torque are required.
- VI. The air compressor produces a bmep_b within the range of 4 – 7 bar. Similar to concepts 1 and 2, bmep_d (within the range of 14 – 0 bar) is sustainable only for a limited number of engine cycles (55 engine cycles – 110 crankshaft revolutions).

7.1.2. Experimental work

7.1.2.1. 4-stroke compressor

- I. imep_b is a strong function of GVO and GVC events. Maximum imep_b is realized for GVO at 10° BIVC. Retarded GVO timing by 5° CA results to a decrease in imep_b by

approximately 20%. Advanced GVO timing by 5° CA results to a decrease in $imep_b$ by approximately 12%. Maximum $imep_b$ is also realized for GVC at 15° ATDC. Retarded GVC timing by 5° CA results to a decrease in $imep_b$ by 4% – 16%, depending on the engine speed.

- II. Airtank pressure is a strong function of GVC rather than GVO. Optimal airtank charging is achieved for GVO at 10° BIVC. However, retarding or advancing of the GVO timing by 10° CA does not importantly affect the airtank charging efficiency. On the other hand, optimal airtank charging is also achieved for GVC at 15° ATDC. Retarded GVC timing by 5° CA results to a decrease in maximum achievable airtank pressure by 3% – 20%, depending on the engine speed.
- III. Maximum achievable airtank pressure is significantly affected by engine speed. It asymptotically reaches a limiting pressure of 4 – 5.5 bar at low and mid-range engine speeds, while it drops down to 1.5 – 2.5 bar at high engine speeds. $Bmep_b$ is a strong function of airtank pressure and therefore it follows the same pattern.

7.1.2.2. 2-stroke air compressor

- I. $imep_b$ is a function of IVO and GVC events. Maximum $imep_b$ is realized for IVO at TDC – 5° ATDC, depending on the engine speed. The experimental results proved that retarding or advancing the IVO timing does not play any significant role to the performance of the air compressor. However, $imep_b$ is a strong function of engine speed. Maximum $imep_b$ is also realized for GVC at 5° ATDC. Similarly to IVO event, the experimental results proved that $imep_b$ is a strong function of engine speed rather than GVC timing.
- II. Airtank pressure is also a strong function of engine speed. Maximum achievable airtank pressure is within the range of 4 bar and 10 bar. Optimal airtank charging is realized for IVO at TDC – 5° ATDC and GVC at 5° ATDC. However, retarded or advanced IVO and GVC events cause a decrease in maximum airtank pressure by 5% – 21%, depending on the engine speed.
- III. Maximum achievable airtank pressure is asymptotically reaching a limiting pressure of 10 – 11.5 bar at low and mid-range engine speeds, while it drops down to 5 – 7.5 bar at high engine speeds. $Bmep_b$ is a strong function of airtank pressure and therefore it follows the same pattern.

7.1.2.3. 4-stroke expander

- I. The investigation of the compressed air discharge efficiency indicated that optimal gas transfer valve timing is GVO at 5° ATDC and GVO at 10° AEVO. Advanced GVO or GVC timings by 5° CA cause a drop in compressed air discharge efficiency by 13%.
- II. Similarly to the predicted driving torque sustainability, the experimental results indicated that the driving torque of the engine is sustainable for a limited number of engine cycles (37 cycles – 74 crankshaft revolutions).

7.1.3. Vehicle simulation

- I. In recovering and recycling kinetic energy, losses exist due to losses in the devices used to process, store and reuse the recovered energy. Another factor that strongly influences the amount of the possibly recovered energy is that part of the braking energy must be absorbed by the frictional brake system when the braking power demand exceeds the capability of the regenerative braking system.
- II. Concept engine 1 displays low energy storage efficiency (66.6%) throughout the NEDC. However, this air hybrid engine is favoured by the specific driving conditions of the 10-15 Mode driving cycle, where its energy storage efficiency is elevated to 75.9%. It also displays satisfactory energy regeneration efficiency, as high as 3.4% throughout the NEDC and 3.9% throughout the 10-15 Mode driving cycle. Therefore, concept engine 1 is more suitable for vehicles driven throughout the Japanese driving cycle.
- III. Concept engine 2 displays higher energy storage efficiency than concept engine 1 throughout the NEDC (68%). However, this air hybrid engine is not favoured by the specific driving conditions of the 10-15 Mode driving cycle, where its energy storage efficiency is the lowest among the three concepts (57.5%). Furthermore, it displays satisfactory energy regeneration efficiency throughout the NEDC, as high as 3.3%, and the highest among the three concepts throughout the 10-15 Mode driving cycle (4.9%). Therefore, concept engine 1 is more suitable for vehicles driven throughout the European driving cycle if the emphasis is been put on energy storage, while it is more preferable for vehicles driven throughout the Japanese driving cycle if the emphasis is been put on energy regeneration.

- IV. Concept engine 3 displays the highest energy storage efficiency among the three concepts throughout both driving cycles. However, its energy regeneration efficiency is the lowest among the three concepts throughout both driving cycles. Therefore, concept engine 3 would be more suitable for vehicles driven throughout extra-urban driving cycles, where the emphasis is solely given to decelerations (it is assumed that no engine hybridization is possible during cruising).
- V. The global energy (and thus fuel) savings displayed by each one of the aforementioned concepts would be further elevated if the fuel economy originated from the ability of stopping the engine during idling periods (which comprise a significant percentage of the total cycle running time) could be taken into account.

7.2. Recommendations for further work

Considerable progress was made towards realising the air hybrid engine concepts and understanding the effects of the various gas exchange processes on the performance of the air compressor and the air expander. The results of the application of these concepts on a vehicle driven in real-life driving conditions indicate the potentials and benefits of energy regeneration yet to be exploited. However, there is a number of aspects of this research that can be extended upon.

7.2.1. Modelling work

The modelling work undertaken in this study includes simple forms of air compressor and air expander cycles. Therefore, the air hybrid engine has not been tested in its entirety. To fully prove the concept and investigate the potentials of engine performance and energy saving, it is suggested that other engine cycles (such as supercharged and undercharged engine operations) described by other researchers should be modelled [49,50,58,59,67,68]. In addition, further optimization of operating parameters such as buffer chamber, auxiliary chamber and airtank volume, valve timing, etc, by means of more extensive systematic studies, would be desirable. Finally, investigations could also look at the possibility of introducing a heat recuperator between the engine and the air storage compartment for intercepting the thermal energy locally and keeping it at high temperature, thus improving the reversibility of the gas exchange process and recovering most of the thermal energy included in the total energy delivered by the working medium.

7.2.2. Experimental work

The experimental test engine which was set up and commissioned has been developed to a prototype stage and therefore it was not equipped with cooling, ignition and fuelling systems. It is estimated that the presence of the aforementioned systems would importantly influence the experimental results. For that reason, experimental work undertaken on a fully operational IC engine would be desirable. Further work is also required to the direction of monitoring other operation parameters, such as compressed air charge mass and temperature, induced air mass and temperature, etc, in order to compute more performance coefficients (e.g. CATC). In this study, only the perspective of using compressed air to start then engine and/or motor it in very low engine speeds has been investigated. The commission of a firing IC engine, in conjunction with convenient hardware, would allow for the use of compressed air to propel the vehicle at high engine speeds. That would also give further insight into the potentials of the realization of other engine operating cycles, such as supercharged and undercharged engine operations.

7.2.3. Vehicle simulation

One European (NEDC) and one Japanese (10-15 Mode) modal cycle has been used for the vehicle simulation section of this study. It would be desirable to extend the vehicle simulation research to other driving cycles, especially US cycles which are transient and they give a better representation of real driving patterns than the modal cycles. It is also suggested that the effects of stopping the engine during periods of engine idling, which is an important engine management strategy whose benefits were not investigated in this study, should be examined. The estimation of fuel savings rather than kinetic energy savings throughout the driving cycle would be advisable as it gives a better representation of the effects of engine hybridization on the improvement of the specific fuel consumption, which is the ultimate objective of the air hybrid concept.

Finally, in order to assess the full potential of the air hybrid engine, the vehicle simulation should be extended to include both engine performance modelling and vehicle simulation in real time. This could be realized by setting up an interactive path between WAVE, the engine simulation model and the driving cycle simulator under the MATLAB Simulink environment. The extended modelling capability would allow the analysis to be carried out on the effects of different strategies of air hybrid operation, such as stop-and-start, turbo lag compensation, etc.

References

1. Rogers, G. and Mayhew, Y., "Engineering Thermodynamics, Work and Heat Transfer", Fourth Edition, pp.51-52, Prentice Hall, ISBN 0-582-04566-5, 1992.
2. Petrucci, R., Harwood, W. and Herring, G., "General Chemistry: Principles and Modern Applications", Eighth Edition, Chapter 7-3, Prentice Hall, ISBN 0-130-14329-4, 2001.
3. Heywood, J., "Internal Combustion Engine Fundamentals", pp.48-54, McGraw-Hill International Editions, ISBN 0-07-100499-8, 1988.
4. Moore, T., "Tools and Strategies for Hybrid-Electric Drive System Optimization", SAE paper 961660, 1996.
5. Gao, Y., Rahman, K. and Ehsani, M., "Parametric Design of the Drive Train of an Electrically Peaking Hybrid (ELPH) Vehicle", SAE paper 970294, 1997.
6. Rahman, Z., Butler, K. and Ehsani, M., "Design Studies of a Series Hybrid Heavy-Duty Transit Bus Using V-ELPH 2.01", IEEE paper 0-7803-5565-2/99, 1999.
7. "Hybrid Synergy Drive Information Terminal", obtained from <http://www.hybridsynergydrive.com>, last visited March 2007.
8. Kelly, K., Mihalic, M. and Zolot, M., "Battery Usage and Thermal Performance of the Toyota Prius and Honda Insight for Various Chassis Dynamometer Test Procedures", NREL Internal Report, 2001.
9. Hellman, K., Peralta, M. and Piotrowski, G. "Evaluation of a Toyota Prius Hybrid System (THS)", United States Environmental Protection Agency EPA420-R-98-006, 1998.
10. Pourmovahed, A., "Sizing Energy Storage Units for Hydraulic Hybrid Vehicle Applications", ASME Advanced Automotive Technologies, vol.52, 1993.
11. "How Hydraulic Power Assist Works", obtained from <http://jcwinnie.biz/wordpress/imageSnag/HowHPAWorks.jpg>, last visited March 2007.

12. Motavalli, J., "From Stops, Energy to Go", New York Times Automobiles Section, Page F1, 22nd March, 2002.
13. Kepner, R., "Hydraulic Power Assist – A Demonstration of Hydraulic Hybrid Vehicle Regenerative Braking in a Road Vehicle Application", SAE paper 2002-01-3128, 2002.
14. Wicks, F., Maleszewski, J., Wright, C., and Zarybnicky, J., "Analysis of compressed air regenerative braking and a thermally enhanced option", 2002 37th Intersociety Energy Conversion Engineering Conference (IECEC), 2004.
15. Walker, M. and Lampirth, U., "Electric Motors and Generators in Hybrid-Electric Powertrains", SAE paper 2003-01-2313, 2003.
16. Miller, J.M., "Power Electronics in Hybrid Electric Vehicle Applications", Eighteenth Annual Applied Power Electronics Conference and Exposition IEEE, vol.1, pp.23- 29, 2003.
17. Cuenca, M., Gaines, L. and Vyas, A., "Evaluation of Electric Vehicle Production and Operating Costs", Argonne National Laboratory Report, 1999.
18. La Plante, J., Anderson, J. and Auld, J., "Development of a Hybrid Electric Vehicle for the US Marine Corps.", SAE paper 951905, 1995.
19. An, F., Vyas, A., Anderson J. and Santini, D., "Evaluating Commercial and Prototype HEVs", SAE paper 2001-01-0951, 2001.
20. Gao, Y., Chen, L. and Eshani, M., "Investigation of the Effectiveness of Regenerative Braking for EV and HEV", SAE paper 1999-01-2910, 1999.
21. Cikanek, S. and Bailey, K., "Energy Recovery Comparison Between Series and Parallel Braking System for Electric Vehicles Using Various Driving Cycles", Advanced Automotive Technologies, ASME, DSC vol.56 / DE vol.86, pp.17-31, 1995.
22. Brahma, Y., Guezennec, Y. and Rizzoni, G., "Optimal Energy Management in Series Hybrid Electric Vehicles", Proceedings of the American Control Conference, Chicago Illinois, vol.1, issue 6, pp.60-64, 2000.

23. Jalil, N., Kheir, N. and Salman, M., "A Rule-Based Energy Management Strategy for a Series Hybrid Vehicle", Proceedings of the American Control Conference, vol.1, pp.689-693, 1997.
24. Barsali, S., Miulli, C. and Possenti, A., "A Control Strategy to Minimize Fuel Consumption of Series Hybrid Electric Vehicles", Transactions on Energy Conversion, IEEE, vol.19, issue 1, pp.187-195, 2004.
25. Salman, S., Schouten, N. and Kheir, N., "Control Strategies for Parallel Hybrid Vehicles", Proceedings of the American Control Conference, vol.1, issue 6, pp.524-528, 2000.
26. Powell, B., Bailey, K. and Cikanek, S., "Dynamic Modelling and Control of Hybrid Electric Vehicle Powertrain Systems", IEEE Control Systems Magazine, vol.18, issue 5, pp.17-33, 1998.
27. Panagiotidis, M., Delagrammatikas, G. and Assanis, D., "Development and Use of a Regenerative Braking Model for a Parallel Hybrid Electric Vehicle", SAE paper 2000-01-0995, 2000.
28. Paganelli, G., Delprat, S., Guerra, M., Rimaux, J. and Santin, J., "Equivalent Consumption Minimization Strategy for Parallel Hybrid Powertrains", 55th Vehicular Technology Conference, IEEE vol.4, pp.2076-2081, 2002.
29. Burke, A., "On-Off Engine Operation for Hybrid Electric Vehicles", SAE paper 930042, 1993.
30. Chau, K. T. and Wong, Y.S., "Overview of Power Management in Hybrid Electric Vehicles", Energy Conversion and Management, vol.43, issue 15, pp.1953-1968, 2002.
31. Pullen, R., Lampirth, U. and Etemad, R., "A Parametric Optimization Study of Diesel and Gas Turbine Series: Hybrid Electric Vehicles, "31st International symposium on automotive technology and automation (ISATA), Düsseldorf Germany 2-5 June 1998, pp.179-187, 1998.

32. Assanis, D. et al, "An Optimization Approach to Hybrid electric Propulsion System Design", Automotive Research Center, College of Engineering, The University of Michigan, 1999.
33. Zoelch, U. and Schroeder, D., "Dynamic Optimization Method for Design and Rating of the Components of a Hybrid Vehicle", International Journal of Vehicle Design, vol.19, issue 1, pp.1-13, 1998.
34. Bumby, R. and Forster, I., "Optimization and Control of a Hybrid Electric Car", IEEE Proceedings D. Control Theory and Applications, vol.134, pp.373-387, 1987.
35. Kalhammer, R., Kozawa, A., Moyer, C. and Owens B., "Performance and Availability of Batteries for Electric Vehicles", Report of the Battery Technology Advisory Panel, California, 1995.
36. Yeo, H. and Kim, H., "Hardware-in-the-Loop Simulation of Regenerative Braking for a Hybrid Electric Vehicle", IMechE, vol.216, part D, 2002.
37. Bitterly, J., "Flywheel Technology: Past, Present and 21st Century Projections", Aerospace and Electronic Systems Magazine, vol.13, issue 8, pp.13-16, 1998.
38. Herbst, J. D., "Design, Fabrication, and Testing of 10 MJ Composite Flywheel Energy Storage Rotors", Proceedings of the Aerospace Power Systems Conference, SAE, Williamsburg, USA, pp.235-244, 1998.
39. Grudkowski, T., Dennis, A., Meyer, T. and Wawrzonek, P., "Flywheels for Energy Storage", Society for the Advancement of Material and Process Engineering (SAMPE), vol.32, issue 1, pp.65-69, 1996.
40. Christopher, D. G. and Beach, R., "Flywheel Technology Development Program for Aerospace Applications", Proceedings of the Aerospace and Electronics Conference, IEEE, vol.2, pp.602-608, 1997.
41. Pieronek, T. J., Decker, D. K. and Spector, V. A., "Spacecraft Flywheel Systems - Benefits and Issues", Proceedings of the National Aerospace and Electronics Conference, IEEE, vol.2, pp.589-593, 1997.

42. Edwards, J., Aldrich, J. W., Christopher, D. A., Beach, R. F. and Barton, J. R., "Flight Test Demonstration of a Flywheel Energy Storage System on the International Space Station", Proceedings of the Aerospace and Electronics Conference, IEEE, vol.2, pp.617-621, 1997.
43. Shen, S. and Veldpaus, F.E., "Analysis and Control of a Flywheel Hybrid Vehicular Powertrain", Transactions on Control Systems Technology, IEEE, vol.12, issue 5, pp.645-660, 2004.
44. Serrarens A., Shen, S. and Veldpaus, F. E., "Control of a Flywheel Assisted Driveline with Continuously Variable Transmission", Journal of Dynamic Systems, Measurement and Control, vol.125, issue 3, pp.455-461, 2003.
45. Rosen, H. and Castelman, D., "Flywheels in Hybrid Vehicles", Scientific American Magazine, vol.277, no.4, pp.75-77, 1997.
46. Jefferson, C. and Ackerman M., "A flywheel Variator Energy Storage System", Energy Conversion and Management, vol.37, no.10, pp.1481-1491, 1996.
47. Pneumatic Options Research Library, obtained from <http://www.aircaraccess.com>, last visited March 2007.
48. Motor Development International (MDI), obtained from <http://www.theaircar.com>, last visited March 2007.
49. Huang, K. D., Tzeng, S. C. and Chang, W. C., "Energy-Saving Hybrid Vehicle Using a Pneumatic-Power System" Applied Energy, vol.81, issue 1, pp.1-18, 2005.
50. Huang, K. D., Tzeng, S. C., Ma, W. and Chang, W. C., "Hybrid Pneumatic-Power System Which Recycles Exhaust Gas of an Internal-Combustion Engine", Applied Energy, vol.82, issue 2, pp.117-132, 2005.
51. Huang, K. D. and Tzeng, S. C., "Development of a Hybrid Pneumatic-Power Vehicle", Applied Energy, vol.80, issue 1, pp.47-59, 2005.
52. Turner, J., Kenchington, S. A. and Stretch, D. A., "Production AVT Development: Lotus and Eaton's Electrohydraulic Closed-Loop Fully Variable Valve Train System",

Fortschritt Berichte - VDI Reihe 12 Verkehrstechnik Fahrzeugtechnik, vol.1, issue 566, pp.331-346, 2004.

53. Schechter M. and Levin, M., "Camless Engine", SAE paper 1996-96-0581, 1996.
54. Landerl, C., Klauer, N., Schunemann, E. and Luttermann, C., "The New BMW Row Six Cylinder Petrol Engine With VALVETRONIC", ATZ Automobiltechnische Zeitschrift, vol.107, pp.70-87, May 2005.
55. Brustle, C. and Schwarzenthal, D., "VarioCam Plus – A Highlight of the Porsche 911 Turbo Engine", SAE paper 2001-01-0245, 2005.
56. Hosaka, T. and Hamazaki, M., "Development of the Variable Valve Timing and Lift (VTEC) Engine for the Honda NSX", SAE transactions, ISSN 0096-736X, vol.100, no.3, pp.1-7, 1991.
57. Allen, J. and Law, D., "Production Electro-Hydraulic Variable Valve-Train for a New Generation of I.C. Engines", SAE paper 2002-01-11089, 2002.
58. Andersson, M., Johansson, B. and Hultqvist, A., "An Air Hybrid for High Power Absorption and Discharge", SAE paper 2005-01-2137, 2005.
59. Andersson, M., "An Air Hybrid for High Power Absorption and Discharge", Thesis for the degree of M.Sc., Lund Institute of Technology, ISSN 0282-1990, 2004.
60. Tai, C. and Tsao, T., "Using Camless Valvetrain for Air Hybrid Optimization", SAE paper 2003-01-0038, 2003.
61. The University of California, "UCLA Study Suggests Air Hybrid Car Could Improve Fuel Efficiency", obtained from <http://www.newsroom.ucla.edu/page.asp?id=4420>, last visited March 2007.
62. Schechter, M., "New Cycles for Automobile Engines", SAE paper 1999-01-0623, 1999.
63. Schechter, M., "Regenerative Compression Braking – a Low Cost Alternative to Electric Hybrids", SAE paper 2000-01-1025, 2000.

64. Turner, J., Bassett, M., Pearson, R., Picher, G. and Douglas, K., "New Operating Strategies afforded by Fully Variable Valve Trains", SAE paper 2004-01-1386, 2004.
65. Turner J., Pearson, R. and Kenchington, S. A., "Concepts for Improved Fuel Economy from Gasoline Engines", International Journal of Engine Research, vol.6, no.2, pp.137-157, 2005.
66. Alexander, D., "Scuderi's split-cycle solutions", Automotive Engineering International, vol.114, no.5, May 2006, pp.24-26.
67. Higelin, P., Vsile, I., Charlet, A. and Chamaillard, Y., "Parametric Optimization of a New Hybrid Pneumatic-Combustion Engine Concept", International Journal of Engine Research, vol.5, no.2, pp.205-217, 2004.
68. Higelin, P. and Charlet, A., "Thermodynamic cycles for a new hybrid pneumatic-combustion engine concept", 5th International Conference on Internal Combustion Engines (ICE2001), Naples, Italy, HM1-2201-01-033, 2001.
69. Higelin, P., Charlet A. and Chamaillard, Y., "Thermodynamic simulation of a hybrid pneumatic-combustion engine concept". International Journal of Applied Thermodynamics, March 2002, vol.5, no.1, pp.1-12, 2002.
70. "Compressed Air Car with Quasiturbine Pneumatic Engine (Quasiturbine Air Motor)", obtained from <http://www.quasiturbine.com/QTVehiculePneumatique.html>, last visited March 2007.
71. Heywood, J., Weiss, M., Schafer, A., Bassene, S. and Natarajan, V., "The Performance of Future ICE and Fuel Cell Powered Vehicles and Their Potential Fleet Impact", SAE paper 04P-254, 2004.
72. Douglas, K. J., Milovanovic, N., Turner J. W. G. and Blundell, D., "Fuel Economy Improvement Using Combined CAI and Cylinder Deactivation (CDA) – An Initial Study", SAE paper 2005-01-0110, 2005.
73. Kreuter, P., Heuser, P., Murmann, J., Zrz, R., Stein, P. and Peter, U., "Meta – CVD System -- An Electro-Mechanical Cylinder and Valve Deactivation System", SAE paper 20011999-01-0240, 2001.

74. Ricardo WAVE 5.1 basic user manual, paragraphs 2.3.1, 2.3.2, 2.3.3, October 2003.
75. Chen, S. K. and Flynn, P. F., "Development of Single Cylinder Compression Ignition Research Engine", SAE paper 650733, 1965.
76. Ricardo WAVE 5.1 manual, engine user manual: Formulation and Basic Elements, October 2003.
77. Ricardo WAVE 5.1 help, reed valve types, October 2003.
78. AVT user manual, version 8, vol.1, Group Lotus plc, 2005.
79. Kistler Instruments Limited, piezoelectric pressure transducer type 7061 user manual.
80. Lancaster, D. R., Krieger, R. B., Lienesch, J. H., "Measurement and Analysis of Engine Pressure Data", SAE paper 750026, 1975.
81. Zhao, H. and Ladommatos, N., "Engine Combustion Instrumentation and Diagnostics", pp.73-74, SAE international, ISBN 0-7680-0665-1, 2001.
82. Randolph, A. L., "Cylinder-Pressure-Based Combustion Analysis in Race Engines," SAE paper 1994-94-2487, 1994.
83. Randolph, A. L., "Methods of Processing Cylinder-Pressure Transducer Signals to Maximize Data Accuracy," SAE paper 1990-90-0170, 1990.
84. Kistler Instruments Limited, piezoresistive pressure transducer type 4045A50 user manual.
85. Heywood, J., "Internal Combustion Engine Fundamentals", pp.43-44, McGraw-Hill International Editions, ISBN 0-07-100499-8, 1988.
86. Lotus engineering vehicle simulation software version 3.11g, user manual, tire data variables, 2001.
87. Heisler, H., "Advanced Vehicle Technology", p.593, Butterworth-Heinemann publications, ISBN 0-7506-5131-8.
88. Castillo, J., M., "The Analytical of the Efficiency of Planetary Gear Trains", Mechanism and Machine Theory, vol.37, pp.197-214, 2002.

89. Razimovski, E., I., "A Simplified Approach for Determining Power Losses and Efficiencies of Planetary Gear Drives", *Machine Design*, vol.9, pp.101-110, 1956.
90. Castillo, J., M., "A New Approach for the Determination of the Efficiency of Planetary Gear Trains", *Mechanism and Machine Theory*, vol.3, pp.151-156, 2001.
91. MacMillan, R., H., "Epicyclic Gear Efficiencies", *The Engineer*, vol.23, pp.727-728, 1949.
92. Montazeri, M. and Naghizadeh, M., "Development of Car Drive Cycle for Simulation of Emissions and Fuel Economy", *Proceedings of the 15th European Simulation Symposium*, 2003.
93. ADVISOR documentation, obtained from Powertrain Engineering and Testing Solutions For the Automotive Industry, <http://www.avl.com>, last visited June 2007.
94. National Renewable Energy Laboratory (NREL), obtained from <http://www.nrel.gov/vehiclesandfuels/vsa>, last visited June 2007.
95. Wipke, K.B., Cuddy, M.R. and Burch, S.D., "ADVISOR 2.1: A User-Friendly Advanced Powertrain Simulation Using a Combined Backward/Forward Approach", NREL/JA-540-26839, 1999.
96. Stone, R. and Ball, J., "Automotive Engineering Fundamentals", p.429, SAE International, ISBN 0-7680-0987-1, 2004.
97. Ricardo WAVE blocks manual, p.5-28, October 2003.
98. Triger, L., Paterson, J. and Drozd, P., "Hybrid Vehicle engine Size Optimization", SAE paper 1993-93-1793, 1993.
99. Cuddy, M. and Wipke, K., "Analysis of the Fuel Economy Benefit of Drivetrain Hybridization", SAE paper 1997-97-0289, 1997.
100. Nobuo, I., "Analysis of fuel economy and advanced systems of hybrid vehicles", Japanese SAE, 1997.

101. Soga, M., Shimada, M., Sakamoto, J., Otomo, A., “Development of Vehicle Dynamics Management System for Hybrid Vehicles: ECB System for Improved Environmental and Vehicle Dynamic Performance”, JSAE paper 20024667, 2002.

Appendix

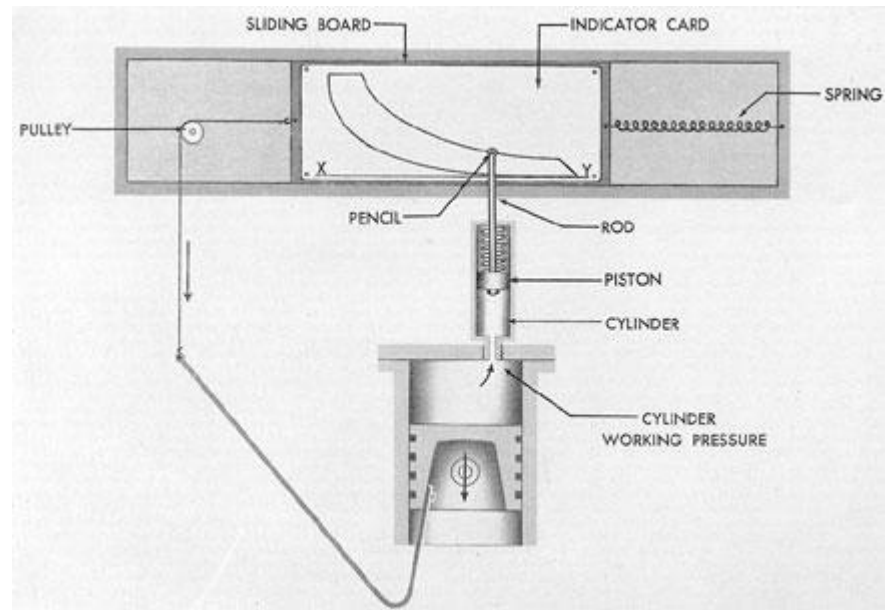


Figure A1: Engine Indicator.

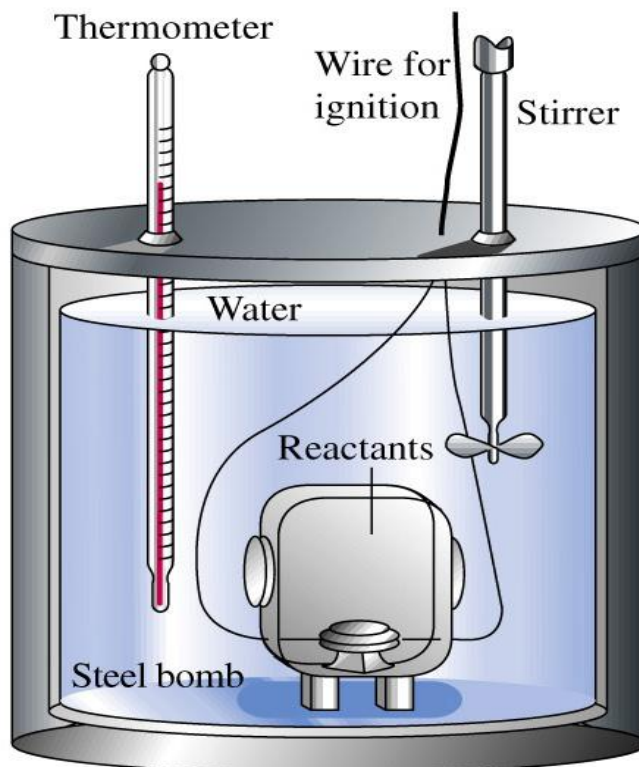


Figure A2: Bomb calorimeter [2].

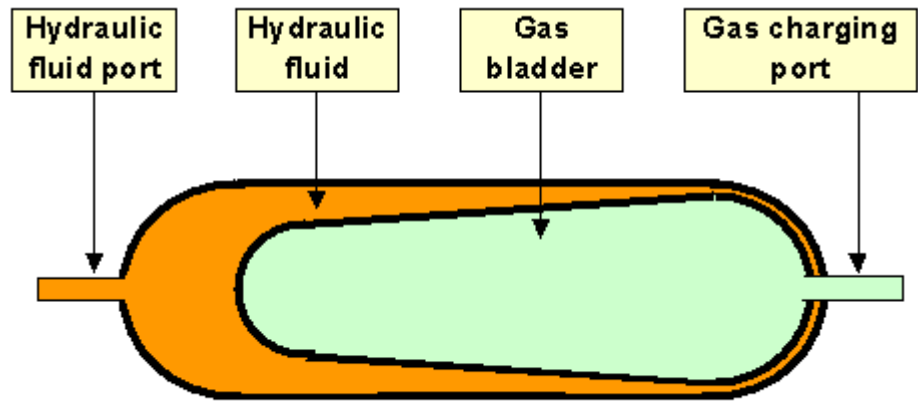


Figure A3: Accumulator.

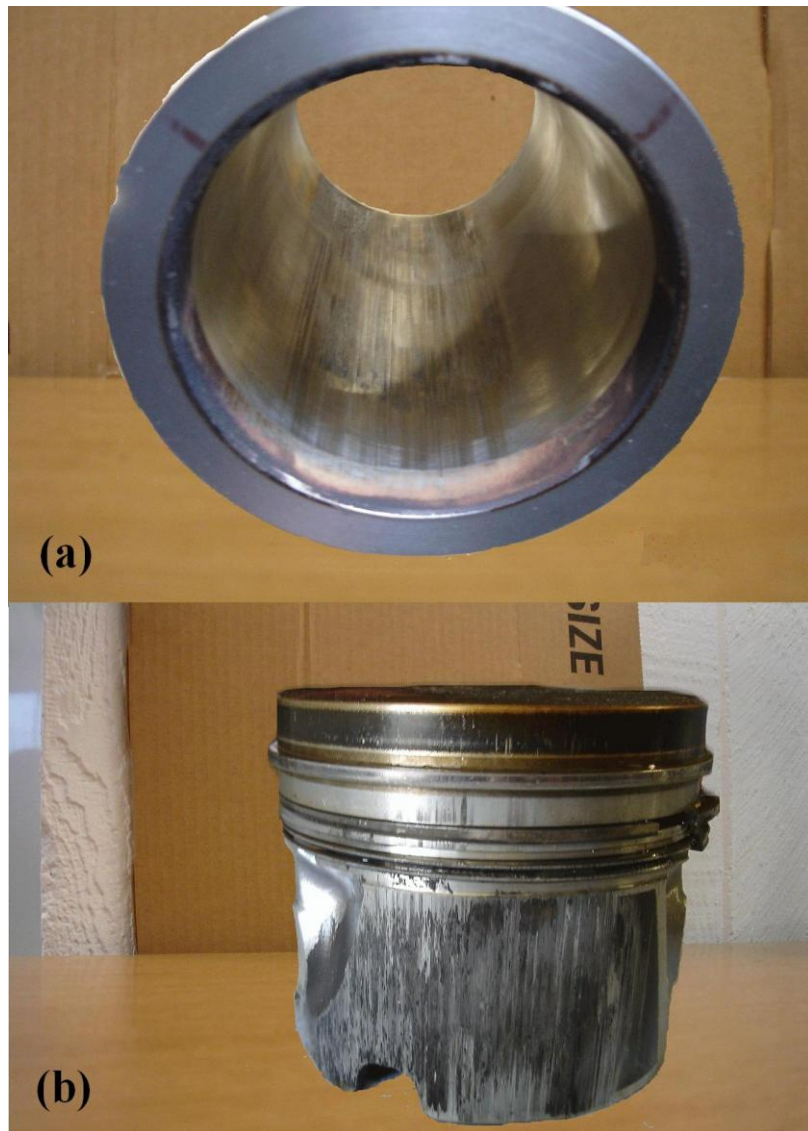


Figure A4: Seized cylinder liner (a) and piston (b).

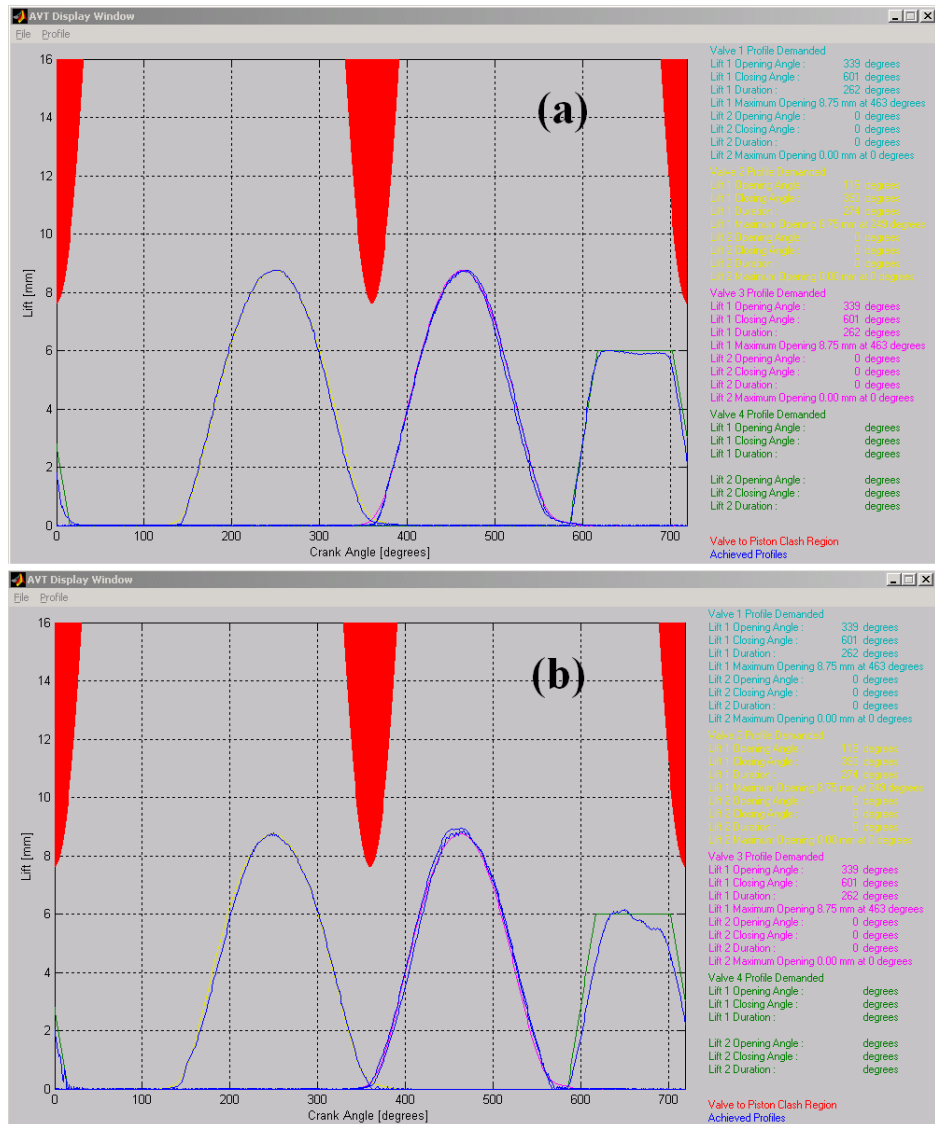


Figure A5: Desired and achieved valve lift profiles at 1000 rpm (a) and 4000 rpm (b).

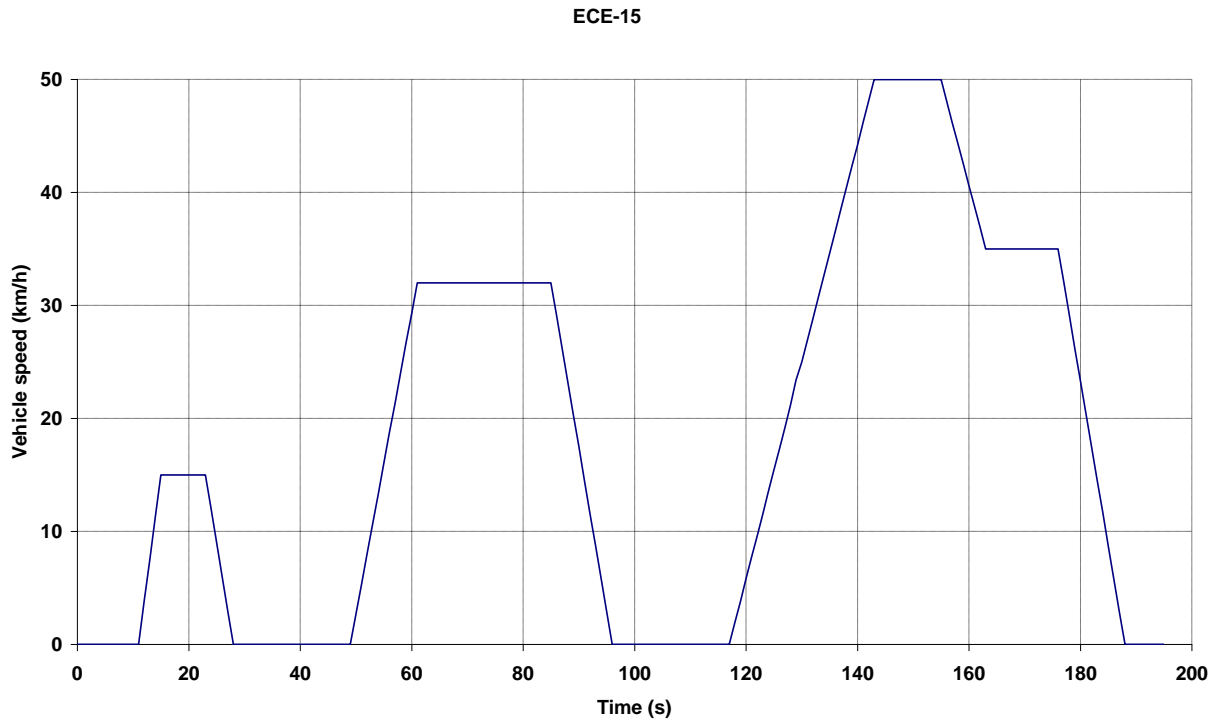


Figure A6: ECE-15 driving cycle time-speed diagram [93-95].

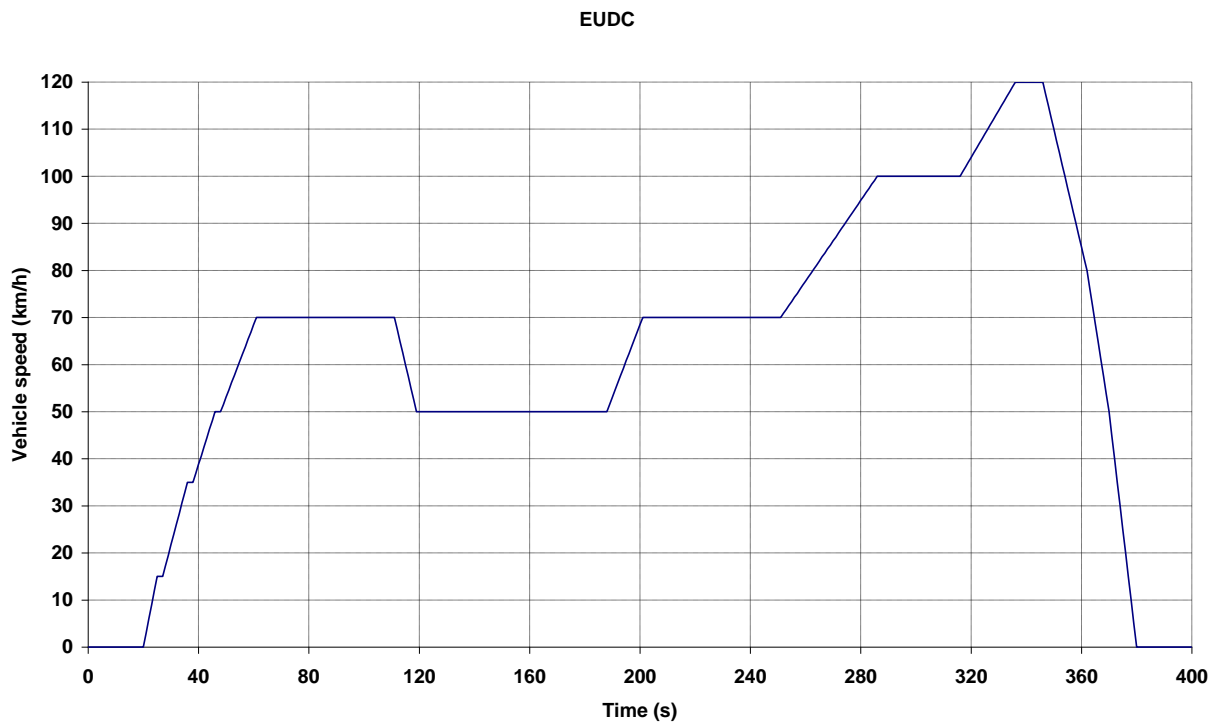


Figure A7: EUDC driving cycle time-speed diagram [93-95].

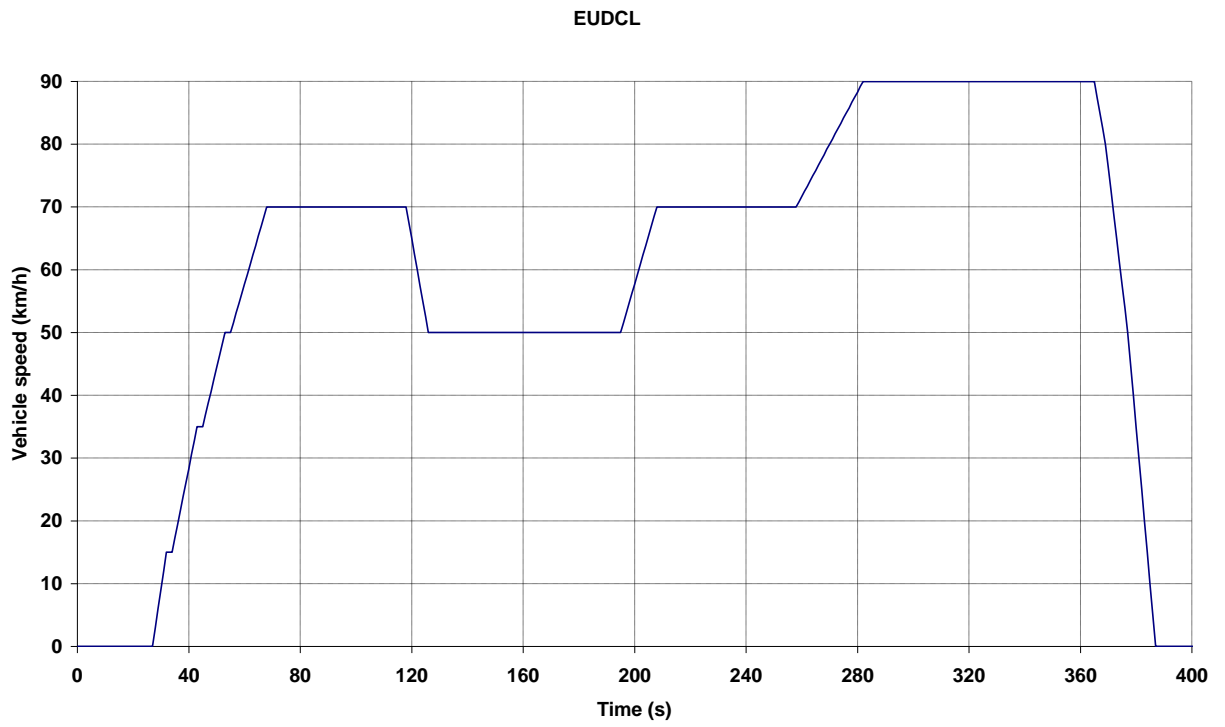


Figure A8: EUDCL driving cycle time-speed diagram [93-95].

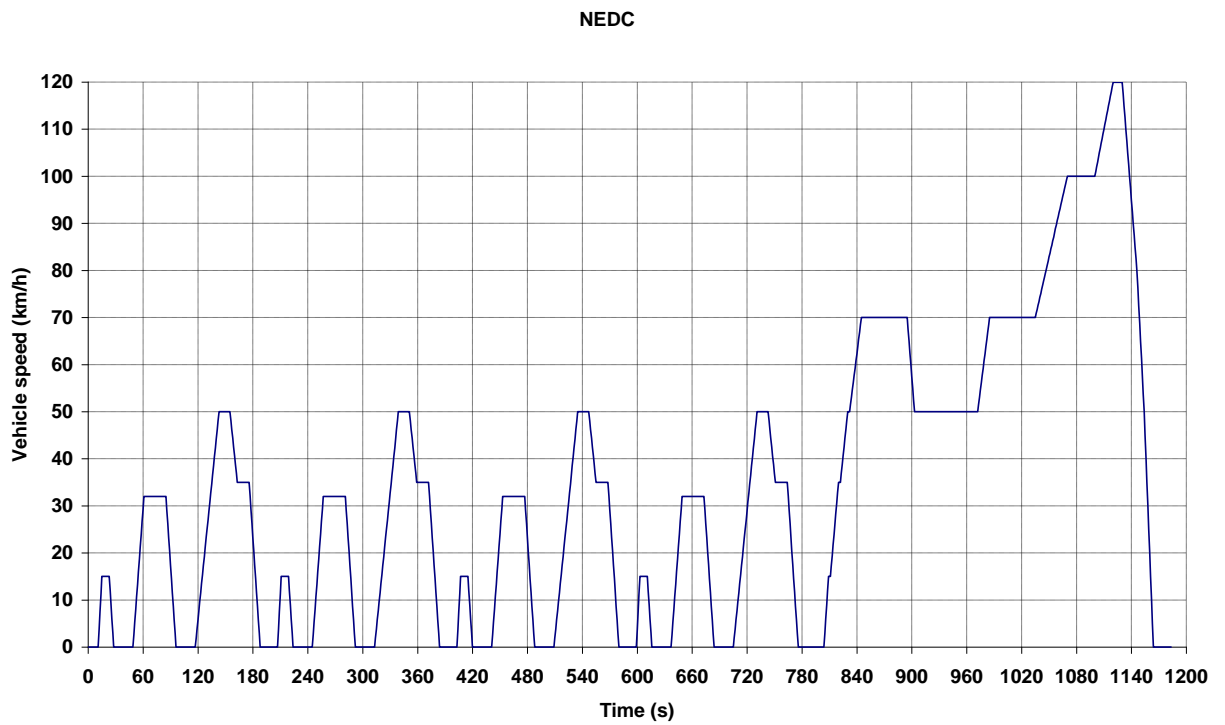


Figure A9: NEDC driving cycle time-speed diagram [93-95].

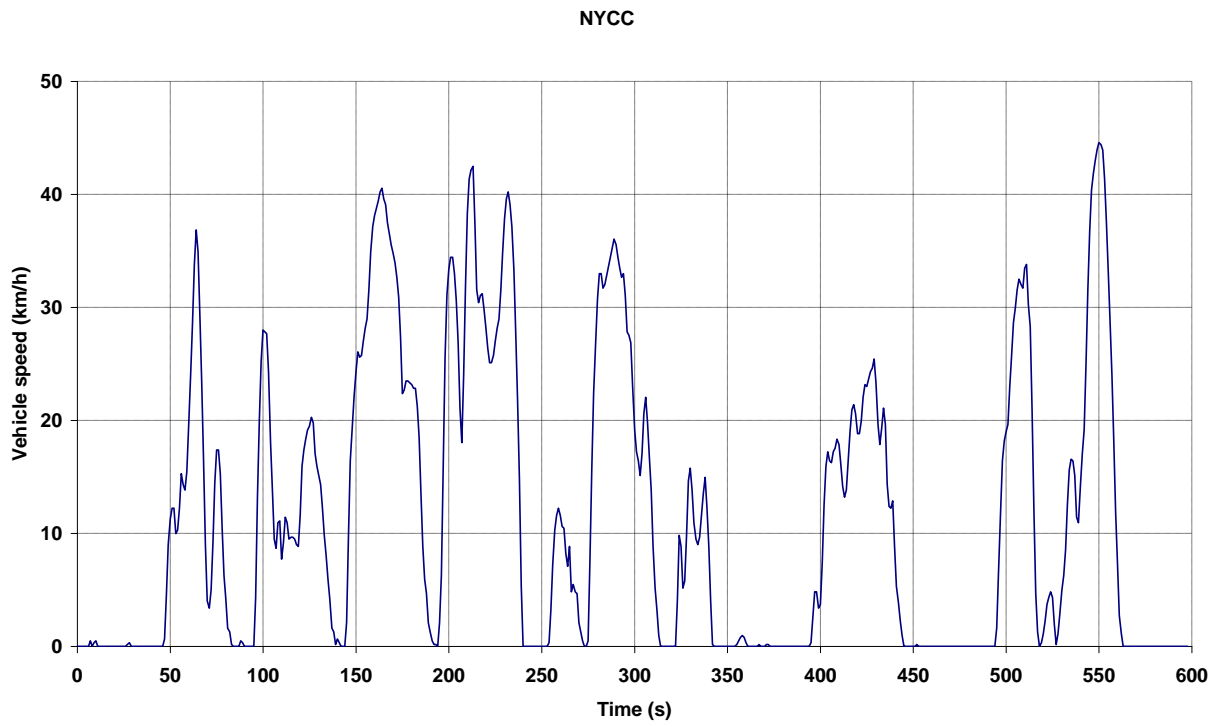


Figure A10: NYCC driving cycle time-speed diagram [93-95].

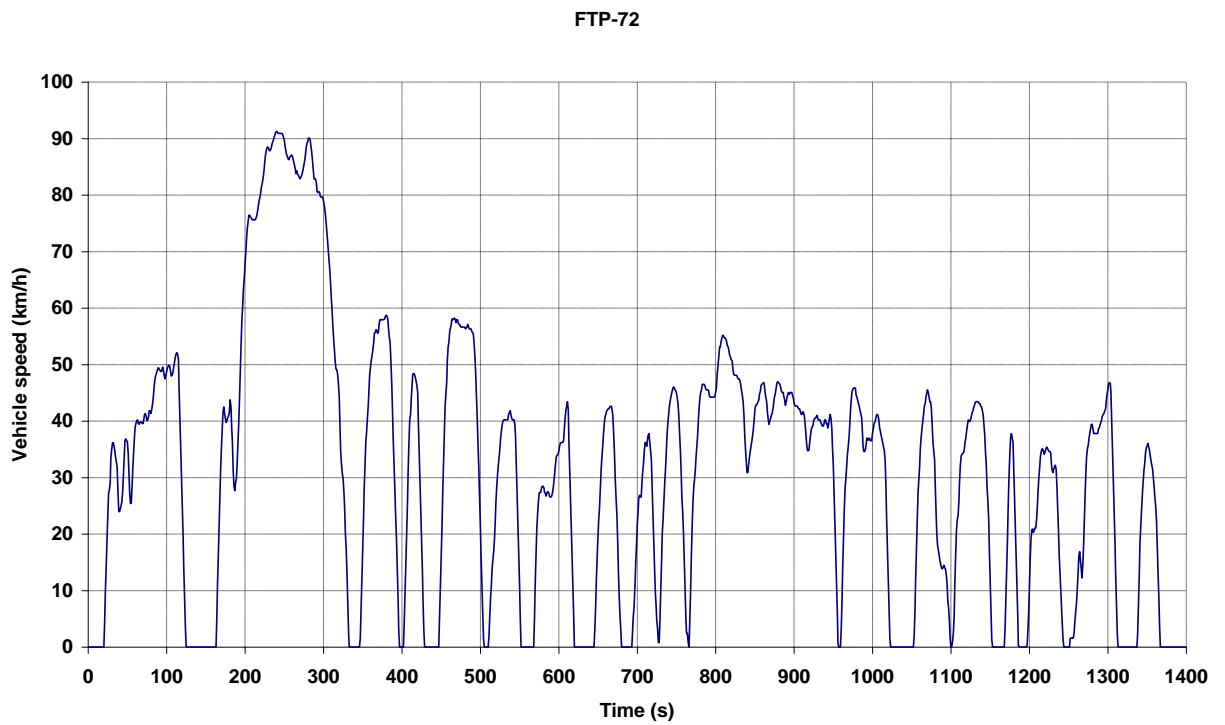


Figure A11: FTP-72 driving cycle time-speed diagram [93-95].

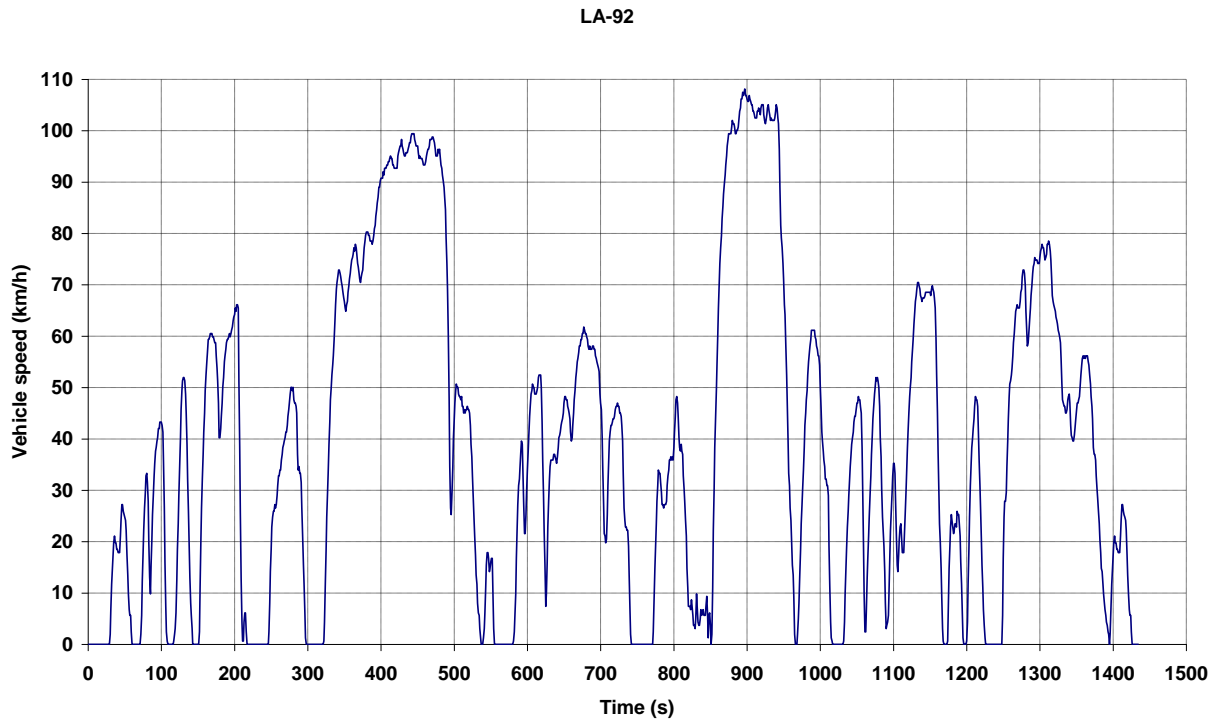


Figure A12: LA-92 driving cycle time-speed diagram [93-95].

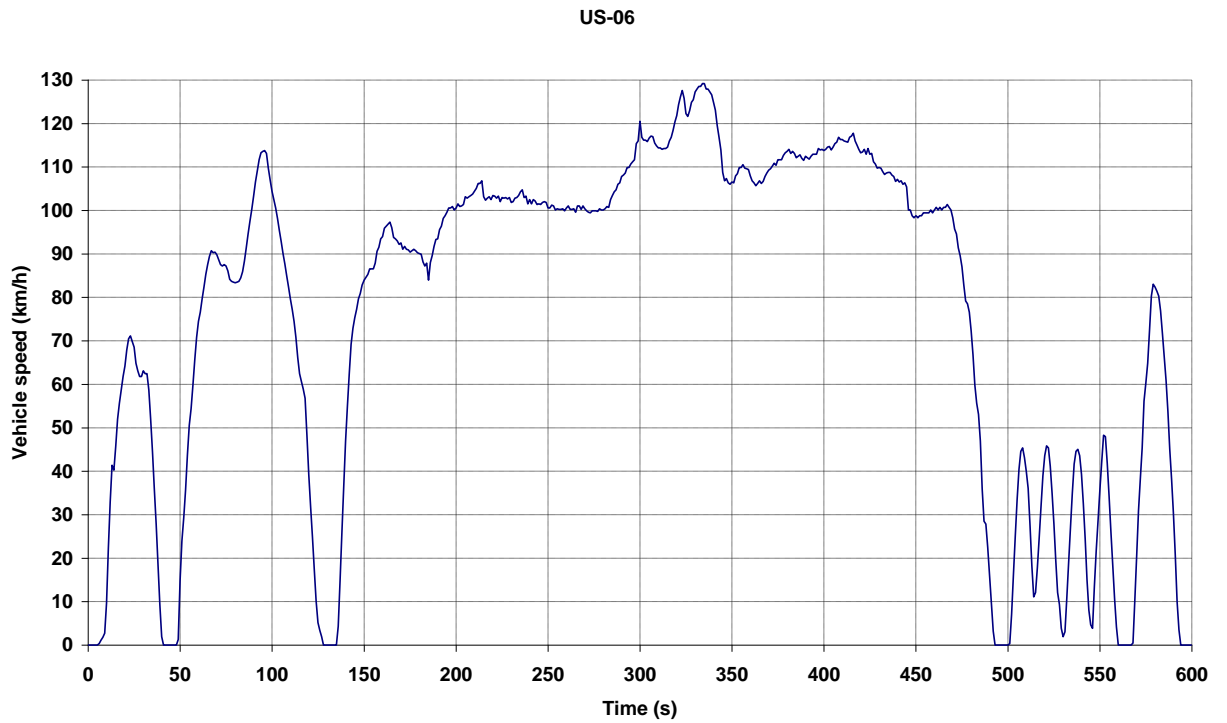


Figure A13: US-06 driving cycle time-speed diagram [93-95].

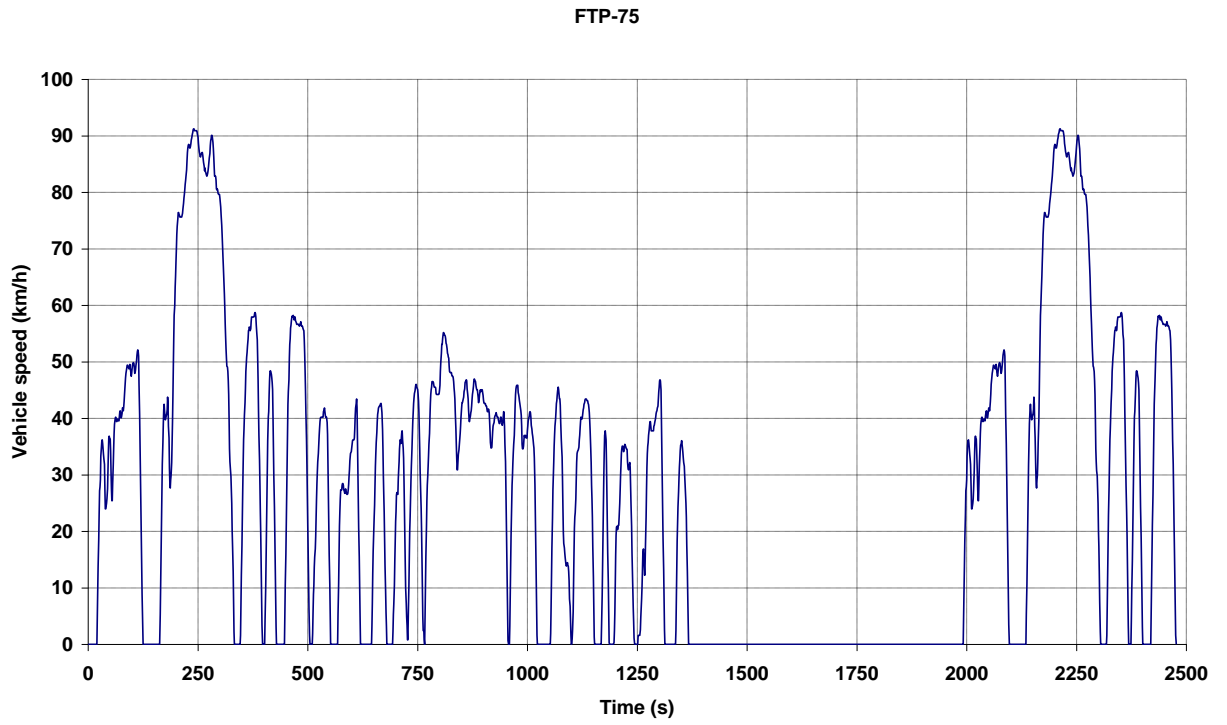


Figure A14: FTP-75 driving cycle time-speed diagram [93-95].

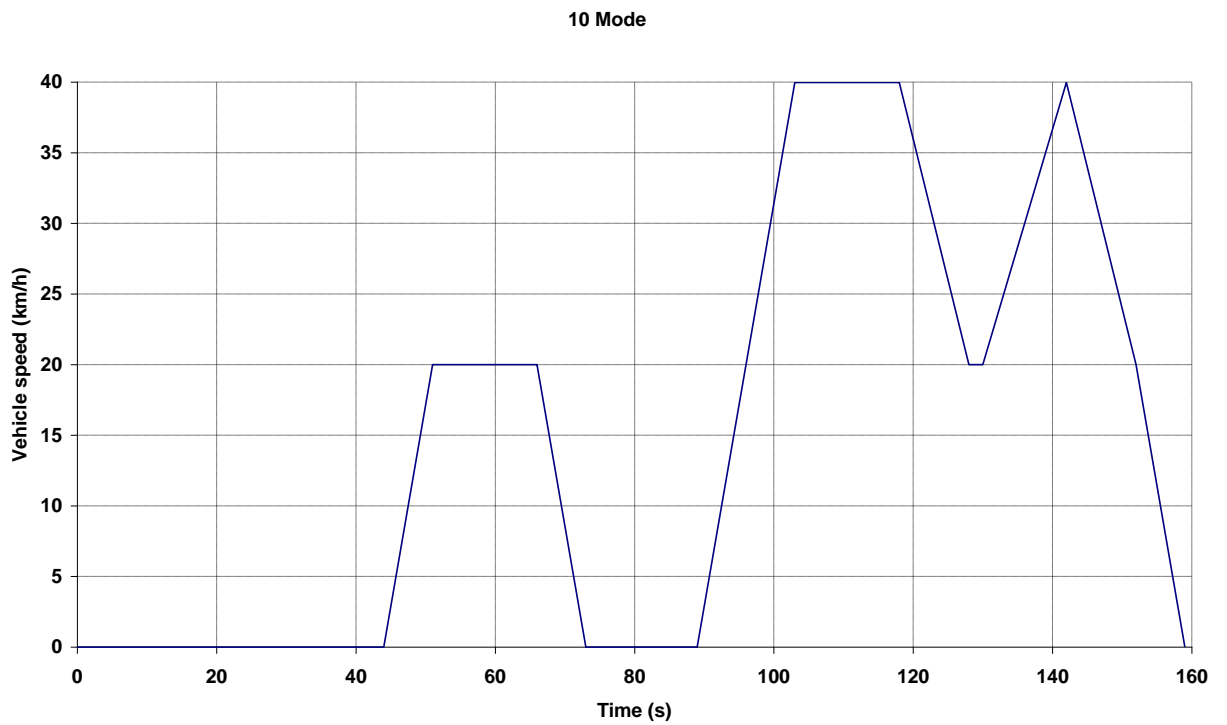


Figure A15: 10 Mode driving cycle time-speed diagram [93-95].

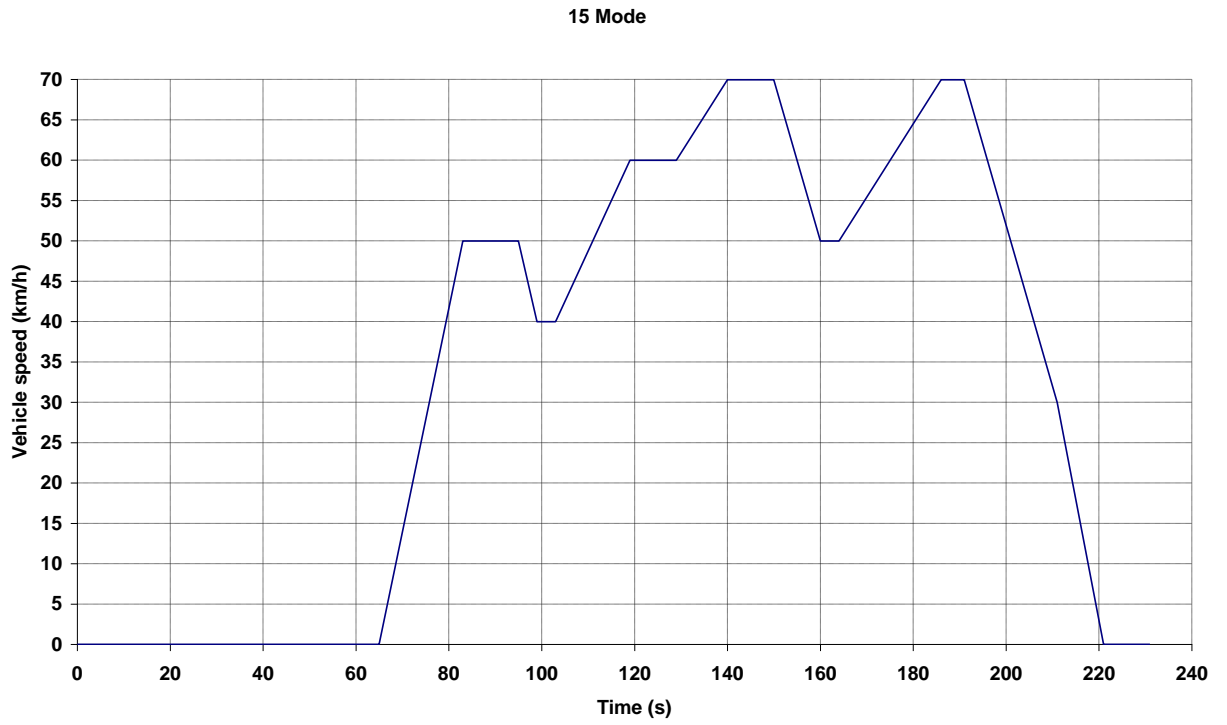


Figure A16: 15 Mode driving cycle time-speed diagram [93-95].

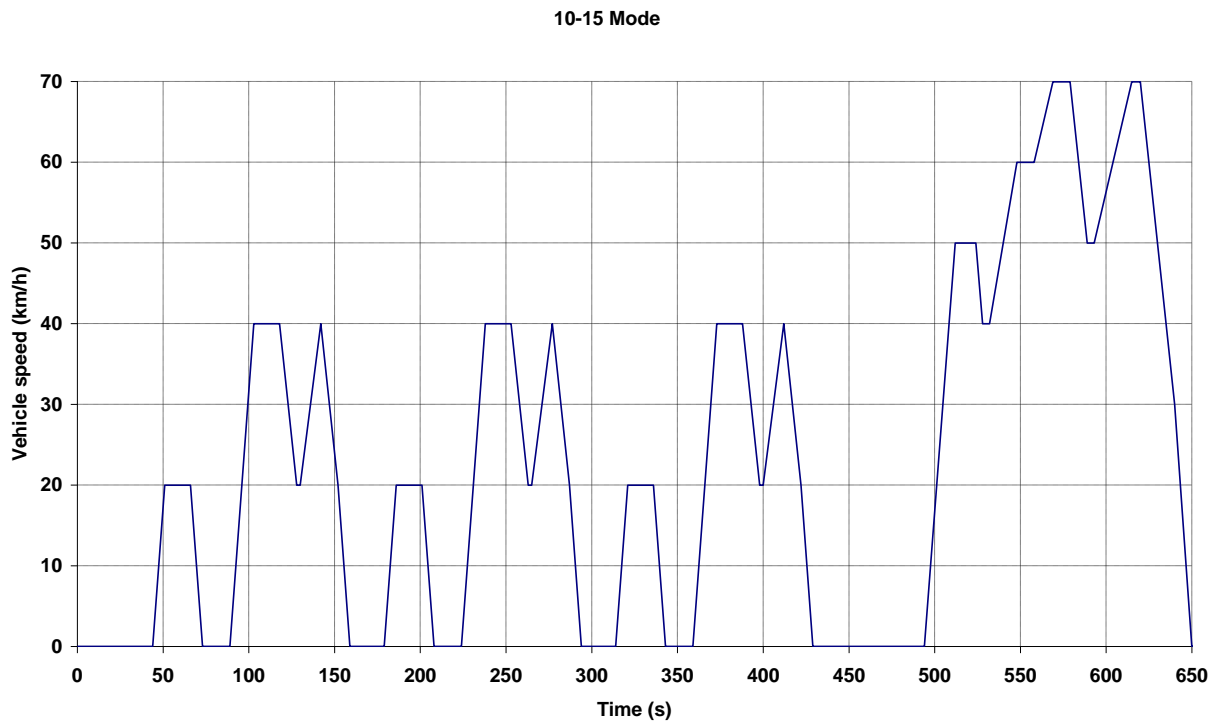


Figure A17: 10-15 Mode driving cycle time-speed diagram [93-95].